

Microscopic Theory of Linear and Nonlinear Terahertz Spectroscopy of Semiconductors

Dissertation
zur
Erlangung des Doktorgrades
der Naturwissenschaften
(Dr. rer. nat.)

dem Fachbereich Physik
der Philipps-Universität Marburg
vorgelegt

von
Johannes Steiner

aus Attendorn

Marburg(Lahn), 2008

Vom Fachbereich Physik der Philipps-Universität Marburg
als Dissertation angenommen am 24.11.2008

Erstgutachter: Prof. Dr. M. Kira
Zweitgutachter: Prof. Dr. F. Gebhard
Externer Gutachter: Prof. Dr. I. Galbraith

Tag der mündlichen Prüfung: 09.12.2008

Zusammenfassung

Seit der Entwicklung moderner Methoden des Kristallwachstums hat die Halbleitertechnologie enorme Fortschritte gemacht. Dank neuer Verfahren können sehr reine Halbleiterheterostrukturen hergestellt werden, deren Beschaffenheit mit nahezu atomarer Präzision kontrolliert werden kann. Dies hat zur Entwicklung vieler Anwendungen geführt, wie z.B. zur Herstellung von hochwertigen Computerchips, von Leuchtdioden (LEDs) und von Halbleiterlasern. Die Erforschung von Halbleitern ist vor allem aus zwei Gründen von Interesse für die theoretische Physik: Erstens erfordert die Weiterentwicklung und Verbesserung elektronischer und optoelektronischer Bauelemente ein detailliertes Verständnis der zugrundeliegenden mikroskopischen Prozesse und zweitens sind die hochwertigen Nanostrukturen, die heute künstlich hergestellt werden können, ideale Modellsysteme, um fundamentale physikalische Anregungen in Festkörpern zu untersuchen.

Experimentell können die quantenmechanischen Prozesse in Halbleitern gut durch optische Experimente untersucht werden. Es liegt nahe, in diesen Experimenten Licht aus einem Frequenzbereich zu verwenden, dessen Energie ungefähr der Bandlückenenergie entspricht, da so Elektronen vom Valenz- ins Leitungsband angehoben werden können, wobei ein positiv geladenes Loch im Valenzband zurückbleibt. Die Bandlückenenergie in typischen Halbleitern beträgt ungefähr ein Elektronenvolt ($1 \text{ eV} \hat{=} 1240 \text{ nm} \hat{=} 242 \text{ THz}$), so dass Experimente bisher vor allem sichtbares Licht bzw. Licht aus dem nah-infraroten Teil des elektromagnetischen Spektrums verwendet haben. Dank der Entwicklung des modengekoppelten Lasers in den 80er Jahren konnten Experimentalphysiker Halbleiter mit optischen Pulsen anregen, die kürzer als eine Pikosekunde ($1 \text{ ps} = 10^{-12} \text{ s}$) sind, um so die Halbleiterdynamik auf dieser Zeitskala zu untersuchen. Mit der Entwicklung von Methoden der kohärenten Spektroskopie wie des Vier-Wellen-Mischens [1–3] und der Anreg-Abtast-Experimente [4, 5] (engl. pump-probe experiments) wurde es möglich, Streuprozesse von Ladungsträgern direkt nach der optischen Anregung zu untersuchen.

Die einfachste theoretische Beschreibungsmöglichkeit für die Dynamik von optisch angeregten Halbleitern stellen sogenannte mean-field Theorien dar, die davon ausgehen, dass jeder Ladungsträger sich effektiv wie ein einzelnes Teilchen im mittleren Feld der übrigen Teilchen verhält. Allerdings versagt die mean-field Theorie als Beschreibungsmodell, wenn die Dynamik durch Korrelationseffekte bestimmt wird. In Halbleitern ist dies selbst bei niedrigen Dichten der Fall, da die durch die optische Anregung erzeugten Elektronen und Löcher stark miteinander Coulomb wechselwirken. Daher stellt der optisch angeregte Halbleiter ein ideales Modellsystem dar, um Korrelationseffekte und die Vielteilchenquantendynamik zu untersuchen. Das inkohärente Exziton [6, 7] ist eines der berühmtesten Beispiele für Korrelationen in Halbleitern, denn es besteht aus einem Elektron und einem Loch, die aufgrund der anziehenden Coulombwechselwirkung ein echt gebundenes Teilchen bilden. Das Exziton ähnelt in vielerlei Hinsicht einem Wasser-

stoffatom, das aus einem Elektron und einem Proton besteht. Ein weiteres Beispiel für Korrelationen in Halbleitern ist das Plasmon [8], eine kollektive Ladungszillation in dem optisch angeregten Elektron-Loch-Plasma. Die Erforschung von Korrelationen zwischen Teilchen ist nicht nur ein zentrales Anliegen der Halbleiterphysik, sondern auch der Festkörperphysik im Allgemeinen und ist noch immer Thema vieler experimenteller und theoretischer Untersuchungen.

Optische Experimente, die sichtbares oder nah-infrarotes Licht verwenden, sind nur bedingt dazu geeignet, Korrelationseffekte wie Exzitonen und Plasmonen in Halbleitern zu untersuchen, da die Energien dieser sogenannten Quasiteilchen einem anderen Frequenzbereich des Lichts entsprechen. So entspricht die Bindungsenergie eines Exzitons typischer Weise Frequenzen, die im Terahertz (THz) - Bereich des elektromagnetischen Spektrums liegen ($4.13 \text{ meV} \hat{=} 300 \mu\text{m} \hat{=} 1 \text{ THz}$). In Halbleitern gilt dasselbe in der Regel für die Frequenz des Plasmons, d.h. für die Frequenz kollektiver Ladungszillationen. Daher liegt es natürlich nahe, diese Vielteilcheneffekte mit Licht aus dem THz-Bereich des elektromagnetischen Spektrums zu untersuchen.

Erst in den letzten Jahrzehnten wurde es dank der Entwicklung effizienter kohärenter THz-Quellen wie optisch gepumpter Molekularlaser [9], freier Elektronenlaser (FEL) [10] und *p*-Germanium Laser [11] möglich, in Experimenten Licht aus dem THz-Bereich zu verwenden. Der FEL ist besonders dazu geeignet, da er hohe Intensitäten liefert, dabei aber kontinuierlich stimmbar im THz-Bereich ist. Allerdings sind FEL sehr aufwändige Anlagen, so dass bisher nur wenige gebaut wurden. In den letzten Jahren sind hochwertige kohärente THz-Quellen auch für einzelne Labore zugänglich geworden - vor allem dank Fortschritten in der THz-Erzeugung durch optische Pulse [12]. Dabei werden optische Femtosekunden-Laser Pulse genutzt, um THz-Strahlung zu erzeugen, z.B., indem ultraschnelle Photoströme induziert werden oder durch optische Gleichrichtung in nicht-linearen Kristallen. Zusammen mit passenden Detektoren, z.B. dem elektro-optischen Sampling [13], können diese Quellen für die zeitaufgelöste THz-Spektroskopie genutzt werden. THz-Felder können verwendet werden, um interne Übergänge von Exzitonen und Plasmonen, aber auch um Gitterschwingungen und Subbandübergänge in Halbleiternanostrukturen anzuregen.

In einem typischen Experiment erzeugt eine optische Interbandanregung einen bestimmten Vielteilchenzustand, der dann durch einen schwachen THz-Puls abgetastet wird. Anhand des Absorptionsverhaltens lassen sich dann Aussagen über die vorhandenen Quasiteilchen machen: Ist z.B. eine Exzitonenpopulation vorhanden, so zeigt das THz-Spektrum charakteristische Absorptionslinien, die den möglichen intraexzitonischen Übergängen im THz-Bereich entsprechen und so experimentell identifiziert werden können. Diese exzitonische THz-Spektroskopie ähnelt der Spektroskopie von atomaren Gasen, bei der die Existenz einer bestimmten Art von Atomen aus dem Absorptionsspektrum eines schwachen optischen Pulses abgeleitet wird. Wegweisende Experimente [14–18] konnten sich mit Hilfe der THz-Spektroskopie der zentralen Frage zuwenden, ob und unter welchen Umständen sich nach einer optischen Anregung eine echte Exzitonenpopulation bildet. Die THz-Spektroskopie ist nicht auf Halbleiter beschränkt. Da THz-Felder auch Vibrations- und Rotationsübergänge in Molekülen anregen können [19, 20], werden sie verwendet, um chemische Moleküle und biologische Systeme zu untersuchen.

Außerdem gibt es Anwendungen in den Materialwissenschaften, der tomographischen Bildgebung und der Sicherheitstechnik [21].

In dieser Arbeit stelle ich eine mikroskopische Theorie dar, um THz-induzierte Prozesse in Halbleitern zu beschreiben. Der Prozess der Entstehung von Exzitonen und anderen Quasiteilchen nach optischer Anregung wurde theoretisch detailliert und für viele unterschiedliche Bedingungen untersucht [6, 22–26]. Ich werde den Bildungsprozess hier nicht modellieren, sondern einen realistischen Vielteilchenzustand als Anfangszustand annehmen. Im Zentrum meiner Untersuchungen stehen Fälle, bei denen der durch optische Anregung erzeugte Vielteilchenzustand durch *starke* THz Felder angeregt wird. Während schwache Pulse dazu dienen, den Vielteilchenzustand abzutasten, so können starke THz-Pulse die Quasiteilchen auf eine Art und Weise manipulieren, wie es mit konventionellen Methoden nicht möglich ist. Die nichtlineare THz-Dynamik von Exzitonenpopulationen ist von besonderem Interesse, da Ähnlichkeiten und Unterschiede zu atomaren Systemen untersucht werden können. Eine theoretische Untersuchung des nichtlinearen THz-Regimes in Halbleitern ist zeitgemäß, da Experimentalphysiker seit der Entwicklung effizienter und erschwinglicher Hochfeld-THz-Quellen [27] vermehrt starke THz-Anregungen in Halbleitern untersuchen [28–33].

Die hier dargestellte Theorie basiert auf einer Dichtematrixtheorie, die die sogenannte Cluster Entwicklungsmethode für Halbleiter verwendet. Mit Hilfe dieser Methode kann die Wechselwirkung von THz-Licht mit korrelierten Quasiteilchen wie Exzitonen konsistent beschrieben werden. In Kapitel 2 stelle ich den Hamiltonoperator des wechselwirkenden Systems vor und leite im Anschluss in Kapitel 3 die Gleichungen her, die die THz-Dynamik sowohl im kohärenten als auch im inkohärenten Regime beschreiben. Das kohärente Regime besteht nur wenige Pikosekunden nach der optischen Anregung, während noch Interbandkohärenzen vorhanden sind. Das inkohärente Regime dagegen bezeichnet das Zeitintervall, in dem die Interbandkohärenzen bereits zerfallen sind, die optisch angeregten Ladungsträger aber noch nicht rekombiniert sind.

In Kapitel 4 stelle ich die lineare und nichtlineare THz-Spektroskopie von Halbleitern dar. Bei der linearen Spektroskopie werden schwache Pulse verwendet, bei der nichtlinearen dagegen starke. Insbesondere identifiziere ich die physikalischen Größen, die in typischen Experimenten zugänglich sind. Die lineare THz-Antwort wird analytisch für allgemeine Bedingungen gelöst und es wird die sogenannte *THz-Elliott-Formel* hergeleitet, mit der, wie in Kapitel 5 ausgeführt wird, gezeigt werden kann, dass schwache THz-Pulse zum Nachweis von Exzitonenpopulationen und Plasmonen verwendet werden können. Im Gegensatz zur THz-Spektroskopie sind Interband-Spektroskopie und Photolumineszenz-Experimente nicht dazu geeignet, Exzitonenpopulationen eindeutig nachzuweisen [7, 34].

Um nichtlineare THz-Anregungen zu untersuchen, wende ich die entwickelte Theorie auf wohldefinierte Situationen an. In Kapitel 6 untersuche ich zunächst, wie starke THz-Anregungen das lineare optische Absorptionsspektrum beeinflussen. Neben einer ausschließlich theoretischen Analyse stelle ich auch einen quantitativen Vergleich mit einem vor kurzem durchgeführten Experiment dar. Da das THz-Feld optisch-helle und optisch-dunkle Zustände miteinander koppelt, z.B. die $1s$ und $2p$ Exzitonzustände, führt die THz-Anregung zu charakteristischen Änderungen in den optischen Spektren.

Eine besondere Eigenschaft nichtlinearer THz-Anregungen besteht darin, dass die Rabi-Frequenz oft in der Größenordnung der $1s-2p$ Übergangsfrequenz liegt, so dass extrem nichtlineare Effekte auftreten. Ich identifiziere auch die ponderomotiven Beiträge, die entstehen, weil das THz-Feld langsam genug oszilliert, so dass Elektronen und Löcher auf das elektrische THz-Feld klassisch reagieren.

In Kapitel 7 untersuche ich starke THz-Anregungen einer existierenden $1s$ -Exzitonpopulation. Die THz-Dynamik von inkohärenten Exzitonen ähnelt in vielerlei Hinsicht der der Optik an atomaren Systemen. Ich stelle unterschiedliche Anregungsbereiche dar und identifiziere so Rabioszillationen von Exzitonpopulationen, die Erzeugung von ballistischen Elektronen-Loch-Wellenpaketen sowie die Erzeugung höherer Harmonischer. Außerdem zeige ich, dass mit Hilfe der Theorie auch die Ergebnisse von vor kurzem durchgeführten nichtlinearen THz-Experimenten in Cu_2O erklärt werden können, die Rabioszillationen zwischen zwei optisch-dunklen Zuständen untersucht haben. Neben Ähnlichkeiten zu atomaren Systemen gibt es wichtige Unterschiede, die durch Vielteilchenstreuung und die fermionische Substruktur in Halbleitern entstehen. Selbst bei niedrigen Dichten führen diese Effekte zu viel kürzeren Dephasierungszeiten und zu ponderomotiven Beiträgen in der THz-Antwort. Ich beschreibe die ponderomotiven Beiträge detailliert und zeige, dass sie in der Regel vom messbaren Signal isoliert werden können.

In Kapitel 8 untersuche ich schließlich die nichtlineare Anregung eines korrelierten Elektronen-Loch-Plasmas, bei dem exzitonische Effekte vernachlässigt werden können. In diesem Fall zeigt sich, dass die THz-Kopplung eine Erwärmung des Plasmas bewirkt. Die Theorie der Cluster-Entwicklung ermöglicht ein anschauliches und detailliertes Verständnis dieser Prozesse.

Eine Aufgabe der nahen Zukunft wird sein, die theoretische Beschreibung von THz Prozessen im Rahmen der Cluster Entwicklung zu erweitern. Man könnte Konfigurationen theoretisch modellieren bei denen mehrere THz-Pulse den Vielteilchenzustand anregen, um so die Möglichkeit des THz Vier-Wellen-Mischens oder des adiabatischen Transfers von Exzitonpopulationen zu untersuchen. Wenn das THz-Feld vollständig quantisiert wird, kann man Effekte wie z.B THz-Lumineszenz oder quantenoptische Effekte in exzitonischen Zweiniveausystemen untersuchen.

Acknowledgments

First, I want to thank my parents who supported me throughout the course of my studies and ultimately made possible this Thesis.

I especially thank Professor Mack Kira for being an ideal supervisor who successfully guided me throughout my PhD time giving expert advice on all the small and large problems I had.

Just as much I want to thank Professor Stephan Koch for his friendly reception in the group and his ever competent and motivating feedback on my work.

I also thank Professor Peter Thomas and the rest of the group for the pleasant and relaxed atmosphere and for many interesting discussions about physics and other topics.

Especially, I'd like to thank Ada and Noemi for being fun roommates as well as Walter and Daniel for many fruitful "terahertz"-discussions which always brought forward my work.

Thanks also to Professor Florian Gebhard and Professor Ian Galbraith for agreeing to evaluate my Thesis.

This work would not have been possible in its present form without the experiments which I had the opportunity to analyze. In particular, I am indebted to many valuable and productive discussions with Professor Yun-Shik Lee, Dr. Rupert Huber, Dr. Sangam Chatterjee, Torben Grunwald and Professor Martin Hofmann.

Last but not least, I want to thank Sandra for all the time and fun we had together and for her support in all aspects of life.

Author's Contributions

Publications

- (I) J. T. Steiner, M. Kira, and S. W. Koch, "Generation of terahertz radiation using semiconductor heterostructures", Proc. SPIE **6468** (2007)
- (II) C. Brenner, S. Hoffmann, M. R. Hofmann, M. R. M. Salhi, M. Koch, A. Klehr, G. Erbert, G. Tränkle, J. T. Steiner, M. Kira, and S. W. Koch, "Detection of THz radiation with semiconductor diode lasers", Appl. Phys. Lett. **91**, 101107 (2007)
- (III) J. R. Danielson, Y.-S. Lee, J. P. Prineas, J. T. Steiner, M. Kira, and S. W. Koch, "Interaction of strong single-cycle terahertz pulses with semiconductor quantum wells", Phys. Rev. Lett. **99**, 237401 (2007)
- (IV) J. T. Steiner, M. Kira, S. W. Koch, T. Grunwald, D. Köhler, S. Chatterjee, G. Khitrova, H. M. Gibbs "Interaction of THz radiation with semiconductors: microscopic theory and experiments", Adv. in Sol. State Phys. **47**, 223 (2008)
- (V) J. T. Steiner, M. Kira, and S. W. Koch, "Optical nonlinearities and Rabi flopping of an exciton population in a semiconductor interacting with strong terahertz fields", Phys. Rev. B **77**, 165308 (2008)
- (VI) J. T. Steiner, M. Kira, and S. W. Koch, "Nonlinear excitations of semiconductor quantum wells with intense terahertz fields", Proc. SPIE **6889** (2008)
- (VII) J. T. Steiner, M. Kira, and S. W. Koch, "Semiconductor excitons in strong terahertz fields", phys. stat. sol. (c), accepted (2008)
- (VIII) S. Leinß, T. Kampfrath, K. v. Volkman, M. Wolf, J. ,T. Steiner, M. Kira, S. W. Koch, A. Leitenstorfer, and R. Huber, "Terahertz coherent control of optically dark paraexcitons in Cu₂O", Phys. Rev. Lett. **101**, 246401 (2008)
- (IX) S. Chatterjee, T. Grunwald, D. Köhler, T. Jung, K. Pierz, G. Khitrova, H. M. Gibbs, D. Golde, J. T. Steiner, M. Kira, and S. W. Koch, "Terahertz signatures of plasmons in quasi-two-dimensional semiconductor systems", in preparation (2008)

Original Contributions

When I started out as a PhD student in Marburg, my main project was to investigate strong THz excitations of incoherent excitons, i.e., truly bound electron-hole pairs in semiconductors which I had already started to work on during my diploma thesis. At the time, our group had already developed a theoretical framework to describe the *linear* THz coupling and numerical evaluations of the theory had shown that THz spectroscopy is well suited to monitor exciton formation processes in semiconductors. I generalized the THz theory to the *nonlinear* regime and implemented the numerical code which describes strong THz excitations of incoherent excitons in quantum wires. The numerical evaluation is complex because the description of nonlinear THz processes requires the inclusion of correlation effects and the symmetry breaking induced by intraband processes.

As there were only few previous theoretical investigations of strong-field THz excitations of incoherent excitons, I focused on identifying and understanding the basic processes. Varying the THz pulses and system parameters, I mapped out different excitation regimes; I found excitonic Rabi-flopping, ionization-effects and high-harmonic generation for an excitonic initial many-body state, as well as a Drude-like carrier heating for a plasma-like initial many-body state. In particular, I investigated phenomena which are not necessarily expected from simple analogies between incoherent excitons in semiconductors and atomic systems. I investigated, e.g., ponderomotive and extreme-nonlinear effects as well as intraexcitonic transitions that depend on the center-of-mass motion. While the linear response of incoherent excitons has been solved analytically in our group a few years ago and is just reviewed in this Thesis, I derived new analytical results for the nonlinear regime which describe, e.g., the density dynamics during Rabi flopping and the THz-induced heating rate of a correlated electron-hole plasma. My original theoretical results concerning the THz dynamics of incoherent excitons are presented in this Thesis and are published mainly in Paper [V] but also in Paper [I].

A substantial – if not the largest – part of my PhD time was devoted to the theoretical analysis and explanation of experimental data. In the experiment performed by Y.-S. Lee *et al.* (Oregon State Univ.), a THz-pump and optical probe configuration was used to study time-resolved nonlinear effects in AlGaAs/GaAs multi quantum wells; they were hoping to demonstrate THz-induced Rabi flopping between the $1s$ and $2p$ exciton states. To reproduce and explain the experimental results, I extended the nonlinear THz theory to the coherent regime and implemented the numerics for two-dimensional quantum wells. For a quantitative theoretical analysis, it was necessary to include the light propagation through the experimental sample. The relevant bandstructure parameters for the heterostructure I obtained from the standard program used in our group. To reproduce the experimental data, it was crucial that ponderomotive contributions due to the strong THz field were treated correctly. Understanding how ponderomotive contributions exactly enter into our microscopic theory was a central issue of my investigations. Although we could not demonstrate clear Rabi-flopping in the experiment, we arrived at one of the first quantitative experiment-theory comparisons for this kind of THz experiment demonstrating time-resolved ponderomotive and extreme-nonlinear

effects. I presented these findings in Paper [III]. Moreover, I analyzed the THz dynamics of coherent excitons for idealized conditions. These theoretical results are presented in this Thesis and in Paper [VI].

Another experiment that I analyzed was performed by R. Huber *et al.* (Univ. of Konstanz, Free Univ. of Berlin). They investigated nonlinear THz excitations of incoherent, optically-dark excitons in cuprous oxide (Cu_2O). The analysis of the experimental results was an excellent proving ground for the theory which I had developed for GaAs-type systems. I extended the theory to cuprous oxide where the consistent inclusion of band-structure effects was the main difficulty. Here, I also obtained very good quantitative agreement between experiment and theory. Especially, it turned out that ponderomotive contributions masked the more interesting THz-induced nonlinearities. For the understanding of the experimental results, it was thus crucial to develop a scheme (presented in Paper [VII]) that rigorously removes the ponderomotive contributions. The results of the experiment-theory comparison are presented in this Thesis and in Paper [VIII].

I also analyzed experiments performed by M. Hofmann *et al.* (Univ. of Bochum). The experiments showed that strong THz radiation leads to carrier heating which can be reliably detected via a semiconductor diode laser. Here, we did not aim for a quantitative experiment-theory comparison but I used our microscopic theory to explain the underlying heating mechanisms. The results are presented in this Thesis and in Paper [II]. Finally, I have also collaborated with experimentalists in Marburg and contributed to Paper [IX]. I have presented results on conferences giving an invited talk at SPIE Photonics West 2008 in San Jose, USA and presenting a poster at the NOEKS09 in Müritz, Germany.

Contents

1. Introduction	1
2. System Hamiltonian	5
2.1. Hamiltonian in First Quantization	5
2.2. Light-Matter Interaction in Second Quantization	6
2.3. Complete Hamiltonian in Second Quantization	11
3. Semiconductor Response to Classical Terahertz Excitation	13
3.1. Light Propagation	13
3.2. Hierarchy Problem and Cluster-Expansion Approach	14
3.3. Singlet Equations in the Coherent Regime	18
3.3.1. Maxwell-Semiconductor-Bloch Equations	18
3.3.2. Simultaneous Optical and THz Excitation	19
3.4. Singlet-Doublet Equations in the Incoherent Regime	22
4. Linear and Nonlinear Terahertz Spectroscopy	25
4.1. Linear Terahertz Susceptibility	25
4.2. Terahertz-Elliott Formula	27
4.3. Signatures of Nonlinear Terahertz Excitations	31
5. Detection of Exciton Populations and Plasmons	33
5.1. Bound Exciton Populations	33
5.2. Exciton Populations and Correlated Electron-Hole Plasma	38
5.3. Plasmon Resonance	41
6. Interband Polarization in Strong Terahertz Fields	43
6.1. Rabi Splitting and Ponderomotive Shifts in Optical Transmission	43
6.2. Extreme-Nonlinear Dynamics	48
6.3. Analytic Solution within the Rotating-Wave Approximation	49
6.4. Interaction of Intense Single-Cycle Terahertz Pulses with AlGaAs/GaAs Quantum Wells	51
7. Exciton Populations in Strong Terahertz Fields	55
7.1. Basic Terahertz-Induced Processes	56
7.1.1. Exciton-Population Transfer	56
7.1.2. Dynamics of Pair-Correlation function	57
7.1.3. Dynamics of Carrier Distributions	59

7.2.	Rabi-flopping of an Exciton Populations	62
7.2.1.	Population Dynamics and Terahertz Current	63
7.2.2.	Removal of Ponderomotive Contributions	64
7.2.3.	Rabi Sidebands and Harmonics	68
7.3.	Ionization of an Exciton Population	69
7.3.1.	Creation of Ballistic Wavepackets via Direct Ionization	70
7.3.2.	High-Harmonic Generation	73
7.4.	Coherent Control of 1s-Para Excitons in Cu_2O	76
8.	Heating of a Correlated Electron-Hole Plasma	85
8.1.	Kinetic Energy and Pair-Correlation Function	85
8.2.	Analytic Solution	88
8.3.	Absorption of Terahertz Photons	90
9.	Conclusion and Outlook	93
A.	$k \cdot p$ Theory	95
B.	Multiband Hamiltonian for Confined Systems	97
B.1.	Quantum-Well Confinement	97
B.2.	Quantum-Wire Confinement	98
C.	Singlet-Doublet Dynamics of Carriers	101
C.1.	Off-resonant Interband Transitions	101
C.2.	Explicit Dynamics of Two-Particle Correlations	104
C.3.	Scattering Contributions	105
D.	Exciton Basis	107
D.1.	Wannier Equation	107
D.2.	Pair-Correlation Function and Exciton Populations	108
D.3.	Singlet Dynamics in Exciton Basis	109
D.4.	Singlet-Doublet Dynamics in Exciton Basis	110
D.5.	Solutions of the Terahertz-Bloch Equations	111

1. Introduction

The development of modern-crystal growth techniques has triggered a remarkable progress in semiconductor technology. The ability to grow semiconductor heterostructures with almost atomic precision and a high degree of purity has led to many applications including efficient integrated circuits in modern computers, light-emitting diodes (LEDs) and semiconductor lasers. For a theorist, there are two central motivations to study the physics of semiconductors. First, the demand for ever faster and smaller electronic and optoelectronic devices requires a detailed understanding of the optical and electronic processes on a quantum-mechanical level. Second, the high-quality nanostructures which can be fabricated today constitute ideal model systems to study fundamental physical excitations in condensed matter.

Optical experiments are a powerful tool to study such microscopic processes. Since the bandgap in typical semiconductors is around one electronvolt ($1 \text{ eV} \hat{=} 1240 \text{ nm} \hat{=} 242 \text{ THz}$), it is natural that experiments have concentrated on the visible and near-infrared regime of the electromagnetic spectrum. In this frequency range, light has a photon energy close to the bandgap energy such that it can lift electrons from the valence band into the conduction band thus leaving behind a positively charged hole in the valence band. The development of the mode-locked Ti:sapphire laser in the 1980s has allowed experimentalists to study the semiconductor dynamics with optical pulses of sub-picosecond duration ($1 \text{ ps} = 10^{-12} \text{ s}$). With methods of coherent spectroscopy such as four-wave mixing [1–3] and pump-probe experiments [4, 5], it has become possible to study the onset of scattering processes of carriers after optical excitation.

At the simplest level, the dynamics of optically-excited semiconductors can be described by mean-field theories which assume that each carrier behaves effectively like a single particle influenced by the average field of all other particles. However, an optical excitation creates many electrons and holes which strongly interact via the Coulomb interaction such that many-body correlations build up even at dilute densities. When correlation effects dominate the dynamics, the mean-field description usually breaks down. Thus, the optically-excited semiconductor is an ideal test ground to study the many-body quantum dynamics. The incoherent exciton [6, 7] is one of the most prominent example of correlations in semiconductors because it consists of an electron and a hole forming a truly bound pair due to the attractive Coulomb interaction. The exciton is in many ways similar to the Hydrogen atom which contains a correlated electron and proton. The plasmon [8] represents another correlated quasiparticle; it is a collective charge oscillation in the optically excited electron-hole plasma. The investigation of correlations among strongly Coulomb-interacting particles is a central problem not only in semiconductor physics but in condensed-matter physics in general and has been the focus of many experimental and theoretical investigations.

1. Introduction

Optical techniques that employ only visible or near-infrared light have a limited potential to study these basic correlation effects in semiconductors because the fundamental quasiparticles such as excitons and plasmons have energies which correspond to a completely different frequency range. The exciton binding energy, e.g., typically corresponds to frequencies in the terahertz (THz) range of the electromagnetic spectrum ($4.13 \text{ meV} \hat{=} 300 \mu\text{m} \hat{=} 1 \text{ THz}$). The plasma frequency, i.e., the frequency of collective charge oscillations, is usually also in the THz range for semiconductors. Thus, it is natural to study these many-body correlations with light in the THz regime of the electromagnetic spectrum.

For experimentalists, the THz regime has become fully accessible only in the last decades with the development of coherent THz sources including optically-pumped molecular lasers [9], free-electron lasers (FEL) [10] and *p*-germanium lasers [11]. The FEL is particularly useful since it provides high intensities while being continuously tunable in the THz range. However, FELs are very large projects such that only a few facilities have been built. In recent years, high-quality coherent THz sources have become widely available to individual laboratories mainly due to advances in the THz generation via optical pulses [12]. Here, optical femtosecond laser pulses are used to generate THz radiation, e.g., by inducing ultrafast photocurrents in a photoconductive switch or via optical rectification in nonlinear crystals. Together with suitable detectors, e.g., electro-optic sampling [13], these sources can be used for time-domain THz spectroscopy. Terahertz fields are resonant with internal transitions of excitons and plasmons but can also be used to excite lattice vibrations and intersubband transitions in confined semiconductor nanostructures.

In a typical experiment, an optical interband excitation prepares a certain many-body state which is then probed by a weak THz pulse. When, e.g., an exciton population is present, the transmitted THz spectrum displays characteristic absorption lines corresponding to the possible intraexcitonic transitions in the THz range. Using THz spectroscopy, pioneering experiments [14–18] have thus started answering the old question whether and under which conditions a true exciton population is formed after optical excitation. The concept of excitonic THz spectroscopy is similar to atomic gas spectroscopy where the presence of a certain atom species is derived from distinct absorption resonances that fingerprint them. Similarly, THz experiments [35] have identified and monitored the build up of a plasmon resonance in bulk semiconductors. The concept of THz spectroscopy is not limited to semiconductors. Since THz fields are resonant with vibrational and rotational transitions in molecules [19, 20], they can be used to probe chemical compounds biological systems. Moreover, there are applications in the material sciences, tomographic imaging and security [21].

In this Thesis, I will present a fully microscopic theory to describe THz-induced processes in optically-excited semiconductors. The formation process of excitons and other quasi-particles after optical excitation has been studied in great detail for a variety of conditions [6, 22–26]. Here, I will not model the formation process but assume a realistic initial many-body state. In particular, I will review the linear THz response and demonstrate that correlated quasi-particles such as excitons and plasmons can be unambiguously detected via THz spectroscopy. The focus of the investigations, however,

is on situations where the optically-excited many-body state is excited by *intense* THz fields. While weak pulses detect the many-body state, strong THz pulses control and manipulate the quasi-particles in a way that is not accessible via conventional techniques. The nonlinear THz dynamics of exciton populations is especially interesting because similarities and differences to optics with atomic systems can be studied. A theoretical investigation of the nonlinear THz regime in semiconductors is timely. In recent years, experimentalists have started to explore [28–33] strong-field THz excitations in semiconductors as high-power THz sources [27] are becoming more efficient and widely available.

The Thesis is organized as follows. Chapter 2 introduces the many-body Hamiltonian for the interacting system. I then derive the relevant equations of motion in Chapter 3. The presented microscopic theory consistently includes the correlation effects necessary to describe THz interactions with quasiparticles. Chapter 4 identifies the measurable quantities in linear and nonlinear THz experiments and presents an analytic solution of the linear response. Chapter 5 shows that weak THz fields can detect exciton populations and plasmons in two-dimensional nanostructures. Chapters 6-8 deal with nonlinear THz excitations of interband polarization, exciton populations and correlated electron-hole plasma in semiconductors. I will map out different excitation regimes and present quantitative comparisons to recent experiments.

1. *Introduction*

2. System Hamiltonian

The starting point of my theoretical investigations is the Hamilton operator of the semiconductor system which describes the free motion of non-interacting carriers, photons and phonons as well as the interactions between these quasi-particles. I will summarize the key steps in the derivation of the Hamiltonian and refer to the literature for details. For the description of terahertz (THz) processes in semiconductors, it is particularly important that the coupling of the light field to intraband quantities is consistently included.

2.1. Hamiltonian in First Quantization

In first quantization, a Coulomb-interacting carrier system with N charged particles coupled to a quantized electromagnetic field is described by the minimal-substitution Hamiltonian [36, 37]

$$H = \sum_{j=1}^N \left\{ \frac{1}{2m_0} [\mathbf{p}_j - e\mathbf{A}(\mathbf{r}_j)]^2 + U_L(\mathbf{r}_j) \right\} + \frac{1}{2} \sum_{i \neq j}^N V(|\mathbf{r}_i - \mathbf{r}_j|) + H_{\text{em}} + H_{\text{ph}}. \quad (2.1)$$

Here, \mathbf{p}_j and \mathbf{r}_j are the canonical momentum and position operator of particle j with charge $e = -|e|$ and mass m_0 . The carriers move in a lattice-periodic potential U_L and are coupled to a quantized transversal light field via the vector potential $\mathbf{A}(\mathbf{r})$. We assume that all external longitudinal fields vanish such that no additional potential term appears in Eq. (2.1). Furthermore, $V(\mathbf{r})$ denotes the unscreened Coulomb potential between the carriers, H_{em} is the free-field part of the quantized light field, and H_{ph} includes the interactions with phonons. The explicit forms of H_{em} and H_{ph} can be found, e.g., in Ref. [6]. In the following investigations, we adopt the Coulomb gauge, $\nabla \cdot \mathbf{A} = 0$. As a result, $\mathbf{A}(\mathbf{r})$ and \mathbf{p} commute and Eq. (2.1) can be written as

$$H = \sum_{j=1}^N \left\{ \left[\frac{\mathbf{p}_j^2}{2m_0} + U_L(\mathbf{r}_j) \right] + \frac{|e|}{m_0} \mathbf{A}(\mathbf{r}_j) \cdot \mathbf{p}_j + \frac{|e|^2}{2m_0} \mathbf{A}^2(\mathbf{r}_j) \right\} + \frac{1}{2} \sum_{i \neq j}^N V(|\mathbf{r}_i - \mathbf{r}_j|) + H_{\text{em}} + H_{\text{ph}}. \quad (2.2)$$

For the description of the interacting carrier-photon-phonon system, it is useful to adopt the formalism of second quantization. Most aspects of the second-quantized Hamiltonian have been discussed thoroughly in the literature[6, 8, 37]. Here, only the interaction of

2. System Hamiltonian

carriers with the quantized light field will be discussed in detail. The frequency of the light can be in the optical (i.e., visible or near-visible) or terahertz regime of the electromagnetic spectrum.

It is well known [36, 37] that a gauge transformation of the Hamiltonian, Eq. (2.2), changes the light-matter interaction into a dipole interaction of the form $|e|\mathbf{r}_j \cdot \mathbf{E}$ where $\mathbf{E} = -(\partial/\partial t)\mathbf{A}$ is the operator of the electric field. This $\mathbf{r} \cdot \mathbf{E}$ -representation is often used when studying optical interband transitions since it conveniently introduces the interband dipole-matrix element. However, the description of THz-induced intraband transitions is usually more complicated in the $\mathbf{r} \cdot \mathbf{E}$ -picture such that we keep using the $\mathbf{p} \cdot \mathbf{A}$ -representation of the interaction Hamiltonian.

2.2. Light-Matter Interaction in Second Quantization

In second quantization, the optically active electrons are described by field operators $\Psi_\sigma(\mathbf{r})$ [$\Psi_\sigma^\dagger(\mathbf{r})$] which annihilate [create] an electron at position \mathbf{r} with spin σ . For semiconductors, it is usually advantageous to expand the field operators in the Bloch basis

$$\Psi_\sigma(\mathbf{r}) = \sum_{\lambda, \mathbf{k}} a_{\lambda, \sigma, \mathbf{k}} \phi_{\lambda, \sigma, \mathbf{k}}(\mathbf{r}), \quad \Psi_\sigma^\dagger(\mathbf{r}) = \sum_{\lambda, \mathbf{k}} a_{\lambda, \sigma, \mathbf{k}}^\dagger \phi_{\lambda, \sigma, \mathbf{k}}^*(\mathbf{r}). \quad (2.3)$$

Here, the fermionic operator $a_{\lambda, \sigma, \mathbf{k}}$ ($a_{\lambda, \sigma, \mathbf{k}}^\dagger$) annihilates (creates) an electron with wavevector \mathbf{k} and spin σ in band λ . The single-particle wavefunctions $\phi_{\lambda, \sigma, \mathbf{k}}(\mathbf{r})$ obey

$$\left[\frac{\mathbf{p}^2}{2m_0} + U_L(\mathbf{r}) \right] \phi_{\lambda, \sigma, \mathbf{k}}(\mathbf{r}) = \varepsilon_{\mathbf{k}}^\lambda \phi_{\lambda, \sigma, \mathbf{k}}(\mathbf{r}) \quad (2.4)$$

where $\varepsilon_{\mathbf{k}}^\lambda$ is the bandstructure. The wavefunctions $\phi_{\lambda, \sigma, \mathbf{k}}(\mathbf{r})$ constitute a complete and orthonormal set.

This Thesis concentrates on the interaction of light with planar nanostructures. We investigate either quantum wells (QWs) or planar arrangement of identical quantum wires (QWIs). In the QWI arrangement, the distance between neighboring wires is assumed to be sufficiently large such that they are not electronically coupled but much smaller than the relevant light wavelength such that no diffraction pattern arises. For these conditions, the QWI arrangement best mimics a QW while the numerical complexity is greatly reduced. In the following derivations, QWs are used as an explicit example. The corresponding results for the QWI case are presented in Appendix B.

For QWs, it is useful to separate the three-dimensional space coordinate $\mathbf{r} = (\mathbf{r}_\parallel, z)$ into a two-dimensional coordinate \mathbf{r}_\parallel in the QW plane and a one-dimensional coordinate z perpendicular to it. In envelope-function approximation [8], the Bloch functions are then given by

$$\phi_{\lambda, l, \sigma, \mathbf{k}_\parallel}(\mathbf{r}) = \xi_{\lambda, l}(z) \frac{1}{\sqrt{\mathcal{S}}} e^{i\mathbf{k}_\parallel \cdot \mathbf{r}_\parallel} w_{\lambda, l, \sigma, \mathbf{k}_\parallel}(\mathbf{r}) \quad (2.5)$$

where \mathcal{S} is the quantization area, $w_{\lambda, l, \sigma, \mathbf{k}_\parallel}(\mathbf{r})$ is the lattice-periodic wavefunction and $\xi_{\lambda, l}(z)$ is the confinement function. We also introduced the subband index l and the

2.2. Light-Matter Interaction in Second Quantization

carrier wavevector \mathbf{k}_{\parallel} in the QW plane. To shorten the notation in the following derivations, we use λ as a general index which contains band index λ , subband index l and spin index σ .

To derive the second-quantized form of the transverse electromagnetic field, we start from the sourceless wave equation for the classical vector potential [36]

$$\left[\nabla^2 - \frac{n^2(z)}{c_0^2} \frac{\partial^2}{\partial t^2} \right] \mathbf{A}_0(\mathbf{r}, t) = 0 \quad (2.6)$$

where c_0 denotes the vacuum velocity of light and $n(z)$ is the background refractive index. The steady-state solutions of Eq. (2.6), $\mathbf{U}_{\alpha, \mathbf{q}}$, are called the *mode functions* of the light field; they are given by the Helmholtz equation

$$[\nabla^2 + \mathbf{q}^2 n^2(\mathbf{r})] \mathbf{U}_{\alpha, \mathbf{q}}(\mathbf{r}) = 0 \quad (2.7)$$

where \mathbf{q} is the wavevector and α denotes the polarization direction of the mode. We choose the normalization

$$\int d^3r n^2(z) \mathbf{U}_{\alpha', \mathbf{q}'}(\mathbf{r}) \cdot \mathbf{U}_{\alpha, \mathbf{q}}(\mathbf{r}) = \delta_{\mathbf{q}, \mathbf{q}'} \delta_{\alpha, \alpha'}. \quad (2.8)$$

For perfect translational symmetry in the QW plane, the mode functions can be written as

$$\mathbf{U}_{\alpha, \mathbf{q}}(\mathbf{r}) = \frac{1}{\sqrt{\mathcal{S}}} \mathbf{u}_{\alpha, \mathbf{q}}(z) e^{i\mathbf{q}_{\parallel} \cdot \mathbf{r}_{\parallel}} \quad (2.9)$$

where $\mathbf{q} = (\mathbf{q}_{\parallel}, q_z)$. The z -dependent part, $\mathbf{u}_{\alpha, \mathbf{q}}(z)$, can be determined via a transfer-matrix technique [37] for a specific dielectric structure given by $n(z)$. Since the mode functions, $\mathbf{U}_{\alpha, \mathbf{q}}$, constitute a complete and orthonormal basis set, we find the following mode-expansion for the vector potential

$$\mathbf{A}(\mathbf{r}) = \sum_{\alpha, \mathbf{q}} \frac{\mathcal{E}_{\mathbf{q}}}{\omega_{\mathbf{q}}} [\mathbf{u}_{\alpha, \mathbf{q}}(z) e^{i\mathbf{q}_{\parallel} \cdot \mathbf{r}_{\parallel}} B_{\alpha, \mathbf{q}} + \text{c.c.}] \quad (2.10)$$

with the mode frequency $\omega_{\mathbf{q}} = c_0 |\mathbf{q}|$ and the vacuum-field amplitude $\mathcal{E}_{\mathbf{q}} = \sqrt{\hbar \omega_{\mathbf{q}} / (2\varepsilon_0)}$. According to the canonical quantization procedure [36], the coefficients $B_{\alpha, \mathbf{q}}$ and $B_{\alpha, \mathbf{q}}^*$ are replaced by photon annihilation, $B_{\alpha, \mathbf{q}}$, and creation, $B_{\alpha, \mathbf{q}}^\dagger$, operators which obey bosonic commutation relations. The free-field part of the quantized light field is then found to be [36]

$$H_{\text{em}} = \sum_{\alpha, \mathbf{q}} \hbar \omega_{\mathbf{q}} \left(B_{\alpha, \mathbf{q}}^\dagger B_{\alpha, \mathbf{q}} + \frac{1}{2} \right). \quad (2.11)$$

The kinetic energy and light-matter interaction parts of the Hamiltonian, Eq. (2.2), have the following form in second quantization

$$H_{\text{kin}} = \int d^3r \Psi^\dagger(\mathbf{r}) \left[\frac{\mathbf{p}^2}{2m_0} + U_L(\mathbf{r}) \right] \Psi(\mathbf{r}), \quad (2.12)$$

$$H_{A-p} + H_{A-A} = \int d^3r \Psi^\dagger(\mathbf{r}) \left[\frac{|e|}{m_0} \mathbf{A}(\mathbf{r}) \cdot \mathbf{p} + \frac{|e|^2}{2m_0} \mathbf{A}^2(\mathbf{r}) \right] \Psi(\mathbf{r}). \quad (2.13)$$

2. System Hamiltonian

Inserting Eq. (2.3) into Eqs. (2.12)-(2.13), we obtain

$$H_{\text{kin}} + H_{A,p} + H_{A,A} = \sum_{\lambda, \mathbf{k}_{\parallel}, \lambda', \mathbf{k}'_{\parallel}} a_{\lambda, \mathbf{k}_{\parallel}}^{\dagger} a_{\lambda', \mathbf{k}'_{\parallel}} \left(I_{\lambda', \mathbf{k}'_{\parallel}}^{\lambda, \mathbf{k}_{\parallel}}|_{\text{kin}} + I_{\lambda', \mathbf{k}'_{\parallel}}^{\lambda, \mathbf{k}_{\parallel}}|_{A,p} + I_{\lambda', \mathbf{k}'_{\parallel}}^{\lambda, \mathbf{k}_{\parallel}}|_{A,A} \right) \quad (2.14)$$

with the corresponding matrix elements

$$I_{\lambda', \mathbf{k}'_{\parallel}}^{\lambda, \mathbf{k}_{\parallel}}|_{\text{kin}} = \int d^3r \phi_{\lambda, \mathbf{k}_{\parallel}}^*(\mathbf{r}) \left[\frac{\mathbf{p}^2}{2m} + U_L(\mathbf{r}) \right] \phi_{\lambda', \mathbf{k}'_{\parallel}}(\mathbf{r}), \quad (2.15)$$

$$I_{\lambda', \mathbf{k}'_{\parallel}}^{\lambda, \mathbf{k}_{\parallel}}|_{A,p} = \frac{|e|}{m_0} \int d^3r \phi_{\lambda, \mathbf{k}_{\parallel}}^*(\mathbf{r}) \mathbf{A}(\mathbf{r}) \cdot \mathbf{p} \phi_{\lambda', \mathbf{k}'_{\parallel}}(\mathbf{r}), \quad (2.16)$$

$$I_{\lambda', \mathbf{k}'_{\parallel}}^{\lambda, \mathbf{k}_{\parallel}}|_{A,A} = \frac{|e|^2}{2m_0} \int d^3r \phi_{\lambda, \mathbf{k}_{\parallel}}^*(\mathbf{r}) \mathbf{A}(\mathbf{r}) \cdot \mathbf{A}(\mathbf{r}) \phi_{\lambda', \mathbf{k}'_{\parallel}}(\mathbf{r}). \quad (2.17)$$

The evaluation of the matrix elements, Eq. (2.15)-(2.17) is a standard calculation; the following derivations will briefly overview and extend the central steps based on Refs. [8, 37, 38]. Using Eq. (2.4) and the orthonormality of the wavefunctions $\phi_{\lambda, \mathbf{k}_{\parallel}}(\mathbf{r})$, we immediately find

$$I_{\lambda', \mathbf{k}'_{\parallel}}^{\lambda, \mathbf{k}_{\parallel}}|_{\text{kin}} = \delta_{\lambda, \lambda'} \delta_{\mathbf{k}_{\parallel}, \mathbf{k}'_{\parallel}} \varepsilon_{\mathbf{k}_{\parallel}}^{\lambda} \quad (2.18)$$

which implies that the kinetic part is diagonal in the Bloch basis. Thus, $\varepsilon_{\mathbf{k}_{\parallel}}^{\lambda}$ defines the kinetic energy of the Bloch electrons. For investigations close to the bandgap, it is often a good approximation to assume a parabolic bandstructure [8, 39]

$$\varepsilon_{\mathbf{k}_{\parallel}}^{\lambda} = \varepsilon_0^{\lambda} + \frac{\hbar^2 \mathbf{k}_{\parallel}^2}{2m_{\lambda}} \quad (2.19)$$

where m_{λ} is the effective mass of band λ . A $\mathbf{k} \cdot \mathbf{p}$ -evaluation of $\varepsilon_{\mathbf{k}_{\parallel}}^{\lambda}$ is presented in Appendix A.

For the computation of the remaining matrix elements, it is convenient to introduce a Fourier decomposition of the vector potential with respect to the in-plane coordinates

$$\mathbf{A}(\mathbf{r}) = \sum_{\mathbf{q}_{\parallel}} \mathbf{A}_{\mathbf{q}_{\parallel}}(z) e^{i\mathbf{q}_{\parallel} \cdot \mathbf{r}_{\parallel}}. \quad (2.20)$$

We continue with the evaluation of $I|_{A,p}$ given by Eq. (2.16) where the momentum operator \mathbf{p} acts on the Bloch function $\phi_{\lambda', \mathbf{k}'_{\parallel}}(\mathbf{r})$. By separating the in-plane and z -dependent components, $\mathbf{p} = \mathbf{p}_{\parallel} - \mathbf{e}_z \hbar \partial / \partial z$, and by inserting Eq. (2.5), we find

$$\begin{aligned} \sqrt{S} \mathbf{p} \phi_{\lambda', \mathbf{k}'_{\parallel}}(\mathbf{r}) &= \mathbf{p} \left[e^{i\mathbf{k}'_{\parallel} \cdot \mathbf{r}_{\parallel}} \xi_{\lambda'}(z) w_{\lambda', \mathbf{k}'_{\parallel}}(\mathbf{r}) \right] \\ &= e^{i\mathbf{k}'_{\parallel} \cdot \mathbf{r}_{\parallel}} \xi_{\lambda'}(z) \left[\hbar \mathbf{k}'_{\parallel} + \mathbf{p} \right] w_{\lambda', \mathbf{k}'_{\parallel}}(\mathbf{r}) - i \hbar \mathbf{e}_z e^{i\mathbf{k}'_{\parallel} \cdot \mathbf{r}_{\parallel}} w_{\lambda', \mathbf{k}'_{\parallel}}(\mathbf{r}) \frac{\partial}{\partial z} \xi_{\lambda'}(z). \end{aligned} \quad (2.21)$$

2.2. Light-Matter Interaction in Second Quantization

Inserting Eq. (2.21) into Eq. (2.16), we identify two contributions, $I|_{A,p} = I|_{A,p}^{(1)} + I|_{A,p}^{(2)}$, given by

$$I_{\lambda',\mathbf{k}'_{\parallel}}^{\lambda,\mathbf{k}_{\parallel}}|_{A,p}^{(1)} = \frac{|e|}{m_0} \frac{1}{\mathcal{S}} \sum_{\mathbf{q}_{\parallel}} \int d^3r e^{-i\mathbf{k}_{\parallel}\cdot\mathbf{r}_{\parallel}} \xi_{\lambda}^*(z) w_{\lambda,\mathbf{k}_{\parallel}}^*(\mathbf{r}) \quad (2.22)$$

$$\times \mathbf{A}_{\mathbf{q}_{\parallel}}(z) e^{i\mathbf{q}_{\parallel}\cdot\mathbf{r}_{\parallel}} e^{i\mathbf{k}'_{\parallel}\cdot\mathbf{r}_{\parallel}} \xi_{\lambda'}(z) \cdot [\hbar\mathbf{k}'_{\parallel} + \mathbf{p}] w_{\lambda',\mathbf{k}'_{\parallel}}(\mathbf{r}),$$

$$I_{\lambda',\mathbf{k}'_{\parallel}}^{\lambda,\mathbf{k}_{\parallel}}|_{A,p}^{(2)} = \frac{-i\hbar|e|}{m_0} \frac{1}{\mathcal{S}} \sum_{\mathbf{q}_{\parallel}} \int d^3r e^{-i\mathbf{k}_{\parallel}\cdot\mathbf{r}_{\parallel}} \xi_{\lambda}^*(z) w_{\lambda,\mathbf{k}_{\parallel}}^*(\mathbf{r}) \quad (2.23)$$

$$\times \mathbf{A}_{\mathbf{q}_{\parallel}}(z) \cdot \mathbf{e}_z e^{i\mathbf{q}_{\parallel}\cdot\mathbf{r}_{\parallel}} e^{i\mathbf{k}'_{\parallel}\cdot\mathbf{r}_{\parallel}} w_{\lambda',\mathbf{k}'_{\parallel}}(\mathbf{r}) \frac{\partial}{\partial z} \xi_{\lambda'}(z).$$

Due to the scalar products in Eqs. (2.22) and (2.23), the contributions depend on the propagation direction of the light field. For mode functions, $\mathbf{U}_{s,\mathbf{q}}$, which are polarized perpendicular to the plane of incidence (s -polarized modes), the term $I|_{A,p}^{(2)}$ vanishes while $I|_{A,p}^{(1)}$ is finite. For mode functions, $\mathbf{U}_{p,\mathbf{q}}$, whose polarization direction lies in the plane of incidence (p -polarized modes), both $I|_{A,p}^{(1)}$ and $I|_{A,p}^{(2)}$ can be non-vanishing.

The integration in Eqs. (2.22) and (2.23) can be further simplified by using that the quantities appearing in the integrands vary on different characteristic length scales. The lattice periodic wavefunction $w_{\lambda,\mathbf{k}_{\parallel}}(\mathbf{r})$ changes on the unit-cell length scale which is typically a few Angstroms. The confinement wavefunction $\xi_{\lambda}(z)$ and $e^{i\mathbf{k}_{\parallel}\cdot\mathbf{r}_{\parallel}}$ vary on a mesoscopic nanometer length scale. Finally, the quantities associated with the light field, $e^{i\mathbf{q}_{\parallel}\cdot\mathbf{r}_{\parallel}}$ and $\mathbf{A}_{\mathbf{q}_{\parallel}}(z)$, vary on the scale of the light wavelength which is 400 – 800 nm for visible light and 1 – 300 μm for THz fields. To take advantage of these different length scales, we rewrite the integration in Eq. (2.22) as $\int d^3r = \sum_{\mathbf{R}} \int_{v_{\mathbf{R}}} d^3r$ where $v_{\mathbf{R}}$ is the unit-cell volume around the lattice point $\mathbf{R} = (\mathbf{R}_{\parallel}, Z)$. All factors of the integrand except $w_{\lambda,\mathbf{k}_{\parallel}}(\mathbf{r})$ can be assumed constant over one unit cell such that we obtain

$$I_{\lambda',\mathbf{k}'_{\parallel}}^{\lambda,\mathbf{k}_{\parallel}}|_{A,p}^{(1)} = \frac{|e|}{m_0} \frac{1}{\mathcal{S}} \sum_{\mathbf{q}_{\parallel}} \sum_{\mathbf{R}_{\parallel}, Z} e^{i(\mathbf{k}'_{\parallel} + \mathbf{q}_{\parallel} - \mathbf{k}_{\parallel})\cdot\mathbf{R}_{\parallel}} \xi_{\lambda}^*(Z) \mathbf{A}_{\mathbf{q}_{\parallel}}(Z) \xi_{\lambda'}(Z) \quad (2.24)$$

$$\cdot \int_{v_{\mathbf{R}}} d^3r w_{\lambda,\mathbf{k}_{\parallel}}^*(\mathbf{r}) [\hbar\mathbf{k}'_{\parallel} + \mathbf{p}] w_{\lambda',\mathbf{k}'_{\parallel}}(\mathbf{r}).$$

Due to the periodicity of the wavefunctions $w_{\lambda,\mathbf{k}_{\parallel}}(\mathbf{r})$, the unit-cell matrix element is independent of \mathbf{R} equalling

$$\langle \lambda, \mathbf{k}_{\parallel} | \hbar\mathbf{k}'_{\parallel} + \mathbf{p} | \lambda', \mathbf{k}'_{\parallel} \rangle = \frac{1}{v_0} \int_{v_0} d^3r w_{\lambda,\mathbf{k}_{\parallel}}^*(\mathbf{r}) [\hbar\mathbf{k}'_{\parallel} + \mathbf{p}] w_{\lambda',\mathbf{k}'_{\parallel}}(\mathbf{r}) \quad (2.25)$$

where v_0 is the unit-cell volume around $\mathbf{R} = \mathbf{0}$. Here, we adopted Dirac's abstract notation; the real-space representation of $|\lambda, \mathbf{k}_{\parallel}\rangle$ is $w_{\lambda,\mathbf{k}_{\parallel}}(\mathbf{r}) = \langle \mathbf{r} | \lambda, \mathbf{k}_{\parallel} \rangle$. Since v_0 is infinitesimal compared with spatial variations of the remaining terms, we may replace the sum $\sum_{\mathbf{R}} v_0$ with an integral $\int d\mathbf{R}_{\parallel} dZ$. The \mathbf{R}_{\parallel} -integration in Eq. (2.24) then yields

$$\int d\mathbf{R}_{\parallel} e^{i(\mathbf{k}'_{\parallel} + \mathbf{q}_{\parallel} - \mathbf{k}_{\parallel})\cdot\mathbf{R}_{\parallel}} = \mathcal{S} \delta_{\mathbf{k}'_{\parallel} + \mathbf{q}_{\parallel}, \mathbf{k}_{\parallel}} \quad (2.26)$$

2. System Hamiltonian

such that we obtain

$$I_{\lambda', \mathbf{k}'_{\parallel}}^{\lambda, \mathbf{k}_{\parallel}}|_{A \cdot p}^{(1)} = \frac{|e|}{m_0} \sum_{\mathbf{q}_{\parallel}} \mathbf{A}_{\mathbf{q}_{\parallel}}^{\lambda, \lambda'} \delta_{\mathbf{k}'_{\parallel}, \mathbf{k}_{\parallel} - \mathbf{q}_{\parallel}} \langle \lambda, \mathbf{k}_{\parallel} | \hbar \mathbf{k}'_{\parallel} + \mathbf{p} | \lambda', \mathbf{k}'_{\parallel} \rangle \quad (2.27)$$

where we introduced the abbreviation $\mathbf{A}_{\mathbf{q}_{\parallel}}^{\lambda, \lambda'} = \int dZ \xi_{\lambda}^*(Z) \mathbf{A}_{\mathbf{q}_{\parallel}}(Z) \xi_{\lambda'}(Z)$.

The matrix-element $\langle \lambda, \mathbf{k}_{\parallel} | \hbar \mathbf{k}'_{\parallel} + \mathbf{p} | \lambda', \mathbf{k}'_{\parallel} \rangle$ with $\mathbf{k}'_{\parallel} = \mathbf{k}_{\parallel} - \mathbf{q}_{\parallel}$ is not diagonal with respect to momentum. However, since the wavevector \mathbf{q}_{\parallel} of the light field is at least two orders of magnitude smaller than a typical electronic wavevector \mathbf{k}_{\parallel} , the center-of-mass momentum $\mathbf{k}_{\parallel}^{\text{com}} \equiv (\mathbf{k}_{\parallel} + \mathbf{k}'_{\parallel})/2 = \mathbf{k}_{\parallel} - \mathbf{q}_{\parallel}/2$ is much larger than the relative momentum $\mathbf{k}_{\parallel}^{\text{rel}} \equiv \mathbf{k}_{\parallel} - \mathbf{k}'_{\parallel} = \mathbf{q}_{\parallel}$. In the expansion

$$\langle \lambda, \mathbf{k}_{\parallel} | \hbar \mathbf{k}'_{\parallel} + \mathbf{p} | \lambda', \mathbf{k}'_{\parallel} \rangle = \langle \lambda, \mathbf{k}_{\parallel}^{\text{com}} | \hbar \mathbf{k}_{\parallel}^{\text{com}} + \mathbf{p} | \lambda', \mathbf{k}_{\parallel}^{\text{com}} \rangle + \mathcal{O}(\mathbf{k}_{\parallel}^{\text{rel}}) \quad (2.28)$$

for small relative momenta, we can thus neglect the first-order correction. For the further evaluation of this unit-cell integral, we need additional information about the \mathbf{k}_{\parallel} -dependence of the Bloch functions. In Appendix A, we use second-order $\mathbf{k} \cdot \mathbf{p}$ -theory to show that

$$\langle \lambda, \mathbf{k}_{\parallel} | \hbar \mathbf{k}_{\parallel} + \mathbf{p} | \lambda', \mathbf{k}_{\parallel} \rangle = \delta_{\lambda, \lambda'} \frac{m_0}{\hbar} \frac{\partial \varepsilon_{\mathbf{k}_{\parallel}}^{\lambda}}{\partial \mathbf{k}_{\parallel}} + (1 - \delta_{\lambda, \lambda'}) \mathbf{p}_{\lambda, \lambda'}(\mathbf{k}_{\parallel}). \quad (2.29)$$

where $\mathbf{p}_{\lambda, \lambda' \neq \lambda}(\mathbf{k}_{\parallel}) \equiv \langle \lambda, \mathbf{k}_{\parallel} | \mathbf{p} | \lambda', \mathbf{k}_{\parallel} \rangle$ is the interband momentum-matrix element. For parabolic bands, we have the relation $(\partial \varepsilon_{\mathbf{k}_{\parallel}}^{\lambda} / \partial \mathbf{k}_{\parallel}) = \hbar^2 \mathbf{k}_{\parallel} / m_{\lambda}$. Inserting Eqs. (2.28) and (2.29) into Eq. (2.27), we finally obtain

$$I_{\lambda', \mathbf{k}'_{\parallel}}^{\lambda, \mathbf{k}_{\parallel}}|_{A \cdot p}^{(1)} = - \sum_{\mathbf{q}_{\parallel}} \delta_{\mathbf{k}'_{\parallel}, \mathbf{k}_{\parallel} - \mathbf{q}_{\parallel}} \times \left[\delta_{\lambda, \lambda'} \mathbf{j}_{\lambda} \left(\mathbf{k}_{\parallel} - \frac{\mathbf{q}_{\parallel}}{2} \right) \cdot \mathbf{A}_{\mathbf{q}_{\parallel}}^{\lambda, \lambda'} - (1 - \delta_{\lambda, \lambda'}) \frac{|e|}{m_0} \mathbf{p}_{\lambda, \lambda'} \left(\mathbf{k}_{\parallel} - \frac{\mathbf{q}_{\parallel}}{2} \right) \cdot \mathbf{A}_{\mathbf{q}_{\parallel}}^{\lambda, \lambda'} \right] \quad (2.30)$$

where we identified the current-matrix element

$$\mathbf{j}_{\lambda}(\mathbf{k}_{\parallel}) = - \frac{|e|}{\hbar} \frac{\partial \varepsilon_{\mathbf{k}_{\parallel}}^{\lambda}}{\partial \mathbf{k}_{\parallel}}. \quad (2.31)$$

For parabolic bands, we find $\mathbf{j}_{\lambda}(\mathbf{k}_{\parallel}) = -|e| \hbar \mathbf{k}_{\parallel} / m_{\lambda}$ such that this term is antisymmetric with respect to \mathbf{k}_{\parallel} . We will later see that this contribution can lead to the generation of a macroscopic intraband current.

The evaluation of the remaining $A \cdot p$ -dependent matrix-element, Eq. (2.23), involves similar steps. It is straightforward to show that

$$I_{\lambda', \mathbf{k}'_{\parallel}}^{\lambda, \mathbf{k}_{\parallel}}|_{A \cdot p}^{(2)} = \frac{-i \hbar |e|}{m_0} \sum_{\mathbf{q}_{\parallel}} \delta_{\mathbf{k}'_{\parallel}, \mathbf{k}_{\parallel} - \mathbf{q}_{\parallel}} \delta_{\lambda, \lambda'} \mathbf{e}_z \cdot \mathbf{A}_{\mathbf{q}_{\parallel}}^{\lambda, \partial \lambda'} \quad (2.32)$$

2.3. Complete Hamiltonian in Second Quantization

where we introduced the abbreviation $\mathbf{A}_{\mathbf{q}_{\parallel}}^{\lambda, \partial\lambda'} = \int dZ \xi_{\lambda}^*(Z) \mathbf{A}_{\mathbf{q}_{\parallel}}(Z) (\partial/\partial Z) \xi_{\lambda'}(Z)$. For the A^2 -dependent matrix element, Eq. (2.17), we similarly find

$$I_{\lambda', \mathbf{k}'_{\parallel}}^{\lambda, \mathbf{k}_{\parallel}} |_{A.A} = \sum_{\mathbf{q}_{\parallel}, \mathbf{q}'_{\parallel}} \delta_{\mathbf{k}'_{\parallel} - \mathbf{q}'_{\parallel}, \mathbf{k}_{\parallel} - \mathbf{q}_{\parallel}} \delta_{\lambda, \lambda'} \frac{|e|^2}{2m_0} A_{\mathbf{q}_{\parallel}, -\mathbf{q}'_{\parallel}}^{(2), \lambda, \lambda'} \quad (2.33)$$

with $A_{\mathbf{q}_{\parallel}, -\mathbf{q}'_{\parallel}}^{(2), \lambda, \lambda'} = \int dZ \xi_{\lambda}^*(Z) \mathbf{A}_{\mathbf{q}_{\parallel}}(Z) \cdot \mathbf{A}_{-\mathbf{q}'_{\parallel}}(Z) \xi_{\lambda'}(Z)$.

2.3. Complete Hamiltonian in Second Quantization

To obtain the final form of the light-matter interaction Hamiltonian in the Bloch basis, we insert Eqs. (2.30)-(2.33) into Eq. (2.14). The result is

$$\begin{aligned} H_{A.p} + H_{A.A} = & - \sum_{\lambda} \sum_{\mathbf{q}_{\parallel}, \mathbf{k}_{\parallel}} \mathbf{j}_{\lambda}(\mathbf{k}_{\parallel}) \cdot \mathbf{A}_{\mathbf{q}_{\parallel}}^{\lambda, \lambda} a_{\lambda, \mathbf{k}_{\parallel} + \frac{\mathbf{q}_{\parallel}}{2}}^{\dagger} a_{\lambda, \mathbf{k}_{\parallel} - \frac{\mathbf{q}_{\parallel}}{2}} \\ & + \sum_{\lambda \neq \lambda'} \sum_{\mathbf{q}_{\parallel}, \mathbf{k}_{\parallel}} \frac{|e|}{m_0} \mathbf{p}_{\lambda, \lambda'}(\mathbf{k}_{\parallel}) \cdot \mathbf{A}_{\mathbf{q}_{\parallel}}^{\lambda, \lambda'} a_{\lambda, \mathbf{k}_{\parallel} + \frac{\mathbf{q}_{\parallel}}{2}}^{\dagger} a_{\lambda', \mathbf{k}_{\parallel} - \frac{\mathbf{q}_{\parallel}}{2}} \\ & - \sum_{\lambda, \lambda'} \sum_{\mathbf{q}_{\parallel}, \mathbf{k}_{\parallel}} \delta_{\lambda, \lambda'} \frac{i\hbar|e|}{m_0} \mathbf{e}_z \cdot \mathbf{A}_{\mathbf{q}_{\parallel}}^{\lambda, \partial\lambda'} a_{\lambda, \mathbf{k}_{\parallel} + \frac{\mathbf{q}_{\parallel}}{2}}^{\dagger} a_{\lambda', \mathbf{k}_{\parallel} - \frac{\mathbf{q}_{\parallel}}{2}} \\ & + \sum_{\lambda} \sum_{\mathbf{q}_{\parallel}, \mathbf{q}'_{\parallel}, \mathbf{k}_{\parallel}} \frac{|e|^2}{2m_0} A_{\mathbf{q}_{\parallel}, -\mathbf{q}'_{\parallel}}^{(2), \lambda, \lambda} a_{\lambda, \mathbf{k}_{\parallel} + \mathbf{q}_{\parallel}}^{\dagger} a_{\lambda, \mathbf{k}_{\parallel} + \mathbf{q}'_{\parallel}}. \end{aligned} \quad (2.34)$$

The first line of Eq. (2.34) describes a process where the electron makes a transition from wavevector $\mathbf{k}_{\parallel} - \mathbf{q}_{\parallel}/2$ to $\mathbf{k}_{\parallel} + \mathbf{q}_{\parallel}/2$ within the same band, i.e., an *intraband* transition. The second line describes an *interband* transition between bands λ and $\lambda' \neq \lambda$ which is allowed whenever the matrix element $\mathbf{p}_{\lambda, \lambda'}$ is non-vanishing. The third line allows for *intersubband* transitions which may occur when a component of the light field is polarized perpendicular to the QW. Note that the subband index is suppressed in our notation; in Appendix B, we explicitly indicate the dependence on the subband index in the Hamiltonian. The fourth line describes two-photon intraband processes where the electron wavevector changes by $\mathbf{q}_{\parallel} - \mathbf{q}'_{\parallel}$. The in-plane carrier momentum is conserved in all processes. It is interesting to note that the current-matrix element contains the effective mass m_{λ} while the other terms contain the free electron mass m_0 . In the derivation of Eq. (2.34), we only demanded that the wavevector of the light field is significantly smaller than the electronic wavevector. Thus, the quantized vector potential in Eq. (2.34) can describe optical fields (i.e., visible or near-visible light) as well as THz fields.

According to Eqs. (2.11), (2.14) and (2.18), the non-interacting part of the Hamiltonian reads

$$H_0 = \sum_{\mathbf{k}_{\parallel}, \lambda} \varepsilon_{\mathbf{k}_{\parallel}}^{\lambda} a_{\lambda, \mathbf{k}_{\parallel}}^{\dagger} a_{\lambda, \mathbf{k}_{\parallel}} + \sum_{\alpha, \mathbf{q}} \hbar\omega_{\mathbf{q}} \left(B_{\alpha, \mathbf{q}}^{\dagger} B_{\alpha, \mathbf{q}} + \frac{1}{2} \right). \quad (2.35)$$

2. System Hamiltonian

For the Coulomb interaction, one easily finds [8]

$$H_C = \frac{1}{2} \sum_{\lambda, \lambda'} \sum_{\mathbf{k}_{\parallel}, \mathbf{k}'_{\parallel}, \mathbf{q}_{\parallel}} V_{\mathbf{q}_{\parallel}}^{\lambda, \lambda'} a_{\lambda, \mathbf{k}_{\parallel} + \mathbf{q}_{\parallel}}^{\dagger} a_{\lambda', \mathbf{k}'_{\parallel} - \mathbf{q}_{\parallel}}^{\dagger} a_{\lambda', \mathbf{k}'_{\parallel}} a_{\lambda, \mathbf{k}_{\parallel}} \quad (2.36)$$

where $V_{\mathbf{q}_{\parallel}}^{\lambda, \lambda'}$ denotes the Coulomb-matrix element of the confined system (see Appendix B). Together with the phonon-interaction H_{ph} , Eqs. (2.34)-(2.36) constitute the system Hamiltonian in the $\mathbf{p} \cdot \mathbf{A}$ -picture

$$H = H_0 + H_{A,p} + H_{A,A} + H_C + H_{ph}. \quad (2.37)$$

The explicit form of H_{ph} can be found, e.g., in Ref. [6, 8]. The corresponding results for QWI arrangements are presented in Appendix B.

The interaction Hamiltonian, Eq. (2.37), is the general starting point for investigations of semiconductor excitations with classical and quantum light sources. This Thesis will concentrate on the semiclassical limit of the light-matter interaction where the carriers are treated quantum mechanically while the light field is treated classically. At this limit, correlations between carriers and the light field are ignored. Furthermore, we always assume that the light propagates perpendicular to the QW leading to a completely homogeneous excitation. In this configuration, the semiclassical factorization [6] yields

$$\langle \mathbf{A}_{\mathbf{q}_{\parallel}} \rangle = \delta_{\mathbf{q}_{\parallel}, \mathbf{0}} \langle \mathbf{A}_{\mathbf{q}_{\parallel}} \rangle. \quad (2.38)$$

The vector potential, Eq. (2.20), then only depends on the z -coordinate and we may write $\langle \mathbf{A}(\mathbf{r}) \rangle = \langle A(z) \rangle \mathbf{e}_A$ where \mathbf{e}_A is the polarization direction of the classical light field in the QW plane. The semi-classical light-matter interaction Hamiltonian then simplifies into

$$\begin{aligned} H_{A,p} + H_{A,A} &= \sum_{\lambda} \sum_{\mathbf{k}_{\parallel}} \left(-j_{\lambda}(\mathbf{k}_{\parallel}) \langle A(z_{QW}) \rangle + \frac{|e|^2}{2m_0} \langle A(z_{QW}) \rangle^2 \right) a_{\lambda, \mathbf{k}_{\parallel}}^{\dagger} a_{\lambda, \mathbf{k}_{\parallel}} \\ &+ \sum_{\lambda \neq \lambda'} \sum_{\mathbf{k}_{\parallel}} \frac{|e|}{m_0} p_{\lambda, \lambda'}(\mathbf{k}_{\parallel}) \langle A(z_{QW}) \rangle a_{\lambda, \mathbf{k}_{\parallel}}^{\dagger} a_{\lambda', \mathbf{k}_{\parallel}} \end{aligned} \quad (2.39)$$

where we introduced $j_{\lambda}(\mathbf{k}_{\parallel}) = \mathbf{j}_{\lambda}(\mathbf{k}_{\parallel}) \cdot \mathbf{e}_A$ and $p_{\lambda, \lambda'}(\mathbf{k}_{\parallel}) = \mathbf{p}_{\lambda, \lambda'}(\mathbf{k}_{\parallel}) \cdot \mathbf{e}_A$. Moreover, we assumed strong confinement such that the vector potential is practically constant over the extension of the QW which is centered around $z = z_{QW}$.

The interaction of semiconductor nanostructures with *classical* THz fields, which is analyzed in this Thesis, is an area of active research – especially the regime of strong-field coherent THz excitations is largely unexplored. Under certain conditions, the *quantum-nature* of the THz light can become relevant. In this case, one has to start from the fully quantized interaction Hamiltonian, Eq. (2.34). References [40, 41] analyze, e.g., the spontaneous emission of THz light from laser-induced plasma rods using a fully quantum-mechanical theory of the light-matter interaction. In general, the analysis of quantum-optical effects is more complicated; in particular, the A^2 -dependent part in Eq. (2.34) requires a careful treatment [40].

3. Semiconductor Response to Classical Terahertz Excitation

In the ground state of a semiconductor, the uppermost valence band is fully occupied with electrons while the conduction band is empty. Optical excitation resonant with the bandgap can coherently lift carriers from the valence band to the conduction band. Such an excitation creates interband polarization, carrier densities, and correlations in the system. While the coherent interband polarization typically decays on a picosecond timescale due to radiative decay and scattering processes, incoherent densities and correlations can remain in the system for several nanoseconds since their lifetime is ultimately limited by the relatively slow radiative recombination processes [6, 7]. We are interested in situations where the optically excited semiconductor is additionally excited with a classical THz field. The THz excitation can occur either in the *coherent* regime shortly after optical excitation when significant interband polarization is still present or in the *incoherent* regime when all interband coherences have already decayed.

In this Chapter, I will present a microscopic theory based on an equation-of-motion and cluster-expansion approach which can efficiently describe such processes. In recent years, this theory has been successfully applied to investigate the decay of interband polarization and the formation process of the incoherent many-body state for various optical excitation conditions [22–26, 37]. The focus of this Thesis is not so much on the scattering processes relevant for the formation dynamics but rather to reveal new aspects about the coupling of the optically-excited state to the THz field. Since THz excitations are resonant with intraband transitions, the THz coupling is quite different from interactions with optical fields. I will explicitly study systems which can be described by one conduction band and one valence band. The confinement is assumed to be strong such that only the lowest confinement level is excited. The generalization to multiple bands is straightforward.

3.1. Light Propagation

As a first step, we discuss the coupling of the semiconductor to a classical electromagnetic field described by the vector potential $\langle \mathbf{A}(\mathbf{r}) \rangle$. We assume that the field is linearly polarized in x -direction and that it propagates perpendicular to the nanostructure such that we can write $\langle \mathbf{A}(\mathbf{r}) \rangle = \langle A(z) \rangle \mathbf{e}_x$. The classical wave equation for the vector potential with the full coupling with intraband quantities is given by [6, 38]

$$\left[\frac{\partial^2}{\partial z^2} - \frac{n_0^2}{c_0^2} \frac{\partial^2}{\partial t^2} \right] \langle A \rangle = -\mu_0 g(z) \left[J_{\text{THz}} + J_{A,m_0} + \frac{\partial P}{\partial t} \right] \quad (3.1)$$

3. Semiconductor Response to Classical Terahertz Excitation

where n_0 is the constant background refractive index of the semiconductor QW, μ_0 the vacuum permittivity and $g(z) = g^{\lambda,\lambda'}(z) = \xi_\lambda^*(z)\xi_{\lambda'}(z)$ the confinement. We assume that the confinement wavefunctions are independent of the bulk-band index λ and that the QW is positioned at the origin. The right-hand side of Eq. (3.1) contains the intraband THz current

$$J_{\text{THz}} = \frac{1}{\mathcal{S}} \sum_{\lambda, \mathbf{k}_\parallel} j_\lambda(\mathbf{k}_\parallel) \langle a_{\lambda, \mathbf{k}_\parallel}^\dagger a_{\lambda, \mathbf{k}_\parallel} \rangle, \quad (3.2)$$

the macroscopic interband polarization

$$\frac{\partial P}{\partial t} = -\frac{1}{\mathcal{S}} \sum_{\lambda \neq \lambda', \mathbf{k}_\parallel} \frac{|e|}{m_0} p_{\lambda, \lambda'}(\mathbf{k}_\parallel) \langle a_{\lambda, \mathbf{k}_\parallel}^\dagger a_{\lambda', \mathbf{k}_\parallel} \rangle, \quad (3.3)$$

and an $\langle A \rangle$ -dependent intraband contribution

$$J_{A, m_0} = -\frac{1}{\mathcal{S}} \sum_{\lambda, \mathbf{k}_\parallel} \frac{|e|^2}{m_0} \langle A \rangle \langle a_{\lambda, \mathbf{k}_\parallel}^\dagger a_{\lambda, \mathbf{k}_\parallel} \rangle. \quad (3.4)$$

The subscript m_0 indicates that J_{A, m_0} current depends on the bare electron mass m_0 rather than the effective electron mass m_λ of band λ . The derivation [6, 38] of Eq. (3.1) shows that J_{A, m_0} directly results from the A^2 -dependent part of the interaction Hamiltonian, Eq. (2.34). Its physical meaning will be discussed in Section 4.2. For the QWI arrangement, we have to substitute $1/\mathcal{S} \rightarrow n_{\text{QWI}}/\mathcal{L}$ in Eqs. (3.1)-(3.4) where \mathcal{L} is the quantization length and n_{QWI} is the density of wires. The QW density n_{2D} is replaced via $n_{2D} \rightarrow n_{\text{QWI}} n_{1D}$ where n_{1D} the density within one quantum wire. .

The wave equation (3.1) describes the interaction of matter with light in the optical or THz regime of the electromagnetic spectrum. We next determine the matter response, i.e., polarization and currents via an equation-of-motion technique.

3.2. Hierarchy Problem and Cluster-Expansion Approach

In order to evaluate the source terms, Eqs. (3.2)-(3.4), in Maxwell's wave equation (3.1), we need to determine the single-particle expectation values $\langle a_{\lambda, \mathbf{k}_\parallel}^\dagger a_{\lambda', \mathbf{k}_\parallel} \rangle$. For a two-band system with one conduction band (c) and one valence band (v), these are given by the incoherent electron and hole distributions

$$f_{\mathbf{k}_\parallel}^e = \langle a_{c, \mathbf{k}_\parallel}^\dagger a_{c, \mathbf{k}_\parallel} \rangle, \quad f_{\mathbf{k}_\parallel}^h = 1 - \langle a_{v, \mathbf{k}_\parallel}^\dagger a_{v, \mathbf{k}_\parallel} \rangle \quad (3.5)$$

and the coherent microscopic transition amplitude

$$P_{\mathbf{k}_\parallel} = \langle a_{v, \mathbf{k}_\parallel}^\dagger a_{c, \mathbf{k}_\parallel} \rangle. \quad (3.6)$$

3.2. Hierarchy Problem and Cluster-Expansion Approach

With these quantities, Eqs. (3.2) and (3.4) read

$$J_{\text{THz}} = \frac{1}{\mathcal{S}} \sum_{\mathbf{k}_{\parallel}} \left(j_e(\mathbf{k}_{\parallel}) f_{\mathbf{k}_{\parallel}}^e + j_h(\mathbf{k}_{\parallel}) f_{\mathbf{k}_{\parallel}}^h \right), \quad (3.7)$$

$$J_{A,m_0} = -\frac{1}{\mathcal{S}} \sum_{\mathbf{k}_{\parallel}} \left(\frac{|e|^2}{m_0} f_{\mathbf{k}_{\parallel}}^e + \frac{|e|^2}{m_0} (1 - f_{\mathbf{k}_{\parallel}}^h) \right) \langle A \rangle \quad (3.8)$$

where we used $\sum_{\mathbf{k}_{\parallel}} j_v(\mathbf{k}_{\parallel}) = 0$ and defined $j_e(\mathbf{k}_{\parallel}) = j_c(\mathbf{k}_{\parallel})$ and $j_h(\mathbf{k}_{\parallel}) = -j_v(\mathbf{k}_{\parallel})$. The divergent contribution in Eq. (3.8) proportional to $\sum_{\mathbf{k}_{\parallel}} 1$ does not contribute to the response as shown in Appendix C.1. The THz current J_{THz} vanishes for a system in equilibrium because then the carrier densities are even functions of carrier momentum, $f_{-\mathbf{k}_{\parallel}}^{e(h)} = f_{\mathbf{k}_{\parallel}}^{e(h)}$, while the current-matrix element is an odd function of carrier momentum, $j_{e(h)}(-\mathbf{k}_{\parallel}) = -j_{e(h)}(\mathbf{k}_{\parallel})$. The interband polarization, Eq. (3.3), is given by

$$\frac{\partial P}{\partial t} = -\frac{1}{\mathcal{S}} \sum_{\mathbf{k}_{\parallel}} \left(\frac{|e|}{m_0} p_{v,c}(\mathbf{k}_{\parallel}) P_{\mathbf{k}_{\parallel}} + \frac{|e|}{m_0} p_{v,c}^*(\mathbf{k}_{\parallel}) P_{\mathbf{k}_{\parallel}}^* \right). \quad (3.9)$$

In principle, the quantum dynamics of the expectation value of any operator \mathcal{O} can be obtained via the Heisenberg Equation of Motion

$$i\hbar \frac{\partial}{\partial t} \langle \mathcal{O} \rangle = \langle [\mathcal{O}, H] \rangle. \quad (3.10)$$

where H is the system Hamiltonian. However, it is well known that the dynamics of the single-particle quantities, Eqs. (3.5)-(3.6), does not yield a closed set of equations because the many-body Coulomb and phonon interactions lead to the so-called *hierarchy problem*. For example, the commutator of $a_{\lambda, \mathbf{k}_{\parallel}}$ and the Coulomb Hamiltonian produces the operator equation

$$i\hbar \frac{\partial}{\partial t} a_{\lambda, \mathbf{k}_{\parallel}} \Big|_{H_C} = \sum_{\nu, \mathbf{k}'_{\parallel}, \mathbf{q}_{\parallel}} V_{\mathbf{q}_{\parallel}} a_{\nu, \mathbf{k}'_{\parallel}}^{\dagger} a_{\nu, \mathbf{k}'_{\parallel} + \mathbf{q}_{\parallel}} a_{\lambda, \mathbf{k}_{\parallel} - \mathbf{q}_{\parallel}}. \quad (3.11)$$

In general, an N -particle correlation consisting of N fermion creation and N fermion annihilation operators,

$$\langle N \rangle = \langle a_{\lambda_1, \mathbf{k}_{1\parallel}}^{\dagger} \cdots a_{\lambda_N, \mathbf{k}_{N\parallel}}^{\dagger} a_{\nu_N, \mathbf{p}_{N\parallel}} \cdots a_{\nu_1, \mathbf{p}_{1\parallel}} \rangle, \quad (3.12)$$

couple to an $(N+1)$ -particle correlation because of the many-body interactions which leads to an infinite hierarchy of equations. Schematically, the hierarchy problem is described by

$$i\hbar \frac{\partial}{\partial t} \langle N \rangle = T[\langle N \rangle] + V[\langle N+1 \rangle] \quad (3.13)$$

where T and V are known functionals. We here apply the Cluster-Expansion (CE) Approach [6, 42–45] to consistently truncate the hierarchy because that method has

3. Semiconductor Response to Classical Terahertz Excitation

been successfully applied in quantum chemistry [46], in semiconductors [6, 22–26, 37] as well as in quantum optics [6, 26]. Here, the basic concept of the CE is outlined based mainly on Refs. [6, 45]. The idea of this scheme is to express N -particle correlations in terms of lower-order correlations (clusters). A consistent approximation retains all clusters up to a certain order and neglects all higher-order clusters. At the lowest level, this approximation is identical to the Hartree-Fock approximation. An N -particle correlation is expressed by one-particle correlations (singlet-clusters) according to

$$\langle N \rangle_S = \sum_{\pi} (-1)^{\pi} \prod_{i=1}^N \langle a_{\mathbf{k}_i}^{\dagger} a_{\mathbf{p}_{\pi[i]}} \rangle \quad (3.14)$$

where we introduced the notation $\mathbf{k}_i = (\lambda_i, \mathbf{k}_{i\parallel})$ and $\mathbf{p}_j = (\nu_j, \mathbf{p}_{j\parallel})$ and where π is a permutation of the \mathbf{k}_i with sign $(-1)^{\pi}$. For a generalization of Eq. (3.14), we need to express the N -particle correlation $\langle N \rangle$ in terms of independent single particles (singlets), correlated pairs (doublets) and so on, up to correlated N -particle clusters. This is done recursively via

$$\begin{aligned} \langle 1 \rangle &= \langle 1 \rangle_S \\ \langle 2 \rangle &= \langle 2 \rangle_S + \Delta \langle 2 \rangle \\ \langle 3 \rangle &= \langle 3 \rangle_S + \langle 1 \rangle \Delta \langle 2 \rangle + \Delta \langle 3 \rangle \\ \langle N \rangle &= \langle N \rangle_S + \langle N-2 \rangle \Delta \langle 2 \rangle + \langle N-4 \rangle \Delta \langle 2 \rangle \Delta \langle 2 \rangle \\ &\quad + \dots + \langle N-3 \rangle \Delta \langle 3 \rangle + \dots + \Delta \langle N \rangle. \end{aligned} \quad (3.15)$$

Here, each term represents a sum over all possibilities to rearrange the N coordinates among singlets, doublets and so on. The sign depends on how many permutations of carrier operators are performed before the factorization. The identified $\Delta \langle N \rangle$ denotes the purely correlated part of an N -particle correlation and is obtained by subtracting all lower-order contributions from the full correlation. In an intuitive picture, $\Delta \langle N \rangle$ describes an entity consisting of N correlated particles.

The equations of motion for the singlets have the general form

$$i\hbar \frac{\partial}{\partial t} \langle 1 \rangle = T_1[\langle 1 \rangle] + V_1[\langle 2 \rangle_S] + V_1[\Delta \langle 2 \rangle]. \quad (3.16)$$

In the singlet-approximation, the genuine two-particle correlations, $V_1[\Delta \langle 2 \rangle]$, are neglected. Often, $V_1[\Delta \langle 2 \rangle]$ is not set to zero but replaced with a scattering expression which accounts for the dominant higher-order effects (see Ref. [6] for more details). To describe the dynamics of correlated pairs, e.g., exciton populations, which are truly bound electron-hole pairs, Eq. (3.16) is not sufficient since correlations are described by doublets or higher-order clusters. The equations of motion for the singlet and doublet quantities have the general form

$$i\hbar \frac{\partial}{\partial t} \langle 1 \rangle = T_1[\langle 1 \rangle] + V_1[\langle 2 \rangle_S] + V_1[\Delta \langle 2 \rangle], \quad (3.17)$$

$$i\hbar \frac{\partial}{\partial t} \Delta \langle 2 \rangle = T_2[\Delta \langle 2 \rangle] + V_2[\langle 3 \rangle_{SD}] + V_2[\Delta \langle 3 \rangle], \quad (3.18)$$

3.2. Hierarchy Problem and Cluster-Expansion Approach

with $\langle 3 \rangle_{\text{SD}} = \langle 3 \rangle_{\text{S}} + \langle 1 \rangle \Delta \langle 2 \rangle$. The singlet-doublet approximation neglects pure triplets $\Delta \langle 3 \rangle$ and higher-order clusters such that the Eqs. (3.17)-(3.18) are closed. For a more accurate description, $\Delta \langle 3 \rangle$ can also be included at the scattering level without the need to include more equations [6].

For homogeneous excitation conditions, the in-plane momentum must be conserved in all quantities. Thus, one only generates singlets

$$\langle a_{\lambda, \mathbf{k}_{\parallel}}^{\dagger} a_{\lambda', \mathbf{k}'_{\parallel}} \rangle = \delta_{\mathbf{k}_{\parallel}, \mathbf{k}'_{\parallel}} \langle a_{\lambda, \mathbf{k}_{\parallel}}^{\dagger} a_{\lambda', \mathbf{k}_{\parallel}} \rangle \quad (3.19)$$

that are diagonal in \mathbf{k}_{\parallel} . As a result, $f_{\mathbf{k}_{\parallel}}^e$, $f_{\mathbf{k}_{\parallel}}^h$ and $P_{\mathbf{k}_{\parallel}}$ are the only relevant singlets for the homogeneous two-band system. Correspondingly, the two-particle correlations must be of the form

$$\begin{aligned} c_{\lambda, \nu; \nu', \lambda'}^{\mathbf{q}_{\parallel}, \mathbf{k}'_{\parallel}, \mathbf{k}_{\parallel}} &\equiv \Delta \langle a_{\lambda, \mathbf{k}_{\parallel}}^{\dagger} a_{\nu, \mathbf{k}'_{\parallel}}^{\dagger} a_{\nu', \mathbf{k}'_{\parallel} + \mathbf{q}_{\parallel}} a_{\lambda', \mathbf{k}_{\parallel} - \mathbf{q}_{\parallel}} \rangle \\ &\equiv \langle a_{\lambda, \mathbf{k}_{\parallel}}^{\dagger} a_{\nu, \mathbf{k}'_{\parallel}}^{\dagger} a_{\nu', \mathbf{k}'_{\parallel} + \mathbf{q}_{\parallel}} a_{\lambda', \mathbf{k}_{\parallel} - \mathbf{q}_{\parallel}} \rangle - \langle a_{\lambda, \mathbf{k}_{\parallel}}^{\dagger} a_{\nu, \mathbf{k}'_{\parallel}}^{\dagger} a_{\nu', \mathbf{k}'_{\parallel} + \mathbf{q}_{\parallel}} a_{\lambda', \mathbf{k}_{\parallel} - \mathbf{q}_{\parallel}} \rangle_S. \end{aligned} \quad (3.20)$$

In our analysis, the incoherent doublets, i.e., the electron-electron correlations $c_{c,c;c,c}$, the hole-hole correlations $c_{v,v;v,v}$ and the exciton correlations $c_X \equiv c_{c,v;c,v}$ will be the most relevant.

Note that the exciton correlations

$$c_X^{\mathbf{q}_{\parallel}, \mathbf{k}'_{\parallel}, \mathbf{k}_{\parallel}} = \Delta \langle a_{c, \mathbf{k}_{\parallel}}^{\dagger} a_{v, \mathbf{k}'_{\parallel}}^{\dagger} a_{c, \mathbf{k}'_{\parallel} + \mathbf{q}_{\parallel}} a_{v, \mathbf{k}_{\parallel} - \mathbf{q}_{\parallel}} \rangle \quad (3.21)$$

obviously describe correlated electron-hole pairs, i.e., exciton populations since they describe correlations among the electron-hole creation (index \mathbf{k}) and the electron-hole destruction (index \mathbf{k}'). This quantity exists only if electron-hole pairs are correlated which is the necessary requirement for true excitons. The same correlations can be transformed into

$$c_{eh}^{\mathbf{p}_{\parallel}, \mathbf{k}'_{\parallel}, \mathbf{k}_{\parallel}} \equiv c_X^{\mathbf{k}_{\parallel} + \mathbf{p}_{\parallel}, \mathbf{k}'_{\parallel}, \mathbf{k}_{\parallel}} = \Delta \langle a_{c, \mathbf{k}_{\parallel}}^{\dagger} a_{v, \mathbf{k}'_{\parallel}}^{\dagger} a_{c, \mathbf{k}_{\parallel} + \mathbf{p}_{\parallel}} a_{v, \mathbf{k}'_{\parallel} - \mathbf{p}_{\parallel}} \rangle \quad (3.22)$$

which describes correlations between an electron density (index \mathbf{k}) and a hole density (index \mathbf{k}'). In this format, c_X rather describes correlations in an electron-hole plasma. Since c_X is solved with all momentum combinations in the consistent singlet-doublet approximation, the full solution contains both exciton populations and electron-hole plasma correlations.

The CE approach is appealing since it maps the complicated many-body dynamics onto a closed set of equations for the physically relevant quantities. In many cases, it is justified to truncate the hierarchy at the singlet or singlet-doublet level since semiconductor electrons often behave like effective single-particles or are truly coupled only to nearby electrons. For these cases, a numerical solution of the resulting equations of motion is feasible with modern computer systems. Another advantage of the CE approach is that the correlated doublets, triplets, etc. have a straightforward intuitive interpretation as particle clusters involving only a few number of correlated particles.

3.3. Singlet Equations in the Coherent Regime

In this Section, I will evaluate the Heisenberg equations of motion of the single-particle quantities $P_{\mathbf{k}_{\parallel}}$, $f_{\mathbf{k}_{\parallel}}^e$ and $f_{\mathbf{k}_{\parallel}}^h$. The analysis will extend the standard derivation [8] because I will exclusively use the $\mathbf{p} \cdot \mathbf{A}$ -picture and investigate how THz and optical contributions appear in the equation structure. The dynamics is determined by the system Hamiltonian, Eq. (2.37), with the semi-classical light-matter interaction, Eq. (2.39). After presenting the general equations of motion, I will derive the dynamics for simultaneous optical and THz excitation taking advantage of the different energy scales of optical and THz fields.

3.3.1. Maxwell-Semiconductor-Bloch Equations

We analyze the dynamics of the singlets, Eqs. (3.5)-(3.6), via the Heisenberg equations of motion (3.10). A straightforward evaluation of the commutators and singlet factorizations yields the following set of equations

$$i\hbar \frac{\partial}{\partial t} P_{\mathbf{k}_{\parallel}} = \left[\tilde{\varepsilon}_{\mathbf{k}_{\parallel}} - j(\mathbf{k}_{\parallel}) \langle A(0, t) \rangle \right] P_{\mathbf{k}_{\parallel}} - \left[1 - f_{\mathbf{k}_{\parallel}}^e - f_{\mathbf{k}_{\parallel}}^h \right] \left[-\frac{|e|}{m_0} p_{c,v}(\mathbf{k}_{\parallel}) \langle A(0, t) \rangle + \sum_{\mathbf{k}'_{\parallel}} V_{\mathbf{k}_{\parallel} - \mathbf{k}'_{\parallel}} P_{\mathbf{k}'_{\parallel}} \right] + \Gamma_{v,c;\mathbf{k}_{\parallel}}^{\text{coul}} + \Gamma_{v,c;\mathbf{k}_{\parallel}}^{\text{phon}}, \quad (3.23)$$

$$\hbar \frac{\partial}{\partial t} f_{\mathbf{k}_{\parallel}}^e = 2\text{Im} \left[P_{\mathbf{k}_{\parallel}} \left(-\frac{|e|}{m_0} p_{c,v}^*(\mathbf{k}_{\parallel}) \langle A(0, t) \rangle + \sum_{\mathbf{k}'_{\parallel}} V_{\mathbf{k}_{\parallel} - \mathbf{k}'_{\parallel}} P_{\mathbf{k}'_{\parallel}}^* \right) + \Gamma_{c,e;\mathbf{k}_{\parallel}}^{\text{coul}} + \Gamma_{c,e;\mathbf{k}_{\parallel}}^{\text{phon}} \right], \quad (3.24)$$

$$\hbar \frac{\partial}{\partial t} f_{\mathbf{k}_{\parallel}}^h = 2\text{Im} \left[P_{\mathbf{k}_{\parallel}} \left(-\frac{|e|}{m_0} p_{c,v}^*(\mathbf{k}_{\parallel}) \langle A(0, t) \rangle + \sum_{\mathbf{k}'_{\parallel}} V_{\mathbf{k}_{\parallel} - \mathbf{k}'_{\parallel}} P_{\mathbf{k}'_{\parallel}}^* \right) - \Gamma_{v,v;\mathbf{k}_{\parallel}}^{\text{coul}} - \Gamma_{v,v;\mathbf{k}_{\parallel}}^{\text{phon}} \right] \quad (3.25)$$

Here, we introduced the current-matrix element $j(\mathbf{k}_{\parallel}) \equiv j_e(\mathbf{k}_{\parallel}) + j_h(\mathbf{k}_{\parallel})$ and the renormalized kinetic electron-hole-pair energy

$$\tilde{\varepsilon}_{\mathbf{k}_{\parallel}} \equiv \varepsilon_{\mathbf{k}_{\parallel}}^e + \varepsilon_{\mathbf{k}_{\parallel}}^h + E_G - \sum_{\mathbf{k}'_{\parallel}} V_{\mathbf{k}_{\parallel} - \mathbf{k}'_{\parallel}} \left(f_{\mathbf{k}'_{\parallel}}^e + f_{\mathbf{k}'_{\parallel}}^h \right), \quad (3.26)$$

with $\varepsilon_{\mathbf{k}_{\parallel}}^e \equiv \varepsilon_{\mathbf{k}_{\parallel}}^c$ and $\varepsilon_{\mathbf{k}_{\parallel}}^h \equiv -\varepsilon_{\mathbf{k}_{\parallel}}^v - E_G$ where E_G is the band-gap energy. The doublet correlations $\Gamma_{\lambda,\lambda';\mathbf{k}_{\parallel}}^{\text{coul}}$ defined via

$$\Gamma_{\lambda,\lambda';\mathbf{k}_{\parallel}}^{\text{coul}} \equiv \sum_{\nu, \mathbf{k}'_{\parallel}, \mathbf{q}_{\parallel} \neq 0} V_{\mathbf{q}_{\parallel}} \left[c_{\lambda,\nu;\nu,\lambda'}^{\mathbf{q}_{\parallel}, \mathbf{k}'_{\parallel}, \mathbf{k}_{\parallel}} - \left(c_{\lambda',\nu;\nu,\lambda}^{\mathbf{q}_{\parallel}, \mathbf{k}'_{\parallel}, \mathbf{k}_{\parallel}} \right)^* \right] \quad (3.27)$$

are generated by the Coulomb interactions. The explicit form of the phonon contributions $\Gamma_{\lambda,\lambda'}^{\text{phon}}$ can be found, e.g., in Ref. [6]. In general, the doublet terms $\Gamma_{\lambda,\lambda'}$ introduce microscopic couplings which describe dephasing and energy renormalizations of the

3.3. Singlet Equations in the Coherent Regime

single-particle quantities as well as relaxation of the carrier densities toward steady-state distributions.

Equations (3.23)-(3.27) fully include the intraband processes induced by the light field. Together with the wave equation (3.1)-(3.4), they generalize the well-known Maxwell-Semiconductor-Bloch Equations (MSBE) [8] in the $\mathbf{p} \cdot \mathbf{A}$ -picture. The derivation of the MSBE shows that the H_{A^2} -part of the interaction Hamiltonian, Eq. (2.39), does not contribute at all to the equations of motion since

$$i\hbar \frac{\partial}{\partial t} P_{\mathbf{k}_{\parallel}} \Big|_{H_{A^2}} = i\hbar \frac{\partial}{\partial t} f_{\mathbf{k}_{\parallel}}^e \Big|_{H_{A^2}} = i\hbar \frac{\partial}{\partial t} f_{\mathbf{k}_{\parallel}}^h \Big|_{H_{A^2}} = 0. \quad (3.28)$$

The $H_{j \cdot A}$ -part of the interaction Hamiltonian, Eq. (2.39), does contribute to the microscopic polarization but not to the carrier densities

$$i\hbar \frac{\partial}{\partial t} P_{\mathbf{k}_{\parallel}} \Big|_{H_{j \cdot A}} = -j(\mathbf{k}_{\parallel}) \langle A(0, t) \rangle P_{\mathbf{k}_{\parallel}}, \quad i\hbar \frac{\partial}{\partial t} f_{\mathbf{k}_{\parallel}}^e \Big|_{H_{j \cdot A}} = i\hbar \frac{\partial}{\partial t} f_{\mathbf{k}_{\parallel}}^h \Big|_{H_{j \cdot A}} = 0. \quad (3.29)$$

Thus, the intraband contributions alter the microscopic polarization by introducing a source proportional to the current matrix element $j(\mathbf{k}_{\parallel})$. Since $j(\mathbf{k}_{\parallel})$ is an odd function of \mathbf{k} , this term changes the symmetry of $P_{\mathbf{k}_{\parallel}}$. It is instructive to divide all singlet quantities into an symmetric (even) and an antisymmetric (odd) contribution via

$$P_{\mathbf{k}_{\parallel}}^{\text{even}} = \frac{1}{2}(P_{\mathbf{k}_{\parallel}} + P_{-\mathbf{k}_{\parallel}}), \quad P_{\mathbf{k}_{\parallel}}^{\text{odd}} = \frac{1}{2}(P_{\mathbf{k}_{\parallel}} - P_{-\mathbf{k}_{\parallel}}) \quad (3.30)$$

$$f_{\mathbf{k}_{\parallel}}^{e(h), \text{even}} = \frac{1}{2}(f_{\mathbf{k}_{\parallel}}^{e(h)} + f_{-\mathbf{k}_{\parallel}}^{e(h)}), \quad f_{\mathbf{k}_{\parallel}}^{e(h), \text{odd}} = \frac{1}{2}(f_{\mathbf{k}_{\parallel}}^{e(h)} - f_{-\mathbf{k}_{\parallel}}^{e(h)}). \quad (3.31)$$

Due to the intraband source term, Eq. (3.29), an evenly distributed $P_{\mathbf{k}_{\parallel}}$ can generate an odd contribution and vice-versa since

$$i\hbar \frac{\partial}{\partial t} P_{\mathbf{k}_{\parallel}}^{\text{odd(even)}} \Big|_{H_{j \cdot A}} = -j(\mathbf{k}_{\parallel}) \langle A(0, t) \rangle P_{\mathbf{k}_{\parallel}}^{\text{even(odd)}}. \quad (3.32)$$

An odd polarization $P_{\mathbf{k}_{\parallel}}^{\text{odd}}$ leads to an odd carrier distributions $f_{\mathbf{k}_{\parallel}}^{e(h), \text{odd}}$ which in turn leads to a non-vanishing THz current, J_{THz} according to Eq. (3.7). As a result, the rotational symmetry of the QW is broken. When numerically solving the generalized SBE (3.23)-(3.27), the full angle dependence has to be taken into account which makes the THz computations challenging.

3.3.2. Simultaneous Optical and THz Excitation

We next consider situations where the semiconductor is excited with both optical (i.e., visible or near-visible) and THz light pulses. The total vector potential and electric field can be divided into an optical and a THz part

$$\langle A(z, t) \rangle = \langle A(z, t) \rangle_{\text{opt}} + \langle A(z, t) \rangle_{\text{THz}}, \quad \langle E(z, t) \rangle = \langle E(z, t) \rangle_{\text{opt}} + \langle E(z, t) \rangle_{\text{THz}}. \quad (3.33)$$

3. Semiconductor Response to Classical Terahertz Excitation

After careful separation of optical and THz contributions, the MSBE (3.1)-(3.4) and (3.23)-(3.27) cast into the form

$$i\hbar\frac{\partial}{\partial t}P_{\mathbf{k}_{\parallel}} = \left[\tilde{\varepsilon}_{\mathbf{k}_{\parallel}} - j(\mathbf{k}_{\parallel})\langle A(0, t) \rangle_{\text{THz}} + \frac{|e|^2}{2\mu(\mathbf{k}_{\parallel})}\langle A(0, t) \rangle_{\text{THz}}^2 \right] P_{\mathbf{k}_{\parallel}} \quad (3.34)$$

$$- \left[1 - f_{\mathbf{k}_{\parallel}}^e - f_{\mathbf{k}_{\parallel}}^h \right] \Omega_{\mathbf{k}_{\parallel}} + \Gamma_{v,c;\mathbf{k}_{\parallel}}^{\text{coul}} + \Gamma_{v,c;\mathbf{k}_{\parallel}}^{\text{phon}},$$

$$\hbar\frac{\partial}{\partial t}f_{\mathbf{k}_{\parallel}}^e = 2\text{Im} \left[P_{\mathbf{k}_{\parallel}}\Omega_{\mathbf{k}_{\parallel}}^* + \Gamma_{c,c;\mathbf{k}_{\parallel}}^{\text{coul}} + \Gamma_{c,c;\mathbf{k}_{\parallel}}^{\text{phon}} \right], \quad (3.35)$$

$$\hbar\frac{\partial}{\partial t}f_{\mathbf{k}_{\parallel}}^h = 2\text{Im} \left[P_{\mathbf{k}_{\parallel}}\Omega_{\mathbf{k}_{\parallel}}^* - \Gamma_{v,v;\mathbf{k}_{\parallel}}^{\text{coul}} - \Gamma_{v,v;\mathbf{k}_{\parallel}}^{\text{phon}} \right] \quad (3.36)$$

with the \mathbf{k}_{\parallel} -dependent reduced effective mass and the renormalized *optical* Rabi frequency

$$\frac{1}{\mu(\mathbf{k}_{\parallel})} = \frac{1}{\hbar^2} \frac{\partial^2 \varepsilon_{\mathbf{k}_{\parallel}}}{\partial k_x^2}, \quad \Omega_{\mathbf{k}_{\parallel}} = d_{c,v}(\mathbf{k}_{\parallel})\langle E(0, t) \rangle_{\text{opt}} + \sum_{\mathbf{k}'_{\parallel}} V_{\mathbf{k}_{\parallel}-\mathbf{k}'_{\parallel}} P_{\mathbf{k}'_{\parallel}} \quad (3.37)$$

where $\varepsilon_{\mathbf{k}_{\parallel}} \equiv \varepsilon_{\mathbf{k}_{\parallel}}^e + \varepsilon_{\mathbf{k}_{\parallel}}^h$. The dipole-matrix element $d_{c,v}$ is introduced below in Eq. (3.43). The propagation of THz and optical fields is described by two separate wave equations

$$\left[\frac{\partial^2}{\partial z^2} - \frac{n_0^2}{c_0^2} \frac{\partial^2}{\partial t^2} \right] \langle A(z, t) \rangle_{\text{THz}} = -\mu_0 g(z) \left[J_{\text{THz}} + J_A \right], \quad (3.38)$$

$$\left[\frac{\partial^2}{\partial z^2} - \frac{n_0^2}{c_0^2} \frac{\partial^2}{\partial t^2} \right] \langle E(z, t) \rangle_{\text{opt}} = \mu_0 g(z) \frac{\partial^2 P}{\partial t^2} \quad (3.39)$$

where J_{THz} is given by Eq. (3.7) and where we defined

$$J_A = -\frac{1}{\mathcal{S}} \sum_{\mathbf{k}_{\parallel}} \left(\frac{|e|^2}{m_e(\mathbf{k}_{\parallel})} f_{\mathbf{k}_{\parallel}}^e + \frac{|e|^2}{m_h(\mathbf{k}_{\parallel})} f_{\mathbf{k}_{\parallel}}^h \right) \langle A \rangle_{\text{THz}}, \quad (3.40)$$

$$P = \frac{1}{\mathcal{S}} \sum_{\mathbf{k}_{\parallel}} \left(d_{v,c}(\mathbf{k}_{\parallel}) P_{\mathbf{k}_{\parallel}} + d_{v,c}^*(\mathbf{k}_{\parallel}) P_{\mathbf{k}_{\parallel}}^* \right). \quad (3.41)$$

As we discuss in the following, a few approximations are necessary to derive Eqs. (3.34)-(3.41) starting from the general MSBE (3.1)-(3.4) and (3.23)-(3.27).

In Eqs. (3.34)-(3.37), we recovered the standard form [8] of the optical Rabi frequency $d_{c,v}(\mathbf{k}_{\parallel})\langle E \rangle_{\text{opt}}$ which contains the dipole-matrix element and the electric field instead of the original expression $-|e|p_{c,v}(\mathbf{k}_{\parallel})/m_0\langle A \rangle_{\text{opt}}$ in Eqs. (3.23)-(3.25) which contains the momentum-matrix element and the vector potential. This replacement is valid for optical fields $\langle A \rangle_{\text{opt}} = A_{\text{env}}(t)e^{-i\omega_0 t}$ which oscillate with frequencies ω_0 close to the band-gap frequency E_G/\hbar . For a slowly varying envelope, we can approximate

$$-\langle E(t) \rangle = \frac{\partial \langle A \rangle}{\partial t} = -i\omega_0 \langle A(t) \rangle + \frac{\partial A_{\text{env}}}{\partial t} e^{-i\omega_0 t} \approx -i\omega_0 \langle A(t) \rangle. \quad (3.42)$$

3.3. Singlet Equations in the Coherent Regime

Using Eq. (3.42) and the general relation between dipole-matrix element and momentum-matrix element (see Appendix A)

$$d_{c,v}(\mathbf{k}_{\parallel}) \approx \frac{i\hbar}{E_G} \frac{|e|p_{c,v}(\mathbf{k}_{\parallel})}{m_0}, \quad (3.43)$$

it is easy to show that indeed $-|e|p_{c,v}(\mathbf{k}_{\parallel})/m_0 \langle A \rangle_{\text{opt}} \approx d_{c,v}(\mathbf{k}_{\parallel}) \langle E \rangle_{\text{opt}}$. In Eqs. (3.34)-(3.36), we also assumed that the optical field does not induce intraband transitions since they are strongly off-resonant. Using similar arguments, one can easily show that only the interband polarization, Eq. (3.41), appears in the optical wave equation (3.39).

One could expect that the interband transitions induced by the off-resonant THz field

$$i\hbar \frac{\partial}{\partial t} P_{\mathbf{k}_{\parallel}} \Big|_{\text{off-res}} = \left[1 - f_{\mathbf{k}_{\parallel}}^e - f_{\mathbf{k}_{\parallel}}^h \right] \frac{|e|}{m_0} p_{c,v}(\mathbf{k}_{\parallel}) \langle A(0, t) \rangle_{\text{THz}}, \quad (3.44)$$

$$\hbar \frac{\partial}{\partial t} f_{\mathbf{k}_{\parallel}}^e \Big|_{\text{off-res}} = -2\text{Im} \left[P_{\mathbf{k}_{\parallel}} \frac{|e|}{m_0} p_{c,v}^*(\mathbf{k}_{\parallel}) \langle A(0, t) \rangle_{\text{THz}} \right], \quad (3.45)$$

$$\hbar \frac{\partial}{\partial t} f_{\mathbf{k}_{\parallel}}^h \Big|_{\text{off-res}} = -2\text{Im} \left[P_{\mathbf{k}_{\parallel}} \frac{|e|}{m_0} p_{c,v}^*(\mathbf{k}_{\parallel}) \langle A(0, t) \rangle_{\text{THz}} \right], \quad (3.46)$$

in Eqs. (3.23)-(3.25) do not contribute at all to the dynamics since THz-induced interband transitions are strongly suppressed. However, for a consistent description of the THz light-matter interaction, it is vital to include these terms. It is shown in Appendix C.1 that the off-resonant terms, Eqs. (3.44)-(3.46), lead (i) to the $\langle A \rangle_{\text{THz}}^2$ -dependent energy renormalization in Eq. (3.34) and (ii) to the appearance of effective masses in the J_A -source term, Eq. (3.40), of the THz wave equation (3.38) (see also Refs. [47, 48]).

Effectively, the THz field only leads to *intraband* contributions in the polarization equation (3.34). The $j \cdot A$ -dependent term changes the symmetry of the polarization while the A^2 -dependent term renormalizes the kinetic energies. Equations (3.34)-(3.41) are a general starting point to investigate THz effects in the coherent regime. The THz field interacts with the coherent interband polarization which is created by the optical pulse.

Using Eqs. (3.23)-(3.25) and (3.7), we can determine the equation of motion for the THz current J_{THz} directly. For the time-interval after optical excitation where the optical pulse vanishes, $E_{\text{opt}} \rightarrow 0$, but interband polarization is still present, we obtain

$$\hbar \frac{\partial}{\partial t} J_{\text{THz}} = \text{Im} \left[\frac{2}{\mathcal{S}} \sum_{\lambda, \mathbf{k}} j_{\lambda}(\mathbf{k}_{\parallel}) (\Gamma_{\lambda, \lambda; \mathbf{k}}^{\text{coul}} + \Gamma_{\lambda, \lambda; \mathbf{k}}^{\text{phon}}) \right] + \text{Im} \left[\frac{2}{\mathcal{S}} \sum_{\mathbf{k}_{\parallel}, \mathbf{k}'_{\parallel}} V_{\mathbf{k}_{\parallel} - \mathbf{k}'_{\parallel}} j(\mathbf{k}_{\parallel}) P_{\mathbf{k}_{\parallel}} P_{\mathbf{k}'_{\parallel}}^* \right] \quad (3.47)$$

According to Eq. (3.32), the THz field can induce an antisymmetric $P_{\mathbf{k}_{\parallel}}$ such that the second term in Eq. (3.47) provides a non-vanishing source for J_{THz} . The scattering contributions in $\Gamma_{\lambda, \lambda; \mathbf{k}}^{\text{coul}}$ and $\Gamma_{\lambda, \lambda; \mathbf{k}}^{\text{phon}}$ mostly lead to a decay of the generated J_{THz} and their contribution can be modelled phenomenologically as discussed in Appendix C.3.

3.4. Singlet-Doublet Equations in the Incoherent Regime

We next focus on situations where a completely incoherent many-body state is excited with a THz pulse. The vector potential is then given by the THz field $\langle A(z, t) \rangle = \langle A(z, t) \rangle_{\text{THz}}$ alone. The consistent singlet-doublet solution requires that the dynamics of the incoherent singlets f^e and f^h as well as of the incoherent doublets $c_{c,c;c,c}$, $c_{v,v;v,v}$, and c_X is solved. The carrier distributions, which determine the THz current, Eq. (3.7), obey

$$\hbar \frac{\partial}{\partial t} f_{\mathbf{k}_{\parallel}}^e = 2\text{Im} \left[\sum_{\mathbf{k}'_{\parallel}, \mathbf{q}_{\parallel}} \left(V_{\mathbf{q}_{\parallel}} c_{c,c;c,c}^{\mathbf{q}_{\parallel}, \mathbf{k}'_{\parallel}, \mathbf{k}_{\parallel}} - V_{\mathbf{k}_{\parallel} - \mathbf{q}_{\parallel} - \mathbf{k}'_{\parallel}} c_X^{\mathbf{q}_{\parallel}, \mathbf{k}'_{\parallel}, \mathbf{k}_{\parallel}} \right) + \Gamma_{c,c;\mathbf{k}_{\parallel}}^{\text{phon}} \right] \quad (3.48)$$

$$\hbar \frac{\partial}{\partial t} f_{\mathbf{k}_{\parallel}}^h = 2\text{Im} \left[\sum_{\mathbf{k}'_{\parallel}, \mathbf{q}_{\parallel}} \left(-V_{\mathbf{q}_{\parallel}} c_{v,v;v,v}^{\mathbf{q}_{\parallel}, \mathbf{k}'_{\parallel}, \mathbf{k}_{\parallel}} + V_{\mathbf{k}_{\parallel} - \mathbf{q}_{\parallel} - \mathbf{k}'_{\parallel}} c_X^{-\mathbf{q}_{\parallel}, \mathbf{k}'_{\parallel}, \mathbf{k}_{\parallel}} \right) - \Gamma_{v,v;\mathbf{k}_{\parallel}}^{\text{phon}} \right]. \quad (3.49)$$

Thus, $f_{\mathbf{k}_{\parallel}}^{\lambda}$ does not couple to the THz field directly in the $\mathbf{p} \cdot \mathbf{A}$ -picture. Rather, their dynamics is determined by the incoherent doublets $c_{\lambda,\nu;\lambda,\nu}$ which may in turn couple to the THz-field. As for the singlet dynamics, the H_{A^2} -part of the interaction Hamiltonian, Eq. (2.39), does not contribute to the doublet dynamics at all

$$i\hbar \frac{\partial}{\partial t} c_{\lambda,\nu;\lambda,\nu}^{\mathbf{q}_{\parallel}, \mathbf{k}'_{\parallel}, \mathbf{k}_{\parallel}} \Big|_{H_{A^2}} = 0. \quad (3.50)$$

The $H_{j,A}$ -part of Eq. (2.39) does contribute to the dynamics of c_X but not to the other incoherent doublets $c_{\lambda,\lambda;\lambda,\lambda}$

$$i\hbar \frac{\partial}{\partial t} c_X^{\mathbf{q}_{\parallel}, \mathbf{k}'_{\parallel}, \mathbf{k}_{\parallel}} \Big|_{H_{j,A}} = -j(\mathbf{k}'_{\parallel} + \mathbf{q}_{\parallel} - \mathbf{k}_{\parallel}) \langle A(0, t) \rangle_{\text{THz}} c_X^{\mathbf{q}_{\parallel}, \mathbf{k}'_{\parallel}, \mathbf{k}_{\parallel}}, \quad (3.51)$$

$$i\hbar \frac{\partial}{\partial t} c_{c,c;c,c}^{\mathbf{q}_{\parallel}, \mathbf{k}'_{\parallel}, \mathbf{k}_{\parallel}} \Big|_{H_{j,A}} = i\hbar \frac{\partial}{\partial t} c_{v,v;v,v}^{\mathbf{q}_{\parallel}, \mathbf{k}'_{\parallel}, \mathbf{k}_{\parallel}} \Big|_{H_{j,A}} = 0. \quad (3.52)$$

Here, we introduced

$$j(\mathbf{k}'_{\parallel} + \mathbf{q}_{\parallel} - \mathbf{k}_{\parallel}) \equiv j_e(\mathbf{k}'_{\parallel} + \mathbf{q}_{\parallel}) - j_e(\mathbf{k}_{\parallel}) + j_h(\mathbf{k}'_{\parallel}) - j_h(\mathbf{k}_{\parallel} - \mathbf{q}_{\parallel}). \quad (3.53)$$

generalizing the definition after Eq. (3.25). Equations (3.48)-(3.53) illustrate the important fact that many-body interactions – in the form of correlations – are needed to generate a THz current. Physically, this is related to the fact that non-interacting carriers cannot absorb light since momentum and energy conservation cannot be simultaneously fulfilled for such a process [8, 39].

We find that the THz dynamics results exclusively from the exciton correlations. A

3.4. Singlet-Doublet Equations in the Incoherent Regime

lengthy but straightforward calculation [6] yields the equation of motion

$$\begin{aligned}
i\hbar \frac{\partial}{\partial t} c_X^{\mathbf{q}_{\parallel}, \mathbf{k}'_{\parallel}, \mathbf{k}_{\parallel}} &= \left[\Delta E_X^{\mathbf{q}_{\parallel}, \mathbf{k}'_{\parallel}, \mathbf{k}_{\parallel}} - j(\mathbf{k}'_{\parallel} + \mathbf{q}_{\parallel} - \mathbf{k}_{\parallel}) \langle A(0, t) \rangle_{\text{THz}} \right] c_X^{\mathbf{q}_{\parallel}, \mathbf{k}'_{\parallel}, \mathbf{k}_{\parallel}} \\
&+ [1 - f_{\mathbf{k}_{\parallel}}^e - f_{\mathbf{k}_{\parallel} - \mathbf{q}_{\parallel}}^h] \sum_{\mathbf{l}_{\parallel}} V_{\mathbf{l}_{\parallel} - \mathbf{k}_{\parallel}} c_X^{\mathbf{q}_{\parallel}, \mathbf{k}'_{\parallel}, \mathbf{l}_{\parallel}} \\
&- [1 - f_{\mathbf{k}'_{\parallel} + \mathbf{q}_{\parallel}}^e - f_{\mathbf{k}'_{\parallel}}^h] \sum_{\mathbf{l}_{\parallel}} V_{\mathbf{l}_{\parallel} - \mathbf{k}'_{\parallel}} c_X^{\mathbf{q}_{\parallel}, \mathbf{l}_{\parallel}, \mathbf{k}_{\parallel}} \\
&+ S_X^{\mathbf{q}_{\parallel}, \mathbf{k}'_{\parallel}, \mathbf{k}_{\parallel}} + D_{X, \text{rest}}^{\mathbf{q}_{\parallel}, \mathbf{k}'_{\parallel}, \mathbf{k}_{\parallel}} + [G_{\text{phon}}]_X^{\mathbf{q}_{\parallel}, \mathbf{k}'_{\parallel}, \mathbf{k}_{\parallel}} + T_X^{\mathbf{q}_{\parallel}, \mathbf{k}'_{\parallel}, \mathbf{k}_{\parallel}}
\end{aligned} \tag{3.54}$$

where we introduced the renormalized kinetic energy of the two-particle state

$$\Delta E_X^{\mathbf{q}_{\parallel}, \mathbf{k}'_{\parallel}, \mathbf{k}_{\parallel}} \equiv \tilde{\varepsilon}_{\mathbf{k}'_{\parallel} + \mathbf{q}_{\parallel}}^e + \tilde{\varepsilon}_{\mathbf{k}'_{\parallel}}^h - \tilde{\varepsilon}_{\mathbf{k}_{\parallel} - \mathbf{q}_{\parallel}}^h - \tilde{\varepsilon}_{\mathbf{k}_{\parallel}}^e. \tag{3.55}$$

The single-particle-scattering source,

$$\begin{aligned}
S_X^{\mathbf{q}_{\parallel}, \mathbf{k}'_{\parallel}, \mathbf{k}_{\parallel}} &\equiv V_{\mathbf{k}_{\parallel} - \mathbf{k}'_{\parallel} - \mathbf{q}_{\parallel}} \left[(1 - f_{\mathbf{k}_{\parallel}}^e)(1 - f_{\mathbf{k}_{\parallel} - \mathbf{q}_{\parallel}}^h) f_{\mathbf{k}'_{\parallel} + \mathbf{q}_{\parallel}}^e f_{\mathbf{k}'_{\parallel}}^h \right. \\
&\quad \left. - f_{\mathbf{k}_{\parallel}}^e f_{\mathbf{k}_{\parallel} - \mathbf{q}_{\parallel}}^h (1 - f_{\mathbf{k}'_{\parallel} + \mathbf{q}_{\parallel}}^e)(1 - f_{\mathbf{k}'_{\parallel}}^h) \right],
\end{aligned} \tag{3.56}$$

describes in- and out-scattering of electrons and holes and leads, e.g., to the equilibration of the carrier system. The Coulomb sums in the second and third line are proportional to $(1 - f^e - f^h)$ and thus, at low densities, they are the dominant contributions [6]. They allow for the possibility of truly bound excitons. At low densities, one often applies the *main-sum approximation* where only these Coulomb sums and the kinetic-energy parts of Eq. (3.54) are taken into account. The remaining Coulomb-induced doublets are given symbolically via $D_{X, \text{rest}}$ and include fermionic exchange, scattering and screening effects. The phonon-correlation contributions are given by $[G_{\text{phon}}]_X$. For their explicit forms consult Appendix C.2 and Ref. [6]. Finally, three-particle correlations are symbolized via T_X and are discussed in App C.3. The carrier-carrier correlations $c_{c,c;c,c}$ and $c_{v,v;v,v}$ obey similar equations as c_X . However, these correlations are not driven by the THz field. As a result, they only lead to a relaxation of carrier distributions (see App C.3). The explicit equations of motion for all incoherent doublets are presented in Appendix C.2.

In Eqs. (3.48)-(3.54), we did not include the interband transitions induced by the off-resonant THz field, Eqs. (3.44)-(3.46). However, as for the singlet equations in the coherent regime, they must not be ignored. In Appendix C.1, we show that they affect only the THz wave equation converting the free electron mass in J_{A, m_0} into effective masses. The propagation of the THz field is then given by the wave equation

$$\left[\frac{\partial^2}{\partial z^2} - \frac{n_0^2}{c_0^2} \frac{\partial^2}{\partial t^2} \right] \langle A(z, t) \rangle_{\text{THz}} = -\mu_0 g(z) \left[J_{\text{THz}} + J_A \right] \tag{3.57}$$

where J_{THz} and J_A are given by Eqs. (3.7) and (3.40), respectively.

3. Semiconductor Response to Classical Terahertz Excitation

Equations (3.48)-(3.57) are a general starting point to study THz effects in the incoherent regime. To obtain more insight into the THz dynamics, we again introduce even and odd parts of the correlations

$$c_{X,\text{even}}^{\mathbf{q}_{\parallel},\mathbf{k}'_{\parallel},\mathbf{k}_{\parallel}} = \frac{1}{2} \left(c_X^{\mathbf{q}_{\parallel},\mathbf{k}'_{\parallel},\mathbf{k}_{\parallel}} + c_X^{-\mathbf{q}_{\parallel},-\mathbf{k}'_{\parallel},-\mathbf{k}_{\parallel}} \right) \quad (3.58)$$

$$c_{X,\text{odd}}^{\mathbf{q}_{\parallel},\mathbf{k}'_{\parallel},\mathbf{k}_{\parallel}} = \frac{1}{2} \left(c_X^{\mathbf{q}_{\parallel},\mathbf{k}'_{\parallel},\mathbf{k}_{\parallel}} - c_X^{-\mathbf{q}_{\parallel},-\mathbf{k}'_{\parallel},-\mathbf{k}_{\parallel}} \right). \quad (3.59)$$

As for the singlet equations in the coherent regime, the THz field breaks the rotational symmetry of the QW thus inducing a macroscopic current

$$i\hbar \frac{\partial}{\partial t} c_{X,\text{odd}(\text{even})}^{\mathbf{q}_{\parallel},\mathbf{k}'_{\parallel},\mathbf{k}_{\parallel}} \Big|_{H_{j \cdot A}} = -j(\mathbf{k}'_{\parallel} + \mathbf{q}_{\parallel} - \mathbf{k}_{\parallel}) \langle A(0, t) \rangle_{\text{THz}} c_{X,\text{even}(\text{odd})}^{\mathbf{q}_{\parallel},\mathbf{k}'_{\parallel},\mathbf{k}_{\parallel}}. \quad (3.60)$$

Combining Eqs. (3.48)-(3.54) and (3.7), we find for the dynamics of the THz current

$$\begin{aligned} \hbar \frac{\partial}{\partial t} J_{\text{THz}} = & \text{Im} \left[\frac{2}{\mathcal{S}} \sum_{\lambda,\mathbf{k},\mathbf{k}'_{\parallel},\mathbf{q}_{\parallel}} V_{\mathbf{q}_{\parallel}} j_{\lambda}(\mathbf{k}_{\parallel}) c_{\lambda,\lambda;\lambda,\lambda}^{\mathbf{q}_{\parallel},\mathbf{k}'_{\parallel},\mathbf{k}_{\parallel}} \right] + G^{\text{phon}} + T^{\text{J}} \quad (3.61) \\ & - \text{Im} \left[\frac{2}{\mathcal{S}} \sum_{\mathbf{k}_{\parallel},\mathbf{k}'_{\parallel},\mathbf{q}_{\parallel}} V_{\mathbf{k}_{\parallel}-\mathbf{q}_{\parallel}-\mathbf{k}'_{\parallel}} (j_e(\mathbf{k}_{\parallel}) - j_h(\mathbf{k}'_{\parallel})) c_X^{\mathbf{q}_{\parallel},\mathbf{k}'_{\parallel},\mathbf{k}_{\parallel}} \right]. \end{aligned}$$

According to Eq. (3.60), the source in the second line of Eq. (3.61) can lead to a non-vanishing current when both exciton correlations and THz fields are present. The Coulomb-induced doublets $c_{\lambda,\lambda;\lambda,\lambda}$, the phonon-induced doublets G^{phon} as well as the triplet contributions T^{J} effectively lead to a damping of the generated current and we treat them phenomenologically as discussed in Appendix C.3. The fact that the THz field directly couples to the incoherent many-body state is remarkable and a unique property of THz excitations. In contrast to optical interband excitations, the THz field does not change the overall density of the system, i.e., the number of excited carriers is conserved.

4. Linear and Nonlinear Terahertz Spectroscopy

Interband spectroscopy is a well-established technique to analyze semiconductors. In typical experiments, one applies optical pulses in the visible or near-infrared regime of the electromagnetic spectrum to excite the semiconductor nanostructure. When collected, the spectrum of the transmitted and reflected fields reveal valuable information about the matter polarization induced in the sample. In linear optical spectroscopy, weak pulses are used to probe the band-to-band transitions revealing, e.g., information about the density of states, excitonic resonances and radiative-coupling effects [49–51]. In nonlinear optical spectroscopy, strong pulses are used to actively control the state of the semiconductor. Here, a variety of techniques such as pump-probe measurements [4, 5], four-wave mixing experiments [1–3], and 2D-Fourier spectroscopy [52, 53] have been developed to detect the ultrafast many-body dynamics in semiconductors revealing, e.g., lifetime of excited states. Moreover, coherent control of the semiconductor many-body state such as interband Rabi-flopping [54, 55] or the generation of spin currents [56, 57] makes nonlinear optical excitations interesting for applications such as ultrafast optical switching and quantum information processes.

The comparatively new field of THz spectroscopy promises to have a similar impact on semiconductor optics. Due to its small photon energy, the THz field is sensitive to internal transitions between different many-body states which correspond to intraband transitions. Thus, weak THz pulses can probe and strong THz pulses can manipulate the quasi-particle state in a way that is not accessible via conventional optical techniques. Sources and detectors of THz radiation have rapidly improved in recent years [12, 13]. In particular, high-intensity sources have become available [27] opening the gate toward nonlinear THz spectroscopy.

In this Chapter, I will identify the quantities that are accessible in typical linear and nonlinear THz experiments. Moreover, I will show that the linear THz response can be solved analytically for general conditions. The analytical result formally resembles the famous Elliott formula [58] which describes the linear response of a semiconductor in the optical regime.

4.1. Linear Terahertz Susceptibility

According to the results of the previous Chapter, the exciting THz field $\langle A(z, t) \rangle_{\text{THz}}$ generates a current $J_{\text{tot}}(z, t) \equiv J_A(z, t) + J_{\text{THz}}(z, t)$ in the QW which couples back to the THz field via Maxwell’s wave equation [see Eqs. (3.38) and (3.57)]. In the linear regime,

4. Linear and Nonlinear Terahertz Spectroscopy

the induced polarization $P_{\text{tot}}(z, t)$ defined via $J_{\text{tot}}(z, t) = (\partial/\partial t)P_{\text{tot}}(z, t)$, is proportional to the electric field $\langle E(z, t) \rangle_{\text{THz}} = -(\partial/\partial t)\langle A(z, t) \rangle_{\text{THz}}$ at the QW position. The optical properties then follow from the local susceptibility

$$\chi_{\text{loc}}(z, \omega) = \frac{g(z)P_{\text{tot}}(z, \omega)}{\varepsilon_0 \langle E(z, \omega) \rangle_{\text{THz}}} = \frac{g(z)J_{\text{tot}}(z, \omega)}{\varepsilon_0 \omega^2 \langle A(z, \omega) \rangle_{\text{THz}}} \quad (4.1)$$

where we used $P_{\text{tot}}(\omega) = iJ_{\text{tot}}(\omega)/\omega$ and $\langle E(z, \omega) \rangle_{\text{THz}} = i\omega \langle A(z, \omega) \rangle_{\text{THz}}$. For QWs whose lateral extension L is small compared to the THz wavelength, the linear response follows from the averaged susceptibility

$$\chi(\omega) = \frac{1}{L} \int_{-L/2}^{L/2} dz \chi_{\text{loc}}(z, \omega) = \frac{1}{L} \frac{J_{\text{tot}}(0, \omega)}{\varepsilon_0 \omega^2 \langle A(0, \omega) \rangle_{\text{THz}}} \quad (4.2)$$

where we approximated $g(z) \approx \delta(z)$. We next show that the susceptibility, Eq. (4.2), can be related to the transmitted, $\langle E_T(z, t) \rangle$, and reflected, $\langle E_R(z, t) \rangle$, THz electric fields which are accessible in experiments. For a thin QW, Maxwell's wave equation (3.38)/(3.57) can be solved analytically. Following the derivations in Ref. [59], one finds that the transmitted and reflected fields at the QW position, $z_{\text{QW}} = 0$, are given by

$$\langle E_T(0, t) \rangle = \langle E_0(0, t) \rangle - \frac{\mu_0 c_0}{2n_0} J_{\text{tot}}(0, t) \quad (4.3)$$

$$\langle E_R(0, t) \rangle = -\frac{\mu_0 c_0}{2n_0} J_{\text{tot}}(0, t) \quad (4.4)$$

where $\langle E_0(0, t) \rangle$ is the incoming THz electric field. It follows that the differential transmission, i.e., the *re-emitted* THz field

$$\Delta \langle E_T(0, t) \rangle = \langle E_T(0, t) \rangle - \langle E_0(0, t) \rangle = -\frac{\mu_0 c_0}{2n_0} J_{\text{tot}}(0, t) \quad (4.5)$$

is directly proportional to the total current induced in the QW. Combining Eqs. (4.2) and (4.5), we find the expression

$$\chi(\omega) = -\frac{2in_0c_0}{\omega L} \frac{\Delta \langle E_T(0, \omega) \rangle}{\langle E_T(0, \omega) \rangle} \quad (4.6)$$

which is valid only for weak THz excitations, i.e., in the linear regime.

It is a special feature of THz spectroscopy that the full waveform of the THz electric field can be measured in experiments, e.g., via electro-optical sampling [28]. Thus, experiments access both amplitude and phase of the $\langle E_T(0, t) \rangle$ and $\Delta \langle E_T(0, t) \rangle$ -signals such that both real and imaginary part of $\chi(\omega)$ are obtained without the need of Kramers-Kronig relations [8]. With the knowledge of the full susceptibility, we can derive the absorption coefficient and refractive index change. The absorption coefficient

$$\alpha(\omega) = 1 - |R(\omega)|^2 - |T(\omega)|^2 \quad (4.7)$$

is defined via the reflection, $R(\omega) = \langle E_R(\omega) \rangle / \langle E_0(\omega) \rangle$, and transmission, $T(\omega) = \langle E_T(\omega) \rangle / \langle E_0(\omega) \rangle$, coefficients. According to Eqs. (4.2)-(4.4), they are given by

$$R(\omega) = \frac{i\xi(\omega)}{1 - i\xi(\omega)}, \quad T(\omega) = \frac{1}{1 - i\xi(\omega)} \quad (4.8)$$

with the quantity $\xi(\omega) \equiv \omega L / (2c_0 n_0) \chi(\omega)$. By inserting Eq. (4.8) into Eq. (4.7), we find

$$\alpha(\omega) = \frac{2\text{Im}[\xi(\omega)]}{1 + |\xi(\omega)|^2 + 2\text{Im}[\xi(\omega)]} \approx 2\text{Im}[\xi(\omega)] = \frac{\omega L}{c_0 n_0} \text{Im}[\chi(\omega)] \quad (4.9)$$

where we assumed $|\xi(\omega)| \ll 1$. The refractive index $n(\omega) = \text{Re}[\sqrt{\varepsilon_T(\omega)}]$ is defined via the transversal dielectric function

$$\varepsilon_T(\omega) = \varepsilon_{\text{BG}} + \chi(\omega) \quad (4.10)$$

with the background dielectric constant $\varepsilon_{\text{BG}} = n_0^2$. When $|\chi(\omega)|$ is much smaller than ε_{BG} , we can expand $\sqrt{\varepsilon_{\text{BG}} + \chi(\omega)}$ to the first order in $\chi(\omega)$ such that the refractive index change is given by

$$\Delta n(\omega) = n(\omega) - n_0 = \frac{\text{Re}[\chi(\omega)]}{2n_0}. \quad (4.11)$$

4.2. Terahertz-Elliott Formula

The susceptibility, $\chi(\omega) = \chi_A(\omega) + \chi_{\text{THz}}(\omega)$, defined in Eq. (4.2) consists of two contributions given by

$$\chi_A(\omega) = \frac{1}{L} \frac{J_A(0, \omega)}{\varepsilon_0 \omega^2 \langle A_T(0, \omega) \rangle}, \quad (4.12)$$

$$\chi_{\text{THz}}(\omega) = \frac{1}{L} \frac{J_{\text{THz}}(0, \omega)}{\varepsilon_0 \omega^2 \langle A_T(0, \omega) \rangle}. \quad (4.13)$$

Here, $\chi_A(\omega)$ is determined by the ponderomotive current J_A which follows from Eq. (3.40) and $\chi_{\text{THz}}(\omega)$ is determined by the THz current J_{THz} which follows from Eq. (3.47) and Eq. (3.61) for coherent and incoherent conditions, respectively. Assuming parabolic bands, we find that the ponderomotive contribution is given by

$$\chi_A(\omega) = -\frac{|e|^2}{\varepsilon_0 \omega^2} \frac{1}{\mathcal{S}L} \sum_{\mathbf{k}_{\parallel}} \left(\frac{f_{\mathbf{k}_{\parallel}}^e}{m_e(\mathbf{k}_{\parallel})} + \frac{f_{\mathbf{k}_{\parallel}}^h}{m_h(\mathbf{k}_{\parallel})} \right) = -\frac{|e|^2 n_{3D}}{\varepsilon_0 \mu \omega^2} = -\frac{\omega_{\text{PL}}^2 \varepsilon_{\text{BG}}}{\omega^2} \quad (4.14)$$

where we identified the reduced mass $\mu = m_e m_h / (m_e + m_h)$, the three-dimensional density $n_{3D} = n_{2D} / L$ and the plasma frequency

$$\omega_{\text{PL}} = \sqrt{\frac{|e|^2 n_{3D}}{\varepsilon_{\text{BG}} \varepsilon_0 \mu}}. \quad (4.15)$$

4. Linear and Nonlinear Terahertz Spectroscopy

Thus, $\chi_A(\omega)$ is simply proportional to the total density of excited carriers n_{3D} . Since the THz field does not change n_{3D} , this contribution is independent of the THz-induced many-body dynamics. Equation (4.14) describes a Drude-like response; $\chi_A(\omega)$ is purely real such that it leads to a refractive index change but not to any absorption of the THz field. Physically, $\chi_A(\omega)$ guarantees that an incident field oscillating with a frequency $\omega \rightarrow 0$, i.e., a ‘‘propagating’’ constant field does not enter the QW. According to Eq. (4.8), $\chi(\omega) = \chi_A(\omega)$ implies

$$R(\omega) = \frac{-i\omega_{\text{PL}}^2 \varepsilon_{\text{BG}} L / (2c_0 n_0 \omega)}{1 + i\omega_{\text{PL}}^2 \varepsilon_{\text{BG}} L / (2c_0 n_0 \omega)} \rightarrow -1, \quad T(\omega) = \frac{1}{1 + i\omega_{\text{PL}}^2 \varepsilon_{\text{BG}} L / (2c_0 n_0 \omega)} \rightarrow 0 \quad (4.16)$$

for $\omega \rightarrow 0$. For semiconductors, the plasma frequency is often in the THz regime such that the ponderomotive contribution can become significant.

True THz absorption can only result from the remaining χ_{THz} part of the susceptibility which is determined by the THz current J_{THz} . In Chapter 3, we found that J_{THz} is generated by the THz-coupling to the microscopic interband polarization $P_{\mathbf{k}_{\parallel}}$ or to the exciton correlations $c_X^{\mathbf{q}_{\parallel}, \mathbf{k}'_{\parallel}, \mathbf{k}_{\parallel}}$. In general, the induced THz current must be determined numerically by solving Eqs. (3.34)-(3.41) and Eqs. (3.48)-(3.57) for coherent and incoherent conditions, respectively. However, following Ref. [38], we now show that the linear response can be solved analytically for certain conditions.

First, we discuss the linear response in the coherent regime for an excitation scenario shown in Fig. 4.1(a). At the time t_{opt} , the QW is excited by a weak optical pulse which generates interband polarization [see Fig. 4.1(b)]. After a delay time $\Delta t = t_{\text{THz}} - t_{\text{opt}} > 0$, the QW is probed with a weak THz pulse. Since the linear optical pulse does not induce significant correlations in the QW, we can use the singlet equations (3.34)-(3.41) to determine the THz response. We assume that the optical pulse, $\langle E_{\text{opt}} \rangle$, has already vanished at the probing time but that the coherent interband polarization has not yet fully decayed. To analytically solve the linear response, it is useful to represent the dynamics of polarization and THz current in an exciton basis. This is done in a Appendix D.3. According to Eq. (D.20), the linearized current dynamics is given by

$$\hbar \frac{\partial}{\partial t} J_{\text{THz}}^{\text{coh}}(\omega) = \frac{2}{\mathcal{S}} \text{Im} \left[\sum_{\lambda, \nu} (E_{\nu} - E_{\lambda}) J_{\lambda, \nu} \left([p_{\lambda}^{(0)}]^* p_{\nu}^{(1)} \right) \right] - \gamma_J J_{\text{THz}}^{\text{coh}} \quad (4.17)$$

where E_{λ} denotes the energy of exciton state λ , $J_{\lambda, \nu}$ is the exciton transition-matrix element between exciton state λ and ν , and γ_J is a phenomenological constant which defines the current decay. The quantity p_{λ} denotes the component of the polarization in exciton state λ . It is related to the microscopic polarization $P_{\mathbf{k}_{\parallel}}$ via

$$p_{\lambda} = \sum_{\mathbf{k}_{\parallel}} \phi_{\lambda}^L(\mathbf{k}_{\parallel}) P_{\mathbf{k}_{\parallel}}, \quad P_{\mathbf{k}_{\parallel}} = \sum_{\lambda} \phi_{\lambda}^R(\mathbf{k}_{\parallel}) p_{\lambda} \quad (4.18)$$

where $\phi_{\lambda}^L(\mathbf{k}_{\parallel})$ is the exciton wavefunction. In Eqs. (4.17), we already split the excitonic polarization $p_{\lambda} = p_{\lambda}^{(0)} + p_{\lambda}^{(1)}$ into a quasi-stationary part, $p_{\lambda}^{(0)}$, which does not couple to

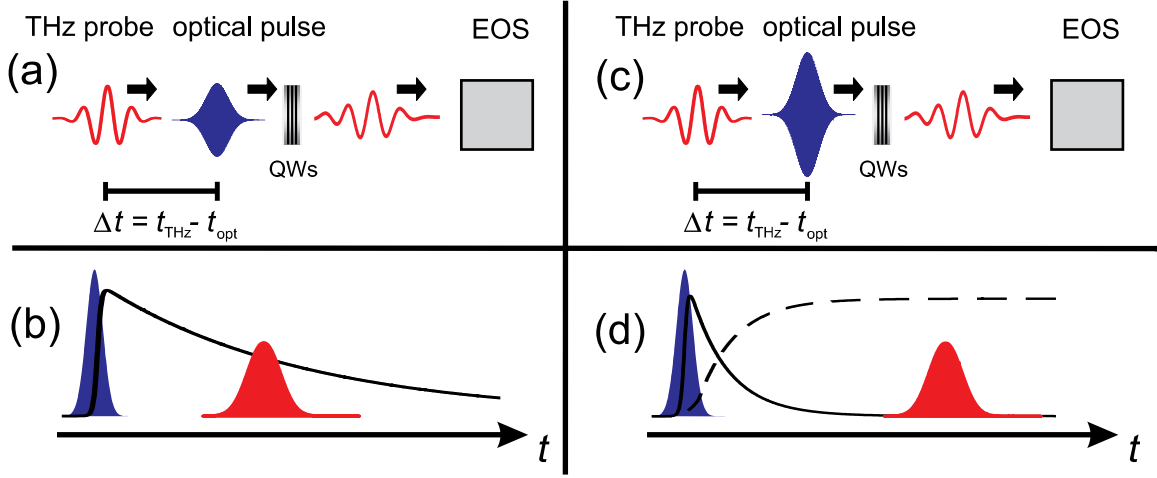


Figure 4.1.: Schematic setup to measure the linear THz response in the coherent and incoherent regimes. (a) The QW is excited with a weak optical pulse (dark shaded area) and a weak THz pulse (solid line). The waveform of the transmitted THz pulse is measured in a detector, e.g., via electro-optic sampling. (b) The optical pulse (dark shaded area) generates coherent interband polarization (solid line) which is probed by the THz pulse (shaded area). (c) and (d) show the same situation as (a) and (b) but for excitation with an optical pulse which also generates significant incoherent correlations indicated by the dashed line in (d).

the THz field and a linear-response part, $p_\lambda^{(1)}$. According to Eq. (D.21), the linearized polarization dynamics in the exciton basis is given by

$$i\hbar \frac{\partial}{\partial t} \left([p_\lambda^{(0)}]^\star p_\nu^{(1)} \right) = (E_\nu - E_\lambda - 2i\gamma_D) \left([p_\lambda^{(0)}]^\star p_\nu^{(1)} \right) - \sum_\beta \left[J_{\nu,\beta} \left([p_\lambda^{(0)}]^\star p_\beta^{(0)} \right) \right] \langle A \rangle_{\text{THz}} \quad (4.19)$$

where γ_D is the dephasing of the interband polarization due to doublets. We notice that the term proportional to $\langle A \rangle_{\text{THz}}$ in Eq. (4.19) represents a source for the THz current when polarization $p_\lambda^{(0)}$ is present. The assumption that $p_\lambda^{(0)}$ is quasi-stationary requires that the THz probe is short.

In this format, Eqs. (4.17) and (4.19) are closed and can easily be solved. First, we solve the polarization dynamics via Fourier transformation with respect to time obtaining

$$\left([p_\lambda^{(0)}]^\star p_\nu^{(1)} \right) (\omega) = \frac{-\sum_\beta \left[J_{\nu,\beta} \left([p_\lambda^{(0)}]^\star p_\beta^{(0)} \right) \right]}{\hbar\omega - E_\nu + E_\lambda + 2i\gamma_D} \langle A(\omega) \rangle_{\text{THz}}. \quad (4.20)$$

We then Fourier transform the current dynamics and insert Eq. (4.20). The final result

4. Linear and Nonlinear Terahertz Spectroscopy

for the THz susceptibility is then

$$\begin{aligned}\chi_{\text{THz}}^{\text{coh}}(\omega) &= \frac{J_{\text{THz}}^{\text{coh}}(\omega)/L}{\varepsilon_0\omega^2\langle A_T(\omega)\rangle} \\ &= \frac{1}{\varepsilon_0L\omega^2(\hbar\omega + i\gamma_J)} \sum_{\lambda,\nu} \left\{ S_{\lambda,\nu}^{\text{coh}}(\omega) \left([p_\lambda^{(0)}]^\star p_\nu^{(0)} \right) - \left[S_{\lambda,\nu}^{\text{coh}}(-\omega) \left([p_\lambda^{(0)}]^\star p_\nu^{(0)} \right) \right]^\star \right\}\end{aligned}\quad (4.21)$$

with the response function

$$S_{\lambda,\nu}^{\text{coh}}(\omega) = \sum_{\beta} \frac{(E_\beta - E_\lambda)J_{\nu,\beta}J_{\beta,\lambda}}{E_\beta - E_\lambda - \hbar\omega - 2i\gamma_D}.\quad (4.22)$$

We find that the linear susceptibility features discrete resonances determined by the separation of exciton energies. The linear response crucially depends on the excitonic polarization $p_\lambda^{(0)}$ present in the system.

Figure 4.1(c) show a typical experimental setup to probe the incoherent regime. An optical pulse creates interband polarization but also carriers and incoherent correlations in the QW [see Figure 4.1(d)]. While the polarization (solid line) decays on a picosecond timescale, the correlations (dashed line) can remain in the system for nanoseconds. Thus, a sufficiently delayed THz pulse only probes the incoherent quasi-particle state.

The correlation and current dynamics is described by Eqs. (3.54)-(3.61). In Appendix D.4, we transform these equations of motion into an exciton basis. According to Eq. (D.24), the current dynamics is given by

$$\hbar\frac{\partial}{\partial t}J_{\text{THz}}^{\text{inc}}(\omega) = \frac{1}{\mathcal{S}}\text{Im} \left[\sum_{\lambda,\nu,\mathbf{q}_\parallel} (E_{\nu;\mathbf{q}} - E_{\lambda;\mathbf{q}}) J_{\lambda,\nu;\mathbf{q}} \Delta N_{\lambda,\nu}(\mathbf{q}_\parallel)_{(1)} \right] - \gamma_J J_{\text{THz}}^{\text{inc}}.\quad (4.23)$$

where $E_{\lambda;\mathbf{q}}$ is again the exciton energy and $J_{\lambda,\nu;\mathbf{q}}$ the exciton transition-matrix element. The quantity

$$\Delta N_{\lambda,\nu}(\mathbf{q}_\parallel) = \sum_{\mathbf{k}_\parallel, \mathbf{k}'_\parallel} \phi_{\lambda;\mathbf{q}}^L(\mathbf{k}_\parallel) \phi_{\nu;\mathbf{q}}^L(\mathbf{k}'_\parallel) c_X^{\mathbf{q}_\parallel, \mathbf{k}'_\parallel, \mathbf{k}_\parallel}\quad (4.24)$$

defines the electron-hole correlations in the exciton basis. The exciton wavefunctions $\phi_{\lambda,\mathbf{q}_\parallel}^L$ – and consequently the exciton energies and matrix elements – can depend on \mathbf{q}_\parallel . In Appendix D, it is shown that the diagonal element $\Delta N_{\lambda,\lambda}(\mathbf{q}_\parallel)$ describes an exciton population in state λ with center-of-mass momentum \mathbf{q}_\parallel . Since we solve the linear response, we have again split the exciton correlation into a quasi-stationary part and a linear-response part via

$$\Delta N_{\lambda,\nu}(\mathbf{q}_\parallel) = \Delta N_{\lambda,\nu}(\mathbf{q}_\parallel)_{(0)} + \Delta N_{\lambda,\nu}(\mathbf{q}_\parallel)_{(1)}.\quad (4.25)$$

According to Eq. (D.21), the exciton-correlation dynamics is given by

$$\begin{aligned}i\hbar\frac{\partial}{\partial t}\Delta N_{\lambda,\nu}(\mathbf{q}_\parallel)_{(1)} &= (E_{\nu;\mathbf{q}} - E_{\lambda;\mathbf{q}} - i\gamma_T) \Delta N_{\lambda,\nu}(\mathbf{q}_\parallel)_{(0)} \\ &+ (E_{\nu;\mathbf{q}} - E_{\lambda;\mathbf{q}}) N_{\lambda,\nu}^S(\mathbf{q}_\parallel)_{(1)} \\ &- \sum_{\beta} [J_{\nu,\beta;\mathbf{q}} \Delta N_{\lambda,\beta}(\mathbf{q}_\parallel)_{(0)} - J_{\lambda,\beta;\mathbf{q}} \Delta N_{\beta,\nu}(\mathbf{q}_\parallel)_{(0)}] \langle A \rangle_{\text{THz}}\end{aligned}\quad (4.26)$$

where γ_T describes the dephasing due to triplets and higher-order correlations. In Eq. (4.26), we neglected exchange and screening contributions which is justified for low densities. As we discuss in detail in Section 5.2, the source term

$$N_{\lambda,\nu}^S(\mathbf{q}_{\parallel}) = \sum_{\mathbf{k}_{\parallel}} \phi_{\lambda;\mathbf{q}}^L(\mathbf{k}_{\parallel}) f_{\mathbf{k}_{\parallel}+\mathbf{q}_{\parallel}}^e f_{\mathbf{k}_{\parallel}-\mathbf{q}_{\parallel}}^h \phi_{\nu;\mathbf{q}}^L(\mathbf{k}_{\parallel}) \quad (4.27)$$

describes correlated-plasma contributions in the electron-hole system. Here, we assume that the linear-response part $N_{\lambda,\nu}^S(\mathbf{q}_{\parallel})_{(1)}$ only leads to an additional damping of the THz current such that we can neglect this contribution in Eq. (4.26). In this format, Eqs. (4.23) and (4.26) have an identical structure as the coherent equations and can be analogously solved. The resulting susceptibility is then

$$\begin{aligned} \chi_{\text{THz}}^{\text{inc}}(\omega) &= \frac{1}{\varepsilon_0 L \mathcal{S} \omega^2 (\hbar\omega + i\gamma_J)} \quad (4.28) \\ &\times \sum_{\lambda,\nu,\mathbf{q}_{\parallel}} \{ S_{\lambda,\nu}^{\text{inc}}(\mathbf{q}_{\parallel}, \omega) \Delta N_{\lambda,\nu}(\mathbf{q}_{\parallel})_{(0)} - [S_{\lambda,\nu}^{\text{inc}}(\mathbf{q}_{\parallel}, -\omega) \Delta N_{\lambda,\nu}(\mathbf{q}_{\parallel})_{(0)}]^* \} \end{aligned}$$

with the response function

$$S_{\lambda,\nu}^{\text{inc}}(\mathbf{q}_{\parallel}, \omega) = \sum_{\beta} \frac{(E_{\beta;\mathbf{q}} - E_{\lambda;\mathbf{q}}) J_{\nu,\beta;\mathbf{q}} J_{\beta,\lambda;\mathbf{q}}}{E_{\beta;\mathbf{q}} - E_{\lambda;\mathbf{q}} - \hbar\omega - i\gamma_T} \quad (4.29)$$

We find that the the THz susceptibility, Eq. (4.28), closely resembles the result for the coherent regime, Eq. (4.21). In the incoherent regime, the linear response directly depends on the many-body state given by the correlations $\Delta N_{\lambda,\nu}(\mathbf{q}_{\parallel})_{(0)}$. Again, the response features resonances when the THz frequency matches internal transitions of the many-body state.

In general, both interband polarization and electron-hole correlations can be present in the optically excited many-body state such that the total linear susceptibility is given by

$$\chi(\omega) = \chi_A(\omega) + \chi_{\text{THz}}^{\text{coh}}(\omega) + \chi_{\text{THz}}^{\text{inc}}(\omega). \quad (4.30)$$

Equation (4.30) together with Eqs. (4.14), (4.21) and (4.28) is called the *THz-Elliott formula* [22] in reference to the famous Elliott formula in the optical regime [58]. In Chapter 5, we evaluate $\chi(\omega)$ for special situations.

4.3. Signatures of Nonlinear Terahertz Excitations

In nonlinear THz spectroscopy, a strong THz pulse excites the optically generated many-body state and the waveform of the transmitted THz pulse is recorded in a detector, as shown in Fig. 4.2(a). Strong THz excitations control and manipulate the quasi-particle state such that the current $J_{\text{tot}}(z, t)$ induced in the sample is no longer proportional to the THz field $\langle A(z, t) \rangle_{\text{THz}}$. As already discussed in the Section 4.1, experiments which

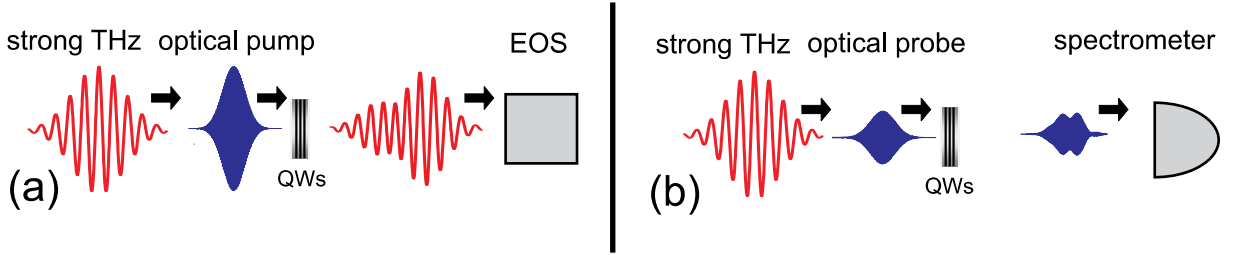


Figure 4.2.: Nonlinear THz excitations. (a) An optical pulse (shaded area) and a strong THz pulse (solid line) excite the QW. The waveform of the transmitted THz pulse is measured. (b) A weak optical probe (shaded area) and a strong THz pulse (solid line) excite the QW. In the detector, the spectrally-resolved intensity of the transmitted optical pulse is measured.

measure the differential THz transmission $\Delta\langle E_T(0, t) \rangle = -\frac{\mu_0 c_0}{2n_0}(J_{\text{THz}}(t) + J_A(t))$ access the full time dependence of the total current $J_{\text{tot}}(t) = J_A(t) + J_{\text{THz}}(t)$. The measured differential transmission

$$\langle \Delta E_T(0, t) \rangle \equiv \Delta E_{\text{THz}} + \Delta E_A, \quad \Delta E_{\text{THz}} = -\frac{\mu_0 c}{2n_0} J_{\text{THz}}, \quad \Delta E_A = -\frac{\mu_0 c}{2n_0} J_A \quad (4.31)$$

is then the superposition of a non-trivial contribution, ΔE_{THz} , due to nonlinear many-body transitions (e.g, excitonic transitions), and a trivial contribution, ΔE_A , due to the ponderomotive current. The ponderomotive contributions can be large and even mask the signatures of the many-body dynamics. In Chapter 7, we evaluate the induced currents for different nonlinear excitation conditions and discuss how ponderomotive parts can be removed from the total re-emitted field.

A different approach to follow the nonlinear THz dynamics is presented in Fig. 4.2(b). The sample is excited by strong THz pulses and probed by weak optical pulses having central times t_{THz} and t_{opt} , respectively. The spectrally-resolved intensity of the transmitted optical pulse is recorded as function of the delay time $\Delta t = t_{\text{THz}} - t_{\text{opt}}$. As a result, this scheme measures the THz-induced changes in the linear optical transmission with a time-resolution set by the delay time Δt . Obviously, this method only detects the THz coupling to the coherent interband polarization since the weak pulse does not generate significant incoherent correlations. This scheme is further discussed in Chapter 6.

This Thesis concentrates on signatures of nonlinear THz excitations that are accessible in transmission and reflection experiments. In principle there are many ways to detect the effect of nonlinear THz excitations. In Ref. [29], e.g., the nonlinear response of magneto-excitons is observed by measuring the THz-induced changes in the interband photoluminescence. In Ref. [60], the nonlinear THz dynamics of low-lying impurity states is monitored by recording the photoconductivity of the sample.

5. Detection of Exciton Populations and Plasmons

I will next evaluate the linear THz response described by the THz-Elliott formula, Eq. (4.30), for experimentally relevant conditions. I will concentrate on the incoherent regime where all interband coherences have decayed such that the THz response follows entirely from incoherent correlations ($\chi_{\text{THz}}^{\text{coh}} = 0$). In particular, I will show that THz light is well suited to probe exciton populations and plasmons.

Optical techniques, which probe band-to-band transitions, cannot directly measure exciton populations. In optical interband spectroscopy, the light-matter interaction is mediated by the optical polarization and existing populations of quasi-particles affect the response only indirectly [61, 62]. In photoluminescence (PL) experiments [63–65], only a subset of exciton states with negligible center-of-mass momentum contributes to the PL signal – aside from materials with large electron-phonon couplings [66]. Moreover, microscopic calculations reveal that PL at excitonic frequencies is not a unique signature of exciton populations since it can also originate from a pure Coulomb-correlated plasma [7, 34].

To evaluate the linear THz response, Eq. (4.28), one has to specify the relevant singlet-doublet correlations which characterize the incoherent many-body state at the probing time. Here, I do not describe the microscopic formation of the incoherent quasi-particle state after optical excitation (see, e.g., Refs [6, 22, 23, 25, 26]) but rather assume a realistic initial state. In particular, I will analyze well-defined situations where exciton populations and/or plasma states are present in the sample. As an example, the THz response is evaluated for GaAs parameters which provide a three-dimensional Bohr radius of $a_0 = 12.5$ nm and a three-dimensional exciton binding energy of $\varepsilon_B = 4.2$ meV. I consider THz excitation of either a 10 nm-wide QW or a planar QWI arrangement where the individual wires have an effective radius of 8.4 nm. For the QW, the $2p$ -exciton energy is 7.7 meV and the $2s$ -exciton energy is 7.9 meV above the $1s$ -exciton energy. For the QWI, the $2p$ -energy is 5.6 meV and the $2s$ -energy is 7.5 meV above the $1s$ -energy.

5.1. Bound Exciton Populations

As a first example, we evaluate the THz-Elliott formula, Eq. (4.28), for a state where all exciton correlations $\Delta N_{\lambda,\nu}$ vanish except for a single diagonal correlation $\Delta N_{\lambda_0,\lambda_0}$ where λ_0 denotes a bound exciton state:

$$\Delta N_{\lambda,\nu}(\mathbf{q}_{\parallel})(0) = \delta_{\lambda,\nu} \delta_{\lambda,\lambda_0} \Delta N_{\lambda_0,\lambda_0}(\mathbf{q}_{\parallel}). \quad (5.1)$$

5. Detection of Exciton Populations and Plasmons

As discussed in Appendix D, $\Delta N_{\lambda_0, \lambda_0}(\mathbf{q}_{\parallel})$ describes an exciton population in state λ_0 with center-of-mass momentum \mathbf{q}_{\parallel} . The \mathbf{q}_{\parallel} -integrated correlation

$$\Delta n_{\lambda_0, \lambda_0} \equiv \frac{\Delta N_{\lambda_0, \lambda_0}}{\mathcal{S}} \equiv \frac{1}{\mathcal{S}} \sum_{\mathbf{q}_{\parallel}} \Delta N_{\lambda_0, \lambda_0}(\mathbf{q}_{\parallel}) = x_{\lambda_0} n_{2D} \quad (5.2)$$

then defines the exciton density of state λ_0 . Here, we normalize $\Delta n_{\lambda_0, \lambda_0}$ with respect to the total density, $n_{2D} = n_{e(h)}$, of excited carriers in the QW such that x_{λ_0} is the exciton fraction for state λ_0 . For the QWI arrangement, we have to substitute $1/\mathcal{S} \rightarrow n_{\text{QWI}}/\mathcal{L}$ and $n_{2D} \rightarrow n_{1D}n_{\text{QWI}}$ in Eq. (5.2) where n_{1D} the density within one quantum wire and n_{QWI} is the density of wires.

We consider the special cases that all electrons and holes are bound to either (i) $1s$ -excitons such that $x_{1s} = 100\%$ or (ii) $2p$ -excitons such that $x_{2p} = 100\%$. We choose the low carrier densities $n_{2D} = 1 \times 10^9/\text{cm}^2$ for the QW and $n_{1D} = 1 \times 10^4/\text{cm}$ for the QWI. Furthermore, we assume that the center-of-mass distribution $\Delta N_{\lambda_0, \lambda_0}(\mathbf{q}_{\parallel})$ follows a Boltzmann distribution and that the carrier densities follow Fermi-Dirac distributions at the temperature of $T = 40$ K. For the conditions studied here, the \mathbf{q}_{\parallel} -dependence of excitonic transition energies and matrix elements is negligible. In Section 7.4, we will get to know a system where the exciton transitions are strongly \mathbf{q}_{\parallel} -dependent.

The contour plots in Fig. 5.1 show the two-particle correlations $\Delta N_{\lambda, \nu}$ as function of exciton energies E_{λ} and E_{ν} for the $1s$ -population [(a1) QWI, (a2) QW] and for the $2p$ -population [(b1) QWI, (b2) QW]. In a strict sense, the bound exciton population $\Delta N_{1s, 1s}$ and $\Delta N_{2p, 2p}$ correspond to singular points in the contour plot. To increase their visibility, we have thus represented the bound states as 2 meV wide areas such that the exciton populations appear as extended points on the diagonal. The thin vertical and horizontal lines indicate the start of the continuum at $E_{\lambda} - E_{1s} = 10.4$ meV and $E_{\lambda} - E_{1s} = 9.5$ meV for QWI and QW, respectively. Constructing the contour plot in this way is very useful because it shows at a glance which kind of electron-hole correlations are present in the many-body state. While diagonal elements correspond to exciton populations, off-diagonal elements represent transition-correlations between different exciton states. In the spirit of Ref. [6], we will make frequent use of this presentation throughout this Thesis. For the single-exciton populations, we find that only a small region of the possible phase space of two-particle correlations is occupied.

The electron-hole pair-correlation function $g_{eh}(\mathbf{r}_{\parallel})$ which is introduced in Appendix D.2 is another useful quantity to characterize the many-body state. It determines the probability to find an electron and a hole separated by the distance \mathbf{r}_{\parallel} and thus identifies the correlations in the electron-hole relative coordinate. According to Eq. (D.12), the correlated part, $\Delta g_{eh}(\mathbf{r}_{\parallel})$, is given by

$$\Delta g_{eh}(\mathbf{r}_{\parallel}) = \sum_{\lambda, \nu} \left(\frac{1}{\mathcal{S}} \sum_{\mathbf{q}_{\parallel}} \Delta N_{\lambda, \nu}(\mathbf{q}_{\parallel}) \right) [\phi_{\lambda}^{\text{R}}(\mathbf{r}_{\parallel})]^* \phi_{\nu}^{\text{R}}(\mathbf{r}_{\parallel}). \quad (5.3)$$

For the state given by Eq. (5.1), we immediately find $\Delta g_{eh}(\mathbf{r}_{\parallel}) = \Delta n_{\lambda_0, \lambda_0} |\phi_{\lambda_0}^{\text{R}}(\mathbf{r}_{\parallel})|^2$. As expected for a single exciton population, the spatial dependence of $\Delta g_{eh}(\mathbf{r}_{\parallel})$ is given by the probability distribution of the exciton wavefunctions in real space.

Figure 5.1 [(c1) QWI, (c2) QW] shows the normalized pair-correlation function, $\Delta\bar{g}_{eh}(r) = \Delta g_{eh}(r)/(n_e n_h)$, along the polarization direction of the THz field for the $1s$ (solid line) and the $2p$ (dashed line) exciton population. For the QW case, the radial probability distribution, $r\Delta\bar{g}_{eh}(r)$, is shown. Obviously, the shape of $\Delta\bar{g}_{eh}(r)$ is determined by the corresponding exciton wavefunction. For the $2p$ state, the probability to find an electron and a hole at the same position vanishes such that this state is optically dark in the GaAs system.

For a state with a single exciton population, Eq. (5.1), the many-body contribution in the THz-Elliott formula, Eq. (4.28), simplifies to

$$\chi_{\text{THz}}^{\lambda_0\text{-pop.}}(\omega) = \frac{1}{\varepsilon_0 L} \sum_{\beta} \frac{|J_{\lambda_0,\beta}|^2}{(\hbar\omega + i\gamma_J)\omega^2} \left\{ \frac{(E_{\beta} - E_{\lambda_0})\Delta n_{\lambda_0,\lambda_0}}{E_{\beta} - E_{\lambda_0} - \hbar\omega - i\gamma_T} - \frac{(E_{\lambda_0} - E_{\beta})\Delta n_{\lambda_0,\lambda_0}}{E_{\lambda_0} - E_{\beta} - \hbar\omega - i\gamma_T} \right\} \quad (5.4)$$

With the excitonic dipole-matrix element $d_{\lambda,\nu} = i\hbar J_{\lambda,\nu}/(E_{\nu} - E_{\lambda})$ (see Appendix D.3), we obtain the more familiar form

$$\chi_{\text{THz}}^{\lambda_0\text{-pop.}}(\omega) = \sum_{\beta} \frac{|d_{\lambda_0,\beta}|^2}{\varepsilon_0 L} \left\{ \frac{\Delta n_{\lambda_0,\lambda_0}}{E_{\beta} - E_{\lambda_0} - \hbar\omega - i\gamma_T} - \frac{\Delta n_{\lambda_0,\lambda_0}}{E_{\lambda_0} - E_{\beta} - \hbar\omega - i\gamma_T} \right\} \quad (5.5)$$

where we assumed that γ_J is small and that the lorentzians are sufficiently narrow such that we can replace $E_{\nu} - E_{\lambda}$ with $\hbar\omega$ in $d_{\lambda,\nu}$ and in the numerator of Eq. (5.5). The susceptibility $\chi_{\text{THz}}^{\lambda_0\text{-pop.}}(\omega)$ corresponds to an atomic susceptibility. The first term describes THz absorption if $E_{\beta} - E_{\lambda_0} > 0$ and the second term describes THz gain if $E_{\lambda_0} - E_{\beta} > 0$ provided that the matrix element $J_{\lambda_0,\beta}$ is non-vanishing. If $E_{\beta} - E_{\lambda_0} < 0$ for the first term or $E_{\lambda_0} - E_{\beta} < 0$ for the second term, the lorentzian peaks at negative frequencies $\hbar\omega < 0$. These non-resonant contributions can be neglected in the linear regime (rotating-wave approximation). It is interesting to note that these non-resonant transitions can, in fact, be excited with intense THz fields leading to extreme-nonlinear optical effects (see Chapters 6 and 7).

Figures 5.1(d)-(e) show the real part (solid line) and the imaginary part (shaded area) of $\omega\chi_{\text{THz}}^{1s\text{-pop.}}$ [(d1) QWI, (d2) QW] and $\omega\chi_{\text{THz}}^{2p\text{-pop.}}$ [(e1) QWI, (e2) QW], respectively. We assume the dephasing constants $\gamma_T = \gamma_J = 1.7$ meV and $\gamma_T = \gamma_J = 2.2$ meV for QWI and QW, respectively. For the $1s$ -exciton population, a clear absorption peak emerges around the energy $\hbar\omega = E_{2p,1s} = E_{2p} - E_{1s}$ for both QW and QWI system. The absorption $\alpha(\omega) \propto \text{Im}[\omega\chi_{\text{THz}}(\omega)]$ mainly results from the $1s$ -to- $2p$ exciton transition, which features the largest matrix element, but also from transitions to higher exciton states. Since the possible transitions are energetically close and the broadening of resonances relatively large, the discrete resonances merge into a single asymmetric peak. Note that the $1s$ - $2p$ transition is more isolated from other transitions for the QWI confinement. For the $2p$ -exciton population, we observe pronounced THz gain around the $1s$ -to- $2p$ transition energy corresponding to transitions from the $2p$ state to the energetically lower $1s$ -exciton state. For low frequencies, we find absorptive behavior corresponding to transitions from the $2p$ state to higher exciton states. Note that we did not plot the ponderomotive contribution $\chi_A(\omega)$, Eq. (4.14), which only leads to a refractive index change leaving the absorption unchanged.

5. Detection of Exciton Populations and Plasmons

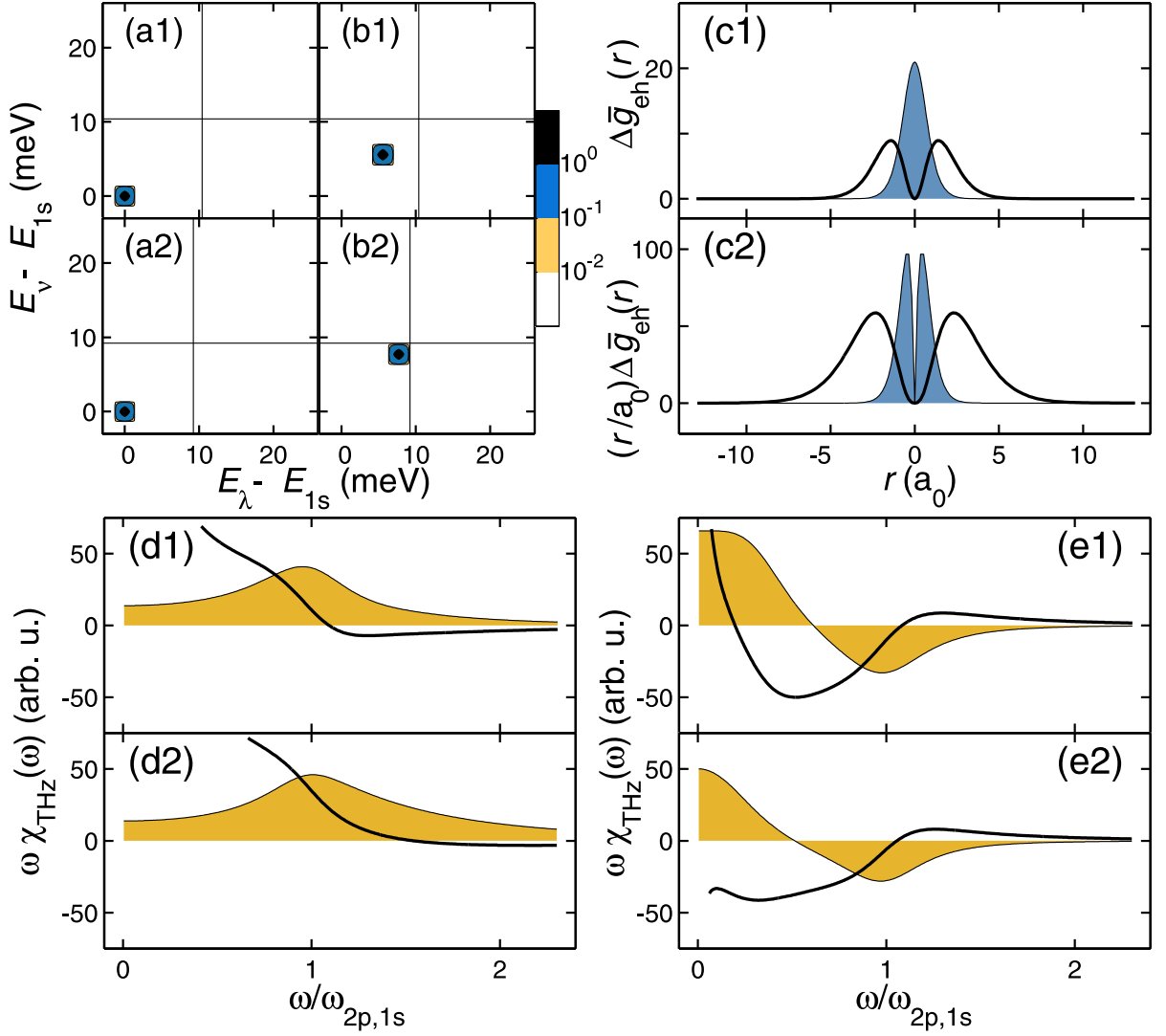


Figure 5.1.: Terahertz susceptibility for bound excitons in a QWI (a1)-(e1) and QW system (a2)-(e2). The contour plots show $|\Delta N_{\lambda,\nu}|$ for the (a) 1s and (b) 2p exciton population. To increase the visibility, we represent the bound states as 2 meV wide areas instead of discrete points. The thin lines indicate the start of the continuum. (c) shows the corresponding pair-correlation function for the 1s (shaded area) and 2p (solid line) states. The resulting real (solid line) and imaginary (shaded area) parts of $\omega \chi_{\text{THz}}^{\lambda_0\text{-pop}}(\omega)$ are shown for the 1s population in (d) and for the 2p population in (e). We choose carrier densities $n_{1D} = 1 \times 10^4/\text{cm}$, $n_{2D} = 1 \times 10^9/\text{cm}^2$ and damping constants $\gamma_T = \gamma_J = 1.7\text{meV}$, $\gamma_T = \gamma_J = 2.2\text{meV}$ for QWI and QW, respectively. The temperature is $T = 40\text{K}$.

We find that the linear THz absorption (i) identifies exciton populations and (ii) clearly distinguishes populations in different exciton states. In the incoherent regime,

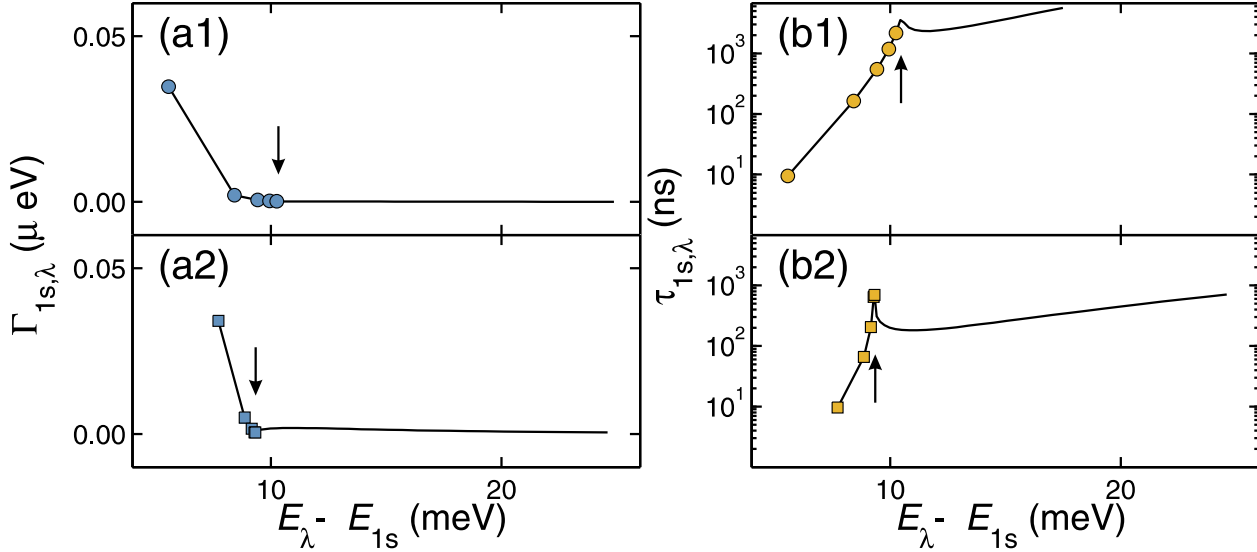


Figure 5.2.: Radiative decay rates for transitions from the $1s$ exciton to p -like exciton states. (a1) and (a2) show the radiative decay constants $\Gamma_{1s,\lambda}^{\text{rad}}$ while (b1) and (b2) show the radiative decay times $\tau_{1s,\lambda}$ for QWI and QW systems, respectively. The arrows indicate the start of the continuum. Note that the line between the bound states is only a guide to the eye since there are no real states in between these points. For transitions from the $1s$ -state into the continuum, the radiative decay constant depends on the grid resolution; if the continuum were modeled with infinitely many points, $\Gamma_{1s,\text{cont}}$ would approach zero. (from Paper [I])

an absorption (gain) peak at the $1s$ -to- $2p$ transition frequency gives unambiguous proof for the presence of a $1s$ ($2p$) exciton population. It is also notable that the THz field detects the total \mathbf{q}_{\parallel} -integrated exciton population.

The idea to detect excitons with weak THz pulses is analogous to the concept of atomic gas spectroscopy where the presence of atoms in a dilute gas can be detected with a weak optical pulse which is sensitive to transitions between different eigenstates of the atom. Throughout this Thesis, we will often discuss analogies and differences to atomic spectroscopy.

According to Eq. (4.9), the magnitude of the THz absorption is determined by the quantity $\xi(\omega) = \omega L / (2c_0 n_0) \chi(\omega)$. Inserting Eq. (5.4) into Eq. (4.9), we find that the radiative coupling of an excitonic transition between states λ_0 and ν field is determined by the *radiative-decay constant*

$$\Gamma_{\lambda_0,\nu}^{\text{rad}}(\omega) = \frac{\mu_0 c_0}{2n_0 \omega} |J_{\lambda_0,\nu}|^2 \Delta n_{\lambda_0,\lambda_0} \quad (5.6)$$

which depends on the transition-matrix element and the exciton concentration in state λ_0 . This quantity also defines the *radiative-decay time*

$$\tau_{\lambda_0,\nu}^{\text{rad}} = \frac{1}{2\Gamma_{\lambda_0,\nu}^{\text{rad}}(\omega_{\lambda_0,\nu})}. \quad (5.7)$$

5. Detection of Exciton Populations and Plasmons

Figure 5.2 shows the radiative decay constants $\Gamma_{1s,\nu}^{\text{rad}}(\omega_{1s,\nu})$ for $\Delta n_{1s,1s} = n_{2D}$ and the corresponding radiative decay times $\tau_{1s,\nu}^{\text{rad}}$. We choose the density of QWIs such that $\Gamma_{1s,2p}^{\text{rad}}$ matches the QW result. We find that the radiative decay times for bound-state transitions are in the nano- and microsecond range, e.g., $\tau_{1s,2p}^{\text{rad}} = 9.6 \text{ ns}$ for the QW indicating that the GaAs semiconductor couples to the THz field rather weakly. For interband transitions, the radiative decay times can be shorter by orders of magnitude. The radiative decay time for the $1s$ -exciton resonance in GaAs, e.g., is roughly $\tau_{1s}^{\text{rad}} = 10 \text{ ps}$ [6].

The unique ability of THz spectroscopy to probe exciton populations has allowed experimentalists to study exciton formation processes in great detail. In Ref. [14], the formation of $1s$ -exciton populations in GaAs after optical excitation is studied via time-resolved THz spectroscopy. For optical excitation resonant with the $1s$ exciton, the formation is found to occur within a few picoseconds; for non-resonant optical excitation, the formation takes roughly one nanosecond. In cuprous oxide (Cu_2O), THz spectroscopy has been used to study the formation of optically dark $1s$ excitons [17] and to observe stimulated emission from the $3p$ -to- $2s$ transition [18]. Direct comparison of photoluminescence (PL) and THz spectra [15] have shown that THz absorption can unambiguously identify exciton populations while PL cannot.

According to microscopic computations of the exciton formation process [22, 23], the incoherent many-body state postulated in Eq. (5.1) is usually not realistic. While it is possible to create large exciton fractions via resonant optical excitation, the exciton fraction is usually much lower than 100%. Moreover, electron-hole scattering inevitably leads to a plasma background which also couples to the THz field. We investigate a more realistic many-body state in the next Section.

5.2. Exciton Populations and Correlated Electron-Hole Plasma

In this Section, we consider a more realistic many-body state which is a mix of a single-exciton populations and a plasma background given by

$$\Delta N_{\lambda,\nu}(\mathbf{q}_{\parallel})_{(0)} = \delta_{\lambda,\nu} \delta_{\lambda_0,\lambda_0} \Delta N_{\lambda_0,\lambda_0}(\mathbf{q}_{\parallel}) + \Delta N_{\lambda,\nu}^{\text{Corr-Pl.}}(\mathbf{q}_{\parallel}). \quad (5.8)$$

Here, the *correlated electron-hole plasma*

$$\Delta N_{\lambda,\nu}^{\text{Corr-Pl.}}(\mathbf{q}_{\parallel}) = -\frac{E_{\nu} - E_{\lambda}}{E_{\nu} - E_{\lambda} - i\gamma_E} \Delta N_{\lambda,\nu}^S(\mathbf{q}_{\parallel}). \quad (5.9)$$

depends on a phenomenological damping constant γ_E and is proportional to

$$N_{\lambda,\nu}^S(\mathbf{q}_{\parallel}) = \sum_{\mathbf{k}_{\parallel}} \phi_{\lambda}^L(\mathbf{k}_{\parallel}) f_{\mathbf{k}_{\parallel}+\mathbf{q}_{\parallel}}^e f_{\mathbf{k}_{\parallel}-\mathbf{q}_{\parallel}}^h \phi_{\nu}^L(\mathbf{k}_{\parallel}) \quad (5.10)$$

which contains the electron and hole distributions and the exciton wavefunctions. Due to the energy difference in the numerator, the diagonal correlations in Eq. (5.9) vanish

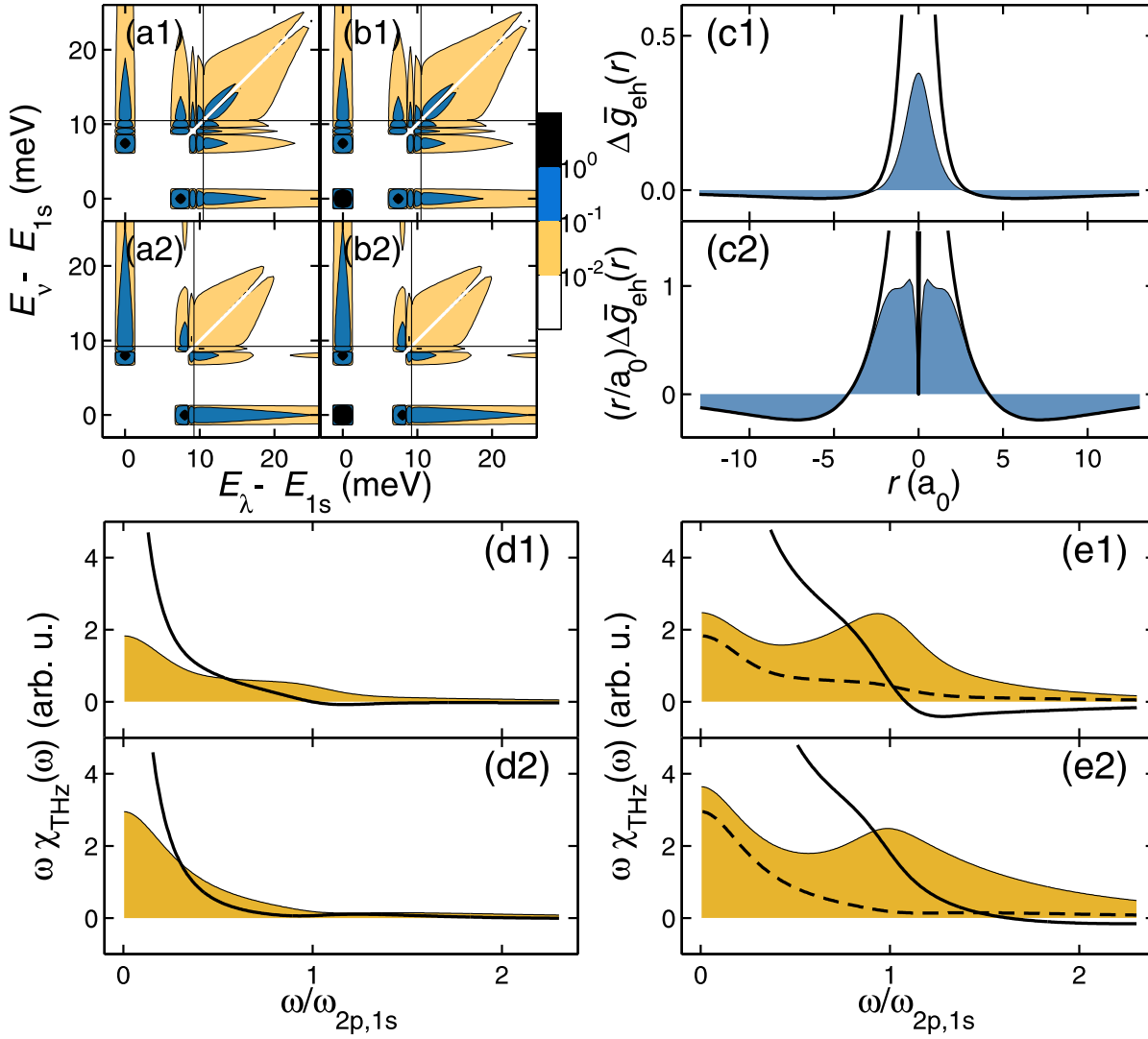


Figure 5.3.: THz susceptibility for a correlated electron-hole plasma with and without 1s-exciton populations in a QWI (a1)-(e1) and QW (a2)-(e2) system. The contour plots show $|\Delta N_{\lambda,\nu}|$ for the correlated plasma (a) without excitons and (b) with a 5% 1s-exciton population. In (c), the normalized pair-correlation function is shown for the plasma with 0% (shaded area) and 5% 1s excitons. The corresponding real (solid line) and imaginary (shaded area) parts of $\omega\chi_{\text{THz}}^{\lambda_0\text{-pop.}}(\omega)$ are shown for the plasma alone in (d) and with the additional exciton population in (e). For comparison, the dashed line in (e) also shows $\text{Im}[\omega\chi_{\text{THz}}(\omega)]$ for 0% 1s-excitons. The parameters are chosen identical to Fig. 5.1. (According to Ref. [6]).

such that the correlated electron-hole plasma does not include any exciton populations. Moreover, $N_{\lambda,\nu}^S(\mathbf{q}_{\parallel})$ vanishes when the exciton states λ and ν do not have the same parity.

5. Detection of Exciton Populations and Plasmons

To motivate the origin of the correlated electron-hole plasma, we consider Eq. (D.21) which describes the dynamics of electron-hole correlations in the exciton basis. When we neglect the THz coupling as well as screening and exchange contributions, $D_{\lambda,\nu}$, and replace the triplet contributions, $T_{\lambda,\nu}$, with a constant dephasing, Eq. (D.21) leads to

$$\frac{\partial}{\partial t} \Delta N_{\lambda,\nu}(\mathbf{q}_{\parallel})_{(0)} = (E_{\nu} - E_{\lambda} - i\gamma_E) \Delta N_{\lambda,\nu}(\mathbf{q}_{\parallel})_{(0)} + (E_{\nu} - E_{\lambda}) \Delta N_{\lambda,\nu}^S(\mathbf{q}_{\parallel}). \quad (5.11)$$

We find that the source term $(E_{\nu} - E_{\lambda}) \Delta N_{\lambda,\nu}^S(\mathbf{q}_{\parallel})$ generates off-diagonal correlations whenever carriers are present. Obviously, the correlated electron-hole plasma, Eq. (5.9), is the steady-state of Eq. (5.11). The build-up time of the steady state is determined by $\tau_{\text{buildup}} = \hbar/\gamma_E$ which is less than a picosecond for typical dephasing constants. Thus, the correlated plasma can be understood as a many-body state where the attractive Coulomb interaction leads to a constant in- and out scattering of correlated electrons and holes. The correlated plasma is characterized by density and temperature of the electron and hole distributions; the dependence on γ_E is usually weak (see also Ref. [6]). Here, we always choose $\gamma_E = \gamma_T$.

Figure 5.3[(a1) QWI, (a2) QW] shows the two-particle correlations $|\Delta N_{\lambda,\nu}|$ for the correlated electron-hole plasma. We choose the same parameters as in Fig. 5.1 and plot only those correlations where both λ and ν have an s -like parity. As expected, only off-diagonal states are occupied. The value of $|\Delta N_{\lambda,\nu}|$ decreases when either E_{λ} or E_{ν} become large. In Fig. 5.3[(b1) QWI, (b2) QW], a small amount ($x_{1s} = 5\%$) of $1s$ -exciton populations is added to the correlated plasma.

Figure 5.3[(c1) QWI, (c2) QW] shows the normalized pair-correlation function along the THz polarization direction for the correlated plasma without (shaded area) and with (solid line) the $1s$ -exciton population. For the correlated plasma alone, $\Delta g_{eh}(r)$ is positive for small values of r and negative for large values of r . The shape of $\Delta g_{eh}(r)$ implies that the probability to find electrons and holes close together is increased. However, this does not mean that exciton populations are present: For the correlated plasma, positive and negative regions compensate each other such that $\int dr \Delta \bar{g}_{eh}(r) = 0$ and $\int dr r \Delta \bar{g}_{eh}(r) = 0$ for QWI and QW system, respectively. When the $1s$ -exciton population is added (solid line), the r -integrated pair-correlation function has a positive value proportional to the exciton concentration.

The THz response for the correlated plasma without exciton populations is shown in Fig. 5.3[(d1) QWI, (d2) QW]. We find that the correlated plasma couples to the THz field as well. The absorption is mostly featureless; it peaks at $\omega = 0$ and decays almost monotonously for increasing frequency. When the $1s$ population is added [Fig 5.3 (e1) QWI, (e2) QW], a pronounced absorption peak emerges at the $1s$ -to- $2p$ transition frequency. Again results are similar for the QW and QWI system. At the low densities considered here, the correlated plasma only weakly couples to the THz field such that the response is dominated by the population contributions. Thus, we find that THz fields can reliably detect even small concentrations of exciton populations. For high densities, the plasma contributions in the THz response become larger and can dominate over the population contributions.

The postulated mix of populations and plasma background can be justified by comparing the ansatz, Eq. (5.8), to microscopic calculations of the exciton-formation dynamics which fully include Coulomb and phonon scattering [22, 23, 67]. These calculations confirm that the many-body state, Eq. (5.8), is indeed realistic for typical excitation conditions and stable on a picosecond timescale. The actual quasi-equilibrium concentration of exciton populations depends on many parameters including density and temperature of the carrier system as well as the optical excitation conditions. The ansatz (5.8), together with the THz Elliott formula, Eq. (4.28), can be used to extract the total exciton concentration from experimental spectra.

5.3. Plasmon Resonance

So far, we have investigated the linear THz response of a semiconductor at low densities and temperatures where exciton-population contributions can dominate over plasma contributions. At elevated densities and temperatures, excitonic effects become less important as the carriers in the semiconductors form a Coulomb-interacting plasma. The linear optical properties of such a plasma are often discussed in terms of the dielectric function [8].

As discussed in Section 4.1, THz transmission and reflection experiments directly access the full transversal dielectric function, Eq. (4.10),

$$\varepsilon_T(\omega) = \varepsilon_{\text{BG}} \left(1 - \frac{\omega_{\text{PL}}^2}{\omega^2} \right) + \chi_{\text{THz}}(\omega). \quad (5.12)$$

Here, ε_{BG} is the background dielectric constant, $\chi_A(\omega) = -\varepsilon_{\text{BG}}\omega_{\text{PL}}^2/\omega^2$ is the ponderomotive contribution with the three-dimensional plasma frequency ω_{PL} [see Eq. (4.14)] and $\chi_{\text{THz}}(\omega)$ is the contribution from many-body transitions [see Eq. (4.28)]. Without $\chi_{\text{THz}}(\omega)$, the dielectric function $\varepsilon_T(\omega)$ vanishes for $\omega = \omega_{\text{PL}}$ such that $1/\varepsilon_T(\omega)$ features a resonance at the three-dimensional plasma frequency.

We next determine the full $\varepsilon_T(\omega)$ for a realistic situation. We evaluate the THz Elliott-formula, Eq. (4.28), for the correlated plasma, Eq. (5.9), assuming the high densities $n_{2D} = 1 \times 10^{10}/\text{cm}^2$ and $n_{1D} = 7.5 \times 10^4/\text{cm}$ for QW and for QWI system, respectively. Furthermore, we choose a temperature of $T = 20$ K and $\gamma_T = \gamma_J$ as in the previous Section. The real (solid line) and imaginary (shaded area) parts of the resulting $\varepsilon_T(\omega)$ are shown in Fig. 5.4(a1) for the planar QWI arrangement and in Fig. 5.4(a2) for the QW. In frames (b1), (b2), we show real (solid line) and imaginary (shaded area) parts of the inverse dielectric function for QWI and QW, respectively. For both systems, we observe a pronounced plasmon peak in the inverse dielectric function. The energetic position of the resonance roughly matches the three-dimensional plasma frequency ω_{PL} (vertical lines).

We thus find a plasmon resonance in the THz response around the three-dimensional plasma frequency ω_{PL} *independent* of the dimension of the nanostructure. This result seems surprising: According to textbook discussions [8] which analyze the longitudinal dielectric function $\varepsilon_L(\omega)$, the plasma frequency is strongly dimension dependent. In

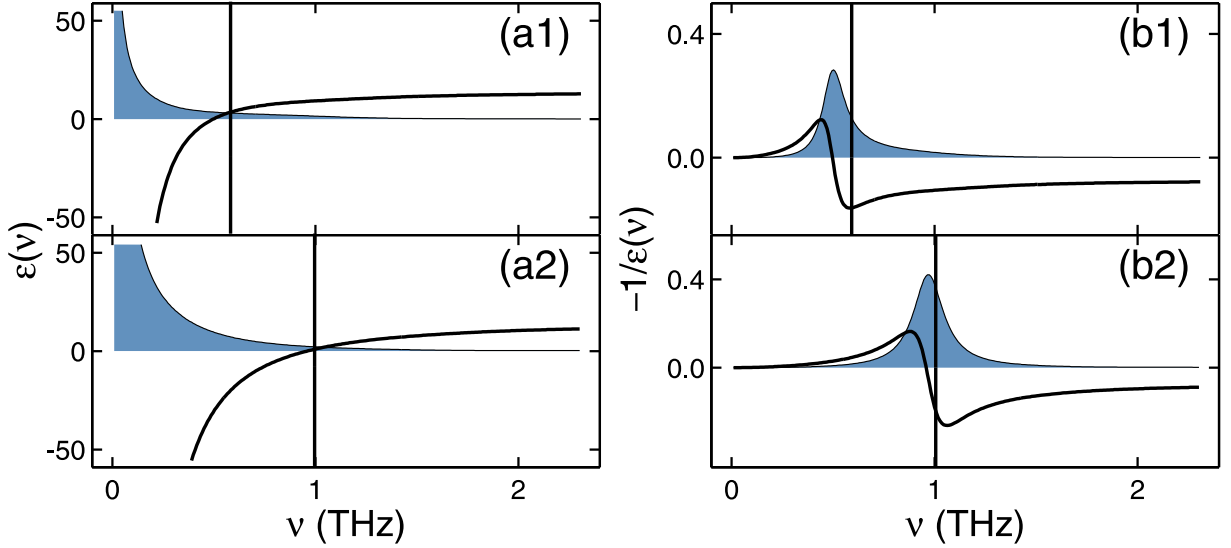


Figure 5.4.: Plasmon resonance of a correlated electron-hole plasma for QWI (a1),(b1) and QW (a2),(b2). (a) Real (solid line) and imaginary (shaded area) part of the full dielectric function $\epsilon(\omega)$. In (b), real (solid line) and imaginary (shaded area) part of $-1/\epsilon(\omega)$ are shown. The vertical lines indicate the three-dimensional plasma frequency. The densities are $n_{1D} = 7.5 \times 10^4/\text{cm}$ and $n_{2D} = 1 \times 10^{10}/\text{cm}^2$. The temperature is $T = 20$ K.

particular, one finds [8] that the one- and two-dimensional plasma frequency vanish in the long-wavelength limit such that one would not expect a plasmon resonance in the THz response of QWs and QWIs.

This apparent discrepancy is resolved once we clearly distinguish between self-consistent and not self-consistent response, as already remarked by Stern [68]. The longitudinal dielectric function $\epsilon_L(\omega)$ relates the *external* to the *internal* longitudinal field which is determined self-consistently via Poisson's equation [8]. Thus, $\epsilon_L(\omega)$ describes the self-consistent response which is dimension dependent. In contrast, the transversal dielectric function $\epsilon_T(\omega)$ is defined via the susceptibility which relates the *internal* matter polarization to the *internal* transversal electric field. Thus, $\epsilon_T(\omega)$ describes the dimension-independent linear response.

6. Interband Polarization in Strong Terahertz Fields

In this Chapter, I will investigate situations where a semiconductor QW is excited simultaneously by a *weak* optical and a *strong* THz pulse. Without THz field, the linear optical spectrum of a QW displays discrete excitonic resonances corresponding to the generation of coherent interband polarization in optically bright exciton states. The strong THz field induces nonlinear transitions between optically-bright (*s*-like) and optically-dark (e.g, *p*-like) exciton states and thus leads to characteristic changes in the linear optical spectrum. For such a configuration, the THz field interacts only with *coherent* excitons, i.e., interband polarization. The nonlinear THz interaction with *incoherent* exciton populations, i.e., genuinely bound electron-hole pairs is discussed in Chapter 7.

The influence of strong THz or mid-infrared (MIR) fields on bulk absorption spectra has been analyzed in both theory [69–71] and experiment [30, 31, 72]. In QW investigations, the strong THz field can have components that are polarized either parallel or perpendicular to the QW plane. For exclusively parallel polarization, the strong THz pulse induces excitonic transitions as discussed theoretically in Refs. [71, 73–75] and experimentally in Refs. [32, 76]. A perpendicular polarization component of the THz pulse induces intersubband transitions as analyzed in Refs. [28, 33, 77–79].

Here, I will consider the case that the THz field is polarized parallel to the QW. In contrast to previous investigations, I do not investigate continuous-wave but pulsed THz excitation and assume that the delay time between optical and THz pulses can be controlled such that time-resolved THz effects can be studied. The generation of coherent interband polarization and the coupling to the THz field are microscopically described by Eqs. (3.34)-(3.41). In Sections 6.1-6.3, I will evaluate the theory for a single QW and typical GaAs parameters. In Section 6.4, the theory is used to quantitatively explain recent experiments in AlGaAs/GaAs multi-QW systems.

6.1. Rabi Splitting and Ponderomotive Shifts in Optical Transmission

We consider the experimental configuration discussed in Section 4.3 and Fig. 4.2(b). A weak optical pulse and a strong THz pulse, having central times t_{opt} and t_{THz} , respectively, propagate perpendicular to a single QW. The spectrally-resolved intensity of the transmitted optical probe is determined as function of the delay time $\Delta t \equiv t_{\text{THz}} - t_{\text{opt}}$ between the two pulses (THz-“pump” and optical-probe configuration).

6. Interband Polarization in Strong Terahertz Fields

For a sufficiently weak optical probe, the carrier densities remain unchanged such that we do not have to solve the full Maxwell-Semiconductor-Bloch equations (3.34)-(3.41); it is enough to solve the polarization dynamics, Eq. (3.34),

$$i\hbar\frac{\partial}{\partial t}P_{\mathbf{k}_{\parallel}} = \left[\tilde{\varepsilon}_{\mathbf{k}_{\parallel}} - j(\mathbf{k}_{\parallel})\langle A(0,t)\rangle_{\text{THz}} + \frac{|e|^2}{2\mu}\langle A(0,t)\rangle_{\text{THz}}^2 - i\gamma \right] P_{\mathbf{k}_{\parallel}} \quad (6.1)$$

$$- \left[1 - f_{\mathbf{k}_{\parallel}}^e - f_{\mathbf{k}_{\parallel}}^h \right] \left[d_{c,v}(\mathbf{k}_{\parallel})\langle E(0,t)\rangle_{\text{opt}} + \sum_{\mathbf{k}'_{\parallel}} V_{\mathbf{k}_{\parallel}-\mathbf{k}'_{\parallel}} P_{\mathbf{k}'_{\parallel}} \right]$$

together with the wave equation (3.39) for the optical field

$$\left[\frac{\partial^2}{\partial z^2} - \frac{n_0^2}{c_0^2} \frac{\partial^2}{\partial t^2} \right] \langle E(z,t)\rangle_{\text{opt}} = \mu_0 \delta(z) \frac{\partial^2 P}{\partial t^2}. \quad (6.2)$$

In Eq. (6.1), we assumed parabolic bands and modeled the polarization decay via a phenomenological constant γ since excitation-induced dephasing [51] is not appreciable in the low-density regime. In Eq. (6.2), we replaced the confinement $g(z)$ with $\delta(z)$ assuming that the QW is thin compared to the optical wavelength. Without THz contributions, Eqs. (6.1) and (6.2) yield the linear optical spectrum.

We solve Eqs. (6.1) and (6.2) for a 10 nm GaAs QW taking into account only the polarization between the heavy-hole (HH) valence band and the conduction band. We assume that both optical and THz fields have a Gaussian envelope. The THz vector potential is given by

$$\langle A(t)\rangle_{\text{THz}} = A_0 e^{-((t-t_{\text{THz}})/\tau_{\text{THz}})^2} \cos(\omega_{\text{THz}}t + \phi) \quad (6.3)$$

where $\tau_{\text{THz}} = 1.5$ ps is the duration, $\phi = 0$ is the carrier-envelope offset phase, and ν_{THz} is the frequency of the THz pulse. We consider resonant excitation of the $1s$ -to- $2p$ exciton transition such that $\nu_{\text{THz}} = \omega_{\text{THz}}/(2\pi) = \nu_{2p,1s}^{\text{HH}} = 1.88$ THz. The peak electric-field strength is $E_0 \approx A_0\omega_{\text{THz}} = 4.8$ kV/cm. The electric field of the optical pulse is given by

$$\langle E(t)\rangle_{\text{opt}} = \tilde{E}_0 e^{-((t-t_{\text{opt}})/\tau_{\text{opt}})^2} \cos(\omega_{\text{opt}}t). \quad (6.4)$$

where $\tau_{\text{opt}} = 50$ fs is the duration, and ω_{opt} is the frequency which we choose to be resonant with the $1s$ -exciton resonance.

Figure 6.1 shows the absolute value of the excitonic polarizations $|p_{\lambda}(t)|$ for $\lambda = 1s$ (solid line) and $\lambda = 2p$ (dashed line). Here, p_{λ} is defined via

$$p_{\lambda} = \sum_{\mathbf{k}_{\parallel}} \phi_{\lambda}^{\text{L}}(\mathbf{k}_{\parallel}) P_{\mathbf{k}_{\parallel}}, \quad P_{\mathbf{k}_{\parallel}} = \sum_{\lambda} \phi_{\lambda}^{\text{R}}(\mathbf{k}_{\parallel}) p_{\lambda}. \quad (6.5)$$

and describes the component of the polarization in the exciton state λ (coherent exciton in state λ). The optical and THz pulses are shown as shaded areas. The delay time is $\Delta t = t_{\text{THz}} - t_{\text{opt}} = 1.0$ ps. While the total polarization decays with a time constant \hbar/γ , the evolution of $|p_{1s}|$ and $|p_{2p}|$ demonstrates Rabi flopping in the time-domain: The

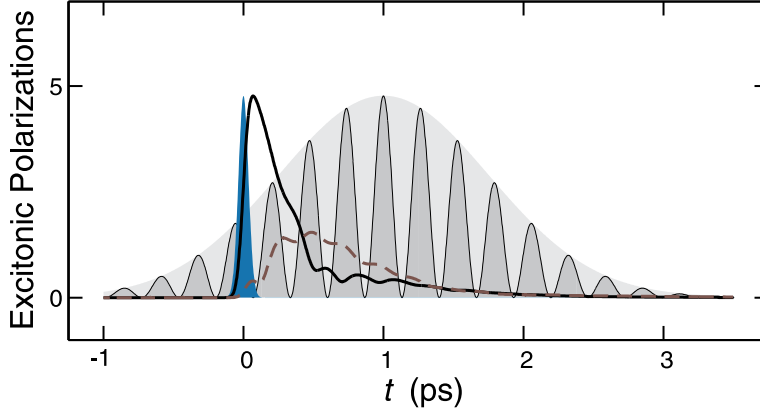


Figure 6.1.: Dynamics of Excitonic Polarizations. A 10 nm-QW is excited with an optical pulse (dark shaded area) and a THz pulse (light shaded area). The resulting excitonic polarizations $|p_{1s}(t)|$ and $|p_{2p}(t)|$ are shown as a solid line and dashed line, respectively. The delay time is $\Delta t = 1$ ps, the field strength is $E_0 = 4.8$ kV/cm, and the polarization damping is given by $\gamma = 0.96$ meV.

strong THz field converts $1s$ -polarization into $2p$ -polarization and back again with the Rabi frequency; we identify at least one Rabi-flop. It is notable that $|p_{1s}|$ and $|p_{2p}|$ show additional superimposed oscillations with twice the THz frequency. We will come back to these features in the next Section.

We next discuss signatures of the strong THz excitation in the optical-transmission spectrum which is accessible in experiments. The transmission is determined by the macroscopic interband polarization, Eq. (3.41),

$$P = \frac{1}{\mathcal{S}} \sum_{\mathbf{k}_{\parallel}} d_{v,c}(\mathbf{k}_{\parallel}) P_{\mathbf{k}_{\parallel}} + \text{c.c.} = \frac{1}{\sqrt{\mathcal{S}}} \sum_{\lambda} \phi_{\lambda}^R(\mathbf{r}_{\parallel} = \mathbf{0}) d_{v,c} p_{\lambda} + \text{c.c.} \quad (6.6)$$

where we inserted Eq. (D.3) and assumed that $d_{v,c}$ is independent of \mathbf{k}_{\parallel} . Thus, P results only from optically-bright exciton states, i.e., states with $\phi_{\lambda}^R(\mathbf{r}_{\parallel} = \mathbf{0}) \neq 0$. By transferring polarization into optically dark states, the strong THz field perturbs the homogeneous decay of $P(t)$. Consequently, the THz field induces changes in the normalized optical transmission probability

$$|T(\omega, \Delta t)|^2 = \left| \frac{\langle E_T(\omega, \Delta t) \rangle_{\text{opt}}}{\langle E_0(\omega) \rangle_{\text{opt}}} \right|^2 \quad (6.7)$$

where $\langle E_T(\omega, \Delta t) \rangle_{\text{opt}}$ and $\langle E_0(\omega) \rangle_{\text{opt}}$ are the transmitted and incoming optical electric fields, respectively. The contour plot in Fig. 6.2(a) shows $1 - |T(\omega, \Delta t)|^2$ as function of delay time. The horizontal lines indicate cross section for the specific delay times $\Delta t = 0.3$ ps and $\Delta t = 1.0$ ps which are presented as solid lines in Figs. 6.2(b) and (c), respectively. For comparison, the shaded area shows $1 - |T(\omega)|^2$ where $|T(\omega)|^2 = |\langle E_T(\omega) \rangle_{\text{opt}} / \langle E_0(\omega) \rangle_{\text{opt}}|^2$ is the normalized transmission without THz field.

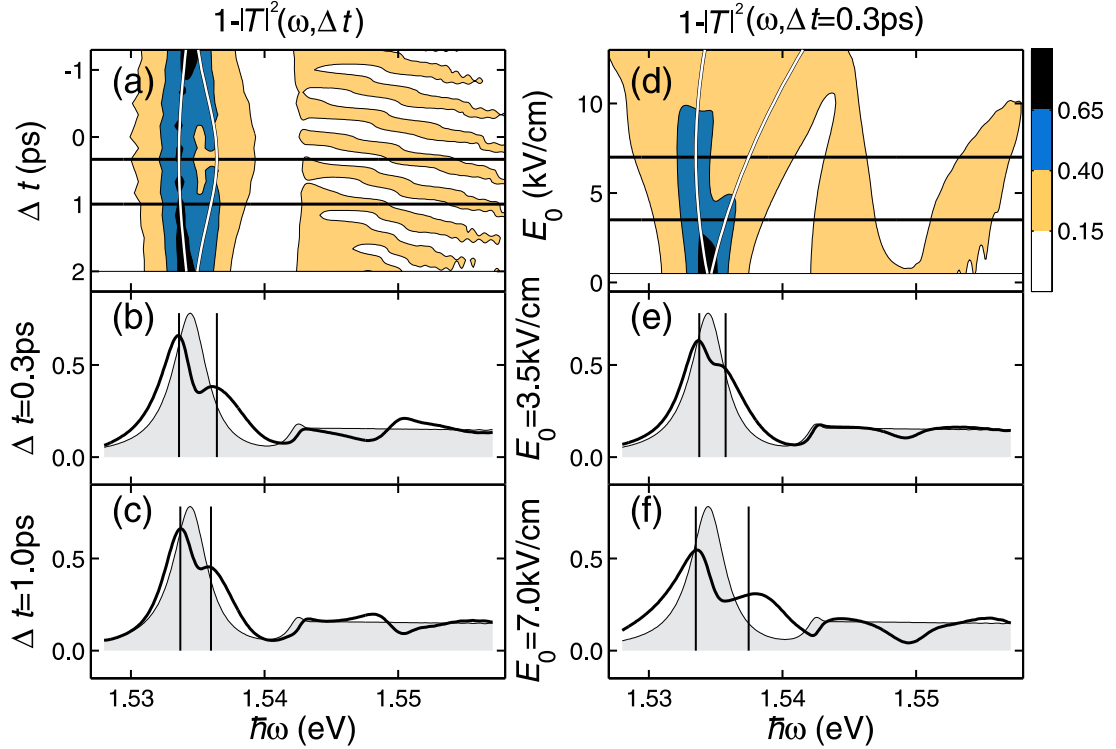


Figure 6.2.: Transmission versus delay time for resonant excitation. (a) shows $1 - |T(\omega, \Delta t)|^2$ as function of frequency ω and delay time Δt for $E_0 = 4.8$ kV/cm. The horizontal lines indicate cross sections which are shown as solid lines in (b) and (c). For comparison, $1 - |T(\omega)|^2$ without THz field is shown as a shaded area. (d) shows $1 - |T(\omega, \Delta t)|^2$ as function of THz intensity for $\Delta t = 0.3$ ps. For the intensities indicated by horizontal lines, cross sections are shown in (e) and (f). The white lines in (a),(d) and the vertical lines in (b),(c) and (e),(f) give the Rabi-peak positions obtained from an analytic solution of the polarization dynamics (see Section 6.3).

We find that the THz field leads to large changes in the optical absorption spectra. The THz-induced changes $\Delta|T|^2(\omega, \Delta t) \equiv |T(\omega)|^2 - |T(\omega, \Delta t)|^2$ are almost 50% of the linear $1 - |T(\omega)|^2$. In particular, we find that the $1s$ -resonance splits into two peaks as a consequence of the Rabi-oscillations induced by the resonant THz field. The peaks are not symmetrically positioned around the $1s$ frequency but shifted toward higher energies. Furthermore, the peaks are not equally large: the high energy peak is much less pronounced than the low energy peak. At high frequencies, around $\hbar\omega = 1.55$ eV, the THz excitation leads to distinct features which oscillate as function of delay time. The energetic position of these signatures is roughly given by $E_{1s} + 2\hbar\nu_{\text{THz}} \approx 1.55$ eV such that these features must be THz-induced high harmonics. In fact, they result from the extreme-nonlinear dynamics induced by the strong THz field and will be discussed in the next Section.

Figure 6.2(d) shows $1 - |T(\omega, \Delta t)|^2$ as function of the peak THz field strength, E_0 ,

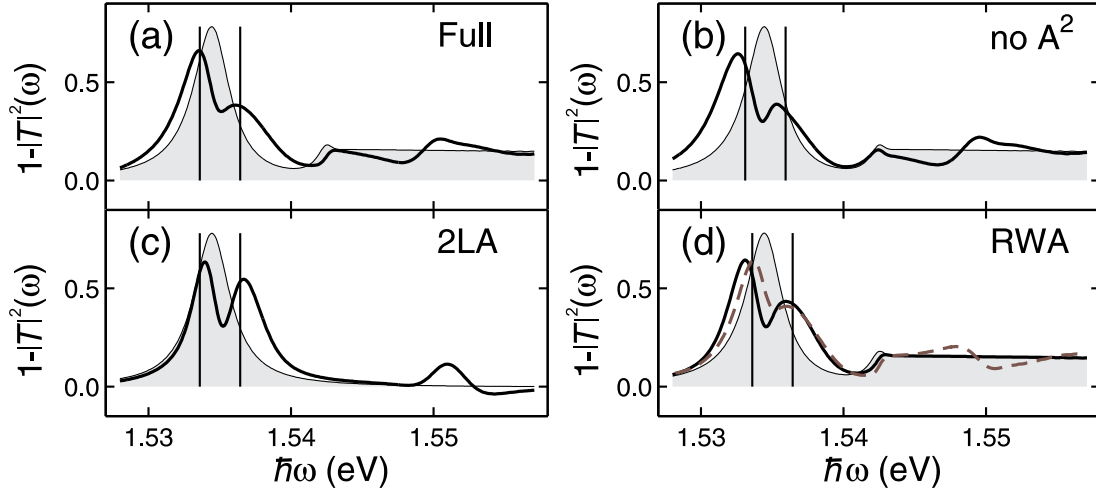


Figure 6.3.: Switch-off Analysis. The linear spectrum $1 - |T(\omega, \Delta t)|^2$ with (solid line) and without (shaded area) THz field is shown for $E_0 = 4.8 \text{ kV/cm}$, $\Delta t = 0.3 \text{ ps}$ and $\phi = 0$. when different terms in Eq. (6.1) are switched off. In (a), the full result is shown, in (b) the A^2 -dependent contribution is switched off, in (c) a two-level approximation is applied and in (d) a rotating-wave approximation is applied to Eq. (6.1). The dashed line in (d) shows the full result for $\phi = 0.5 \pi$.

for the fixed delay time $\Delta t = 0.3 \text{ ps}$. The horizontal lines indicate cross-sections for the two THz-field strengths, $E_0 = 3.5 \text{ kV/cm}$ and $E_0 = 7.0 \text{ kV/cm}$, which are presented as solid lines in Figs. 6.2(e) and (f), respectively. We observe that the Rabi-splitting increases almost linearly with E_0 . The overall blueshift of the resonances seems to increase quadratically with E_0 . Finally, the harmonics around $E_{1s} + 2h\nu_{\text{THz}}$ become more pronounced as the intensity increases. For a field strength $E_0 > 10 \text{ kV/cm}$, the optical spectra are almost completely distorted.

To reveal the origin of the different spectral features, we repeat the numerical computation but switch off different terms in Eq. (6.1). Figure 6.3(a) shows $1 - |T(\omega, \Delta t)|^2$ (solid line) for $E_0 = 4.8 \text{ kV/cm}$ and $\Delta t = 0.3 \text{ ps}$ for the full computation. In Fig. 6.3(b), the corresponding $1 - |T(\omega, \Delta t)|^2$ is shown when the A^2 -dependent intraband contribution in Eq. (6.1) is switched off. Without the A^2 -term, the position of the Rabi peaks is symmetric around the $1s$ -exciton energy. Thus, the A^2 term is responsible for the overall blueshift in the optical spectra. This is not surprising since this term simply renormalizes the kinetic energy by

$$E_{\text{pond}}^{\text{ren}} \equiv \frac{|e|^2}{2\mu} \langle A(0, t) \rangle_{\text{THz}}^2. \quad (6.8)$$

For cw-excitation $\langle A(0, t) \rangle_{\text{THz}} = A_0 \cos(\omega_{\text{THz}} t)$, this energy is identical to

$$E_P = \frac{|e|^2 A_0^2}{4\mu} = \frac{|e|^2 E_0^2}{4\mu\omega_{\text{THz}}^2} \quad (6.9)$$

when averaged over one THz cycle. The energy E_P is called ponderomotive or “wiggle” energy [80] and is proportional to the intensity. It can be understood classically as the cycle-averaged kinetic energy of a charged particle with mass μ in a harmonic electromagnetic field. Since ω_{THz} in the denominator is small, this term can become appreciable in the THz regime. Intuitively, the THz oscillations are slow enough such that electrons and holes “follow” the field in a classical sense acquiring additional kinetic energy. The blueshift associated with the ponderomotive energy is part of the dynamic Franz-Keldysh effect predicted in [69–71]. In the present work, we reproduce these results but we include the microscopic derivation of the A^2 -dependent renormalization (see Appendix C.1). The ponderomotive blueshift has been measured in bulk [30, 31, 72] and QW systems [32].

We conclude that the Rabi-splitting in Fig. 6.3(a) must be due to the remaining $j \cdot A$ -contribution in Eq. (6.1). This term is antisymmetric in \mathbf{k}_{\parallel} such that it can induce nonlinear transitions between excitonic states with different symmetry, e.g., $1s \rightarrow 2p \rightarrow 2d$ etc. . In a dressed state picture [81], the splitting arises because the THz field mixes the bright $1s$ state and the dark $2p$ state leading to a doublet of optically bright states separated by the Rabi frequency (Autler-Townes splitting [71]). We confirm (not shown) that the $j \cdot A$ and A^2 contributions are not additive; the sum of the individual $\Delta|T|^2$ -contributions does not match the differential transmission $\Delta|T|^2$ for the full computation. Since $j \cdot A$ and A^2 terms lead to effects of the same order of magnitude, it can be difficult to disentangle the contributions from an experimental signal (see also Section 6.4).

Figure 6.3(c) shows $1 - |T(\omega, \Delta t)|^2$ when a two-level approximation is applied to Eq. (6.1) where only the $1s$ and $2p$ exciton states are taken into account. We find that the general features of the full calculation are reproduced. However, the Rabi peaks now approximately have the same height. Thus, the asymmetric peak height must be caused by transitions to higher exciton states, e.g., $2p$ -to-continuum transitions. The harmonics are still present in the two-level approximation which means that they do not result from non-resonant transitions. The high energy features completely disappear when a rotating-wave approximation is applied to Eq. (6.1) as shown in Fig. 6.3(d).

6.2. Extreme-Nonlinear Dynamics

In the last Section, we found that the intense THz field leads to harmonics in the linear optical spectrum $1 - |T(\omega, \Delta t)|^2$ around the energetic position $E_{1s} + 2h\nu_{\text{THz}}$ which result from the breakdown of the rotating-wave approximation (RWA). The RWA neglects source terms in the equations of motion which oscillate with two times the excitation frequency, e.g.,

$$A_{\text{env}}(t) \cos(\omega_{\text{THz}} t) e^{i\omega_{\text{THz}} t} = A_{\text{env}}(t) \frac{1}{2} (e^{2i\omega_{\text{THz}} t} + 1) \stackrel{\text{RWA}}{=} \frac{1}{2} A_{\text{env}}(t) \quad (6.10)$$

such that this approximation neglects higher-order processes where two additional THz photons are absorbed. The high-intensity regime where the RWA breaks down is called the regime of extreme-nonlinear optics [82]. In general, *extreme-nonlinear dynamics*

6.3. Analytic Solution within the Rotating-Wave Approximation

occurs when a quantity associated with the light intensity approaches a characteristic transition frequency of the system. In our case, the Rabi frequency ν_R is close to the 1s-to-2p transition frequency. For $E = 4.8 \text{ kV/cm}$, we realize the ratio $\nu_R/\nu_{2p,1s} = 0.37$ at the pulse peak. For these conditions, the THz pulse generates replicas of the Rabi peaks at higher frequencies which is not expected for “traditional” nonlinear optics, i.e., within the RWA [83] (see also analytic solution in the next Section). The regime of extreme-nonlinear dynamics is particularly interesting for THz excitations. Due to small THz photon energy, it is reached already at fairly low intensities. Moreover, Coulomb effects remain important for extreme-nonlinear THz excitations in contrast to extreme-nonlinear optical excitations where many-body effects are virtually negligible [84].

As contributions beyond the RWA become relevant, the induced dynamics depends on the actual THz field $A_{\text{THz}}(t)$ rather than its envelope $A_{\text{env}}(t)$. Thus, extreme-nonlinear effects should depend on the so-called carrier-envelope-offset phase ϕ in $A_{\text{THz}} = A_{\text{env}} \cos(2\pi\nu_{\text{THz}}t + \phi)$ of the exciting field [75, 82]. In Figs. 6.3(a),(d), we indeed find that the shape of the harmonics changes drastically when the carrier-envelope-offset phase is changed from $\phi = 0.0\pi$ (solid line in (a)) to $\phi = 0.5\pi$ (dashed line in (d)).

Here, we focused on the extreme-nonlinear effects related to the $j \cdot A$ contribution. However, also the A^2 -term can lead to harmonics beyond the RWA when the ponderomotive energy is comparable to the THz photon energy [31, 70]. The fact that ponderomotive and Rabi energy have the same order of magnitude as THz photon energy and excitonic transition energies, i.e.,

$$E_P \sim \hbar\omega_R \sim \hbar\omega_{2p,1s} \sim \hbar\omega_{\text{THz}} \quad (6.11)$$

is a unique characteristic of nonlinear THz excitations and leads to a large variety of interesting nonlinear effects.

6.3. Analytic Solution within the Rotating-Wave Approximation

To better understand the Rabi-splitting and the ponderomotive shifts, we give an approximate analytic solution of Eq. (6.1). Previous analytic investigations [70, 71, 73] have concentrated on the THz-induced harmonics in the optical spectrum. The analytic result presented here highlights the interplay of ponderomotive shifts and Rabi splitting. We assume continuous wave (cw) THz-excitation, $A_{\text{THz}}(t) = A_0 \cos(\omega_{\text{THz}}t)$, of a perfect two-level system (TLS) consisting only of the 1s and 2p exciton states. According to Eq. (D.17), the polarization dynamics in the exciton basis is then given by

$$i\hbar \frac{\partial}{\partial t} p_{1s} = (E_{1s} + \frac{e^2}{2\mu} \langle A \rangle_{\text{THz}}^2 - i\gamma) p_{1s} - J_{1s,2p} \langle A \rangle_{\text{THz}} p_{2p} - \sqrt{S} \phi_{1s}^R(\mathbf{0}) d_{c,v} \langle E \rangle_{\text{opt}} \quad (6.12)$$

$$i\hbar \frac{\partial}{\partial t} p_{2p} = (E_{2p} + \frac{e^2}{2\mu} \langle A \rangle_{\text{THz}}^2 - i\gamma) p_{2p} - J_{1s,2p} \langle A \rangle_{\text{THz}} p_{1s}. \quad (6.13)$$

To solve Eqs. (6.12)-(6.13), we introduce the excitonic polarizations in rotating frame via $p_{1s} = \tilde{p}_{1s} e^{-i\omega_{\text{opt}}t}$ and $p_{2p} = \tilde{p}_{2p} e^{-i\omega_{\text{THz}}t} e^{-i\omega_{\text{opt}}t}$ and apply the RWA for both optical

6. Interband Polarization in Strong Terahertz Fields

and THz fields. We thus obtain the linear equations

$$\hbar \frac{\partial}{\partial t} \begin{pmatrix} \tilde{p}_{1s} \\ \tilde{p}_{2p} \end{pmatrix} = \begin{pmatrix} -iE_P/2 - \gamma & i\Omega_R/2 \\ i\Omega_R/2 & -i\Delta - iE_P/2 - \gamma \end{pmatrix} \begin{pmatrix} \tilde{p}_{1s} \\ \tilde{p}_{2p} \end{pmatrix} + \begin{pmatrix} \frac{i}{2}\sqrt{S}\phi_{1s}^R(\mathbf{0})d_{c,v}\bar{E}_0\delta(t) \\ 0 \end{pmatrix} \quad (6.14)$$

where $\Delta = E_{2p,1s} - \hbar\omega_{\text{THz}}$ is the detuning, and $\Omega_R = J_{1s,2p}A_0$ is the Rabi energy. Furthermore, we assumed that the optical pulse is short – in fact, δ -function like – on the THz time scale and resonant with the 1s-exciton energy. It is straightforward to solve Eq. (6.14) such that we obtain for the macroscopic optical polarization

$$P(t) = \frac{1}{\sqrt{S}}d_{v,c}\phi_{1s}^R(\mathbf{r}_{\parallel} = 0)p_{1s}(t) + \text{c.c.} = \theta(t) \frac{|d_{c,v}\phi_{1s}^R(\mathbf{0})|^2 i\bar{E}_0}{4\hbar} \quad (6.15)$$

$$\times e^{i(-E_{1s} - \Delta/2 - E_P/2 - i\gamma)t/\hbar} \left[\left(1 + \frac{\Delta}{\tilde{\Omega}_R}\right) e^{i\tilde{\Omega}_R t/(2\hbar)} + \left(1 - \frac{\Delta}{\tilde{\Omega}_R}\right) e^{-i\tilde{\Omega}_R t/(2\hbar)} \right].$$

where we introduced the renormalized Rabi-energy

$$\tilde{\Omega}_R \equiv \sqrt{\Omega_R^2 + \Delta^2} \equiv \sqrt{(J_{1s,2p}A_0)^2 + \Delta^2}. \quad (6.16)$$

The Fourier transform of Eq. (6.15) yields the optical susceptibility

$$\chi_{\text{opt}}(\omega) = \frac{P(\omega)}{\varepsilon_0 \langle E(\omega) \rangle_{\text{opt}}} = \frac{1}{4\varepsilon_0} |d_{c,v}\phi_{1s}^R(\mathbf{r}_{\parallel} = \mathbf{0})|^2 \quad (6.17)$$

$$\times \left[\frac{1 + \Delta/\tilde{\Omega}_R}{\hbar\omega - \left(E_{1s} + (E_P + \Delta - \tilde{\Omega}_R)/2\right) - i\gamma} + \frac{1 - \Delta/\tilde{\Omega}_R}{\hbar\omega - \left(E_{1s} + (E_P + \Delta + \tilde{\Omega}_R)/2\right) - i\gamma} \right]$$

where we identified the ponderomotive energy $E_P = e^2 A_0^2 / (4\mu)$. Obviously, the 1s-exciton resonance splits into two peaks positioned at

$$E_{\pm}^{\text{res}} \equiv E_{1s} + \frac{E_P + \Delta}{2} \pm \frac{\tilde{\Omega}_R}{2}. \quad (6.18)$$

The splitting energy is determined by the detuning Δ and the Rabi-energy $\Omega_R = J_{1s,2p}A_0$. Note that the peaks are weighted with a factor $1 \pm \Delta/\tilde{\Omega}_R$ which means that peak heights differ for non-vanishing detuning. For large detunings, $|\Delta| \gg \Omega_R$, the THz field only leads to a shift given by

$$\frac{E_P}{2} + \frac{\Delta - \tilde{\Omega}_R^2}{2} = \frac{E_P}{2} + \frac{\Delta - \sqrt{\Omega_R^2 + \Delta^2}}{2} \approx \frac{E_P}{2} + \frac{\Delta - \Delta \left(1 + \frac{\Omega_R^2}{2\Delta^2}\right)}{2} = \frac{E_P}{2} - \frac{\Omega_R^2}{4\Delta}. \quad (6.19)$$

Thus, we find a competition of ponderomotive shifts and the AC-Stark effect [85] in this limit. While E_P always leads to a blueshift of E_{-}^{res} , the second term can lead to a blue or redshift of E_{-}^{res} depending on the sign of Δ . For vanishing detuning, $\Delta = 0$, the resonance splits into two equally large peaks positioned at

$$E_{\pm}^{\text{res}} = E_{1s} + \frac{E_P}{2} \pm \frac{\Omega_R}{2}. \quad (6.20)$$

Thus, the splitting is not symmetric around the 1s-exciton resonance even for $\Delta = 0$.

The analytical solution Eq. (6.17) is valid for cw-THz excitations. For THz excitation with an envelope of finite duration τ , the spectrum looks similar and displays the same Rabi-splitting. However, the peak positions are given by the modified Rabi- and ponderomotive energies

$$\tilde{\Omega}_R \equiv \sqrt{(J_{1s,2p}A_{\text{eff}})^2 + \Delta^2}, \quad E_P = \frac{e^2 A_{\text{eff}}^2}{4\mu} \quad (6.21)$$

which, instead of A_0 , depend on the effective field strength

$$A_0 \rightarrow A_{\text{eff}} = \frac{1}{T} \int_{t_{\text{opt}}}^{t_{\text{opt}}+T} A_{\text{env}}(t) dt, \quad T = \frac{\hbar \ln 2}{\gamma} \quad (6.22)$$

defined via the envelope, $A_{\text{env}}(t)$, of the exciting THz vector potential and the decay constant of the polarization γ . Note that A_{eff} is simply the mean value of $A_{\text{env}}(t)$ over the time interval where significant interband polarization is present.

A comparison to the numerical results in Section 6.1 confirms that the analytic solution, Eqs. (6.15)-(6.22), accurately predicts the peak positions. In Fig. 6.2(a)-(c), we find that the Rabi-splitting depends on the delay time. The splitting is largest for a maximum overlap of polarization and THz pulse. In Fig. 6.2(d)-(f), we nicely observe how the ponderomotive shift exceeds the Rabi-splitting as the intensity increases. For very high intensities, the numerically computed peak positions are no longer reproduced as extreme-nonlinear effects and transitions to higher exciton states dominate the dynamics which are not included in Eqs. (6.15)-(6.22).

6.4. Interaction of Intense Single-Cycle Terahertz Pulses with AlGaAs/GaAs Quantum Wells

In this Section, we apply our microscopic theory to quantitatively explain experimental data from a THz-“pump” and optical-probe measurement. These experiments were performed in Oregon by Y. S. Lee et al. while the theoretical analysis was done in Marburg. The experiment uses strong single-cycle THz pulses and a weak optical probe to study time-resolved nonlinear effects in the optical spectrum in multiple GaAs/AlGaAs QWs.

The measurements were performed using 805-nm, 100-fs pulses from a 1-kHz Ti:sapphire regenerative amplifier (Coherent Inc., Legend). The optical beam was split into two components: the major portion for THz generation and the minor portion for the optical probe. Single-cycle THz pulses were generated by optical rectification in a 1-mm ZnTe crystal. The incident optical pulse energy was 0.8 mJ, irradiated on a roughly 3-mm spot in the ZnTe crystal. The THz pulses were collimated with an off-axis parabolic mirror and the THz beam diameter was 1.5 mm at the focus. The THz pulse shape was measured using electro-optic sampling in a 1-mm ZnTe crystal. The absolute THz power was determined using a Si bolometer at liquid He temperature.

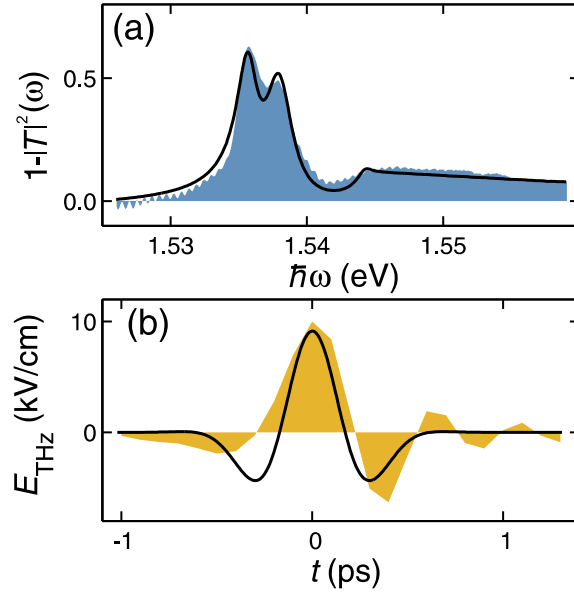


Figure 6.4.: (a) Experimental (shaded area) and theoretical (solid line) $1 - |T(\omega)|^2$. The $1s$ -HH and LH resonances are at $E_{1s}^{\text{HH}} = 1.536$ eV and $E_{1s}^{\text{LH}} = 1.538$ eV, respectively. (b) Electric field of the experimental (shaded area) and theoretical (solid line) THz pulse. (from Paper [III])

The THz electric-field amplitude at the peak is estimated as 10 kV/cm when the optical pump-pulse energy is 0.8 mJ. The real-time waveform of the THz pulse is shown in Fig. 6.4(b) as a shaded area. The GaAs QW sample is put at the focus of the THz pulses and the optical transmission spectra are measured. The sample studied has ten high-quality, undoped 12-nm-wide GaAs QWs separated by 16-nm-wide $\text{Al}_{0.3}\text{Ga}_{0.7}\text{As}$ barriers. The measured normalized transmission without THz field, $1 - |T(\omega)|^2$, is shown as a shaded area in Fig. 6.4(a). Due to strain between the multi QWs and the substrate, the energetic separation of HH and LH $1s$ -exciton resonance is relatively small. The experiment measures the spectrally-resolved intensity of the optical pulse as function of the delay time $\Delta t = t_{\text{THz}} - t_{\text{opt}}$ where t_{THz} and t_{opt} are the central times of THz and optical pulse, respectively. The THz-induced changes appear in the differential spectrum $\Delta|T(\omega, \Delta t)|^2 = |T(\omega)|^2 - |T(\omega, \Delta t)|^2$. Figure 6.5(a) presents the experimental $\Delta|T|^2$ as function of optical energy $\hbar\omega$ and time delay Δt . The horizontal lines indicate energy cross-sections for fixed delay times and the vertical lines time slices for fixed energies.

For the theoretical description of the nonlinear THz experiment, we solve the Maxwell-semiconductor-Bloch equations (3.34) and (3.39) including both heavy-hole (HH) and light-hole (LH) valence bands. The bandstructure and optical-dipole matrix elements are obtained from a standard $8 \times 8 \mathbf{k} \cdot \mathbf{p}$ -band-structure calculation which fully takes into account the material parameters as well as the strain inside the sample. We also treat the light propagation through the experimental multi-QW structure by solving Maxwell's wave equation via a transfer-matrix technique [59]. The resulting linear spectrum without THz pulse, shown as a solid line in Fig. 6.4(a), reproduces

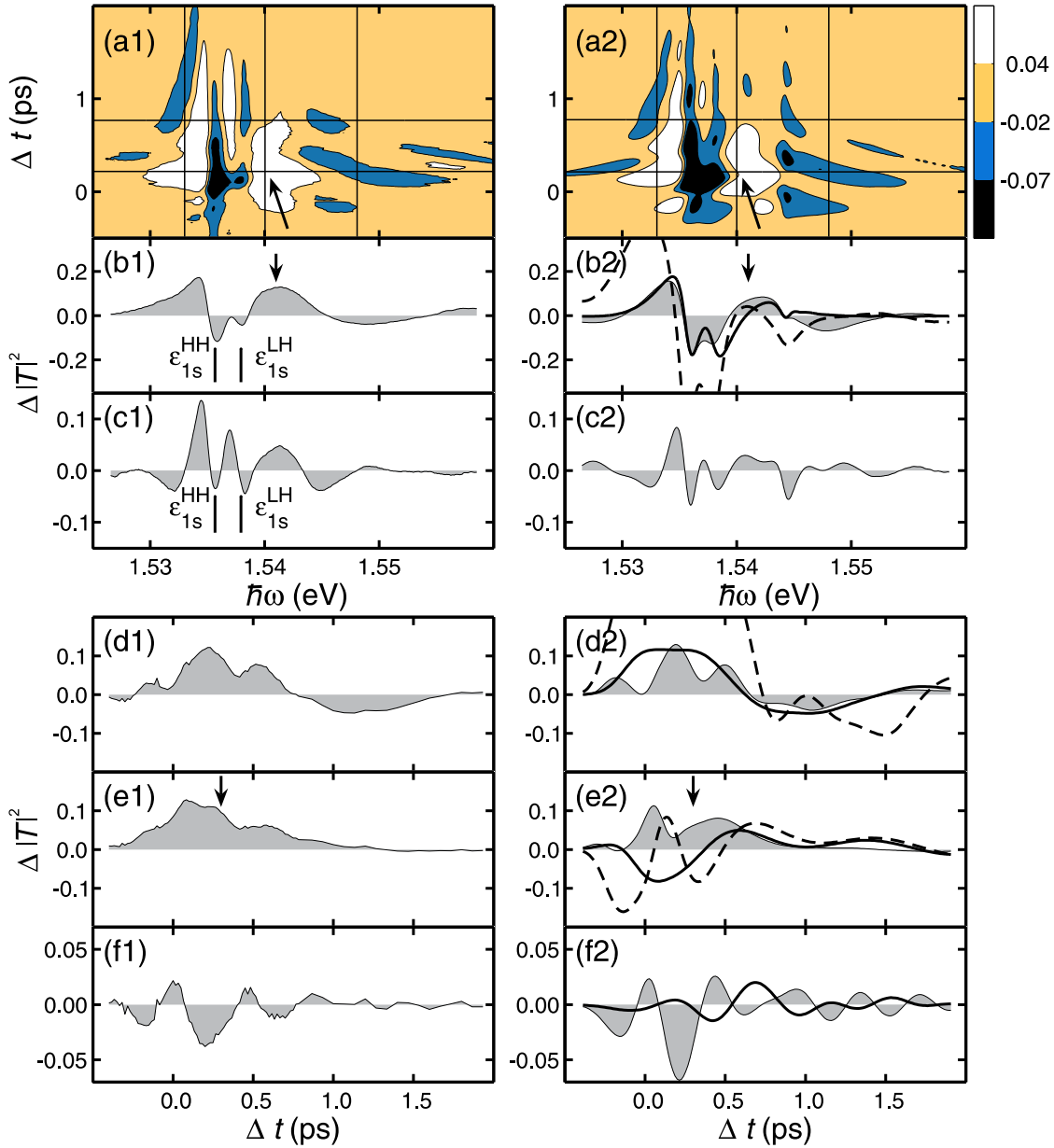


Figure 6.5.: Experimental (a1)-(f1) and theoretical (a2)-(f2) differential spectrum. (a) Contour Plot of $\Delta|T|^2(\omega, \Delta t)$. The horizontal black lines correspond to cross-sections at $\Delta t = 0.22$ ps and $\Delta t = 0.78$ ps shown as a shaded area in (b) and (c), respectively. The black vertical lines correspond to cross-sections for $\hbar\omega = 1.533$ eV, $\hbar\omega = 1.540$ eV and $\hbar\omega = 1.548$ eV which are shown as a shaded area in (d), (e) and (f), respectively. In addition to the results of the full computation, (b2),(d2) and (e2) show the numerical results with the A^2 term switched off (dashed line) and (b2),(d2), (e2) and (f2) show the results when the RWA is applied (solid line). (from Paper [III])

6. Interband Polarization in Strong Terahertz Fields

the experimental spectrum. We assume that the theoretical THz vector potential, $A_{\text{THz}}(t) = A_0 e^{-(t/\tau)^2} \cos(2\pi\nu_{\text{THz}}t + \phi)$, has a Gaussian envelope. We find that the THz electric field $E_{\text{THz}} = -(\partial/\partial t)A_{\text{THz}}$ matches the experimental single-cycle THz pulse when we choose the central frequency $\nu_{\text{THz}} = 0.9$ THz, carrier-envelope offset phase $\phi = \pi/2$, duration $\tau = 300$ fs, and the peak field strength $E_0 = 9.2$ kV/cm [see Fig. 6.4(b)]. The THz frequency is clearly detuned with respect to the $1s$ -to- $2p$ exciton transition frequencies $\nu_{2p,1s}^{\text{HH}} = 1.96$ THz and $\nu_{2p,1s}^{\text{LH}} = 1.65$ THz such that we do not expect that the THz pulse induces Rabi oscillations. However, the experiment accesses the regime of extreme-nonlinear optics since we realize at the pulse peak the ratios $\nu_{\text{R}}^{\text{HH}}/\nu_{2p,1s}^{\text{HH}} = 0.63$ and $\nu_{\text{R}}^{\text{LH}}/\nu_{2p,1s}^{\text{LH}} = 0.79$ between Rabi frequency and $1s$ -to- $2p$ transition frequency.

The theoretically computed THz-induced changes, $\Delta|T(\omega, \Delta t)|^2$, are shown in the right column of Fig. 6.5. We find excellent agreement between experimental and theoretical transients. The theory reproduces the magnitude as well as the spectral and temporal shape of all essential features in $\Delta|T|^2$. We notice that the THz-induced changes are large and we find that several transient features appear in the differential transmission on a sub-picosecond time scale.

In both experiment and theory, we observe a positive $\Delta|T|^2$ transient for small time delays $\Delta t \approx 0.2$ ps and energetically slightly above the $1s$ -LH resonance at $\hbar\omega \approx 1.540$ eV (white region with arrow in the contour plot). The transient exists for about 500 fs and is thus shorter-lived than the other transients around the $1s$ resonances. In the cross-sections (b) and (e), this feature is also indicated by an arrow. To reveal its origin, we perform a switch-off analysis as in Section 6.1. The dashed lines in Fig. 6.5(b2) and (e2) show the computed $\Delta|T|^2$ when the A^2 -dependent term in Eq. (3.34) is switched off. Without the A^2 -term the positive ultrafast $\Delta|T|^2$ feature is almost washed out and the overall shape of the experimental $\Delta|T|^2$ is not reproduced at all. Thus, we can connect this ultrafast transient to ponderomotive contributions induced by the single-cycle THz pulse. Moreover, we conclude that the A^2 and the jA contributions strongly compensate each other in the total signal.

Figures 6.5(d2) and (f2) show the Δt -dependence of the differential optical transmission for the energies $\hbar\omega = 1.533$ eV and $\hbar\omega = 1.548$ eV, respectively. Here, we compare the full theoretical result (shaded area) to computations (solid line) where the RWA is applied to Eq. (3.34). Within the RWA, the fast oscillations in $\Delta|T|^2$ almost vanish. Thus, they can be linked to non-RWA parts due to the extreme-nonlinear THz excitation. Since the energy $\hbar\omega = 1.548$ eV roughly matches $E_{1s} + \Delta/2 + 2h\nu_{\text{THz}}$ where Δ is the detuning of the THz pulse with respect to the $1s$ - $2p$ transition, the shallow resonance at this energy are, in fact, harmonics of the strong THz field. The generation of harmonics requires the absorption of two additional THz photons – a contribution which is neglected in the RWA. Since the THz spectrum is much narrower than the extension of the high energy features, we can rule out the explanation that they arise due to absorption of a single THz photon.

The experiment-theory comparison presented in this Section demonstrates that our microscopic theory is able to quantitatively analyze nonlinear THz effects identifying time-resolved ponderomotive and extreme-nonlinear contributions in the experiment.

7. Exciton Populations in Strong Terahertz Fields

In the previous Chapter, I have investigated the effect of strong THz fields on coherent excitons, i.e., eigenstates of the interband polarization. Typically, the phase coherence of the polarization is destroyed within picoseconds. In contrast, an incoherent exciton population, i.e., a truly bound electron-hole pair can remain in the system for several nanoseconds. As shown in Chapter 5, weak THz fields can unambiguously detect incoherent excitons. Here, I will explore the possibility to control and manipulate incoherent excitons by using strong THz fields.

Incoherent excitons are in many ways analogous to atoms. The attractive electron-hole Coulomb interaction leads to a Hydrogen-like energy spectrum with transition frequencies in the THz range. However, the analogy is not complete. Excitons in semiconductors have typical binding energies of tens of meV as opposed to tens of eV in atoms. Moreover, the dephasing times in semiconductors are usually much shorter than in atoms. In atoms, the coupling to the radiation reservoir is the dominant dephasing mechanism while it is many-body scattering in semiconductors. At elevated carrier densities and temperatures, the fermion substructure of excitons becomes increasingly important leading to plasma and ponderomotive contributions.

Nonlinear optics in atomic systems has reached a high level of sophistication. The availability of tailored high-intensity laser pulses has allowed experiments to control the atomic system to a high degree using, e.g., stimulated Raman adiabatic passage to transfer electron populations between atomic states [86, 87] or laser cooling to reach Bose-Einstein condensation [88]. Nonlinear THz optics of incoherent excitons is only at its beginning since affordable high-intensity THz sources and suitable THz detectors have been developed only recently [27]. While there are numerous investigations of nonlinear THz-spectroscopy of impurities in doped semiconductor systems [28, 60], few investigations focus on strong-field THz excitation of incoherent excitons in intrinsic semiconductors (see, e.g., Section 7.4).

In this Chapter, I will consider low-density and temperature conditions and assume an initial many-body state with a significant population of $1s$ excitons. Due to the numerical complexity of the problem, we I will mainly explore the relevant phenomena using the QWI system. As in Chapter 5, the theory is evaluated for GaAs parameters and the effective wire radius is 8.4 nm.

7.1. Basic Terahertz-Induced Processes

As a first step, I will investigate the basic nonlinear THz processes described by the coupled Eqs. (3.48)-(3.57) for idealized conditions. In particular, I will investigate in how far an approach similar to the well-known two-level treatment of atoms can be applied to describe the THz dynamics of incoherent excitons in semiconductors. The investigations in this Chapter focus on the the low-density limit only such that the exciton-correlation dynamics, Eq. (3.54), can be solved in main-sum approximation. The obtained numerical results are compared to analytical solutions of the nonlinear THz dynamics in the exciton basis.

7.1.1. Exciton-Population Transfer

To understand the basic THz-induced process, we first ignore triplet-scattering effects and carrier equilibration assuming a vanishing dephasing $\gamma = 0$ (see Appendix C.3). We perform a more realistic analysis with full dephasing in Sections 7.2-7.3. Moreover, we consider an initial many-body state where all electrons and holes are bound into $1s$ -excitons such that the $1s$ -exciton fraction is

$$\Delta n_{1s,1s} \equiv \frac{N_{1s,1s}}{S} \equiv \frac{1}{S} \sum_{\mathbf{q}_{\parallel}} \Delta N(\mathbf{q}_{\parallel}) = n_{2D}. \quad (7.1)$$

We also use a very low carrier density of $n_{1D} = 10^3 \text{ cm}^{-1}$ and assume that the initial exciton center-of-mass distribution $\Delta N(\mathbf{q}_{\parallel}) \equiv \Delta N_{1s,1s}(\mathbf{q}_{\parallel}, t = 0)$ follows a thermal distribution at $T = 10 \text{ K}$. We numerically solve Eqs. (3.48)-(3.57) for the QWI arrangement and for resonant excitation of the $1s$ -to- $2p$ exciton transition. The THz pulse, $A_{\text{THz}}(t) = A_{\text{env}}(t) \cos(2\pi\nu_{\text{THz}}t)$, with central frequency $\nu_{\text{THz}} = \omega_{\text{THz}}/(2\pi) = (E_{2p} - E_{1s})/h = 1.43 \text{ THz}$ has a Gaussian envelope, $A_{\text{env}}(t) = A_0 \exp(-(t - t_0)^2/\tau^2)$, where $\tau = 5 \text{ ps}$ is the duration and t_0 the central time of the pulse. The peak field strength of the THz pulse is $E_0 = 0.24 \text{ kV/cm}$ such that the area of the pulse matches $\int J_{1s,2p} A_{\text{env}}(t)/\hbar dt = \pi$. For the conditions studied here, the \mathbf{q}_{\parallel} -dependence of the excitonic-transition energies and matrix elements is negligible.

The dynamics of the exciton populations is shown in Fig. 7.1. We find that the $1s$ -population (solid line) is depleted while the $2p$ -population (shaded area) builds up. At the end of the THz pulse (thin line) the $1s$ - $2p$ subsystem is almost completely inverted. To investigate the influence of higher exciton states, we solve Eqs. (3.48)-(3.57) again but apply a two-level approximation (TLA) to Eq. (3.54). In the numerical calculation, this is achieved by projecting the correlations involving higher exciton states out of c_X at each time step. The resulting $2p$ -population within the TLA shown as a dashed line in Fig. 7.1 is almost identical to the result of the full computation. Thus, the exciton populations are practically restricted to the $1s$ and $2p$ exciton states for the idealized conditions assumed here.

To better understand these results, we solve the correlation dynamics in the exciton basis, Eq. (D.21). When we neglect all source terms in the RHS of Eq. (D.21) except

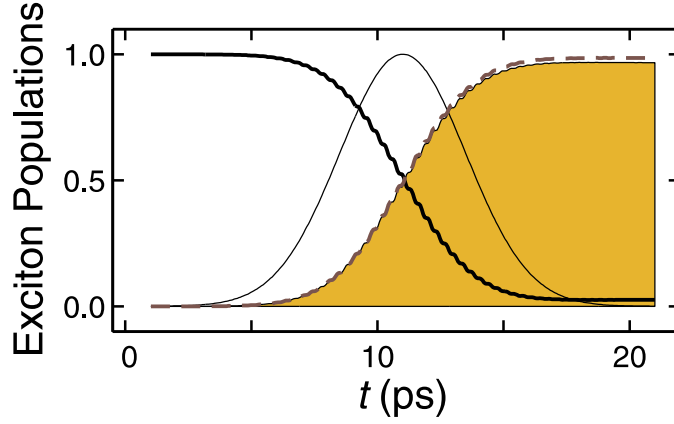


Figure 7.1.: Exciton-Population Inversion. The exciton-populations $\Delta N_{1s,1s}$ (solid line) and $\Delta N_{2p,2p}$ (shaded area) normalized to the total number of electrons are shown for excitation with a Gaussian π -pulse (thin line). For comparison, the dashed line shows $\Delta N_{2p,2p}$ when the TLA is applied. We use $n_{1D} = 10^3 \text{ cm}^{-1}$, $T = 10 \text{ K}$ and $\gamma = 0 \text{ meV}$. (from Paper [V])

the resonant THz contributions which include the matrix element $J_{1s,2p}$, we obtain a closed set of equations for the correlations $\Delta N_{1s,1s}(\mathbf{q}_{\parallel})$, $\Delta N_{2p,2p}(\mathbf{q}_{\parallel})$ and $\Delta N_{1s,2p}(\mathbf{q}_{\parallel})$. With the definitions $S_x = \text{Re}[\sum_{\mathbf{q}_{\parallel}} \Delta N_{1s,2p}(\mathbf{q}_{\parallel})]$, $S_y = \text{Im}[\sum_{\mathbf{q}_{\parallel}} \Delta N_{1s,2p}(\mathbf{q}_{\parallel})]$ and $S_z = \sum_{\mathbf{q}_{\parallel}} \frac{1}{2}[\Delta N_{2p,2p}(\mathbf{q}_{\parallel}) - \Delta N_{1s,1s}(\mathbf{q}_{\parallel})]$, we thus obtain the *THz-Bloch Equations* (TBE) [22]

$$\hbar \frac{\partial}{\partial t} \begin{pmatrix} S_x \\ S_y \\ S_z \end{pmatrix} = \begin{pmatrix} 2J_{1s,2p}A_{\text{THz}} \\ 0 \\ -\hbar\omega_{2p,1s} \end{pmatrix} \times \begin{pmatrix} S_x \\ S_y \\ S_z \end{pmatrix} - \begin{pmatrix} \gamma S_x \\ \gamma S_y \\ 0 \end{pmatrix} \quad (7.2)$$

where $\hbar\omega_{\lambda,\nu} \equiv E_{\lambda,\nu} \equiv E_{\lambda} - E_{\nu}$. The TBE are fully analogous to the optical Bloch equations of atoms [89]. The exciton-population correlations correspond to the population of atomic levels and can be manipulated by strong THz fields in an analogous way to atom optics.

In Appendix D.5, we summarize well-known solutions of the TBE. For resonant excitation and vanishing dephasing, the adiabatic solution within the rotating-wave approximation (RWA) is given by

$$\begin{aligned} \Delta N_{2p,2p}(\mathbf{q}_{\parallel}) - \Delta N_{1s,1s}(\mathbf{q}_{\parallel}) &= -\Delta N(\mathbf{q}_{\parallel}) \cos \Omega_{\text{R}}(t), \\ \Delta N_{1s,2p}(\mathbf{q}_{\parallel}) &= \frac{i}{2} \Delta N(\mathbf{q}_{\parallel}) \sin \Omega_{\text{R}}(t) e^{-i\omega_{\text{THz}}t}. \end{aligned} \quad (7.3)$$

Here we defined $\Omega_{\text{R}}(t) \equiv \int_{-\infty}^t \omega_{\text{R}}(u) du$ with the Rabi frequency $\omega_{\text{R}}(t) \equiv J_{1s,2p}A_{\text{env}}(t)/\hbar$. For $\Omega_{\text{R}}(t) = \pi$, we indeed find inversion of the two-level system.

7.1.2. Dynamics of Pair-Correlation function

We next evaluate the electron-hole pair-correlation function for the π -pulse excitation considered in the previous Section. The numerically computed $\Delta g_{eh}(r, t)$ along the

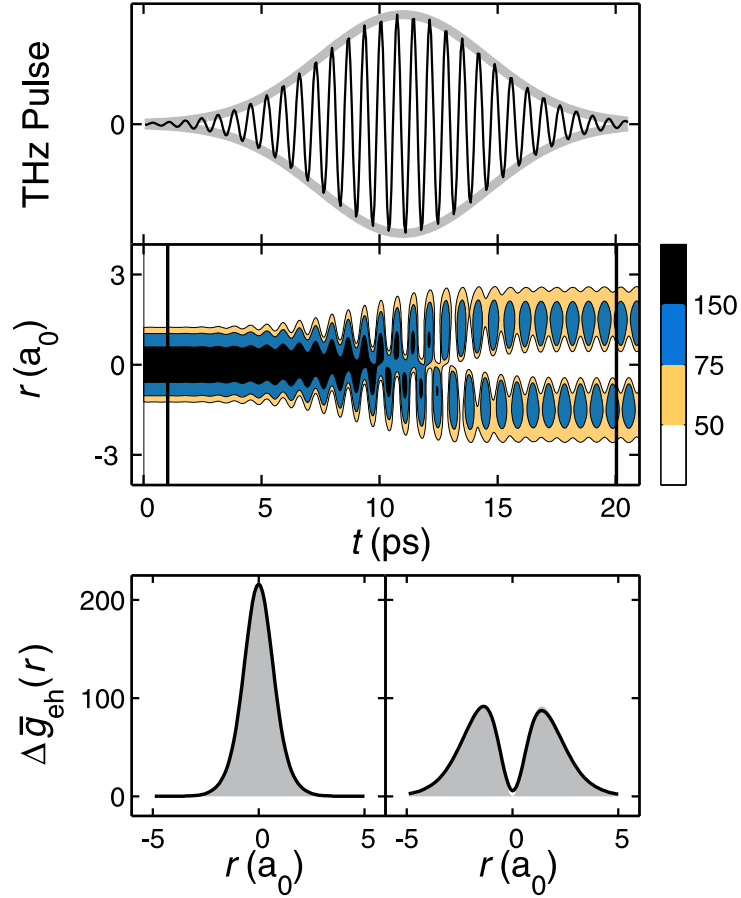


Figure 7.2.: Electron-Hole Pair-Correlation Function for π -pulse. (a) The THz pulse (solid line) and its envelope (thick line) are plotted. (b) The computed $\Delta g_{eh}(r, t)$ along the quantum-wire direction r is shown as a contour plot. The vertical lines indicate cross-sections for fixed times which are presented (solid line) in (c) and (d). For comparison, the scaled exciton wavefunctions $|\phi_{1s}^R(r)|^2$ and $|\phi_{2p}^R(r)|^2$ are shown as a shaded area in (c) and (d), respectively. (from Paper [V])

quantum-wire direction r is shown in Fig. 7.2. As can be seen in Figs. 7.2(c) and (d), the shape of the pair-correlation function changes from a $|\phi_{1s}^R(r)|^2$ -dependence to a $|\phi_{2p}^R(r)|^2$ -dependence. The contour plot shows that the THz field induces dipole oscillations between electrons and holes with the frequency of the exciting pulse.

This result is easily understood in the exciton basis. Inserting the solution (7.3) of the TBE into Eq. (D.12), we immediately find

$$\begin{aligned} \frac{\Delta g_{eh}(r)}{n_{2D}} &= \cos^2\left(\frac{\Omega_R(t)}{2}\right) |\phi_{1s}^R(r)|^2 + \sin^2\left(\frac{\Omega_R(t)}{2}\right) |\phi_{2p}^R(r)|^2 \\ &\quad - \sin \Omega_R(t) \operatorname{Im} \left[e^{-i\omega_{\text{THz}}t} (\phi_{1s}^R(r))^* \phi_{2p}^R(r) \right]. \end{aligned} \quad (7.4)$$

The oscillations observed in Fig. 7.2(b) are explained by the term in the second line of

Eq. (7.4) which obviously describes dipole oscillations arising from the $1s$ - $2p$ superposition state. When the inversion is complete, $\Omega_R(t) = \pi$, we find $\Delta g_{eh}(r) = n_{2D} |\phi_{2p}^R(r)|^2$. Thus, the strong THz field directly manipulates $\Delta g_{eh}(r)$ by inducing internal excitonic transitions analogous to atom optics.

7.1.3. Dynamics of Carrier Distributions

We now analyze the dynamics of the carrier distributions $f_{\mathbf{k}_{\parallel}}^{e/h}$, which are the only relevant singlets in the incoherent regime, for the same resonant π -pulse excitation as in the previous Sections. Since we assume a completely excitonic conditions in Eq. (7.1) where all electrons and holes are bound to $1s$ excitons, the initial carrier distributions are not given by thermal distributions but rather by

$$f_{\mathbf{k}_{\parallel}}^{e(h)} = \sum_{\mathbf{q}_{\parallel}} |\phi_{1s}^R(\mathbf{k}_{\parallel} - \mathbf{q}_{\parallel}^{e(h)})|^2 \Delta N(\mathbf{q}_{\parallel}) \equiv \Phi_{1s}^{e(h)}(\mathbf{k}_{\parallel}). \quad (7.5)$$

Here, $\Phi_{1s}^{e/h}(\mathbf{k}_{\parallel})$ is the distribution consistent with the $1s$ -exciton ground state; it is fully determined by the center-of-mass distribution and the $1s$ -exciton wavefunction in momentum state. For a sufficiently narrow center-of-mass distribution, we can approximate $\Delta N(\mathbf{q}_{\parallel}) \approx \delta_{\mathbf{q}_{\parallel}, \mathbf{0}} \Delta N_{1s,1s}$ such that $\Phi_{1s}^{e/h}(\mathbf{k}_{\parallel}) = \Delta N_{1s,1s} |\phi_{1s}^R(\mathbf{k}_{\parallel})|^2$. In this limit, the electron and hole distributions are simply proportional to the probability distribution of the exciton wavefunction in momentum space.

Figure 7.3 shows the numerically computed electron distribution $f_{\mathbf{k}_{\parallel}}^e$ for different times during the inversion process. We plot the even part $f_{\mathbf{k}_{\parallel}}^{e,\text{even}}$ (solid line) and the odd part $f_{\mathbf{k}_{\parallel}}^{e,\text{odd}}$ (dashed line) of the electron distribution separately [see Eq. (3.30)]. As in Fig. 7.1, we compare the full result (left column) to the results of a computation where a TLA is applied to the exciton correlations in Eq. (3.54) (right column). We find the surprising result that the TLA – which gave the correct dynamics of the exciton populations $\Delta N_{\lambda,\lambda}(\mathbf{q}_{\parallel})$ and the pair-correlation function $\Delta g_{eh}(\mathbf{r}_{\parallel})$ – fails to describe the actual dynamics of the carrier distributions. In particular, the even part $f_{\mathbf{k}_{\parallel}}^{e,\text{even}}$ does not change at all in the TLA even though it should convert into $\Phi_{2p}^e(\mathbf{k}_{\parallel}) \equiv \sum_{\mathbf{q}_{\parallel}} |\phi_{2p}^R(\mathbf{k}_{\parallel} - \mathbf{q}_{\parallel})|^2 \Delta N(\mathbf{q}_{\parallel})$ (shaded area in the lower frames of Fig. 7.3) as in the full computation.

To better understand this shortcoming of the TLA, we analytically solve the carrier dynamics in the exciton basis for a continuous-wave (cw) THz excitation resonant with the $1s$ -to- $2p$ transition. Following Paper [V], we solve Eq. (D.25) separately for $f_{\mathbf{k}_{\parallel}}^{e,\text{even}}$ and $f_{\mathbf{k}_{\parallel}}^{e,\text{odd}}$. Noting that the exciton wavefunctions have a well-defined parity given by $\pi(\lambda) = 1$ for $\phi_{\lambda}(-|\mathbf{k}_{\parallel}|) = \phi_{\lambda}(|\mathbf{k}_{\parallel}|)$ and $\pi(\lambda) = -1$ for $\phi_{\lambda}(-|\mathbf{k}_{\parallel}|) = -\phi_{\lambda}(|\mathbf{k}_{\parallel}|)$, it is easily confirmed that off-diagonal exciton correlations $\Delta N_{\lambda,\nu}$ between states with the same parity drive $f_{\mathbf{k}_{\parallel}}^{e,\text{even}}$ while those with different parity drive $f_{\mathbf{k}_{\parallel}}^{e,\text{odd}}$. Thus, Eq. (D.25) can

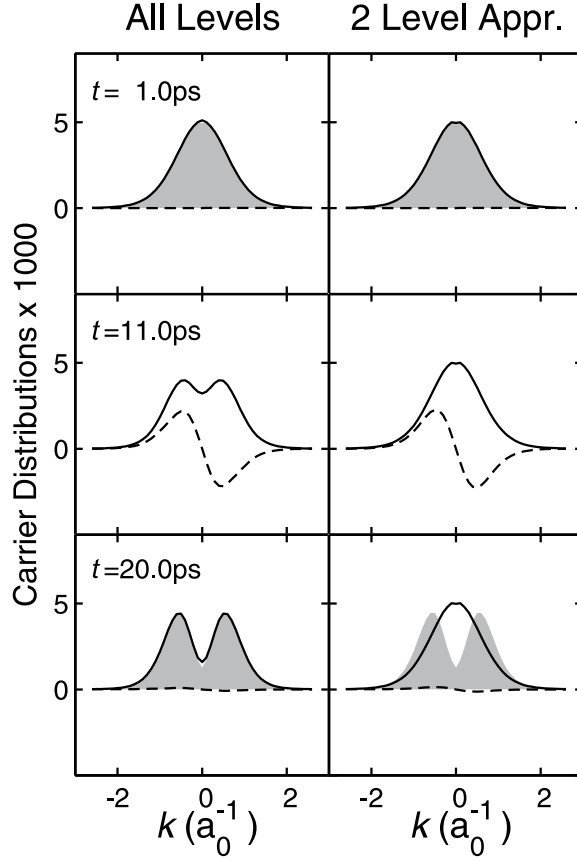


Figure 7.3.: Dynamics of Electron Distribution for π -pulse. The even (solid line) and odd part (dashed line) of the electron density distribution are presented for different times. Results are shown for the full computation (left column) and for a TLA (right column). For comparison, the upper frames show $\Phi_{1s}^e(\mathbf{k}_{\parallel})$ and the lower frames $\Phi_{2p}^e(\mathbf{k}_{\parallel})$ as a shaded area. (from Paper [V])

be written as

$$\hbar \frac{\partial}{\partial t} f_{\mathbf{k}_{\parallel}}^{e,\text{odd}} = \text{Im} \left[\sum_{\substack{\lambda \neq \nu, \mathbf{q}_{\parallel} \\ \pi(\lambda) \neq \pi(\nu)}} \Delta N_{\lambda, \nu}(\mathbf{q}_{\parallel}) E_{\nu, \lambda} \phi_{\lambda}^L(\mathbf{k}_{\parallel} - \mathbf{q}_{\parallel}^e) \phi_{\nu}^R(\mathbf{k} - \mathbf{q}_{\parallel}^e) \right], \quad (7.6)$$

$$\hbar \frac{\partial}{\partial t} f_{\mathbf{k}_{\parallel}}^{e,\text{even}} = \text{Im} \left[\sum_{\substack{\lambda \neq \nu, \mathbf{q}_{\parallel} \\ \pi(\lambda) = \pi(\nu)}} \Delta N_{\lambda, \nu}(\mathbf{q}_{\parallel}) E_{\nu, \lambda} \phi_{\lambda}^L(\mathbf{k}_{\parallel} - \mathbf{q}_{\parallel}^e) \phi_{\nu}^R(\mathbf{k} - \mathbf{q}_{\parallel}^e) \right]. \quad (7.7)$$

In the TLA, $\Delta N_{1s, 2p}(\mathbf{q}_{\parallel})$ contributes to the odd part $f_{\mathbf{k}_{\parallel}}^{e,\text{odd}}$ while no source exists for the even part $f_{\mathbf{k}_{\parallel}}^{e,\text{even}}$. Inserting the solution of the terahertz-Bloch equations (7.3) into Eq. (7.6), we obtain for the odd part

$$\frac{\partial}{\partial t} f_{\mathbf{k}_{\parallel}}^{e,\text{odd}} = \sum_{\mathbf{q}_{\parallel}} \omega_{2p, 1s} \phi_{1s}^L(\mathbf{k}_{\parallel} - \mathbf{q}_{\parallel}^e) \phi_{2p}^R(\mathbf{k}_{\parallel} - \mathbf{q}_{\parallel}^e) \Delta N(\mathbf{q}_{\parallel}) \sin(\omega_R t) \cos(\omega_{\text{THz}} t). \quad (7.8)$$

Integration of Eq. (7.8) yields denominators of the form $\omega_{\text{THz}} \pm \omega_{\text{R}} \approx \omega_{\text{THz}}$ which we approximate assuming that $\hbar\omega_{\text{R}} \ll E_{2p,1s}$. Furthermore, we use that $\phi_{\lambda}^{\text{L}} \approx \phi_{\lambda}^{\text{R}}$ at low densities and obtain as the final result for even and odd parts of the carrier distributions

$$\begin{aligned} f_{\mathbf{k}_{\parallel}}^{e,\text{odd}}(t)|_{\text{TLA}} &= \Phi_{1s,2p}^e(\mathbf{k}_{\parallel}) \sin \Omega_{\text{R}}(t) \sin(\omega_{\text{THz}}t) \\ f_{\mathbf{k}_{\parallel},e}^{\text{even}}(t)|_{\text{TLA}} &= \Phi_{1s}^e(\mathbf{k}_{\parallel}) \end{aligned} \quad (7.9)$$

where $\Phi_{1s,2p}^e(\mathbf{k}_{\parallel}) \equiv \sum_{\mathbf{q}_{\parallel}} \phi_{1s}^{\text{R}}(\mathbf{k}_{\parallel} - \mathbf{q}_{\parallel}^e) \phi_{2p}^{\text{R}}(\mathbf{k}_{\parallel} - \mathbf{q}_{\parallel}^e) \Delta N(\mathbf{q}_{\parallel})$. Here, we replaced again $\omega_{\text{R}}t$ with $\Omega_{\text{R}}(t)$ which is valid for slowly varying envelopes. In other words, the TLA incorrectly predicts an unchanged $f_{\mathbf{k}_{\parallel},e}^{\text{even}}$. Thus, in order to obtain the correct result, we clearly have to extend the analysis beyond the $1s$ and $2p$ levels.

When all exciton levels are taken into account, the dynamics of the odd part of the carrier distribution $f_{\mathbf{k}_{\parallel}}^{e,\text{odd}}$ is the same as for the TLA because $\Delta N_{1s,2p}(\mathbf{q})$ is still the dominant contribution. However, the largest contributions to the even part $f_{\mathbf{k}_{\parallel}}^{e,\text{even}}$ are given by the correlations $\Delta N_{1s,n:s}(\mathbf{q}_{\parallel})$ where $n : s \equiv 2s, 3s, \dots$ and $\Delta N_{2p,n:p}(\mathbf{q}_{\parallel})$ where $n : p \equiv 3p, 4p, \dots$ which directly couple to $\Delta N_{1s,2p}(\mathbf{q}_{\parallel})$. Neglecting all other sources in their equations of motion, Eq. (D.21) produces

$$i\hbar \frac{\partial}{\partial t} \Delta N_{1s,n:s}(\mathbf{q}_{\parallel}) = (E_{n:s} - E_{1s}) \Delta N_{1s,n:s}(\mathbf{q}_{\parallel}) - J_{n:s,2p} \Delta N_{1s,2p}(\mathbf{q}_{\parallel}) A_{\text{THz}}, \quad (7.10)$$

$$i\hbar \frac{\partial}{\partial t} \Delta N_{2p,n:p}(\mathbf{q}_{\parallel}) = (E_{n:p} - E_{2p}) \Delta N_{2p,n:p}(\mathbf{q}_{\parallel}) - J_{n:p,1s} \Delta N_{2p,1s}(\mathbf{q}_{\parallel}) A_{\text{THz}}. \quad (7.11)$$

With $\Delta N_{1s,2p}(\mathbf{q}_{\parallel})$ given by Eq. (7.3), the solution for continuous-wave excitation, $A_{\text{THz}} = A_0 \cos(\omega_{\text{THz}}t)$, is

$$\Delta N_{1s,n:s}(\mathbf{q}_{\parallel}) = \frac{i}{4} \Delta N(\mathbf{q}_{\parallel}) \frac{J_{n:s,2p} A_0}{E_{n:s} - E_{1s}} \sin(\omega_{\text{R}}t), \quad (7.12)$$

$$\Delta N_{2p,n:p}(\mathbf{q}_{\parallel}) = \frac{i}{4} \Delta N(\mathbf{q}_{\parallel}) \frac{J_{n:p,1s} A_0}{E_{2p} - E_{n:p}} \sin(\omega_{\text{R}}t). \quad (7.13)$$

Here, we used again the RWA and assumed that $\hbar\omega_{\text{R}} \ll E_{n:s,1s}, E_{n:p,2p}$. Inserting this result into Eq. (7.7) and solving for $f_{\mathbf{k}_{\parallel}}^{e,\text{even}}$ yields

$$\begin{aligned} f_{\mathbf{k}_{\parallel}}^{e,\text{even}}(t) &= -\frac{1}{2} \cos(\omega_{\text{R}}t) \sum_{\mathbf{q}_{\parallel}} \Delta N(\mathbf{q}_{\parallel}) \\ &\times \left[\sum_{n=2}^{\infty} \frac{J_{n:s,2p}}{J_{1s,2p}} \phi_{1s}^{\text{L}}(\mathbf{k}_{\parallel} - \mathbf{q}_{\parallel}^e) \phi_{n:s}^{\text{R}}(\mathbf{k}_{\parallel} - \mathbf{q}_{\parallel}^e) - \sum_{n=3}^{\infty} \frac{J_{n:p,1s}}{J_{1s,2p}} \phi_{2p}^{\text{L}}(\mathbf{k}_{\parallel} - \mathbf{q}_{\parallel}^e) \phi_{n:p}^{\text{R}}(\mathbf{k}_{\parallel} - \mathbf{q}_{\parallel}^e) \right] + c(\mathbf{k}_{\parallel}) \end{aligned} \quad (7.14)$$

where the constant $c(\mathbf{k}_{\parallel})$ is determined by the initial condition. The expression in brackets can be modified to

$$\begin{aligned} &\left[\sum_{n=1}^{\infty} \left(\frac{J_{n:s,2p}}{J_{1s,2p}} \phi_{1s}^{\text{L}}(\mathbf{k}_{\parallel} - \mathbf{q}_{\parallel}^e) \phi_{n:s}^{\text{R}}(\mathbf{k}_{\parallel} - \mathbf{q}_{\parallel}^e) \right) - |\phi_{1s}^{\text{R}}(\mathbf{k}_{\parallel} - \mathbf{q}_{\parallel}^e)|^2 + |\phi_{2p}^{\text{R}}(\mathbf{k}_{\parallel} - \mathbf{q}_{\parallel}^e)|^2 \right. \\ &\left. - \sum_{n=2}^{\infty} \left(\frac{J_{n:p,1s}}{J_{1s,2p}} \phi_{2p}^{\text{L}}(\mathbf{k}_{\parallel} - \mathbf{q}_{\parallel}^e) \phi_{n:p}^{\text{R}}(\mathbf{k}_{\parallel} - \mathbf{q}_{\parallel}^e) \right) \right] = [|\phi_{2p}^{\text{R}}(\mathbf{k}_{\parallel} - \mathbf{q}_{\parallel}^e)|^2 - |\phi_{1s}^{\text{R}}(\mathbf{k}_{\parallel} - \mathbf{q}_{\parallel}^e)|^2]. \end{aligned} \quad (7.15)$$

7. Exciton Populations in Strong Terahertz Fields

Here, we inserted the definitions $J_{n:s,2p} = \sum_{\mathbf{k}_{\parallel}} \phi_{n:s}^L(\mathbf{k}_{\parallel}) j(\mathbf{k}_{\parallel}) \phi_{2p}^R(\mathbf{k}_{\parallel})$ and $J_{n:p,1s} = \sum_{\mathbf{k}_{\parallel}} \phi_{n:p}^L(\mathbf{k}_{\parallel}) j(\mathbf{k}_{\parallel}) \phi_{1s}^R(\mathbf{k}_{\parallel})$ and used the completeness of the wavefunctions $\phi_{\nu}(\mathbf{k}_{\parallel})$. Inserting Eq. (7.15) into Eq. (7.14) and replacing again $\omega_R t$ with $\Omega_R(t)$ for slowly varying envelopes, we thus find altogether

$$f_{\mathbf{k}_{\parallel}}^{e,\text{odd}}(t)|_{\text{Full}} = f_{\mathbf{k}_{\parallel}}^{e,\text{odd}}(t)|_{\text{TLA}}, \quad (7.16)$$

$$f_{\mathbf{k}_{\parallel}}^{e,\text{even}}(t)|_{\text{Full}} = \cos^2\left(\frac{\Omega_R(t)}{2}\right) \Phi_{1s}^e(\mathbf{k}_{\parallel}) + \sin^2\left(\frac{\Omega_R(t)}{2}\right) \Phi_{2p}^e(\mathbf{k}_{\parallel}). \quad (7.17)$$

For inversion $\Omega_R(t) = \pi$, we find indeed $f_{\mathbf{k}_{\parallel}}^e = \Phi_{2p}^e(\mathbf{k}_{\parallel})!$

The discussed differences between the full analysis and the TLA have important general consequences. In particular, in semiconductors, one cannot resort to a TLA when describing strong THz excitations since then not even the single-particle dynamics of the carrier distributions is described correctly. Rather, we have to appreciate that the THz field always generates two-particle correlations involving all exciton states – all of which are relevant for the dynamics of the full many-body state. Since carrier distributions are decisive in determining nonlinearities such as Pauli-blocking, scattering and screening effects [51], omission of the full $f_{\mathbf{k}_{\parallel}}^{e/h}$ dynamics can significantly impair the analysis.

7.2. Rabi-flopping of an Exciton Populations

In Section 7.1, I have identified the most important basic THz-induced mechanisms for idealized conditions. Now, I will extend these investigations to more complicated situations where dephasing is fully included. As a first application, I investigate the possibility of Rabi-Flopping of exciton populations induced by the strong THz field.

Rabi oscillations are a model example of a non-perturbative nonlinear process in resonantly-excited two-level systems. As the external light field leads to oscillations in the inversion of the two-level system, it is periodically weakened by absorption and amplified by stimulated emission. The ability to induce coherent oscillations in a quantum-mechanical system is often a prerequisite for more systematic and targeted control of the quantum state.

In atoms, Rabi-flopping has been demonstrated a long time ago in nuclear-magnetic resonance experiments [90, 91]. In semiconductors, experiments have demonstrated coherent Rabi oscillations for interband transitions [54, 55, 92], intersubband transitions [28, 33] and even intraexcitonic transitions of low-lying impurity states [60]. Only recently, suitable THz sources and detectors have made it possible to induce coherent intraexcitonic oscillations in intrinsic semiconductors (see, e.g., Section 7.4).

In this Section, the full theory is evaluated for resonant THz excitation of the $1s$ -to- $2p$ exciton resonance. I will discuss signatures of Rabi oscillations in transmission and/or reflection measurements and address ionization and ponderomotive contributions. Since the ponderomotive parts can mask the Rabi-flopping in the measurable signal, I develop a scheme that rigorously removes them from the total signal.

7.2.1. Population Dynamics and Terahertz Current

For the numerical evaluations of the theory in this Section, we assume the carrier density $n = 1 \times 10^4 \text{ cm}^{-3}$ and a lattice temperature of $T = 20 \text{ K}$. The scattering dynamics in Eqs. (3.48)-(3.57) provided by T_X , $c_{c,c,c,c}$ and $c_{v,v,v,v}$ is treated via a phenomenological model discussed in Appendix C.3. In particular, we assume that off-diagonal correlations $\Delta N_{\lambda,\nu}$ with $\lambda \neq \nu$ are damped with a decay constant of $\gamma = 0.42 \text{ meV}$. We consider an initial many-body state where all carriers are bound to $1s$ -excitons, i.e. $\Delta n_{1s,1s}/n = 100\%$. The initial carrier distributions are chosen according to Eq. (7.5). We solve Eqs. (3.48)-(3.57) for resonant excitation of the $1s$ -to- $2p$ transition with a strong THz pulse having an almost box-shaped envelope. The THz electric field strength is given by $E_0 = 1.6 \text{ kV/cm}$ which corresponds to a Rabi-frequency of $\omega_R = 0.3\omega_{2p,1s}$.

Figure 7.4(a) shows the resulting dynamics of the exciton populations $\Delta N_{1s,1s}$ (solid line) and $\Delta N_{2p,2p}$ (dashed line) as well as the sum of all other population correlations $\sum_{\lambda \neq 1s,2p} \Delta N_{\lambda,\lambda}$ (shaded area). We observe damped Rabi oscillations between the $1s$ and $2p$ exciton populations as well as ionization of the $1s$ - $2p$ subsystem as higher exciton states are populated. The contour plots in Fig. 7.4(c) and (d) show snapshots of the exciton correlations $|\Delta N_{\lambda,\nu}|$ as function of E_λ and E_ν . We find that the correlations $\Delta N_{1s,2p}$, $\Delta N_{2p,1s}$ and $\Delta N_{2p,2p}$ are created by the resonant excitation but also exciton correlations involving higher states corresponding to the ionization of exciton populations. Figure 7.4(e) shows the distribution of exciton populations $|\Delta N_{\lambda,\lambda}|$ at the end of the simulated time interval, i.e., at $t = 22 \text{ ps}$. We distinguish states with s -like parity (solid line) and states with p -like parity (shaded area). The continuum states occupied at the final time have mostly s -like parity and are generated via quasi-resonant transitions from the $2p$ -exciton state to the continuum.

According to Eq. (4.31), the detectable signal, ΔE , in nonlinear THz transmission and reflection experiments is proportional to the induced current $J_{\text{THz}}(t) + J_A(t)$. Thus, the total $\Delta E = \Delta E_{\text{THz}} + \Delta E_A$ consists of a contribution ΔE_{THz} resulting from many-body transitions and a trivial ponderomotive contribution ΔE_A . Recall that amplitude *and* phase of the time-dependent reflected and transmitted THz field can be measured in THz spectroscopy [13, 28]. Figure 7.4(f) shows the differential transmission ΔE (solid line) obtained via the full numerical solution. The individual contributions ΔE_{THz} (solid line) and ΔE_A (shaded area) are shown in Fig. 7.4(g). We see that ΔE_{THz} , which results from the THz-induced exciton dynamics, is damped and almost decayed at the end of the pulse. The signal oscillates with the excitation frequency and is modulated with the Rabi frequency $\omega_R = 0.3\omega_{\text{THz}}$. The ΔE_A -contribution is simply proportional to the exciting vector potential A_{THz} . Since the ponderomotive contributions are relatively large, they mask the Rabi-flopping signatures in the total signal ΔE which features only weak residual oscillations. Since experiments cannot directly access ΔE_{THz} , it is desirable to have a scheme that rigorously removes ΔE_A from the total re-emitted field.

We confirm that the results obtained in this chapter are valid also for other envelope shapes of the THz pulse. However, the Rabi frequency $\omega_R(t) = J_{1s,2p}A_{\text{env}}(t)/\hbar$ is then time-dependent.

7. Exciton Populations in Strong Terahertz Fields

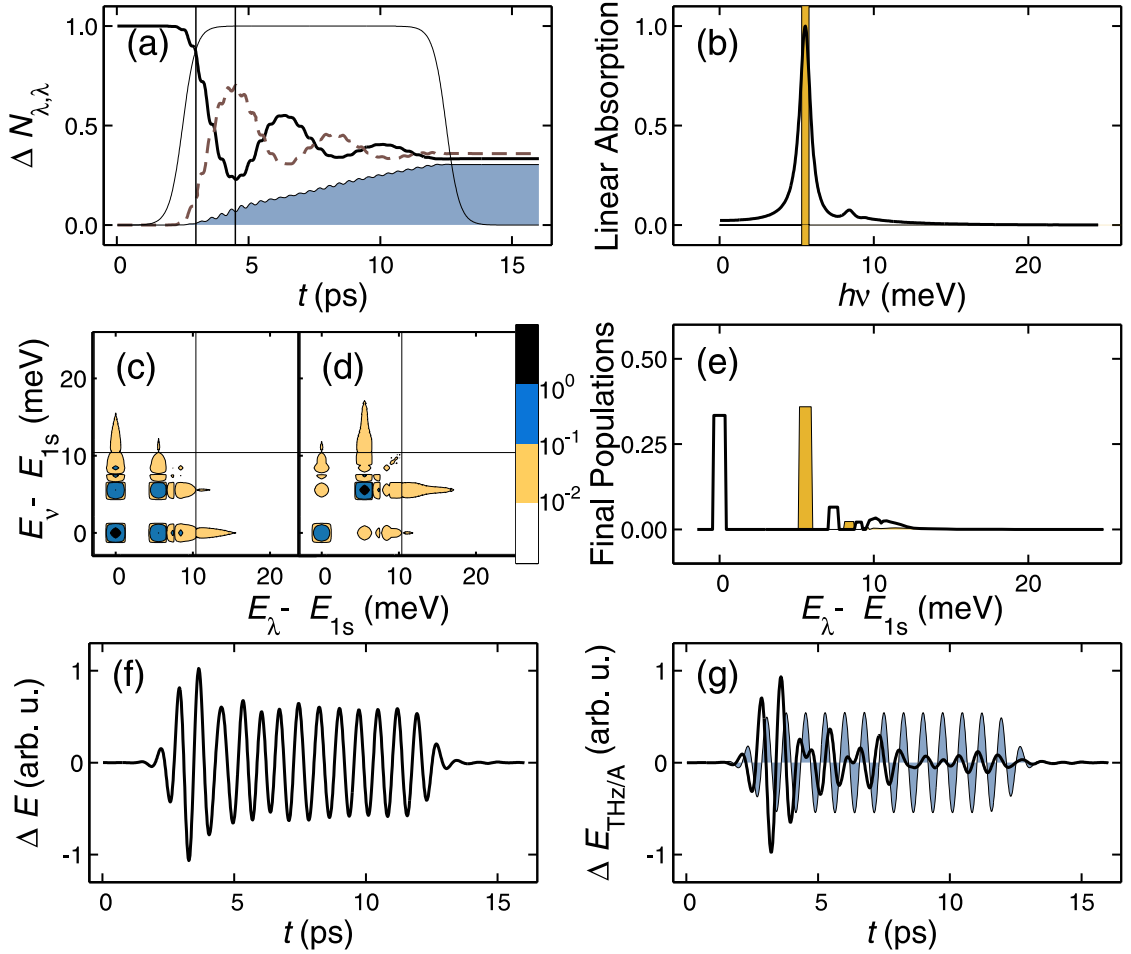


Figure 7.4.: Dynamics of exciton populations and currents for intense resonant $1s$ -to- $2p$ excitation. (a) The computed $\Delta N_{1s,1s}$ (solid line), $\Delta N_{2p,2p}$ (dashed line) and $\sum_{\lambda \neq 1s,2p} \Delta N_{\lambda,\lambda}$ (shaded area) normalized to the total number of electrons are shown for excitation with a box-shaped THz pulse (thin line) with $\omega_R/\omega_{2p,1s} = 0.3$. (b) The linear THz absorption (solid line) is shown and the spectral extension of the THz pulse (full-width at half maximum) is indicated as a shaded area. For the snapshot times indicated by vertical lines in (a), frames (c) and (d) show $|\Delta N_{\lambda,\nu}|$ as function of exciton energies. The final diagonal exciton distribution $\Delta N_{\lambda,\lambda}$ is shown in (e). (f) shows the total re-emitted field $\Delta E = \Delta E_{\text{THz}} + \Delta E_A$ and (g) shows the separate contributions ΔE_{THz} (solid line) and ΔE_A (shaded area). We use $n_{1D} = 10^4 \text{ cm}^{-1}$, $T = 20 \text{ K}$ and $\gamma = 0.42 \text{ meV}$. (according to Paper [V])

7.2.2. Removal of Ponderomotive Contributions

We next develop a scheme that removes the trivial ponderomotive contribution, ΔE_A , from the total re-emitted field ΔE . To this end, we compute the *complex envelope* of the differential transmission (see Paper [VII]).

7.2. Rabi-flopping of an Exciton Populations

We consider excitation with a THz pulse given by

$$A_{\text{THz}}(t) = A_{\text{env}}(t) \cos(\omega_{\text{THz}}t + \phi_0) \quad (7.18)$$

where $A_{\text{env}}(t)$ is an arbitrary envelope, ω_{THz} is the frequency and ϕ_0 is the phase offset of the pulse. For parabolic bands, the ponderomotive current, Eq. (3.40),

$$J_A = -\frac{e^2 n_{2D}}{\mu} A_{\text{THz}} = -\frac{e^2 n_{2D}}{\mu} A_{\text{env}}(t) \cos(\omega_{\text{THz}}t + \phi_0) \quad (7.19)$$

is simply proportional to the THz vector potential. For close-to-resonant $1s$ -to- $2p$ excitation, the dominant contribution to the THz current, J_{THz} , is the $1s$ - $2p$ exciton-transition correlation $S_- = \sum_{\mathbf{q}_{\parallel}} \Delta N_{1s,2p}(\mathbf{q}_{\parallel})$. In a rotating frame, this correlation is given by $\tilde{S}_- \equiv S_- e^{+i(\omega_{\text{THz}}t + \phi_0)}$. We show in Appendix D.5 that the THz current J_{THz} is given by

$$J_{\text{THz}} = \frac{2}{\mathcal{S}} \frac{\omega_{2p,1s}}{\omega_{\text{THz}}} J_{1s,2p} \text{Re} \left[\tilde{S}_- e^{-i(\omega_{\text{THz}}t + \phi_0)} \right] \quad (7.20)$$

whenever \tilde{S}_- varies slowly enough and ionization contributions are small. By inserting Eqs. (7.19) and (7.20) into Eq. (4.31), we find

$$\Delta E = (c_1 \tilde{S}_x + c_2 A_{\text{env}}) \cos(\omega_{\text{THz}}t + \phi_0) + (c_1 \tilde{S}_y) \sin(\omega_{\text{THz}}t + \phi_0) \quad (7.21)$$

where the prefactors have been combined into the constants c_1 and c_2 . Furthermore, \tilde{S}_x and \tilde{S}_y denote real and imaginary part of \tilde{S}_- , respectively. As seen in the previous Sections, \tilde{S}_x and \tilde{S}_y are approximately described by the terahertz-Bloch equations (TBE). The analytic solution of the TBE in Appendix D.5 shows that \tilde{S}_x vanishes for resonant $1s$ -to- $2p$ excitation while \tilde{S}_y oscillates with the Rabi frequency.

We find that *the ponderomotive contribution is synchronized with the cosine part of Eq. (7.21) while the sine part only contains the pure Rabi flopping in \tilde{S}_y* . Since cosine and sine functions represent orthogonal phases, an intelligent Fourier-transformation based algorithm can separate the ponderomotive contribution from the measured ΔE . Following Paper [VII], we next develop this algorithm based on the property of Eq. (7.21).

As a first step, we compute the Fourier transformation of the total differential transmission $\Delta E(\omega) = \int_{-\infty}^{\infty} dt \exp(i\omega t) \Delta E(t)$. In general, real and imaginary parts of $\Delta E(\omega)$ display two pronounced peaks — one around the positive frequency $\omega = \omega_{\text{THz}}$ and one around the negative frequency $\omega = -\omega_{\text{THz}}$. As the next step, we cut off the negative-frequency parts and get $\Delta E(\omega)\theta(\omega)$. We then shift the argument by the central frequency ω_{THz} and obtain $F(\omega) \equiv \Delta E(\omega + \omega_{\text{THz}})\theta(\omega + \omega_{\text{THz}})$. By computing $F(\omega)$, we have effectively shifted the position of the positive-frequency peak of $\Delta E(\omega)$ from $\omega = \omega_{\text{THz}}$ to $\omega = 0$. We then Fourier transform $F(\omega)$ back into time-domain via $F(t) \equiv \int_{-\infty}^{\infty} d\omega/\pi \exp(-i\omega t) F(\omega)$. Since the fast ω_{THz} -oscillations have been removed in $F(t)$, this quantity only contains the dynamics of the envelope of $\Delta E(t)$. In general, $F(t)$ is complex-valued. As the final step, we multiply $F(t)$ with $e^{i\phi_0}$ where ϕ_0 is the phase offset of the excitation pulse. The resulting $f(t) \equiv e^{i\phi_0} F(t)$ is the *complex envelope* of

7. Exciton Populations in Strong Terahertz Fields

the differential transmission $\Delta E(t)$. The definition of $f(t)$ can also be expressed in the more compact form

$$f(t) = e^{i(\omega_{\text{THz}}t + \phi_0)} \int_0^\infty \frac{d\omega}{\pi} e^{-i\omega t} \Delta E(\omega). \quad (7.22)$$

Note that our scheme to compute the complex envelope only requires the knowledge of the differential transmission $\Delta E(t)$ and the electric field $E_{\text{THz}}(t)$ of the excitation pulse which are both accessible in experiments.

It is straightforward to show that $f(t)$ obeys

$$\Delta E(t) = \text{Re}[f(t)] \cos(\omega_{\text{THz}}t + \phi_0) + \text{Im}[f(t)] \sin(\omega_{\text{THz}}t + \phi_0). \quad (7.23)$$

A comparison with Eq. (7.21) directly yields

$$\begin{aligned} \text{Re}[f(t)] &= c_1 \tilde{S}_x(t) + c_2 A_{\text{env}}(t), \\ \text{Im}[f(t)] &= c_1 \tilde{S}_y(t). \end{aligned} \quad (7.24)$$

Thus, we find that the *pure* Rabi oscillations can be identified via oscillations in $\text{Im}[f(t)]$ while the ponderomotive part contributes only to $\text{Re}[f(t)]$. The absolute value of the complex envelope, $|f(t)| = \sqrt{(\text{Re}[f(t)])^2 + (\text{Im}[f(t)])^2}$, is identical to the usual real-valued temporal envelope of ΔE . Thus, according to Eqs. (7.23) and (7.24), one can *rigorously separate the relevant excitonic and the ponderomotive contributions by computing the complex envelope of the detectable $\Delta E(t)$ signal.*

To test this scheme, we compute the complex envelope for the differential transmission ΔE computed in the last Section. Figure 7.5 shows the individual steps that are necessary to obtain the complex envelope. The original ΔE (shaded area in frame (a)) is Fourier transformed with respect to time (frame (b)). The spectrum is truncated and shifted (frame (c)) and then transformed back to time-domain (frame (d)). We find that the thus obtained complex envelope indeed separates excitonic and ponderomotive contributions: The imaginary part, $\text{Im}[f(t)]$ (solid line) oscillates and exhibits distinct zero-crossings after each half Rabi-cycle clearly demonstrating the Rabi flopping of exciton populations. Note that the oscillations are biased slightly below zero due to exciton transitions leading to ionization of the $1s$ - $2p$ two-level system. These transitions contribute to both real and imaginary part of the complex envelope but are usually small for close-to-resonant $1s$ -to- $2p$ excitation. The real part, $\text{Re}[f(t)]$ (dashed line), results mainly from the ponderomotive contribution and thus follows the envelope of the box-shaped excitation pulse. The weak oscillations in $\text{Re}[f(t)]$ at early times are due to ionization contributions. In Fig. 7.5(e), we compare the actual $\Delta E_{\text{THz}}(t)$ (shaded area) with $\text{Im}[f(t)] \sin(\omega_{\text{THz}}t + \phi_0)$ (dashed line) and find that the curves match. As shown in Fig. 7.5(f), the actual $\Delta E_A(t)$ (shaded area) matches $\text{Re}[f(t)] \cos(\omega_{\text{THz}}t + \phi_0)$ (dashed line).

As an application of the presented scheme, we here computed the complex envelope of the differential transmission for resonant THz excitation with a box-shaped envelope. However, our scheme can isolate the pure Rabi-oscillations from the measured $\Delta E(t)$ for

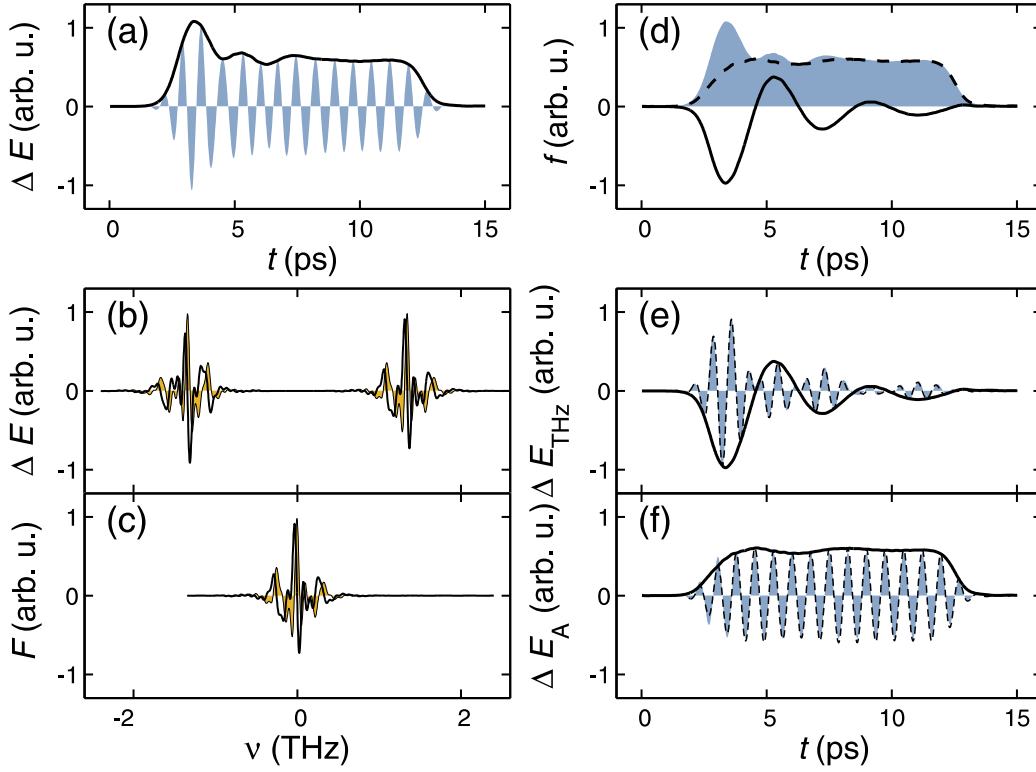


Figure 7.5.: THz currents and complex envelope. (a) The full re-emitted field $\Delta E(t)$ (shaded area) and the absolute value of the complex envelope $|f(t)|$ are shown. Frames (b) and (c) show real (solid line) and imaginary (shaded area) part of $\Delta E(\omega)$ and $F(\omega)$, respectively. (d) $|f(t)|$ (solid line) $\text{Re}[f(t)]$ (dashed line) and $\text{Im}[f(t)]$ (shaded area) are shown. (e) The actual ΔE_{THz} (shaded area) is compared to $\text{Im}[f(t)] \sin(\omega_{\text{THz}}t + \phi_0)$ (dashed line). In (f), the actual ΔE_A (shaded area) is compared to $\text{Re}[f(t)] \cos(\omega_{\text{THz}}t + \phi_0)$ (dashed line). (according to Paper [VII])

arbitrary envelope shapes. For the case that the excitation is detuned from the $1s$ -to- $2p$ resonance, the imaginary part of the complex envelope directly identifies the detuned Rabi oscillations.

The method presented here can easily be extended to the case that the excitation pulse, $A_{\text{THz}}(t) = A_{\text{env}}(t) \cos \Phi(t)$, is chirped such that the phase $\Phi(t)$ cannot be written as $\omega_c t + \phi_0$ with constants ω_c and ϕ_0 . In this case, the complex envelope of the differential transmission is obtained via the following steps. First, $\Phi(t) = \omega_c t + \phi(t)$ is expressed via a time-dependent phase-offset $\phi(t)$ and an arbitrary central frequency ω_c . Then – as for the unchirped case – the central frequency ω_c is “removed” from the signal by computing $e^{i\omega_c t} \int_0^\infty \frac{d\omega}{\pi} e^{-i\omega t} \Delta E(\omega)$. As the final step, the result is multiplied with $e^{i\phi(t)}$. In a compact form, the complex envelope can be written as

$$f(t) = e^{i\Phi(t)} \int_0^\infty \frac{d\omega}{\pi} e^{-i\omega t} \Delta E(\omega). \quad (7.25)$$

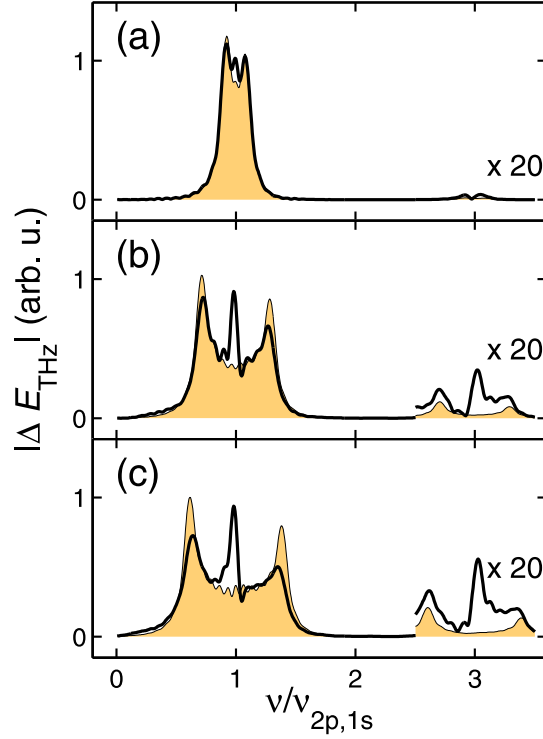


Figure 7.6.: THz response for different intensities and resonant excitation. The spectrum $|J_{\text{THz}}(\omega)|$ for different values of the Rabi frequencies (a) $\omega_R = 0.1\omega_{2p,1s}$, (b) $\omega_R = 0.3\omega_{2p,1s}$, (c) $\omega_R = 0.4\omega_{2p,1s}$ is shown for the full computation (solid line) and for the TLA (shaded area). The region around $\omega/\omega_{2p,1s} = 3$ is magnified. (according to Paper [V])

Again, it is straightforward to show that

$$\Delta E(t) = \text{Re}[f(t)] \cos \Phi(t) + \text{Im}[f(t)] \sin \Phi(t). \quad (7.26)$$

such that $\text{Re}[f(t)] = c_1 \tilde{S}_x(t) + c_2 A_{\text{env}}(t)$ and $\text{Im}[f(t)] = c_1 \tilde{S}_y(t)$. The phase of the excitation pulse has to be determined separately, e.g., via the spectrogram of the measured E_{THz} .

Since the trivial ΔE_A -contribution can always be removed, we only concentrate on ΔE_{THz} to further discuss the Rabi-flopping signatures.

7.2.3. Rabi Sidebands and Harmonics

To further investigate the Rabi flopping signatures in the nonlinear THz response, we analyze the power spectrum spectrum $|\Delta E_{\text{THz}}|$. Figure 7.6 shows $|\Delta E_{\text{THz}}(\omega)|$ for three values of the peak THz field strength E_0 for resonant 1s-to-2p excitation. We present results for the full computation (solid line) and for the two-level approximation (shaded area). We observe that the Rabi oscillations lead to the well-known Rabi sidebands in the spectrum at the energetic position $\omega_{\text{THz}} \pm \tilde{\omega}_R$ where $\tilde{\omega}_R$ is the renormalized Rabi

frequency (see Appendix D.5). The splitting of the Rabi sidebands increases with larger intensity since $\omega_R \propto E_0$.

The solution for the two-level approximation features only two peaks whereas an additional narrow middle peak emerges at ω_{THz} for the full computation. We find that the middle peak broadens for increasing intensity. We verify numerically that the linewidth of the middle peak is independent of the dephasing constant γ used. When we evaluate the ionization rate γ_{ion} defined as $\Delta n_{1s,1s} + \Delta n_{2p,2p} = n_{2D} \exp(-\gamma_{\text{ion}}t/\hbar)$, we find that the linewidth of the middle peak matches with γ_{ion} . Hence, we conclude that the middle peak is a direct signature of the ionization process.

The triplet in the THz power spectrum around the excitation frequency must not be confused with the famous Mollow triplet [93] in the fluorescence spectrum of resonantly driven two-level systems. There, a middle peak and two sidebands emerge with a fixed ratio of linewidths and peak heights which can be explained within the two-level approximation. Here, we monitor the classical reradiation not fluorescence.

The triplet around $3\omega_{\text{THz}}$ in Fig. 7.6 can be attributed to harmonics generated by the strong THz excitation. We observe that the sidebands at $3\omega_{\text{THz}} \pm \omega_R$ are also present in the TLA. As discussed in Section 6.2, harmonics of resonantly excited two-level systems result from the breakdown of the RWA [82]. They are a signature of extreme-nonlinear dynamics and become appreciable when the Rabi frequency approaches the transition frequency. The effect of contributions beyond the RWA is already apparent in Fig. 7.4(a) where these non-RWA parts lead to small superimposed high-frequency oscillations in the exciton-population dynamics.

We have concentrated on the nonlinear THz response of many-body states where all electrons and holes are bound into $1s$ excitons. While it is experimentally possible to obtain exciton fractions $\Delta n_{1s,1s}/n_{2D} > 90\%$ after resonant optical excitation [25], often states with lower exciton fractions are relevant. As discussed in Section 5.2, these states consist of a mix of exciton populations and correlated electron-hole plasma. Like for the linear response, it is easy to verify that the influence of the correlated plasma is small for the low-density conditions. It is shown in Ref. [94] that the Rabi-splitting in the spectrum $|\Delta E_{\text{THz}}(\omega)|$ remains visible for exciton fractions well below 10%. In Ref. [94], it is also confirmed that the qualitative results do not depend on the dimensionality of the semiconductor system. The general features also appear for resonant strong-field THz excitation of a QW.

7.3. Ionization of an Exciton Population

In atom optics, the ionization of atoms with intense femtosecond pulses has been the subject of numerous investigations. For example, the kinetic energy of a photo-electron liberated from an atomic orbital via direct or multiphoton ionization can reveal important information about the electronic structure and other properties of the atom [95, 96]. For very strong excitation with few-cycle pulses, electrons are not only ionized but also strongly accelerated by the laser field leading to a new class of non-perturbative phenomena such as above-threshold ionization [97, 98] and high-harmonic generation [99, 100].

Incoherent excitons in semiconductor are expected to behave similarly under strong THz excitations. As two examples, I will investigate direct and below threshold THz ionization of a $1s$ -exciton population. Density and temperature are chosen as in the previous Section. Again, Eqs. (3.48)-(3.57) are solved in main-sum approximation to Eq. (3.54) and scattering contributions are treated phenomenologically as discussed in Appendix C.3.

7.3.1. Creation of Ballistic Wavepackets via Direct Ionization

In this Section, we investigate direct ionization of an incoherent $1s$ -exciton population with an intense THz pulse. The THz pulse, $A_{\text{THz}} = A_{\text{env}} \cos(2\pi\nu_{\text{THz}}t)$, has a Gaussian envelope $A_{\text{env}} = A_0 \exp(-(t/\tau)^2)$, a duration given by $\tau = 2$ ps, and frequency $\nu_{\text{THz}} = 2.6$ THz such that the photon energy $\hbar\omega_{\text{THz}} = 10.9$ meV is larger than the $1s$ exciton binding energy $E_B \approx 10.4$ meV [see Fig. 7.7(b)]. Furthermore, we choose a large electric field strength $E_0 \approx A_0\omega_{\text{THz}} = 13.1$ kV/cm. As in the previous Sections, we assume that off-diagonal correlations are damped with $\gamma = 0.42$ meV.

Figure 7.7(a) shows the dynamics of the bound exciton populations $\Delta N_{1s,1s}$ (solid line), $\Delta N_{2p,2p}$ (dashed line) and $\sum_{\lambda \neq 1s,2p} \Delta N_{\lambda,\lambda}$ (shaded area). We find that the $1s$ -population is almost completely transferred to higher states. The $2p$ state is populated transiently even though the $1s$ - $2p$ transition is off-resonant. For two times, indicated by vertical lines, we present snapshots of the exciton-correlations $|\Delta N_{\lambda,\nu}|$ as function of E_λ and E_ν in Figs. 7.7(c) and (d). We find that both diagonal and off-diagonal correlations involving continuum states build up during ionization. In particular, a cluster or “blob” of correlations emerges around the diagonal correlation $\Delta N_{\lambda_0,\lambda_0}$ with energy $E_{\lambda_0} \approx E_{1s} + \hbar\omega_{\text{THz}}$. In Fig. 7.7(e), the diagonal populations $\Delta N_{\lambda,\lambda}$ at the final time of the computation $t = 11$ ps are shown. We distinguish s -like (solid line) and p -like (shaded area) exciton states. Beside the main peak at $E_{1s} + \hbar\omega_{\text{THz}}$, the THz ionization leads to smaller peaks around the energies $E_{2p} + \hbar\omega_{\text{THz}}$ and $E_{1s} + 2\hbar\omega_{\text{THz}}$.

To investigate the origin of the peaks in the continuum, we perform a “switch-off” analysis in the numerical computation. We compare the full result to computations where certain correlations $\Delta N_{\alpha,\beta}$ – corresponding to continuous regions in the contour plots, Figs. 7.7(c),(d), – are projected out of c_X at each time step. As a result of this analysis, we can identify the ionization channels shown as dashed lines in Figs. 7.7(c) and (d). We find that the first peak in the final exciton distribution follows from single-photon ionization. Due to parity requirements, mostly p -like correlations are created. The peak with the highest energy around $E_{1s} + 2\hbar\omega_{\text{THz}}$ is generated via the direct, i.e., non-sequential absorption of two photons. In atom optics, the absorption of more photons than needed for ionization is known as Above-Threshold Ionization (ATI). The peak at $E_{2p} + \hbar\omega_{\text{THz}}$ is due to sequential ionization via the $2p$ exciton state even though the $1s$ -to- $2p$ transition is off-resonant. The non-resonant $1s$ -to- $2p$ transition is relevant due to the relatively large line-broadening given by γ and the large $1s$ - $2p$ transition matrix element. In this respect, the THz-induced exciton dynamics is decidedly different from atom optics where the transition linewidth is usually much narrower than the energetic separation between states.

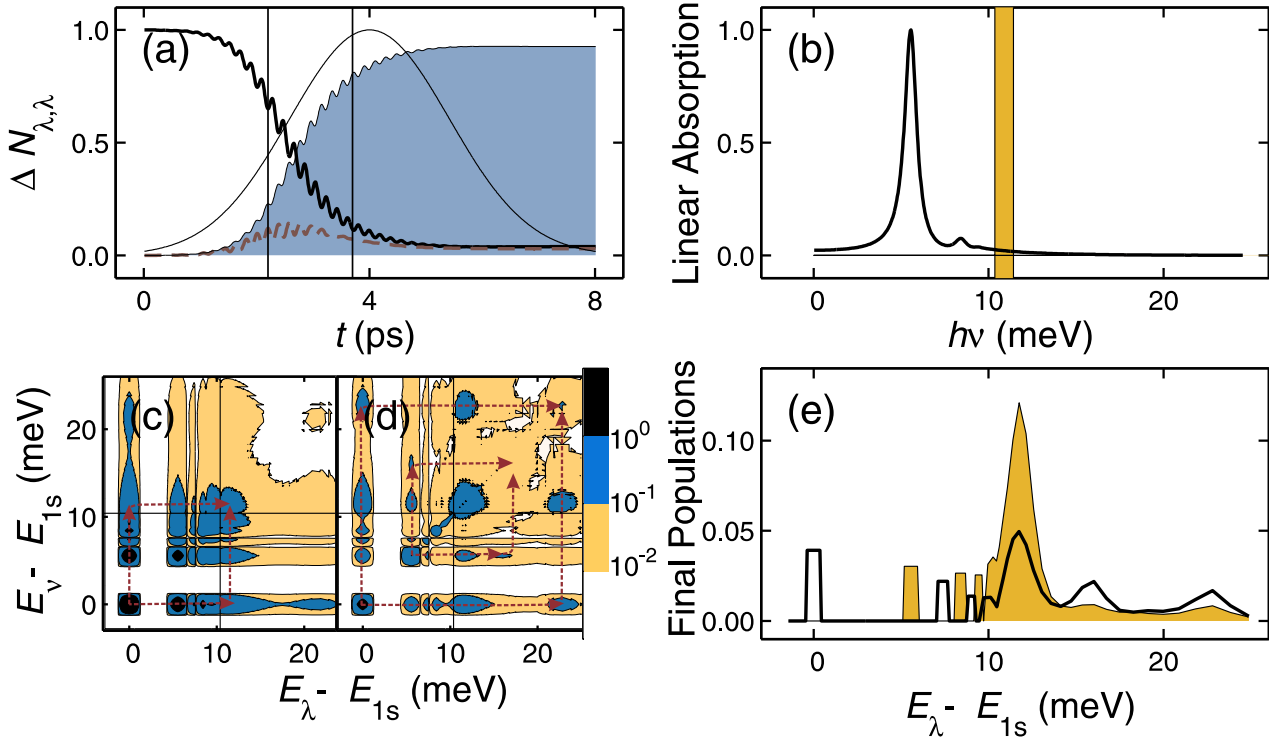


Figure 7.7.: Direct ionization of an exciton population. (a) The populations $\Delta N_{1s,1s}$ (solid line), $\Delta N_{2p,2p}$ (dashed line) and $\sum_{\lambda \neq 1s,2p} \Delta N_{\lambda,\lambda}$ (shaded area) normalized to the total number of electrons are shown for excitation with a Gaussian THz pulse (thin line) with $\nu_{\text{THz}} = 2.6$ THz and $E_0 = 13.1$ kV/cm. (b) shows the linear THz absorption (solid line) and the spectral extension of the THz pulse (shaded area). For the snapshot times indicated by vertical lines in (a), frames (c) and (d) show $|\Delta N_{\lambda,\nu}|$ as function of E_λ and E_ν . The dashed lines with arrows indicate ionization channels. Frame (e) shows the final diagonal exciton distribution $\Delta N_{\lambda,\lambda}$ as function of E_λ .

The contour plot, Fig. 7.8(a), shows the pair-correlation function, $\Delta g_{eh}(r, t)$, along the polarization direction of the THz field. Figure 7.8(b) shows $\Delta g_{eh}(r)$ for the snapshot times $t = 4$ ps (solid line) and $t = 5.5$ ps (shaded area). Initially, $\Delta g_{eh}(r, t)$ is proportional to $|\phi_{1s}^R(r)|^2$ corresponding to the presence of incoherent $1s$ -excitons. As the exciton is ionized, the probability to find an electron and hole close together is reduced. We find the intriguing result that electron and hole move apart with a constant velocity indicated by the dashed line in Fig. 7.8(a). Thus, the strong THz pulse creates a ballistic electron-hole wavepacket. The peak height decreases in time such that the wavepacket's lifetime is about 3 – 4 ps.

The wavepacket moves with a velocity $v_{\text{wp}} = \Delta r / \Delta t = 100$ nm/ps. It is directly related to the “blob” of correlations around $\Delta N_{\lambda_0, \lambda_0}$ with $E_{\lambda_0} \approx E_{1s} + \hbar\omega_{\text{THz}}$ since the kinetic energy of the wavepacket $E_{\text{wp}} = \mu v_{\text{wp}}^2 / 2 = 1.6$ meV matches the kinetic energy of the continuum state as E_{λ_0} is approximately 1.4 meV above the start of the

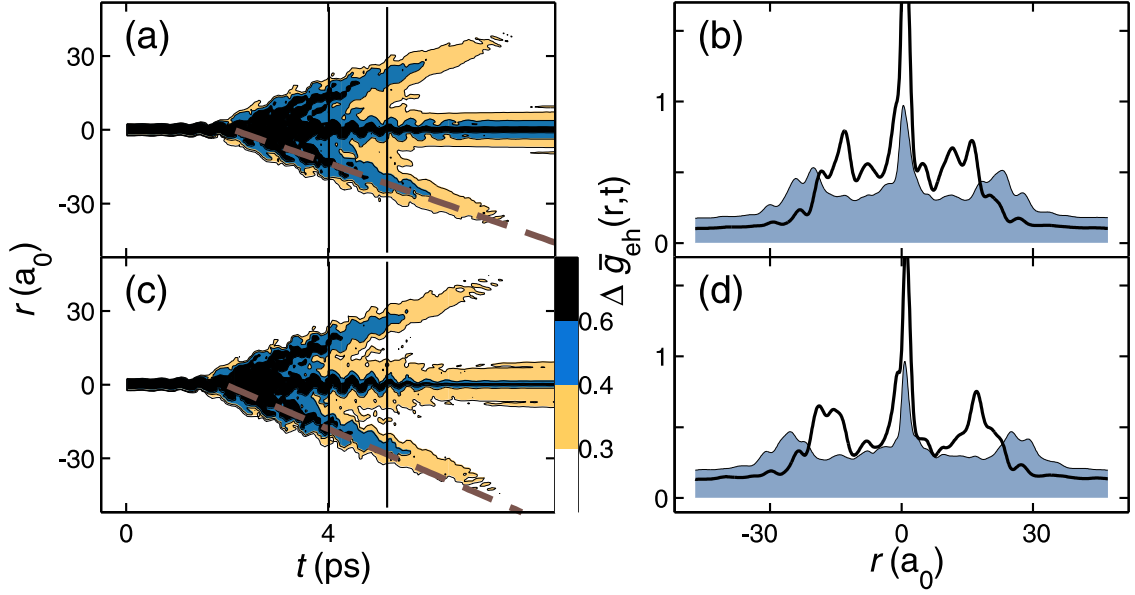


Figure 7.8.: Pair-correlation function during ionization. (a) and (c) show $\Delta g_{eh}(r, t)$ along the quantum-wire direction for THz frequencies $\nu_{THz} = 2.6$ THz and $\nu_{THz} = 3.0$ THz. In (b) and (d), cross-sections for $t = 4$ ps (solid line) and $t = 5.5$ ps (shaded area) are presented. The Gaussian wavepacket is highlighted by dashed lines in (a),(c).

continuum. Figures 7.8(c) and (d) show the pair-correlation function for THz frequency $\nu_{THz} = 3.0$ THz and peak field strength $E_0 = 22.6$ kV/cm. The velocity of the wavepacket $v_{wp} = 170$ nm/ps is larger since continuum correlations with higher energies are created by the strong THz pulse. We thus find that the properties of the wavepacket can be controlled via duration and frequency of the THz pulse.

To better understand the origin of the wavepacket, we give an approximate analytic expression for its dynamics. We assume that the continuum wavefunctions are given by plane waves $\phi_\lambda(\mathbf{r}_\parallel, t) = \exp(i\mathbf{k}_\lambda \cdot \mathbf{r}_\parallel - E_\lambda t/\hbar)/\sqrt{\mathcal{S}}$ characterized by the momentum \mathbf{k}_λ and the energy $E_\lambda = \hbar k_\lambda^2/(2\mu)$. Furthermore, we approximate the exciton correlations after ionization by

$$\Delta n_{\lambda,\nu} = n_0 e^{-(k_\lambda - k_0)^2/\Delta k^2} e^{-(k_\nu - k_0)^2/\Delta k^2} e^{-\gamma t/\hbar} \quad (7.27)$$

where $k_0 = \sqrt{2\mu E_{\lambda_0}}/\hbar$ is the momentum of the exciton state at the center of the “blob” and Δk the width of the distribution. The factor $e^{-\gamma t/\hbar}$ accounts for dephasing of correlations due to scattering. According to Eq. (D.12), the correlated part of the pair-correlation function along the QWI direction is then given by

$$\begin{aligned} \Delta g_{eh}(r, t) &\propto n_0 e^{-\gamma t/\hbar} \sum_{\lambda} e^{-(k_\lambda - k_0)^2/\Delta k^2} e^{-i(k_\lambda r - E_\lambda t/\hbar)} \\ &\times \sum_{\nu} e^{-(k_\nu - k_0)^2/\Delta k^2} e^{i(k_\nu r - E_\nu t/\hbar)}. \end{aligned} \quad (7.28)$$

Since the continuum states are continuous, the sums can be evaluated as integrals which leads to

$$\Delta g_{eh}(r, t) \propto \frac{1}{\sqrt{1 + \delta^2}} \exp \left\{ -\frac{(r - \frac{\hbar k_0}{\mu} t)^2}{2\Delta k^2(1 + \delta^2)} \right\} e^{-\gamma t/\hbar}, \quad \delta = \frac{\hbar t}{2\mu\Delta k^2}. \quad (7.29)$$

Equation (7.29) describes a wavepacket with group velocity $\hbar k_0/\mu$ and width $\Delta k^2(1 + \delta^2)$. The peak height of the wavepacket decreases in time since the wavepacket disperses and the correlations decay. For our parameters, the decay of the wavepacket is dominated by the correlation decay, $e^{-\gamma t/\hbar}$, such that there is no significant broadening of the wavepacket during its lifetime.

The wavepacket dynamics does not leave direct signatures in the differential THz transmission since its dynamics is connected to the final state after ionization rather than the created currents. It may be possible to detect the signatures of the wavepacket via photoluminescence experiments or with a second delayed THz probe.

7.3.2. High-Harmonic Generation

We next investigate strong-field excitation of a $1s$ -exciton population with a THz pulse $A(t) = A_0 \exp(-t^2/\tau^2) \cos(2\pi\nu_{\text{THz}}t)$ whose frequency $\nu_{\text{THz}} = 0.5$ THz is such that $\hbar\omega_{\text{THz}} = 2.1$ meV is below the ionization potential $E_B \approx 10.4$ meV. We choose a duration of $\tau = 2$ ps such that the pulse comprises only a few cycles. At the same time, we choose a relatively large intensity given by $E_0 = 2.6$ kV/cm.

Figure 7.9(a) shows the exciton-population dynamics. We find that the $1s$ -exciton population is completely ionized. The snapshots of the exciton correlations in Figs. 7.9 (c) and (d) reveal that the pulse creates correlations $\Delta N_{\lambda,\nu}$ involving exciton states λ, ν with energies up to 20 meV above the $1s$ energy. The final exciton distribution shown in Fig. 7.9(e) displays a series of ATI peaks separated by one photon energy. In atom-ionization experiments, such ATI peaks have been observed in the photo-electron spectrum for similar excitation conditions. In semiconductors, the final exciton distribution cannot directly be measured.

In Fig. 7.10(a), we plot the power spectrum $|\Delta E_{\text{THz}}|$ (shaded area) of the re-emitted field on a logarithmic scale. We find that high harmonics of the THz field are generated up to the 15th order. The magnitude of the signal decreases rapidly for the first few peaks, then reaches a plateau and decays abruptly after the last peak. In Fig. 7.10(b), we solve the THz response for the same conditions but increase the field strength to $E_0 = 3.77$ kV/cm. In this case, we find even higher harmonics up to the 23th order.

This particular form of high-harmonic generation (HHG) is well-known from atom optics. where intense femtosecond laser pulses are used to excite, e.g., noble gases [99, 100]. The strong light-matter interaction can lead to the generation of harmonics up to the 160th order [101]. The HHG from atoms can be used to generate coherent pulse trains of attosecond duration with frequencies in the x-ray region [99]. The generation mechanism of HHG can be explained to some degree by the semi-classical three step model introduced in Ref. [98] as follows: As the first step, the electron is ionized at

7. Exciton Populations in Strong Terahertz Fields

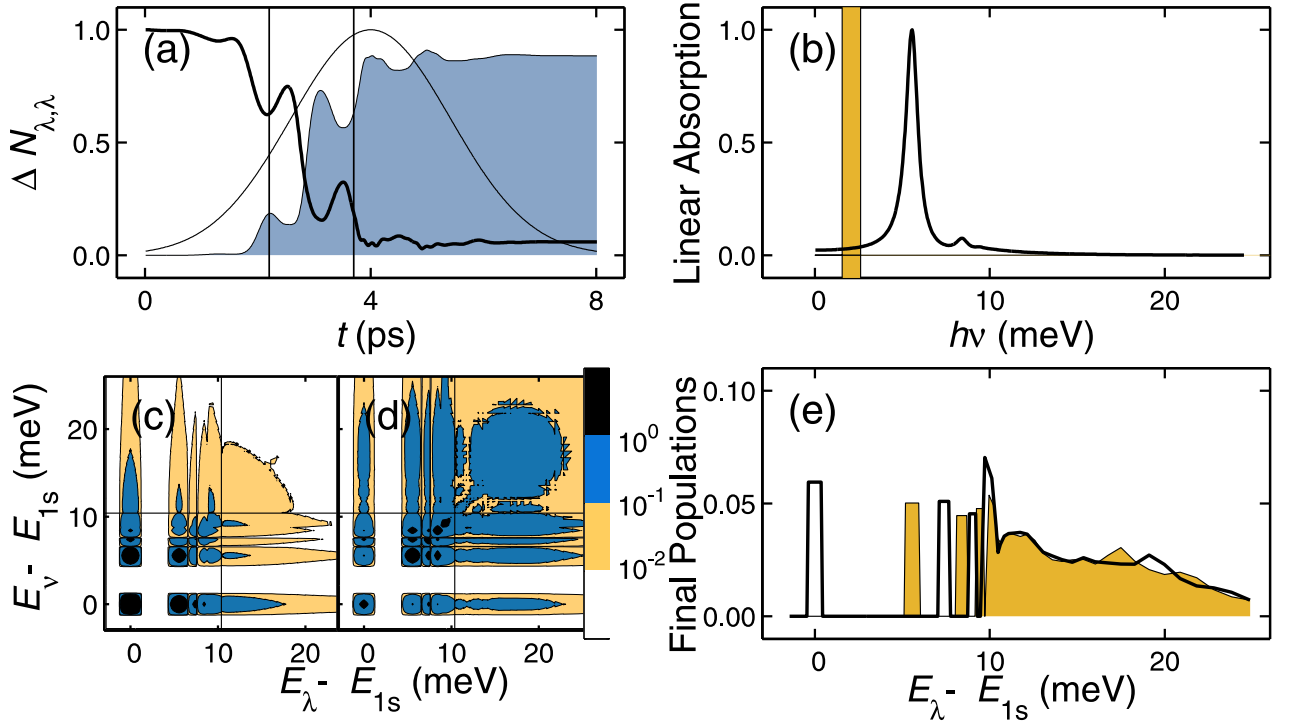


Figure 7.9.: Below Threshold Ionization of an Exciton Population. (a) The dynamics of $\Delta N_{1s,1s}$ (solid line) and $\sum_{\lambda \neq 1s, 2p} \Delta N_{\lambda,\lambda}$ (shaded area) are shown for excitation with a Gaussian THz pulse (thin line) with frequency $\nu_{\text{THz}} = 0.5$ THz, peak field strength $E_0 = 2.6$ kV/cm and $\phi = 0.25\pi$. (b) shows the linear THz absorption (solid line) and the spectral position of the THz pulse (shaded area). For two snapshot times indicated by vertical lines in (a), frames (c) and (d) show $|\Delta N_{\lambda,\nu}|$. In (e), the final diagonal exciton distribution $\Delta N_{\lambda,\lambda}$ is shown.

some instant in time. In the second step, the electron is accelerated by the laser electric field. For suitable conditions, the electron can return to the core where it was created (its birth place) having acquired a certain kinetic energy. In the third step, the electron can undergo scattering back to the ground state which leads to the quantum-mechanical emission of a photon. While this model cannot explain the details of the HHG, it predicts a cut off for the harmonics which depends on the maximum energy that the electron acquires during the acceleration by the laser field. According to the semi-classical model, the highest harmonics is given by

$$N_{\text{cutoff}} = \frac{E_B + 3.17E_P}{\hbar\omega_{\text{THz}}} \quad (7.30)$$

where E_B is the binding energy, E_P is the ponderomotive energy and $\hbar\omega_{\text{THz}}$ is the photon energy.

In Figs. 7.10(a) and (b), we find that the theoretical cutoff $\nu_{\text{cutoff}} = N_{\text{cutoff}}\nu_{\text{THz}}$ (vertical lines) quite accurately predicts the highest harmonics in our numerical simulation. We

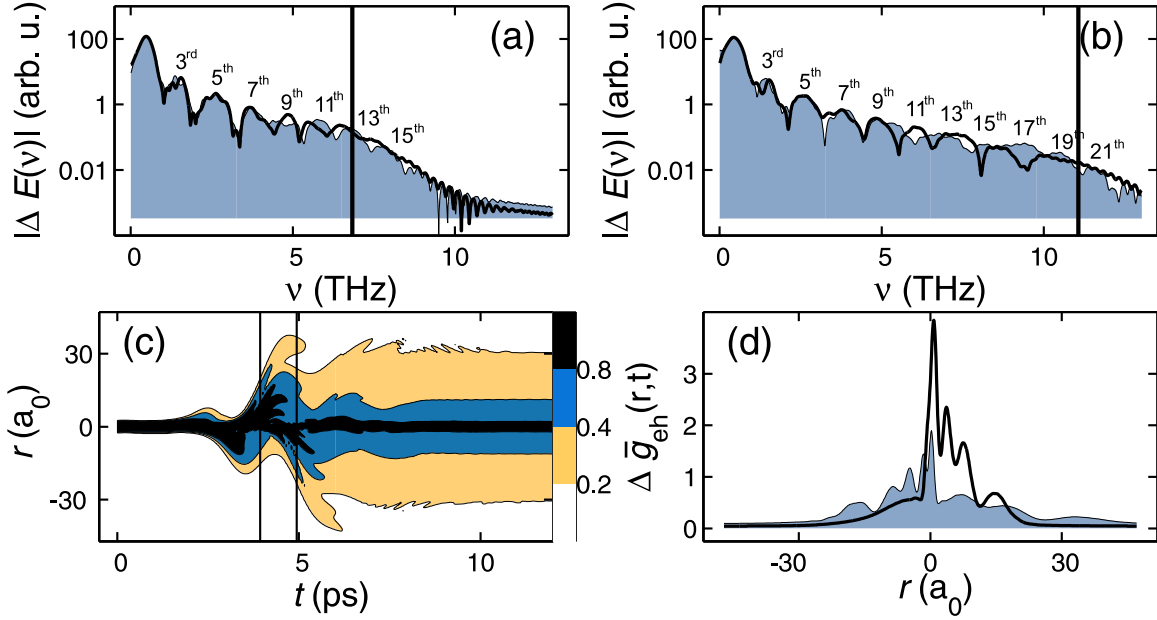


Figure 7.10.: High-Harmonic Generation. (a) The power spectrum of the re-emitted field $|\Delta E_{\text{THz}}|$ (shaded area) is presented on a logarithmic scale for the excitation shown in Fig. 7.9 with $E_0 = 2.6 \text{ kV/cm}$ and $\phi = 0.25\pi$. The solid line shows the result when the offset phase is changed to $\phi = 0.75\pi$. (b) shows the resulting $|\Delta E_{\text{THz}}|$ for $\phi = 0.25\pi$ (shaded area) and $\phi = 0.75\pi$ (solid line) when the field strength is increased to $E_0 = 3.77 \text{ kV/cm}$. (c),(d) The pair-correlation $\Delta g(r, t)$ and two snapshots at $t = 4.2 \text{ ps}$ (shaded area) and $t = 4.8 \text{ ps}$ (solid line) for the excitation in Fig. 7.9 are shown.

also find that the HHG spectrum looks different when the offset phase of the THz pulse is changed from $\phi = 0.25\pi$ (shaded area) to $\phi = 0.75\pi$ (solid line). While the highest harmonics are clearly resolved for $\phi = 0.25\pi$, they are washed out for $\phi = 0.75\pi$. The dependence on the carrier-envelope offset phase indicates that HHG is, in fact, an extreme nonlinear process [102, 103]. The extreme-nonlinear character of HHG is explained by the commensurability of ponderomotive energy and exciton binding energy. For our parameters, we indeed find the ratios $E_P/E_B = 0.50$ for $E_0 = 2.6 \text{ kV/cm}$ and $E_P/E_B = 1.0$ for $E_0 = 3.77 \text{ kV/cm}$.

The dynamics of the electron-hole pair-correlation function presented in Fig 7.10(c),(d) supports the semi-classical picture of the ionization process. We find that $\Delta g(r, t)$ “follows” the oscillations of the THz electric field in a classical sense. The electron-hole wavepacket is displaced by as much as $10a_0$.

We have demonstrated that HHG from THz-ionization of exciton populations can be detected in the re-emitted field. In atom optics, HHG not only provides a convenient X-ray source but it can also be used to reconstruct the actual quantum state of the electron before it is ionized as shown in Ref [104]. There, HHG spectra from N_2 were recorded in many different directions. Via a tomographic reconstruction algorithm, this data was

used to determine the wavefunction of the highest occupied molecular orbital. It would be interesting to investigate if HHG from THz ionization can be used to reconstruct the exciton wavefunction.

7.4. Coherent Control of 1s-Para Excitons in Cu₂O

In this Section, we use our microscopic theory to explain linear and nonlinear THz experiments on cuprous oxide (Cu₂O). The experiments were performed by R. Huber et al. in Berlin and Konstanz while the theoretical analysis was done in Marburg. Cuprous oxide is a direct-gap semiconductor with unusual properties. Due to an inversion symmetry of the lattice, the dipole-matrix element between the Γ_7^+ valence band and the Γ_6^+ conduction band vanishes. As a result, the linear optical absorption spectrum does not show the typical resonances of *s*-like exciton states. Instead, symmetry requires that only states with *p*-like symmetry appear in the optical absorption as shown theoretically in Ref. [49] and experimentally in Ref. [105]. The energies of the *p*-like excitons (so-called yellow exciton series) are accurately given by a Rydberg series $-\varepsilon_B/n^2$, $n = 2, 3, \dots$ with $\varepsilon_B = 98$ meV.

It is another special feature of Cu₂O that the 1*s*-exciton Bohr radius $a_0 \approx 7 \text{ \AA}$ is comparable to the lattice constant $a_L = 4.26 \text{ \AA}$. As a result, the 1*s*-exciton wavefunction in momentum-space extends into the region of the Brillouin zone where the bands are strongly non-parabolic. This leads to an anomalously large 1*s*-exciton binding energy of $E_{1s} = 153$ meV. Another effect of the small exciton radius is that spin-dependent exchange interactions are large such that the energies of the 1*s*-singlet state and the 1*s*-triplet state split by 12 meV (2.9 THz). The lower-lying singlet state, called 1*s*-para exciton, is non-degenerate and has a Γ_2^+ symmetry. The triplet state, called 1*s*-ortho exciton, is triply degenerate and has a Γ_5^+ symmetry. The so-called central-cell corrections which arise from the small Bohr radius are further discussed in Ref. [106]. The schematic bandstructure relevant for the investigations in this Section is shown in Fig. 7.11(c).

Using symmetry arguments, it can be shown [107] that interband recombination of ortho excitons is dipole forbidden while para states are optically dark to all multipole orders due to their spin of unity. This fact ensures long lifetimes on the μs scale and makes 1*s*-para excitons interesting for quasi-equilibrium BEC [108–110]. On the other hand, the same selection rules prohibit the direct observation and control of para states via optical interband transitions. Terahertz pulses have the obvious advantage that they directly couple to the internal excitations of quasiparticles, irrespective of interband dipoles. Studies of intraexcitonic absorption have provided novel insight into the formation dynamics, fine structure, density, and temperature of excitons in Cu₂O [17, 18, 111].

To apply our theory to bulk Cu₂O, we need to generalize the THz coupling to three-dimensional systems. It is straightforward to show that the singlet-doublet equations in the incoherent regime for bulk systems have the same format as Eqs. (3.48)-(3.57) for QW and QWI systems. For Cu₂O-bulk systems, we have to replace the two-dimensional wavevectors with three-dimensional wavevectors $\mathbf{k}_{\parallel} \rightarrow \mathbf{k}$ and use the three-dimensional

Coulomb-matrix element $V_{\mathbf{q}} = e^2/(\varepsilon_0\varepsilon_{\text{BG}}\mathcal{V}\mathbf{q}^2)$ where \mathcal{V} is the quantization volume, and $\varepsilon_{\text{BG}} = 7.5$ is the background dielectric constant of Cu₂O. The THz response follows from Maxwell's wave equation

$$\left[\nabla^2 - \frac{n_0^2}{c^2} \frac{\partial^2}{\partial t^2} \right] A_{\text{THz}} = -\mu_0 (J_{\text{THz}} + J_A) \quad (7.31)$$

with the THz current $J_{\text{THz}} = 1/\mathcal{V} \sum_{\lambda, \mathbf{k}} j_{\lambda}(\mathbf{k}) f_{\mathbf{k}}^{\lambda}$ and the ponderomotive current $J_A = -e^2/(\hbar^2\mathcal{V}) \sum_{\mathbf{k}, \lambda} (\partial^2 \varepsilon_{\mathbf{k}}^{\lambda} / \partial k_x^2) f_{\mathbf{k}}^{\lambda} A_{\text{THz}}$. For the thin samples studied here, propagation effects are negligible such that the re-emitted field ΔE is proportional to the total induced current $J_{\text{THz}} + J_A$ just as in the QW case.

Since we only consider the low-density regime where large fractions of exciton populations can exist, it is convenient to solve the linear and nonlinear current dynamics in the exciton basis. According to Eq. (D.4), the exciton energies and three-dimensional wavefunction are determined by the Wannier equation

$$(\tilde{\varepsilon}_{\mathbf{k}+\mathbf{q}^e}^e + \tilde{\varepsilon}_{\mathbf{k}-\mathbf{q}^h}^h) \phi_{\lambda; \mathbf{q}}^{\text{R}}(\mathbf{k}) - (1 - f_{\mathbf{k}+\mathbf{q}^e}^e - f_{\mathbf{k}-\mathbf{q}^h}^h) \sum_{\mathbf{k}'} V_{\mathbf{k}'-\mathbf{k}} \phi_{\lambda; \mathbf{q}}^{\text{R}}(\mathbf{k}') = E_{\lambda; \mathbf{q}} \phi_{\lambda; \mathbf{q}}^{\text{R}}(\mathbf{k}). \quad (7.32)$$

We solve Eq. (7.32) for a realistic band structure of Cu₂O [112] which includes the correct non-parabolicity of the valence bands. Thus, we obtain a realistic energy spectrum for the para-exciton series of Cu₂O; in particular, we find $E_{2p; \mathbf{0}}^{\text{para}} - E_{1s; \mathbf{0}}^{\text{para}} = 129$ meV which matches the value of the 1s-to-2p para-exciton transition in the experiment. To describe the ortho-exciton series we use the same exciton energies and wavefunction as for the para states but shift the 1s-energy by 12 meV such that $E_{2p; \mathbf{0}}^{\text{ortho}} - E_{1s; \mathbf{0}}^{\text{ortho}} = 116$ meV matches the 1s-to-2p ortho-exciton transition in the experiment. As discussed in Appendix D.1, the non-parabolicity of the bandstructure can lead to a strong center-of-mass (CM) dependence of exciton energies and wavefunctions. For Cu₂O, we find that the CM dependence of exciton energies is roughly parabolic

$$E_{\lambda, |\mathbf{q}|} = E_{\lambda, \mathbf{0}} + \frac{\hbar^2 |\mathbf{q}|^2}{2M_{\lambda}}. \quad (7.33)$$

We find the values $M_{1s} = 3.0m_0$ and $M_{2p} = 1.9m_0$ which are close to the literature values [106]. Thus, the 1s-to-2p transition energy is strongly \mathbf{q} -dependent [see also Fig. 7.11(c)]. The dipole-matrix element of the 1s-to-2p transition is found to be $d_{1s, 2p; \mathbf{0}} = 3.5e\text{\AA}$. In our numerical computations, we take into account all exciton levels with *s*, *p*, and *d*-like symmetry including the continuum states.

The sample used in the experiment is a naturally grown single crystal of Cu₂O (thickness: 264 μm) kept at a temperature of $T_{\text{L}} = 5$ K. To measure the time-resolved *linear* THz response, the experiment employs a low-noise Ti:sapphire amplifier for intense 12-fs pulses centered at a photon energy of 1.55 eV (repetition rate: 0.8 MHz). Part of the output creates unbound *e-h* pairs with a homogeneous density of $n_{e/h} = 2 \times 10^{16} \text{ cm}^{-3}$ via two-photon absorption. A second branch generates multi-THz pulses by optical rectification in GaSe. These transients are transmitted through the sample. Phase-matched electro-optic detection yields the temporal waveform of the probe field for selected delay

times Δt between the near-infrared pump and the THz probe. This two-dimensional scheme [13] affords simultaneous access to pump-induced changes of the absorption coefficient and the refractive index as a function of Δt as shown in Fig. 7.11(a),(b).

Starting with an almost Drude-like response of the photogenerated unbound e - h pairs, at $\Delta t = 100$ fs, the linear THz spectra change dramatically on a few-ps scale. After $\Delta t = 11$ ps, the hallmark $1s$ - $2p$ lines are evidence of a population of $1s$ -para and ortho states [17]. Both lines narrow and shift to lower frequencies during the first 100 ps, while the ratio of para versus ortho densities increases. Due to different effective masses of $1s$ and $2p$ states [Fig. 7.11(c)], the temperature T_{1s} of the ensemble is encoded in the THz line shape [17, 113]. We compare the experimental response for $\Delta t = 100$ ps to results from our microscopic theory. We find good agreement when we assume densities of $n_{1s}^{\text{para}} = 0.77 \times 10^{16} \text{ cm}^{-3}$ and $n_{1s}^{\text{ortho}} = 0.47 \times 10^{16} \text{ cm}^{-3}$ and a temperature of $T_{1s} = 10 \pm 4$ K [Fig. 7.11(a),(b)]. Note that the ponderomotive current J_A yields a real-valued Drude-like contribution $\chi_A(\omega) = -\omega_{\text{PL}}^2 \varepsilon_{\text{BG}} / \omega^2$ which gives rise only to a refractive index change; the absorption follows entirely from J_{THz} . We find that the measured refractive index change for $\Delta t = 100$ ps (shaded area with dots in Fig. 7.11(a)) is explained only by the full theory (solid line) in contrast to calculations without the ponderomotive contribution (dashed line).

As the next step, the experiment actively controls the internal quantum state of the dark quasiparticles via *nonlinear* THz excitations. Intense THz transients E_{THz} resonant with the $1s$ - $2p$ para transition (photon energy: 129 meV) are generated by optical rectification of 0.2 mJ pulses from a high-power Ti:sapphire amplifier (repetition rate: 1 kHz) [28]. Optimally shaped laser pulses from an acousto-optic modulator and tight focusing of the multi-THz beam to a diffraction limited spot of $35 \mu\text{m}$ (FWHM of the field) allow us to reach peak fields of $E_{\text{THz}}^{\text{peak}} = 0.5 \text{ MV/cm}$ [upper panel in Fig. 7.13(a)]. Due to the Gaussian TEM₀₀ profile of the THz beam, the excitation is spatially inhomogeneous such that excitons at different locations are exposed to different intensities.

The curves in the lower panel of Fig. 7.13(a) represent the response of $1s$ -para excitons to the incident waveform E_{THz} at six different peak fields $E_{\text{THz}}^{\text{peak}}$. All THz traces are recorded directly in the time domain by ultrabroadband electro-optic detection [114], resolving both amplitude and phase of the electric field. At low excitation intensity [curves (i) and (ii)], the re-emitted field reaches its maximum towards the end of the driving pulse E_{THz} and then decays with a finite dephasing time of 0.7 ps. For intermediate and high intensities of the driving field [curves (iii)-(vi)], the response is not a linearly increased version of the low-field case. Rather, the re-emitted field rises more rapidly, reaches its maximum before the peak of the pump transient, and decreases within the coherence window. Moreover, the maximum value of the amplitude saturates for increasing excitation density. This intensity-dependent response, in particular the temporal shift of the amplitude maximum from $t = 0.25$ ps [curve (i)] to $t = -0.25$ ps [curve (vi)], shows clearly that the THz field saturates the $1s$ - $2p$ transition inducing a coherent nonlinearity. Most remarkably, curves (v) and (vi) exhibit a structured envelope with a first maximum at $t = -0.25$ ps and a second less pronounced side peak at 0.25 ps (v) and 0.24 ps (vi), respectively. The onset of an oscillatory behavior indicates that the intense THz beam leads to nonlinear dynamics of dark exciton populations well

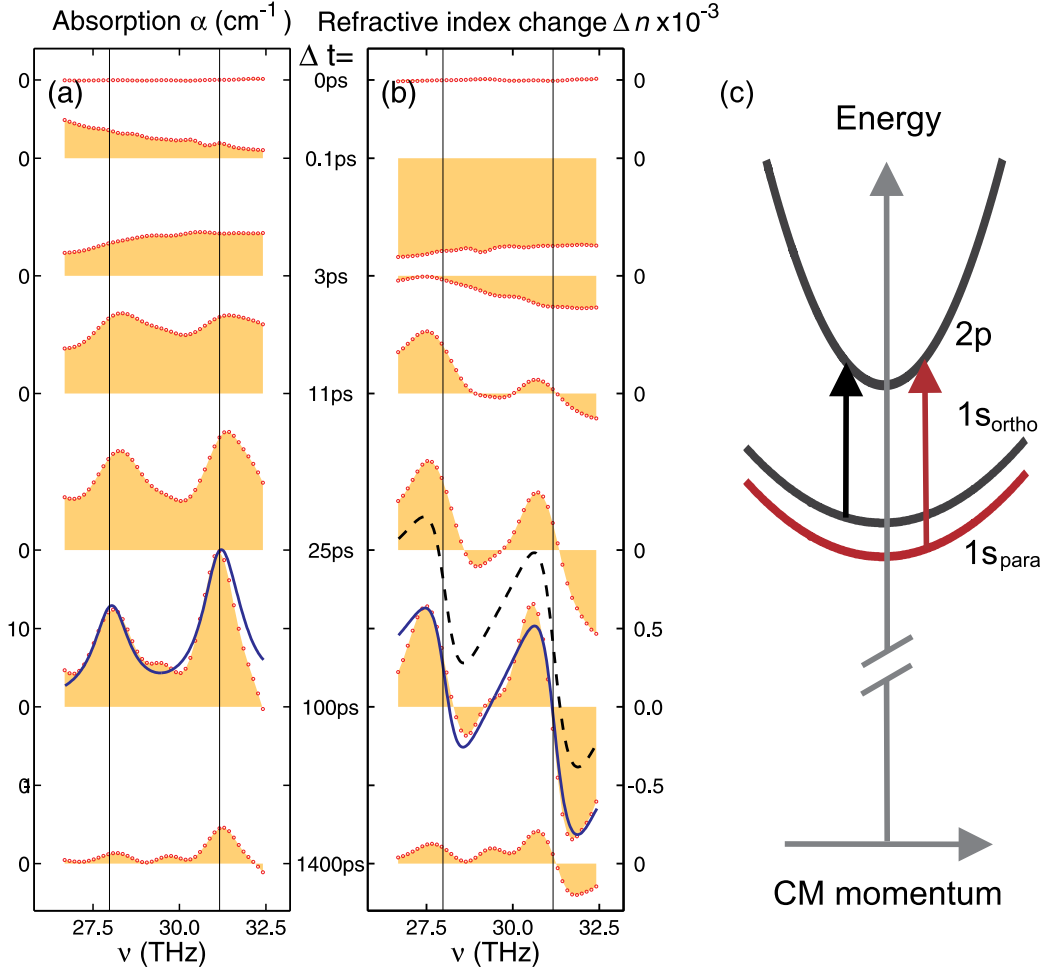


Figure 7.11.: Linear Response of Cu₂O. (a),(b) Formation and cooling dynamics of 1s excitons in Cu₂O probed by multi-THz spectroscopy: Pump-induced changes of absorption $\Delta\alpha$ and refractive index Δn (shaded area with dots) for various delay times Δt after two-photon absorption of 12-fs pulses centered at 1.55 eV. Vertical lines: 1s-2p resonances at vanishing center-of-mass momentum. Solid line: Theoretical result with $n_{1s}^{\text{para}} = 0.77 \times 10^{16} \text{cm}^{-3}$, $n_{1s}^{\text{ortho}} = 0.47 \times 10^{16} \text{cm}^{-3}$ and $T_{1s} = 10$ K. Dashed line: Theoretical Δn without ponderomotive contribution. (c) Due to different effective masses of 1s and 2p excitons, THz transitions (arrows) depend on the center-of-mass momentum. (from Paper [VIII])

beyond the perturbative regime.

To evaluate the nonlinear response in our theory, we solve the current dynamics using the exact temporal and spatial profile of the experimental excitation pulses. Since the experiment excites the 1s-2p para transition, we assume that initially all electron-hole pairs exist as 1s-para excitons. In the experiment, the size of the optical spot is larger than that of the THz spot. The intensity distribution of the THz spot has a Gaussian

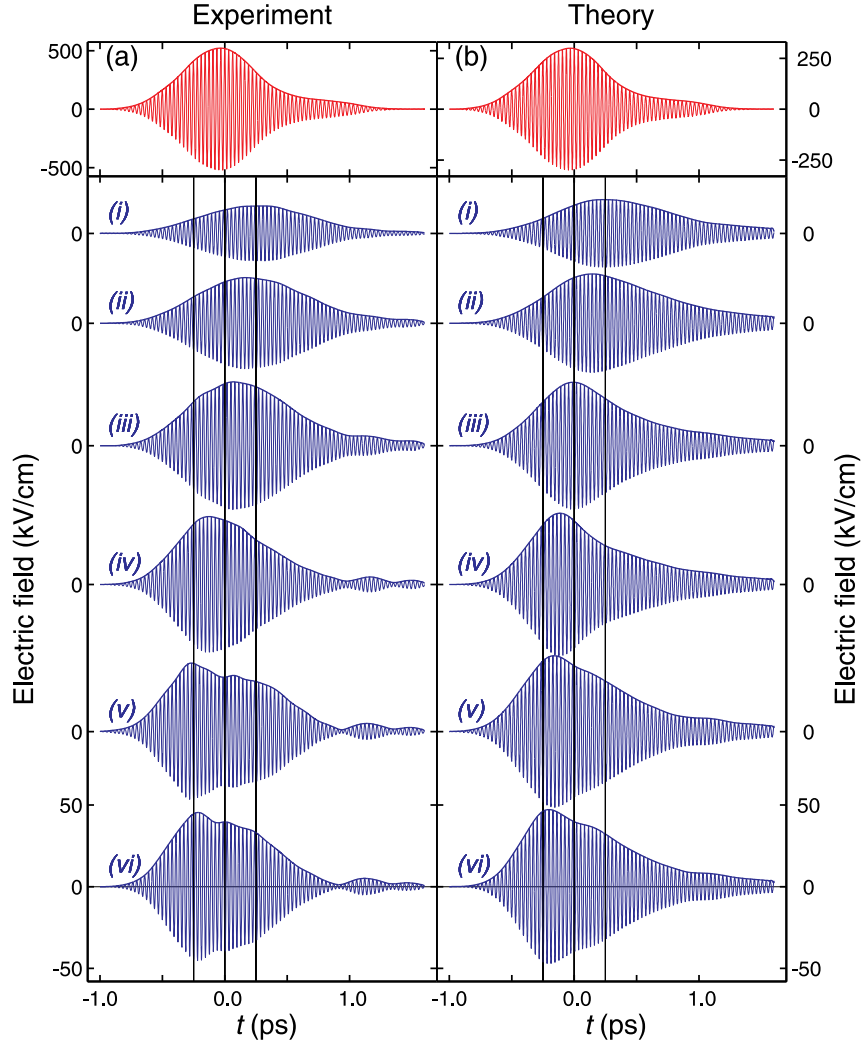


Figure 7.12.: Nonlinear THz response of 1s para excitons ($\Delta t = 1$ ns): quantitative comparison of (a) experiment and (b) microscopic theory. Upper panels: Real-time profile of the exciting THz pulse E_{THz} . Lower panels: Re-emitted THz field ΔE (vertically offset) for six values of the peak driving field, with $E_{\text{THz}}^{\text{peak}} = 0.13, 0.24, 0.45, 0.67, 0.92, 1.0 \times E_m$ for curves (i)-(vi), respectively ($E_m = 510$ kV/cm in experiment and $E_m = 300$ kV/cm in theory). (from Paper [VIII]).

TEM₀₀ profile such that the optically-excited exciton gas is excited with multiple THz intensities. The detector then measures an intensity-averaged signal. When πR_D^2 is the detection area, the averaged differential transmission is given by

$$\Delta E^{\text{avg}}(t) = \frac{\int d^2r \Delta E(r, t)}{\pi R_D^2} = \frac{2\pi}{\pi R_D^2} \int dr r \Delta E(r, t) = \frac{R^2}{R_D^2} \int_0^{I_m} \frac{dI}{I} \Delta E(I, t) \quad (7.34)$$

where $\Delta E(r, t)$ is the differential transmission at a distance r from the spot center and

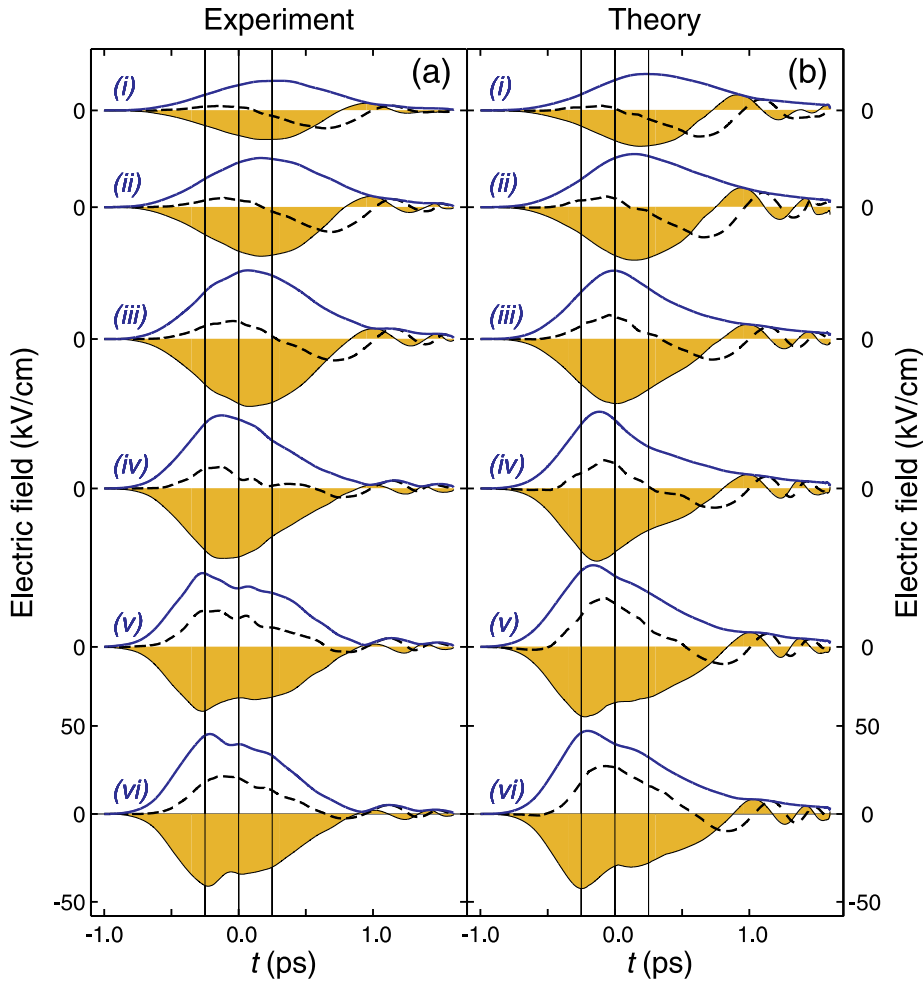


Figure 7.13.: Complex envelope of experimental (left column) and theoretical (right column) nonlinear transients. Real (dashed line), imaginary (shaded area) and absolute value (solid line) of $f(t)$ are shown where $f(t)$ is the complex envelope of the transients shown in Fig. 7.12.

$\Delta E(I, t)$ is the re-emitted field for fixed intensity. In Eq. (7.34), we used the substitution

$$I(r) = I_m e^{-\left(\frac{r}{R}\right)^2} \Rightarrow r = R \sqrt{\ln \left(\frac{I_m}{I} \right)} \quad (7.35)$$

where I_m is the maximum intensity and R the width of the Gaussian. In order to compare theory to experiment, we compute $\Delta E(I, t)$ for many different fixed intensities and then average according to Eq. (7.34). Note that the weight factor $g(I) \equiv 1/I$ becomes very large for small I .

The calculated re-emitted fields ΔE are shown in Fig. 7.12(b). We find that our microscopic theory reproduces all key signatures of Fig. 7.12(a), including the temporal shift and saturation of the maximum amplitude as well as the structured envelope for the two highest intensities. We already suspect that the small oscillations in the temporal

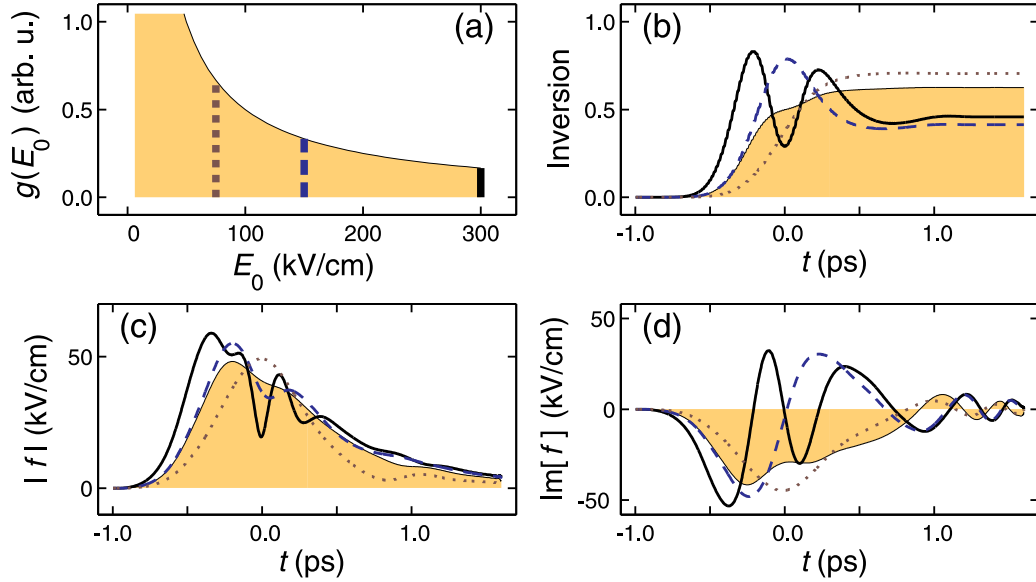


Figure 7.14.: Effect of spatial averaging. (a) The shaded area shows the weight function $g(I) \propto 1/I$ when the peak field strength at the spot center is $E_0 = 300$ kV/cm. For the three intensities, $E = 300$ kV/cm (solid line), $E_0 = 0.5 \times 300$ kV/cm (dashed line) and $E_0 = 0.25 \times 300$ kV/cm (dotted line), indicated by vertical lines in (a) inversion of the $1s$ - $2p$ system, $|f(t)|$ and $\text{Im}[f(t)]$ are shown in (b), (c) and (d), respectively. The averaged quantities are shown as the shaded area. (according to Paper [VIII])

envelope are related to Rabi oscillations of para-excitons in the $1s$ - $2p$ subsystem. To further analyze the THz transients, we compute the complex envelope $f(t)$ introduced in Section 7.2.2 for both experiment and theory. Since the experimental pulse is chirped, we have to use Eq. (7.25) to determine $f(t)$. According to Eq. (7.26), the complex envelope should directly identify any Rabi oscillations.

In Fig. 7.13, the resulting complex envelopes for experiment (left column) and theory (right column) are shown for the different excitation intensities [curves (i)-(vi)]. We show real (dashed line), imaginary part (shaded area) and absolute value (solid line) of the complex envelope. As for the original ΔE -transients, we find very good agreement between experiment and theory. In both cases, the imaginary part, $\text{Im}[f(t)]$, is negative for early times with a minimum shifting towards earlier times for increasing intensity. For the highest intensities, $\text{Im}[f(t)]$ shows additional modulation around the minimum and even a clear double-peak structure. Moreover, the peak minimum value saturates for increasing intensity. For late times, $t > 1.0$ ps, the imaginary part starts to oscillate around zero. The real part, $\text{Re}[f(t)]$, shows a different behavior: For early times, $\text{Re}[f(t)]$ is positive with a maximum roughly at the pulse maximum, i.e., at $t = 0$ ps. The maximum value at $t = 0$ ps increases almost linearly with the peak field strength $E_{\text{THz}}^{\text{peak}}$. For later times, the real part becomes negative and also starts to oscillate around zero for $t > 1.0$ ps

The behavior of the real part of the complex envelope, implies that a ponderomotive contribution is present: Since the ponderomotive part ΔE_A is proportional to the incoming THz vector potential, the real part, $\text{Re}[f(t)]$, contains a contribution proportional to the envelope $A_{\text{env}}(t)$ which is centered around $t = 0$ [see Eq. (7.26)]. This contribution is expected to grow linearly with the peak field strength of the incoming pulse. Since we see such a contribution in both experiment and theory, we conclude that the ponderomotive current is present.

The oscillations in real and imaginary part at late times $t > 1.0$ ps are not related to true Rabi-oscillations even though $\text{Im}[f(t)]$ exhibits zero-crossings. The origin of the oscillations is the chirp of the experimental pulse. While the pulse is on resonance for early times, it is strongly detuned from the 1s-to-2p transition for late times $t > 1.0$ ps. The large detuning implies that the renormalized Rabi-frequency $\tilde{\omega}_R = \sqrt{\omega_R^2 + (\Delta/\hbar)^2}$ is large even for low intensity which leads to the oscillations in $\text{Re}[f(t)]$ and $\text{Im}[f(t)]$. These detuned, trivial Rabi-oscillations do not correspond to significant oscillations in the inversion [see also Fig. 7.14(b)].

The fact that the minimum of $\text{Im}[f(t)]$ (as well as the maximum of $|f(t)|$) shifts toward earlier times for increasing intensities does imply that the THz pulse induces strong nonlinearities in the excitonic system. However, $\text{Im}[f(t)]$ does not directly cross zero after the first minimum as would be expected for Rabi-oscillations (see Section 7.2.2). Instead, we observe only residual oscillatory modulations in $\text{Im}[f(t)]$ for the largest intensities. The fact that the signatures of Rabi oscillations are washed out is related to the intensity averaging due to the inhomogeneous THz excitation.

It is intuitively clear that the spatial averaging suppresses the Rabi-flopping signatures: While the excitons at the center of the THz spot perform multiple Rabi-flops, the pulse area decreases continuously outside the center. Figure 7.14(a) shows the weight function $g(I)$ derived in Eq. (7.34). For the three intensities, $E_0 = 300$ kV/cm (solid line), $E_0 = 0.5 \times 300$ kV/cm (dashed line) and $E_0 = 0.25 \times 300$ kV/cm (dotted line), we show the inversion of the 1s-2p system, $|f(t)|$ and $\text{Im}[f(t)]$ in frames (b), (c) and (d), respectively. The averaged quantities are shown as shaded areas. For the highest intensity, i.e., at the pulse center, we observe more than two Rabi oscillations and for $E_0 = 0.5 \times 300$ kV/cm, we observe at least one Rabi flop. The averaging, however, obscures the Rabi-flopping signatures in the measured signal. Nevertheless, our theoretical analysis allows us to conclude that the experiment induces non-perturbative THz nonlinearities with approximately two Rabi cycles at the spot center.

7. *Exciton Populations in Strong Terahertz Fields*

8. Heating of a Correlated Electron-Hole Plasma

In this Chapter, I will investigate strong-field THz excitations of a correlated electron-hole plasma in the high-density regime. I will show that the THz field efficiently couples to the correlated plasma leading to a significant increase in temperature. It is well known that a non-interacting carrier plasma does not absorb light since momentum and energy cannot be simultaneously conserved for such a process. In order to absorb photons, carriers must additionally interact with other carriers, phonons or impurities. When the plasma absorption is modelled with a simple Drude model [39, 115], such scattering processes are usually described via a phenomenological damping constant. In contrast to these simple approaches, the many-body theory used here includes a consistent microscopic description of scattering processes.

The carrier heating affects the optical and electronic properties of a semiconductor. The change of the electron mobility due to the electron's higher average kinetic energy leads, e.g., to characteristic changes in the conductivity [116, 117]. In this investigation, the focus is not so much on experimental signatures of the carrier heating but rather on the exact microscopic heating mechanism. As in the last Chapter, I consider completely incoherent conditions where optical fields and interband coherences vanish. Numerical results are presented only for the QWI arrangement.

8.1. Kinetic Energy and Pair-Correlation Function

We investigate continuous-wave (cw) THz excitation of a correlated electron-hole plasma with temperature $T = 40$ K and a density $n = 5 \times 10^5 \text{ cm}^{-3}$ which is above the Mott density [8]. For these conditions, excitonic effects are negligible and in- and out-scattering of electrons and holes dominates the dynamics. To simplify the analysis, we can thus neglect the main-sum contributions as well as the D_X -contributions in Eq. (3.54) and take into account only the singlet-scattering source S_X . Moreover, we replace the triplet scattering T_X with a constant dephasing term $-i\gamma c_X$ where γ is assumed to be small.

8. Heating of a Correlated Electron-Hole Plasma

The simplified singlet-doublet equations, Eqs. (3.48)-(3.54), are then given by

$$\hbar \frac{\partial}{\partial t} f_{\mathbf{k}_{\parallel}}^e = -2\text{Im} \left[\sum_{\mathbf{k}'_{\parallel}, \mathbf{p}_{\parallel}} V_{\mathbf{p}_{\parallel}} c_{eh}^{\mathbf{p}_{\parallel}, \mathbf{k}'_{\parallel}, \mathbf{k}_{\parallel}} \right], \quad (8.1)$$

$$\hbar \frac{\partial}{\partial t} f_{\mathbf{k}_{\parallel}}^h = +2\text{Im} \left[\sum_{\mathbf{k}'_{\parallel}, \mathbf{p}_{\parallel}} V_{\mathbf{p}_{\parallel}} c_{eh}^{-\mathbf{p}_{\parallel}, \mathbf{k}_{\parallel}, \mathbf{k}'_{\parallel}} \right], \quad (8.2)$$

$$i\hbar \frac{\partial}{\partial t} c_{eh}^{\mathbf{p}_{\parallel}, \mathbf{k}'_{\parallel}, \mathbf{k}_{\parallel}} = \left[\Delta E_{eh}^{\mathbf{p}_{\parallel}, \mathbf{k}'_{\parallel}, \mathbf{k}_{\parallel}} - j(\mathbf{p}_{\parallel}) \langle A(t) \rangle_{\text{THz}} - i\gamma \right] c_{eh}^{\mathbf{p}_{\parallel}, \mathbf{k}'_{\parallel}, \mathbf{k}_{\parallel}} + S_{eh}^{\mathbf{p}_{\parallel}, \mathbf{k}'_{\parallel}, \mathbf{k}_{\parallel}}. \quad (8.3)$$

Here, we present the electron-hole correlations dynamics via the quantity $c_{eh}^{\mathbf{p}_{\parallel}, \mathbf{k}'_{\parallel}, \mathbf{k}_{\parallel}} = c_X^{\mathbf{k}_{\parallel} + \mathbf{p}_{\parallel} - \mathbf{k}'_{\parallel}, \mathbf{k}'_{\parallel}, \mathbf{k}_{\parallel}}$ which we already introduced at the end of Section 3.2. Similarly, we introduced $S_{eh}^{\mathbf{p}_{\parallel}, \mathbf{k}'_{\parallel}, \mathbf{k}_{\parallel}} = S_X^{\mathbf{k}_{\parallel} + \mathbf{p}_{\parallel} - \mathbf{k}'_{\parallel}, \mathbf{k}'_{\parallel}, \mathbf{k}_{\parallel}}$ and $\Delta E_{eh}^{\mathbf{p}_{\parallel}, \mathbf{k}'_{\parallel}, \mathbf{k}_{\parallel}} = \Delta E_X^{\mathbf{k}_{\parallel} + \mathbf{p}_{\parallel} - \mathbf{k}'_{\parallel}, \mathbf{k}'_{\parallel}, \mathbf{k}_{\parallel}}$. Equations (8.1)-(8.3) illustrate that any THz-induced change of the carrier distributions is mediated by electron-hole correlations. We assume that the initial carrier densities $f_{\mathbf{k}_{\parallel}}$ follow Fermi-Dirac distributions and that the initial electron-hole correlations are given by

$$c_{eh}^{\mathbf{p}_{\parallel}, \mathbf{k}'_{\parallel}, \mathbf{k}_{\parallel}} = - \frac{S_{eh}^{\mathbf{p}_{\parallel}, \mathbf{k}'_{\parallel}, \mathbf{k}_{\parallel}}}{\Delta E_{eh}^{\mathbf{p}_{\parallel}, \mathbf{k}'_{\parallel}, \mathbf{k}_{\parallel}} - i\gamma} \quad (8.4)$$

which is the steady state of Eq. (8.3) without THz contributions. We choose a THz pulse $\langle A \rangle_{\text{THz}} = A_0 \cos(\omega_{\text{THz}} t)$ with a constant envelope, frequency $\nu_{\text{THz}} = 2.6$ THz and field strength $E_0 = A_0 \omega_{\text{THz}} = 4.8$ kV/cm. In singlet-doublet approximation, the total energy of the many-body state is given by $E_{\text{tot}} = E_{\text{kin}} + E_C^S + E_C^D$ where

$$E_{\text{kin}} = \sum_{\mathbf{k}_{\parallel}} \left(\varepsilon_{\mathbf{k}_{\parallel}}^e f_{\mathbf{k}_{\parallel}}^e + \varepsilon_{\mathbf{k}_{\parallel}}^h f_{\mathbf{k}_{\parallel}}^h \right) \quad (8.5)$$

is the kinetic energy,

$$E_C^S = \frac{1}{2} \sum_{\mathbf{k}_{\parallel}, \mathbf{k}'_{\parallel} \neq \mathbf{k}_{\parallel}} V_{\mathbf{k}_{\parallel} - \mathbf{k}'_{\parallel}} \left(f_{\mathbf{k}_{\parallel}}^e f_{\mathbf{k}'_{\parallel}}^e + f_{\mathbf{k}_{\parallel}}^h f_{\mathbf{k}'_{\parallel}}^h \right) \quad (8.6)$$

is the singlet part of the Coulomb energy, and

$$E_C^D = - \sum_{\mathbf{k}'_{\parallel}, \mathbf{k}_{\parallel}, \mathbf{p}_{\parallel}} V_{\mathbf{p}_{\parallel}} c_{eh}^{\mathbf{p}_{\parallel}, \mathbf{k}'_{\parallel}, \mathbf{k}_{\parallel}} \quad (8.7)$$

is the correlated part of the electron-hole Coulomb energy. Figure 8.1(a) shows the change of E_{kin}/N (shaded area), E_C^D/N (solid line) and E_C^S/N , (dashed line) due to the THz excitation. We observe a linear increase of the kinetic energy per particle. Correspondingly, the carrier densities in Fig. 8.1(b) evolve to Fermi-Dirac distributions which

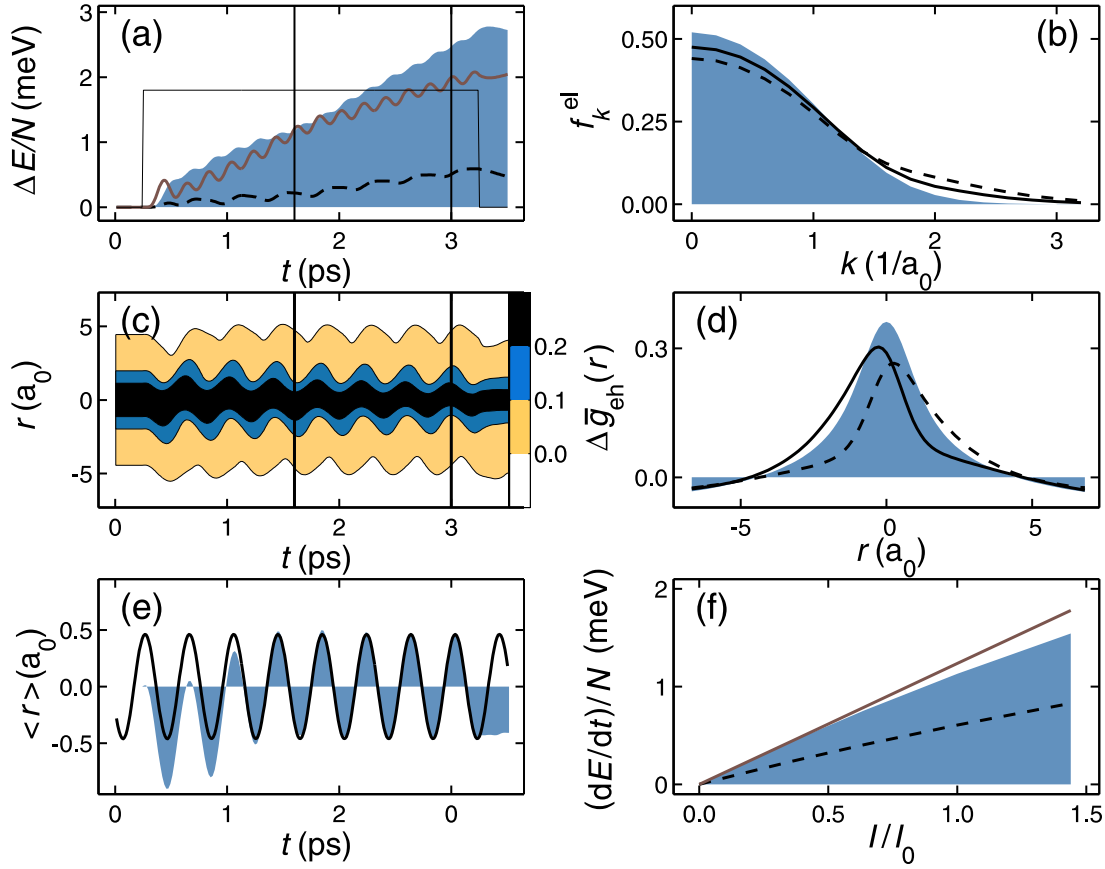


Figure 8.1.: Carrier Heating. (a) The change of energies E_{kin} (shaded area), E_C^D (solid line) and E_C^S , (dashed line) per particle are shown for cw THz excitation (thin line). (c) Correlated part of the electron-hole pair-correlation function. (b) and (d) show electron density and pair-correlation function, respectively, for $t = 0$ ps (shaded area), $t = 1.6$ ps (dashed line) and $t = 3.0$ ps (dashed line). (e) Mean displacement $\langle r \rangle$ of the electron hole pair (shaded area) and classical trajectory $x(t) = \frac{eA_0}{\mu\omega} \sin \omega t$ (solid line). (f) Kinetic energy flux $(\partial/\partial t)E_{\text{kin}}/N$ (dashed line) and total energy flux $(\partial/\partial t)E_{\text{tot}}/N$ (shaded area) directed to the carrier system as function of THz field strength. For comparison, the solid line shows the analytical solution which is presented in the next Section. (according to Paper [II])

extend to larger momenta. Thus, the THz excitation leads to a linear heating of the carriers in the semiconductor; the average energy changes roughly by 1.0 meV/ps. In reality, the coupling to phonons, which we neglected in our computation, saturates the heating leading to an elevated steady-state temperature. In Fig. 8.1(f), we find that the rates of change of kinetic energy $(\partial/\partial t)E_{\text{kin}}/N$ (dashed line) and total energy $(\partial/\partial t)E_{\text{tot}}/N$ (shaded area) per particle are roughly proportional to the intensity indicating that the heating corresponds to a THz-induced nonlinearity of the second order.

The interaction of THz field with correlated plasma is also reflected in the pair-

8. Heating of a Correlated Electron-Hole Plasma

correlation function

$$\Delta g_{eh}(\mathbf{r}_{\parallel}) = \frac{1}{\mathcal{S}^2} \sum_{\mathbf{p}_{\parallel}, \mathbf{k}'_{\parallel}, \mathbf{k}_{\parallel}} c_{eh}^{\mathbf{p}_{\parallel}, \mathbf{k}'_{\parallel}, \mathbf{k}_{\parallel}} e^{i\mathbf{p}_{\parallel} \cdot \mathbf{r}_{\parallel}} \quad (8.8)$$

which is presented in Figs. 8.1(c) and (d) along the QWI direction. Without THz field, $\Delta g_{eh}(r)$ (shaded area in (d)) peaks at $r = 0$. When the THz field is switched on, it induces large dipole oscillations in the correlated electron-hole plasma with the frequency of the THz pulse. Figure 8.1(e) shows that the mean displacement of the electron-hole pair given by $\langle r \rangle = \int r \Delta g(r) dr$ (shaded area) oscillates sinusoidally.

Classically, the trajectory $x(t)$ of a charged particle with reduced μ under the influence of a harmonic field is given by

$$\mu \ddot{x} - \kappa \dot{x} = -eE_0 \sin(\omega t). \quad (8.9)$$

The solution $x(t) = \frac{eA_0}{\mu\omega} \sin \omega t$ for $\kappa = 0$ is shown as a solid line in Fig. 8.1(e). We find that $x(t)$ almost matches the mean value of the pair-correlation function, $\langle r(t) \rangle$ suggesting that the mean displacement of the electron-hole wavepacket follows a classical trajectory.

8.2. Analytic Solution

In this Section, we give an approximate analytic solution of Eqs. (8.1)-(8.3) for continuous-wave THz excitation, $\langle A \rangle_{\text{THz}} = A_0 \cos(\omega_{\text{THz}} t)$. Combining Eqs. (8.1) and (8.5), we find that the rate of change of the kinetic energy, i.e., the energy-flux directed to the system is determined by the imaginary part of the electron-hole correlations

$$\frac{\partial}{\partial t} E_{\text{kin}} = \frac{2}{\hbar} \sum_{\mathbf{k}'_{\parallel}, \mathbf{k}_{\parallel}, \mathbf{p}_{\parallel}} \left(\varepsilon_{\mathbf{k}'_{\parallel}}^h - \varepsilon_{\mathbf{k}_{\parallel}}^e \right) V_{\mathbf{p}_{\parallel}} \text{Im} \left[c_{eh}^{\mathbf{p}_{\parallel}, \mathbf{k}'_{\parallel}, \mathbf{k}_{\parallel}} \right]. \quad (8.10)$$

Assuming that the carrier distributions are constant (Markov approximation), we can formally solve the correlation dynamics, Eq. (8.3), which yields

$$c_{eh}(t) = e^{-\frac{i}{\hbar}(\Delta E_{eh} - i\gamma)t} e^{\frac{i}{\hbar} \frac{jA_0}{\omega_{\text{THz}}} \sin \omega_{\text{THz}} t} \times \left\{ -\frac{S_{eh}}{\Delta E_{eh} - i\gamma} + \frac{S_{eh}}{i\hbar} \int_0^t e^{\frac{i}{\hbar}(\Delta E_{eh} - i\gamma)u} e^{-\frac{i}{\hbar} \frac{jA_0}{\omega_{\text{THz}}} \sin \omega_{\text{THz}} u} du \right\}. \quad (8.11)$$

Here, we adopted a schematic notation where the momentum dependence is suppressed. Since we expect the carrier heating to be a second-order nonlinearity, we expand the exponential function with respect to the peak THz vector potential A_0 yielding

$$e^{\pm \frac{i}{\hbar} \frac{jA_0}{\omega_{\text{THz}}} \sin \omega_{\text{THz}} t} = 1 \pm \frac{i}{\hbar} \frac{jA_0}{\omega_{\text{THz}}} \sin \omega_{\text{THz}} t + \frac{1}{2} \left(\frac{i}{\hbar} \frac{jA_0}{\omega_{\text{THz}}} \sin \omega_{\text{THz}} t \right)^2 \pm \mathcal{O}(A_0^3). \quad (8.12)$$

Inserting the expansion (8.12) into Eq. (8.11), we can easily determine the perturbative solution $c_{eh} = c_{eh}^{(0)} + c_{eh}^{(1)} + c_{eh}^{(2)} + \dots$ where $c_{eh}^{(0)}$ is independent of the THz field, $c_{eh}^{(1)}$ is the first-order contribution, and $c_{eh}^{(2)}$ is the second-order contribution. We explicitly find

$$c_{eh}^{(0)}(t) = -\frac{S_{eh}}{\Delta E_{eh} - i\gamma} \quad (8.13)$$

for the zeroth-order and

$$\begin{aligned} c_{eh}^{(1,a)}(t) &= -i \frac{jA_0}{\hbar\omega_{\text{THz}}} \sin \omega_{\text{THz}} t \frac{S_{eh}}{\Delta E_{eh} - i\gamma}, \\ c_{eh}^{(1,b)}(t) &= \frac{S_{eh}}{2} \frac{jA_0}{\hbar\omega_{\text{THz}}} \left[\frac{e^{i\omega_{\text{THz}}t} - e^{-\frac{i}{\hbar}(\Delta E_{eh} - i\gamma)t}}{\Delta E_{eh} + \hbar\omega_{\text{THz}} - i\gamma} - \frac{e^{-i\omega_{\text{THz}}t} - e^{-\frac{i}{\hbar}(\Delta E_{eh} - i\gamma)t}}{\Delta E_{eh} - \hbar\omega_{\text{THz}} - i\gamma} \right] \end{aligned} \quad (8.14)$$

for the first-order contributions. The second-order contributions are given by

$$\begin{aligned} c_{eh}^{(2,a)}(t) &= \frac{1}{2} \left(\frac{jA_0}{\hbar\omega_{\text{THz}}} \right)^2 \sin^2 \omega_{\text{THz}} t \frac{S_{eh}}{\Delta E_{eh} - i\gamma}, \\ c_{eh}^{(2,b)}(t) &= \frac{iS_{eh}}{2} \left(\frac{jA_0}{\hbar\omega_{\text{THz}}} \right)^2 \sin \omega_{\text{THz}} t \left[\frac{e^{i\omega_{\text{THz}}t} - e^{-\frac{i}{\hbar}(\Delta E_{eh} - i\gamma)t}}{\Delta E_{eh} + \hbar\omega_{\text{THz}} - i\gamma} - \frac{e^{-i\omega_{\text{THz}}t} - e^{-\frac{i}{\hbar}(\Delta E_{eh} - i\gamma)t}}{\Delta E_{eh} - \hbar\omega_{\text{THz}} - i\gamma} \right], \\ c_{eh}^{(2,c)}(t) &= -\frac{S_{eh}}{8} \left(\frac{jA_0}{\hbar\omega_{\text{THz}}} \right)^2 \left[\frac{e^{2i\omega_{\text{THz}}t} - e^{-\frac{i}{\hbar}(\Delta E_{eh} - i\gamma)t}}{\Delta E_{eh} + 2\hbar\omega_{\text{THz}} - i\gamma} \right. \\ &\quad \left. - 2 \frac{1 - e^{-\frac{i}{\hbar}(\Delta E_{eh} - i\gamma)t}}{\Delta E_{eh} - i\gamma} - \frac{e^{-2i\omega_{\text{THz}}t} - e^{-\frac{i}{\hbar}(\Delta E_{eh} - i\gamma)t}}{\Delta E_{eh} - 2\hbar\omega_{\text{THz}} - i\gamma} \right]. \end{aligned} \quad (8.15)$$

Using Dirac's identity

$$\frac{1}{\Delta E_{eh} - i\gamma} = \mathcal{P} \frac{1}{\Delta E_{eh}} + i\pi \delta(\Delta E_{eh}) \quad (8.16)$$

with the principal value \mathcal{P} which holds for sufficiently small γ , it can easily be shown that – of all terms in Eqs. (8.13)-(8.15) – only the imaginary part of $c_{eh}^{(2,b)}$ contributes to the carrier heating, Eq. (8.10).

Inserting Eq. (8.15) into Eq. (8.10), we find that the rate of change of the kinetic energy per particle is given by

$$\begin{aligned} \frac{\partial}{\partial t} E_{\text{kin}} &= \frac{\pi}{\hbar} \sum_{\mathbf{k}_{\parallel}, \mathbf{k}'_{\parallel}, \mathbf{p}_{\parallel}} \left(\varepsilon_{\mathbf{k}_{\parallel}}^e - \varepsilon_{\mathbf{k}'_{\parallel}}^h \right) V_{\mathbf{p}_{\parallel}} S_{eh}^{\mathbf{p}_{\parallel}, \mathbf{k}'_{\parallel}, \mathbf{k}_{\parallel}} \sin^2(\omega_{\text{THz}} t) \left(\frac{j(\mathbf{p}_{\parallel}) A_0}{\hbar\omega_{\text{THz}}} \right)^2 \\ &\quad \times \left[\delta \left(\Delta E_{eh}^{\mathbf{p}_{\parallel}, \mathbf{k}'_{\parallel}, \mathbf{k}_{\parallel}} + \hbar\omega_{\text{THz}} \right) + \delta \left(\Delta E_{eh}^{\mathbf{p}_{\parallel}, \mathbf{k}'_{\parallel}, \mathbf{k}_{\parallel}} - \hbar\omega_{\text{THz}} \right) \right]. \end{aligned} \quad (8.17)$$

In Eq. (8.17) we have found a microscopic expression which describes the carrier heating in a compact form. We find that the heating is determined by the Coulomb interaction

V^2 between electrons and holes as well as the THz coupling strength $(jA_0)^2$. When the correlated plasma absorbs a THz photon, both electron and hole states change momentum and energy.

We evaluate Eq. (8.17) for the QWI system. The solid line in Fig. 8.1(f) shows the resulting heating rate – averaged over one THz cycle – as function of THz intensity. We find that the analytical solution matches the numerically computed $(\partial/\partial t)E_{\text{tot}}/N$ (shaded area) but is larger than the numerically computed $(\partial/\partial t)E_{\text{kin}}/N$ (dashed line). The analytic solution overestimates the change of the kinetic energy because it assumes that carrier densities remain practically constant (Markov approximation) which is not the case for substantial carrier heating.

The analytic solution, Eqs. (8.13)-(8.15), also explains the why the mean value of the electron-hole pair-correlation functions follows a classical trajectory. We verify numerically that the dominant contributions to $\Delta g_{eh}(r)$ are given by $c_{eh}^{(0)}(t)$, $c_{eh}^{(1,a)}(t)$ and $c_{eh}^{(2,a)}(t)$. Inserting these correlations into Eq. (8.8), we find

$$\begin{aligned}
 \Delta g_{eh}(r) &= \frac{1}{\mathcal{S}^2} \sum_{p,k',k} e^{ipr} \frac{-S_{eh}^{p,k',k}}{\Delta E_{eh}^{p,k',k} - i\gamma} \\
 &\times \left(1 + i \frac{j(p)A_0}{\hbar\omega_{\text{THz}}} \sin(\omega_{\text{THz}}t) - \frac{1}{2} \left[\frac{j(p)A_0}{\hbar\omega_{\text{THz}}} \sin(\omega_{\text{THz}}t) \right]^2 + \mathcal{O}(A_0^3) \right) \\
 &= \left(1 + \frac{eA_0}{\mu\omega_{\text{THz}}} \sin(\omega_{\text{THz}}t) \frac{\partial}{\partial r} + \frac{1}{2} \left[\frac{eA_0}{\mu\omega_{\text{THz}}} \sin(\omega_{\text{THz}}t) \right]^2 \frac{\partial^2}{\partial r^2} + \mathcal{O}(A_0^3) \right) \Delta g_{eh}^0(r) \\
 &= \left(e^{i \frac{eA_0}{\mu\omega_{\text{THz}}} \sin(\omega_{\text{THz}}t) \frac{\partial}{\partial r}} \right) \Delta g_{eh}^0(r) + \mathcal{O}(A_0^3) = \Delta g_{eh}^0 \left(r + \frac{eA_0}{\mu\omega} \sin \omega t \right) + \mathcal{O}(A_0^3)
 \end{aligned} \tag{8.18}$$

where Δg_{eh}^0 is the correlated part of the pair-correlation in the steady state, Eq. (8.4). Equation (8.18) explains the classical oscillatory motion in the relative electron-hole pair coordinate. Note that the oscillations in $\Delta g_{eh}(\mathbf{r}_{\parallel})$ are simple dipole oscillations which do not contain any energy. Thus, they are only indirectly related to the carrier heating.

8.3. Absorption of Terahertz Photons

The analytic solution of the correlation dynamics, Eqs. (8.13)-(8.15), allows us to better understand the heating mechanism. In particular, it is interesting to see how the coupling of the THz field to *two*-particle correlations affects the corresponding *single*-particle quantities. For this purpose, we define the generalized pair-correlation function

$$\begin{aligned}
 \Delta \tilde{g}(\mathbf{r}_{\parallel}, \mathbf{r}'_{\parallel}) &= \Delta \langle \psi_e^\dagger(\mathbf{r}_{\parallel}) \psi_e(\mathbf{r}'_{\parallel}) \psi_h^\dagger(\mathbf{0}) \psi_h(\mathbf{0}) \rangle \\
 &= \frac{1}{\mathcal{S}^2} \sum_{\mathbf{p}_{\parallel}, \mathbf{k}'_{\parallel}, \mathbf{k}_{\parallel}} e^{-i\mathbf{k}_{\parallel} \cdot \mathbf{r}_{\parallel} + i(\mathbf{k}_{\parallel} + \mathbf{p}_{\parallel}) \cdot \mathbf{r}'_{\parallel}} c_{eh}^{\mathbf{p}_{\parallel}, \mathbf{k}'_{\parallel}, \mathbf{k}_{\parallel}}
 \end{aligned} \tag{8.19}$$

which describes hole-assisted transition amplitudes between electronic states at different positions. The diagonal part, $\Delta \tilde{g}(\mathbf{r}_{\parallel}, \mathbf{r}_{\parallel})$, is identical to the electron pair-correlation

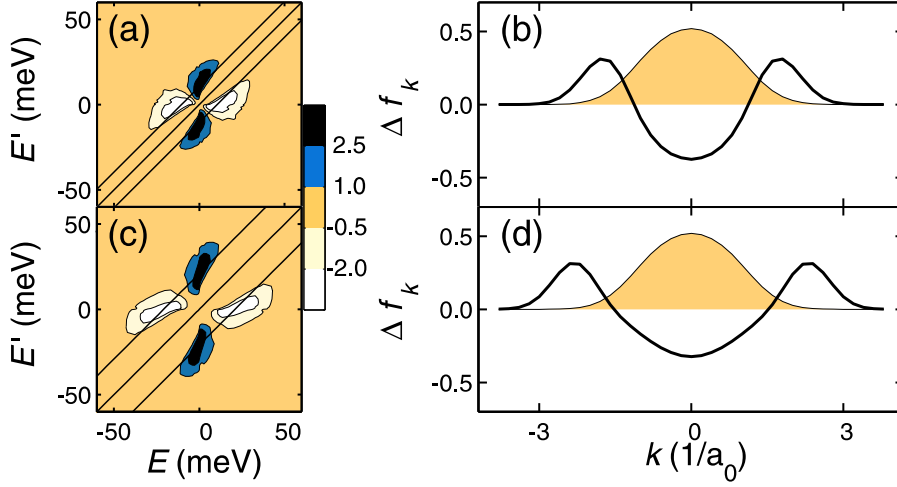


Figure 8.2.: Electronic transitions due to absorption of a THz photon. (a) and (c) show the transition amplitude $\text{Im}[\Delta\tilde{g}(E, E')]$ for $\hbar\omega_{\text{THz}} = 10.9\text{meV}$ and $\hbar\omega_{\text{THz}} = 21.8\text{meV}$, respectively. The diagonal lines are separated by one photon energy. (b) and (d) show the electron density (shaded area) and the magnified change of the electron density Δf_k^e (solid line) due to the scattering.

function $\Delta g_{eh}(\mathbf{r}_{\parallel})$. The Fourier transform

$$\Delta\tilde{g}(\mathbf{k}_{\parallel}, \mathbf{k}'_{\parallel}) = \int d\mathbf{r}_{\parallel} d\mathbf{r}'_{\parallel} e^{i\mathbf{k}_{\parallel}\cdot\mathbf{r}_{\parallel}} e^{-i\mathbf{k}'_{\parallel}\cdot\mathbf{r}'_{\parallel}} \Delta\tilde{g}(\mathbf{r}_{\parallel}, \mathbf{r}'_{\parallel}) = \sum_{\mathbf{q}_{\parallel}} c_{eh}^{\mathbf{k}'_{\parallel}-\mathbf{k}_{\parallel}, \mathbf{q}_{\parallel}, \mathbf{k}_{\parallel}}. \quad (8.20)$$

describes hole-assisted transitions of the electron in \mathbf{k} -space and visualizes how electrons acquire momentum when the electron-hole pair absorbs a photon in the scattering process. Inserting Eq. (8.20) into Eq. (8.1), we find that $\Delta\tilde{g}(\mathbf{k}_{\parallel}, \mathbf{k}'_{\parallel})$ determines the rate of change of the electron distribution via

$$\frac{\partial}{\partial t} f_{\mathbf{k}_{\parallel}}^e = -\frac{2}{\hbar} \sum_{\mathbf{k}'_{\parallel}} V_{\mathbf{k}_{\parallel}-\mathbf{k}'_{\parallel}} \text{Im}[\Delta\tilde{g}(\mathbf{k}_{\parallel}, \mathbf{k}'_{\parallel})]. \quad (8.21)$$

We next evaluate Eqs. (8.20) and (8.21) for the QWI system inserting only the contribution $c_{eh}^{(2,b)}(t)$, which is responsible for the carrier heating, into Eq. (8.20). Figure 8.2(a) shows the resulting $\text{Im}[\Delta\tilde{g}(k, k')]$ as function of energy, i.e., $\text{Im}[\Delta\tilde{g}(E, E')]$ where $E = \hbar k^2/(2\mu)$ for $k > 0$ and $E = -\hbar k^2/(2\mu)$ for $k < 0$ (analogous for E'). The diagonal lines are separated by the THz photon energy $\hbar\omega_{\text{THz}}$. We find that the electron makes a discrete transitions in momentum space which corresponds to the quantum-mechanical absorption of a THz photon. In Fig. 8.2(b), the electron distribution (shaded area) together with the quantity $\Delta f_k^e = -\frac{2}{\hbar} \sum_{k'} V_{k-k'} \text{Im}[\Delta\tilde{g}(k, k')]$ (solid line, scaled) are shown. We indeed find that the scattering leads to a symmetric change in the single-particle distribution as electrons are transferred into higher momentum states. When

8. Heating of a Correlated Electron-Hole Plasma

we double the THz photon energy from $\hbar\omega_{\text{THz}} = 10.9\text{meV}$ to $\hbar\omega_{\text{THz}} = 21.8\text{meV}$, the electronic transitions correspond to a larger change in the kinetic energy, as shown in Fig. 8.2(c) and (d).

In the simple Drude model, Eq. (8.9), the dissipated energy

$$\left\langle \frac{dE_{\text{diss}}}{dt} \right\rangle = \frac{1}{T} \int_0^T \frac{dE_{\text{diss}}}{dt} = \frac{(eE_0)^2 \kappa}{2\mu(\kappa^2 + \omega^2)} \quad (8.22)$$

is also proportional to the intensity. However, the heating mechanism is unspecified and entirely determined by a phenomenological damping constant κ . By contrast, our microscopic model gives a quantitative estimate for the electron heating and fully includes phase-space filling effects. We identify a two-step mechanism: In the first step, the two-particle correlations are driven by the THz field. In the second step, the correlation energy is irreversibly converted into kinetic energy via electron-hole scattering.

Recent Experiments in Paper [II] have demonstrated that the THz-induced carrier heating in a semiconductor-diode laser can be used to reliably detect the THz intensity. These experimental results are qualitatively explained by our microscopic theory.

9. Conclusion and Outlook

In this Thesis, I have presented a fully microscopic theory to describe THz interactions in optically-excited semiconductors. I have discussed the concept of linear and nonlinear THz spectroscopy with classical THz sources and evaluated the theory for experimentally relevant conditions.

In general, THz spectroscopy has become a widely used method to investigate inorganic, organic and biological systems since THz light is often resonant with elementary excitations of molecules and quasi-particles in solids. In semiconductors, THz excitations are especially interesting since they directly probe correlations by inducing many-body transitions. Whereas an interband excitation with visible or near-infrared light creates polarization, carriers and correlations in the semiconductor, the THz couples to the many-body state without changing the total number of excited carriers. Thus, THz spectroscopy accesses a completely new possibility to detect and control the many-body state in semiconductors. Terahertz spectroscopy is especially useful in conjunction with conventional optical techniques.

The theoretical approach presented here is based on a density-matrix theory which uses the cluster expansion approach for semiconductors. The scheme truncates the many-body hierarchy by factorizing higher-dimensional expectation values into lower-dimensional expectation values, the so-called clusters. Since the clusters have a clear physical and intuitive interpretation, the truncation can be controlled in a physically meaningful way. In particular, correlated quasi-particles such as bound electron-hole pairs, i.e., true excitons can be described consistently. I have derived the reduced set of equations which describes the THz dynamics in the coherent and incoherent regimes.

The linear THz response can be solved analytically for general conditions and leads to the *THz-Elliott formula* which demonstrates that weak THz pulses identify exciton population and plasmons. In contrast to THz spectroscopy, interband spectroscopy and photoluminescence experiments cannot unambiguously detect exciton populations.

To investigate nonlinear THz excitations, I have applied the theory to well-defined situations. In the first scenario, I have investigated the effect of strong THz excitations on the linear optical absorption spectra. Besides a purely theoretical analysis, I have presented a quantitative comparison to a recent experiment. Since the THz field couples optically-bright and optically-dark states, e.g., the $1s$ and $2p$ exciton states, the THz excitation leads to characteristic changes in the optical spectra. As a special feature of nonlinear THz excitations, the Rabi frequency is often close to the $1s$ -to- $2p$ transition frequency even for relatively low THz intensities such that extreme-nonlinear effects occur. I also identified ponderomotive contributions which arise since the THz field oscillates slowly enough such that electrons and holes follow the THz electric field in a classical sense.

9. Conclusion and Outlook

In the second scenario, I have investigated strong-field THz excitations of an existing $1s$ -exciton population. The THz dynamics of incoherent excitons is in many ways similar to atomic optics with coherent laser pulses. Mapping out different excitation regimes, I have identified Rabi-oscillations of exciton populations, the creation of ballistic electron-hole wavepackets and high-harmonic generation. Moreover, I showed that the theory is able to explain recent nonlinear THz experiments in Cu_2O which investigate Rabi oscillations between two optically-dark states. Besides the analogies, I have found notable differences to atomic systems which arise from the many-body scattering in semiconductors and the fermionic substructure of excitons. Even at low densities, these effects lead to much shorter dephasing times and to ponderomotive contributions in the THz response. I have discussed the ponderomotive contributions in detail and showed that they can usually be removed from the measurable signal.

As a third example, I have considered nonlinear THz excitation of a correlated electron-hole plasma where excitonic effects are negligible. Here, the THz coupling is shown to generate heating of the plasma. The cluster expansion approach allows for an intuitive and detailed understanding of the heating mechanism.

The investigations presented here focus on basic linear and nonlinear THz excitations of many-body states which are typical after optical excitation of a semiconductor. However, the microscopic theory could also be used to study the THz response of more exotic many-body states, e.g., of a quantum degenerate state seeded by interband excitation with completely incoherent light. Moreover one could allow for multiple THz pulses which excite the many-body state to investigate four-wave mixing configurations or explore the possibility of adiabatic exciton-population transfer. When the THz field is fully quantized, a new class of effects can be studied such as THz luminescence or quantum-optical effects in excitonic two-level systems. Here, it is particularly interesting to compare the quantum-optical effects in the THz regime and visible regime of the electromagnetic spectrum in order to investigate the effects of ponderomotive and extreme-nonlinear contributions. For further investigations of THz dynamics, it is advantageous to fully include microscopic scattering processes in order to eliminate the need for phenomenological constants.

A. $\mathbf{k} \cdot \mathbf{p}$ Theory

In this appendix, we use $\mathbf{k} \cdot \mathbf{p}$ -theory to discuss some qualitative aspects of the band-structure. The Bloch functions $\phi_{\lambda, \mathbf{k}}(\mathbf{r})$ are defined via Eq. (2.4). For a periodic lattice that extends into three dimensions, we can make the Ansatz

$$\phi_{\lambda, \mathbf{k}}(\mathbf{r}) = e^{i\mathbf{k} \cdot \mathbf{r}} w_{\lambda, \mathbf{k}}(\mathbf{r}) \quad (\text{A.1})$$

with a lattice-periodic function $w_{\lambda, \mathbf{k}}(\mathbf{r})$. The Ansatz leads to

$$\left[H_0 + \frac{\hbar}{m_0} \mathbf{k} \cdot \mathbf{p} \right] |\lambda, \mathbf{k}\rangle = \left[\varepsilon_{\mathbf{k}}^\lambda - \frac{\hbar^2 \mathbf{k}^2}{2m_0} \right] |\lambda, \mathbf{k}\rangle \quad (\text{A.2})$$

where, according to Dirac's notation, the real-space representation of $|\lambda, \mathbf{k}\rangle$ is given by $w_{\lambda, \mathbf{k}}(\mathbf{r}) = \langle \mathbf{r} | \lambda, \mathbf{k} \rangle$. Furthermore, we introduced $H_0 \equiv \mathbf{p}^2 / (2m_0) + U_L$. Assuming that the eigenvalue problem $H_0 |\lambda\rangle = \varepsilon_{\mathbf{0}}^\lambda |\lambda\rangle$ with $|\lambda\rangle \equiv |\lambda, \mathbf{0}\rangle$ is solved, we can treat the $\mathbf{k} \cdot \mathbf{p}$ -term as a perturbation. In second-order non-degenerate perturbation theory, we find for the wavefunctions in the vicinity of the Γ -point, i.e., around $\mathbf{k} = \mathbf{0}$,

$$|\lambda, \mathbf{k}\rangle = |\lambda\rangle + \frac{\hbar}{m_0} \sum_{\eta \neq \lambda} \frac{|\eta\rangle \mathbf{k} \cdot \langle \eta | \mathbf{p} | \lambda \rangle}{\varepsilon_{\mathbf{0}}^\lambda - \varepsilon_{\mathbf{0}}^\eta} \quad (\text{A.3})$$

and for the energies

$$\varepsilon_{\mathbf{k}}^\lambda = \varepsilon_{\mathbf{0}}^\lambda + \frac{\hbar^2 \mathbf{k}^2}{2m_0} + \frac{\hbar^2}{m_0^2} \sum_{\eta \neq \lambda} \frac{(\mathbf{k} \cdot \langle \lambda | \mathbf{p} | \eta \rangle)(\mathbf{k} \cdot \langle \eta | \mathbf{p} | \lambda \rangle)}{\varepsilon_{\mathbf{0}}^\lambda - \varepsilon_{\mathbf{0}}^\eta}. \quad (\text{A.4})$$

Here, we assumed that the wavefunctions have a well defined parity at the Γ -point such that $\langle \lambda | \mathbf{p} | \lambda \rangle = 0$. Applying the isotropic approximation

$$(\mathbf{k} \cdot \langle \lambda | \mathbf{p} | \eta \rangle)(\mathbf{k} \cdot \langle \eta | \mathbf{p} | \lambda \rangle) = \mathbf{k}^2 \langle \lambda | p | \eta \rangle \langle \eta | p | \lambda \rangle \quad (\text{A.5})$$

with $p = \mathbf{p} \cdot \mathbf{e}_x$, we find that the energies

$$\varepsilon_{\mathbf{k}}^\lambda = \varepsilon_{\mathbf{0}}^\lambda + \frac{\hbar^2 \mathbf{k}^2}{2m_\lambda} \quad (\text{A.6})$$

are characterized by an effective mass m_λ given by

$$\frac{1}{m_\lambda} = \frac{1}{m_0} + \frac{2}{m_0^2} \sum_{\eta \neq \lambda} \frac{\langle \lambda | p | \eta \rangle \langle \eta | p | \lambda \rangle}{\varepsilon_{\mathbf{0}}^\lambda - \varepsilon_{\mathbf{0}}^\eta}. \quad (\text{A.7})$$

A. $\mathbf{k} \cdot \mathbf{p}$ Theory

More generally, the $\mathbf{k} \cdot \mathbf{p}$ -perturbation theory can be applied around a finite \mathbf{k}_0 . Inserting $\mathbf{k} = \mathbf{k}_0 + \Delta\mathbf{k}$ into Eq. (A.2), we find

$$\begin{aligned} \left[H_0 + \frac{\hbar}{m_0} \mathbf{k}_0 \cdot \mathbf{p} + \frac{\hbar}{m_0} \Delta\mathbf{k} \cdot (\mathbf{p} + \hbar\mathbf{k}_0) + \frac{\hbar^2 \Delta\mathbf{k}^2}{2m_0} \right] |\lambda, \mathbf{k}_0 + \Delta\mathbf{k}\rangle \\ = \left[\varepsilon_{\mathbf{k}_0 + \Delta\mathbf{k}}^\lambda - \frac{\hbar^2 \mathbf{k}_0^2}{2m_0} \right] |\lambda, \mathbf{k}_0 + \Delta\mathbf{k}\rangle. \end{aligned} \quad (\text{A.8})$$

Second-order perturbation theory in $\Delta\mathbf{k}$ yields

$$|\lambda, \mathbf{k}_0 + \Delta\mathbf{k}\rangle = |\lambda, \mathbf{k}_0\rangle + \frac{\hbar}{m_0} \sum_{\eta \neq \lambda} \frac{|\eta, \mathbf{k}_0\rangle \Delta\mathbf{k} \cdot \langle \phi_{\eta, \mathbf{k}_0} | \mathbf{p} | \phi_{\lambda, \mathbf{k}_0} \rangle}{\varepsilon_{\mathbf{k}_0}^\lambda - \varepsilon_{\mathbf{k}_0}^\eta} \quad (\text{A.9})$$

and

$$\begin{aligned} \varepsilon_{\mathbf{k}_0 + \Delta\mathbf{k}}^\lambda = \varepsilon_{\mathbf{k}_0}^\lambda + \frac{\hbar}{m_0} \Delta\mathbf{k} \cdot \langle \phi_{\lambda, \mathbf{k}_0} | \mathbf{p} | \phi_{\lambda, \mathbf{k}_0} \rangle \\ + \frac{\hbar^2 \Delta\mathbf{k}^2}{2m_0} + \frac{\hbar^2}{m_0^2} \sum_{\eta \neq \lambda} \frac{\Delta\mathbf{k} \cdot \langle \phi_{\lambda, \mathbf{k}_0} | \mathbf{p} | \phi_{\eta, \mathbf{k}_0} \rangle \Delta\mathbf{k} \cdot \langle \phi_{\eta, \mathbf{k}_0} | \mathbf{p} | \phi_{\lambda, \mathbf{k}_0} \rangle}{\varepsilon_{\mathbf{k}_0}^\lambda - \varepsilon_{\mathbf{k}_0}^\eta} \end{aligned} \quad (\text{A.10})$$

with $\phi_{\lambda, \mathbf{k}_0}(\mathbf{r}) = \langle \mathbf{r} | \phi_{\lambda, \mathbf{k}_0} \rangle$. Here, we used that

$$\langle \lambda, \mathbf{k} | \mathbf{p} + \hbar\mathbf{k} | \lambda', \mathbf{k} \rangle = \langle \lambda, \mathbf{k} | e^{-i\mathbf{k} \cdot \mathbf{r}} \mathbf{p} e^{i\mathbf{k} \cdot \mathbf{r}} | \lambda', \mathbf{k} \rangle = \langle \phi_{\lambda, \mathbf{k}} | \mathbf{p} | \phi_{\lambda', \mathbf{k}} \rangle \equiv \mathbf{p}_{\lambda, \lambda'}(\mathbf{k}). \quad (\text{A.11})$$

With help of Eqs. (A.10) and (A.11), we find the relation

$$\langle \lambda, \mathbf{k} | \mathbf{p} + \hbar\mathbf{k} | \lambda', \mathbf{k} \rangle = \delta_{\lambda, \lambda'} \frac{m_0}{\hbar} \frac{\partial \varepsilon_{\mathbf{k}}^\lambda}{\partial \mathbf{k}} + (1 - \delta_{\lambda, \lambda'}) \mathbf{p}_{\lambda, \lambda'}(\mathbf{k}). \quad (\text{A.12})$$

Here, $\mathbf{p}_{\lambda, \lambda' \neq \lambda}(\mathbf{k}) = \langle \phi_{\lambda, \mathbf{k}} | \mathbf{p} | \phi_{\lambda', \mathbf{k}} \rangle = \langle \lambda, \mathbf{k} | \mathbf{p} | \lambda', \mathbf{k} \rangle$ is the interband momentum-matrix element. It can easily be shown [8] that it is related to the interband dipole-matrix element via

$$\mathbf{d}_{\lambda, \lambda'}(\mathbf{k}) \equiv \langle \lambda, \mathbf{k} | (-|e|\mathbf{r}) | \lambda', \mathbf{k} \rangle = \frac{i\hbar|e| \mathbf{p}_{\lambda, \lambda'}(\mathbf{k})}{m_0 \varepsilon_{\mathbf{k}}^\lambda - \varepsilon_{\mathbf{k}}^{\lambda'}} \quad (\text{A.13})$$

for $\lambda \neq \lambda'$. According to Eq. (A.10), the energies around a finite \mathbf{k}_0 are characterized by the generalized effective mass

$$\frac{1}{m_\lambda(\mathbf{k})} = \frac{1}{\hbar^2} \frac{\partial^2 \varepsilon_{\mathbf{k}}^\lambda}{\partial k_x^2} = \frac{1}{m_0} + \frac{2}{m_0^2} \sum_{\eta \neq \lambda} \frac{p_{\lambda, \eta}(\mathbf{k}) p_{\eta, \lambda}(\mathbf{k})}{\varepsilon_{\mathbf{k}}^\lambda - \varepsilon_{\mathbf{k}}^\eta}. \quad (\text{A.14})$$

where we have again used the isotropic approximation, Eq. (A.5), and defined $p_{\lambda, \lambda'}(\mathbf{k}) = \langle \lambda, \mathbf{k} | \mathbf{p} \cdot \mathbf{e}_x | \lambda', \mathbf{k} \rangle$. For a two-band system with one conduction band (c) and one valence band (v), we can introduce the effective electron, $m_e = m_c$, and hole, $m_h = -m_v$, masses and define the reduced electron-hole mass via

$$\frac{1}{\mu(\mathbf{k})} = \frac{1}{m_e(\mathbf{k})} + \frac{1}{m_h(\mathbf{k})} = \frac{4|p_{c,v}(\mathbf{k})|^2}{m_0^2(\varepsilon_{\mathbf{k}}^c - \varepsilon_{\mathbf{k}}^v)} \quad (\text{A.15})$$

The results presented in this Appendix are valid also for QW systems when the envelope-function approximation, Eq. (2.5), is used and \mathbf{k} is replaced by \mathbf{k}_\parallel .

B. Multiband Hamiltonian for Confined Systems

In this Appendix, we present the fully quantized interaction Hamiltonian, Eq. (2.34), for quantum-well (QW) and quantum-wire (QWI) systems.

B.1. Quantum-Well Confinement

In envelope-function approximation, the Bloch functions, Eq. (2.4), for the QW are given by $\phi_{\lambda,l,\mathbf{k}_{\parallel}}(\mathbf{r}) = \xi_{\lambda,l}(z)e^{i\mathbf{k}_{\parallel}\cdot\mathbf{r}_{\parallel}}w_{\lambda,l,\mathbf{k}_{\parallel}}(\mathbf{r})/\sqrt{\mathcal{S}}$ where \mathcal{S} is the quantization area, $w_{\lambda,l,\sigma,\mathbf{k}_{\parallel}}(\mathbf{r})$ is the lattice-periodic wavefunction and $\xi_{\lambda,l}(z)$ is the confinement function. Within the effective mass approximation, the confinement functions obey

$$\left[-\frac{\hbar^2}{2m_{\lambda}}\frac{\partial^2}{\partial z^2} + V_{\text{conf}}^{\lambda}(z)\right]\xi_{\lambda,l}(z) = \varepsilon_{\mathbf{0}}^{\lambda,l}\xi_{\lambda,l}(z). \quad (\text{B.1})$$

For a box-like confinement potential, $V_{\text{conf}}^{\lambda}$, with infinitely high walls, the eigenfunctions are given by

$$\xi_{\lambda,l}(z) = \begin{cases} \cos(l\frac{\pi}{L}z) & l = 1, 3, 5, \dots \\ \sin(l\frac{\pi}{L}z) & l = 2, 4, 6, \dots \end{cases} \quad (\text{B.2})$$

where L is the width of the box extending from $-L/2$ to $L/2$. The Hamiltonian, Eq. (2.37), reads

$$H_0 = \sum_{\lambda,l,\mathbf{k}_{\parallel}} \varepsilon_{\mathbf{k}_{\parallel}}^{\lambda,l} a_{\lambda,l,\mathbf{k}_{\parallel}}^{\dagger} a_{\lambda,l,\mathbf{k}_{\parallel}} + \sum_{\alpha,\mathbf{q}} \hbar\omega_{\mathbf{q}} \left(B_{\alpha,\mathbf{q}}^{\dagger} B_{\alpha,\mathbf{q}} + \frac{1}{2} \right) \quad (\text{B.3})$$

$$H_{A.p} = - \sum_{\lambda,l} \sum_{\mathbf{q}_{\parallel},\mathbf{k}_{\parallel}} \mathbf{j}_{\lambda,l}(\mathbf{k}_{\parallel}) \cdot \mathbf{A}_{\mathbf{q}_{\parallel}}(z_{\text{QW}}) a_{\lambda,l,\mathbf{k}_{\parallel}+\frac{\mathbf{q}_{\parallel}}{2}}^{\dagger} a_{\lambda,l,\mathbf{k}_{\parallel}-\frac{\mathbf{q}_{\parallel}}{2}} \quad (\text{B.4})$$

$$+ \sum_{\lambda \neq \lambda',l} \sum_{\mathbf{q}_{\parallel},\mathbf{k}_{\parallel}} \frac{|e|}{m_0} \mathbf{p}_{\lambda,\lambda'}^{l,l}(\mathbf{k}_{\parallel}) \cdot \mathbf{A}_{\mathbf{q}_{\parallel}}(z_{\text{QW}}) a_{\lambda,l,\mathbf{k}_{\parallel}+\frac{\mathbf{q}_{\parallel}}{2}}^{\dagger} a_{\lambda',l,\mathbf{k}_{\parallel}-\frac{\mathbf{q}_{\parallel}}{2}}$$

$$- \sum_{\lambda,l \neq l'} \sum_{\mathbf{q}_{\parallel},\mathbf{k}_{\parallel}} \mathbf{J}_{l,l'} \cdot \mathbf{A}_{\mathbf{q}_{\parallel}}(z_{\text{QW}}) a_{\lambda,l,\mathbf{k}_{\parallel}+\frac{\mathbf{q}_{\parallel}}{2}}^{\dagger} a_{\lambda,l',\mathbf{k}_{\parallel}-\frac{\mathbf{q}_{\parallel}}{2}}$$

$$H_{A.A} = \sum_{\lambda,l} \sum_{\mathbf{q}_{\parallel},\mathbf{q}'_{\parallel},\mathbf{k}_{\parallel}} \frac{|e|^2}{2m_0} \mathbf{A}_{\mathbf{q}_{\parallel}}(z_{\text{QW}}) \cdot \mathbf{A}_{-\mathbf{q}'_{\parallel}}(z_{\text{QW}}) a_{\lambda,l,\mathbf{k}_{\parallel}+\mathbf{q}_{\parallel}}^{\dagger} a_{\lambda,l,\mathbf{k}_{\parallel}+\mathbf{q}'_{\parallel}} \quad (\text{B.5})$$

$$H_C = (1/2) \sum_{\lambda,\lambda'} \sum_{l,l',l'',l'''} \sum_{\mathbf{k}_{\parallel},\mathbf{k}'_{\parallel},\mathbf{q}_{\parallel}} V_{l,l',l'',l'''}^{\lambda,\lambda'} |_{\mathbf{q}_{\parallel}} a_{\lambda,l,\mathbf{k}_{\parallel}+\mathbf{q}_{\parallel}}^{\dagger} a_{\lambda',l',\mathbf{k}'_{\parallel}-\mathbf{q}_{\parallel}}^{\dagger} a_{\lambda',l'',\mathbf{k}'_{\parallel}} a_{\lambda,l''',\mathbf{k}_{\parallel}}. \quad (\text{B.6})$$

B. Multiband Hamiltonian for Confined Systems

where we explicitly denoted the dependence on the subband index l . We assumed that each \mathbf{q}_{\parallel} -component of the vector potential is practically constant over the extension of the QW and that the confinement functions are independent of the bulk band index such that

$$\mathbf{A}_{\mathbf{q}_{\parallel}}^{\lambda,l,\lambda',l'} = \int dz \xi_{\lambda,l}^*(z) \mathbf{A}_{\mathbf{q}_{\parallel}}(z) \xi_{\lambda',l'}(z) \approx \delta_{l,l'} \mathbf{A}_{\mathbf{q}_{\parallel}}(z_{\text{QW}}). \quad (\text{B.7})$$

where $z_{\text{QW}} = 0$ is the center of the QW. Furthermore, we defined the intersubband matrix element via

$$\mathbf{J}_{l,l'} = \frac{i\hbar|e|}{m_0} \mathbf{e}_z \int dz \xi_{\lambda,l}^*(z) \frac{\partial}{\partial z} \xi_{\lambda',l'}(z). \quad (\text{B.8})$$

The Coulomb-matrix element is

$$V_{l,l',l'',l'''}^{\lambda,\lambda'} |_{\mathbf{q}_{\parallel}} = \frac{e^2}{4\pi\epsilon_0\epsilon_{\text{BG}}\mathcal{S}} \int dz dz' d\mathbf{r}_{\parallel} e^{-i\mathbf{q}_{\parallel}\cdot\mathbf{r}_{\parallel}} \frac{\xi_{\lambda,l}^*(z) \xi_{\lambda',l'}^*(z') \xi_{\lambda'',l''}(z') \xi_{\lambda''',l'''}(z)}{\sqrt{\mathbf{r}_{\parallel}^2 + (z-z')^2}}. \quad (\text{B.9})$$

When the \mathbf{r}_{\parallel} -intergration in Eq.(B.9) is evaluated, one finds

$$V_{l,l',l'',l'''}^{\lambda,\lambda'} |_{\mathbf{q}_{\parallel}} = \frac{e^2}{2\epsilon_0\epsilon_{\text{BG}}\mathcal{S}|\mathbf{q}_{\parallel}|} \int dz dz' e^{-|\mathbf{q}_{\parallel}(z-z')|} \xi_{\lambda,l}^*(z) \xi_{\lambda',l'}^*(z') \xi_{\lambda'',l''}(z') \xi_{\lambda''',l'''}(z). \quad (\text{B.10})$$

The explicit form of phonon contributions can be found in Ref. [6].

B.2. Quantum-Wire Confinement

The case of one-dimensional confinement can be treated analogously to the QW case. In envelope-function approximation [8], the Bloch functions are given by

$$\phi_{\lambda,l,k_{\parallel}}(\mathbf{r}) = \xi_{\lambda,l}(\mathbf{r}_{\perp}) \frac{e^{ik_{\parallel}r_{\parallel}}}{\sqrt{\mathcal{L}}} w_{\lambda,l,k_{\parallel}}(\mathbf{r}) \quad (\text{B.11})$$

where \mathcal{L} is the confinement length and l denotes the wire and confinement index. Here, the perpendicular coordinate $\mathbf{r}_{\perp} = (y, z)$ is two-dimensional while the parallel coordinate $r_{\parallel} = x$ is one-dimensional. Within effective mass approximation, the confinement functions are given by

$$\left[-\frac{\hbar^2}{2m_{\lambda}} \left(\frac{\partial^2}{\partial y^2} + \frac{\partial^2}{\partial z^2} \right) + V_{\text{conf}}^{\lambda}(y, z) \right] \xi_{\lambda,l}(y, z) = \varepsilon_{\mathbf{0}}^{\lambda,l} \xi_{\lambda,l}(y, z) \quad (\text{B.12})$$

where $V_{\text{conf}}^{\lambda}(y, z)$ is the two-dimensional confinement potential. For cylindrical wires with parabolic confinement, one finds [118] for the lowest confinement level

$$\xi_{\lambda,0}(\mathbf{r}_{\perp}) = \sqrt{\pi} R^2 e^{-\mathbf{r}_{\perp}^2/R^2} \quad (\text{B.13})$$

where R is the effective wire radius.

In QWI investigations, we always assume that the carriers are confined to the lowest confinement level. In the following, l denotes the wire-index in the planar arrangement of identical wires. The Hamiltonian, Eq. (2.37), then reads

$$H_0 = \sum_{\lambda,l,k_{\parallel}} \varepsilon_{k_{\parallel}}^{\lambda,l} a_{\lambda,l,k_{\parallel}}^{\dagger} a_{\lambda,l,k_{\parallel}} + \sum_{\alpha,\mathbf{q}} \hbar\omega_{\mathbf{q}} \left(B_{\alpha,\mathbf{q}}^{\dagger} B_{\alpha,\mathbf{q}} + \frac{1}{2} \right) \quad (\text{B.14})$$

$$H_{A\cdot p} = - \sum_{\lambda,l} \sum_{q_{\parallel},k_{\parallel}} \mathbf{j}_{\lambda}(k_{\parallel}) \cdot \mathbf{A}_{q_{\parallel}}(z_{\text{QW}}) a_{\lambda,l,k_{\parallel}+\frac{q_{\parallel}}{2}}^{\dagger} a_{\lambda,l,k_{\parallel}-\frac{q_{\parallel}}{2}} \quad (\text{B.15})$$

$$+ \sum_{\lambda \neq \lambda',l} \sum_{q_{\parallel},k_{\parallel}} \frac{|e|}{m_0} \mathbf{p}_{\lambda,\lambda'}(k_{\parallel}) \cdot \mathbf{A}_{q_{\parallel}}(z_{\text{QW}}) a_{\lambda,l,k_{\parallel}+\frac{q_{\parallel}}{2}}^{\dagger} a_{\lambda',l,k_{\parallel}-\frac{q_{\parallel}}{2}}$$

$$H_{A\cdot A} = \sum_{\lambda,l} \sum_{q_{\parallel},q'_{\parallel},k_{\parallel}} \frac{|e|^2}{2m_0} \mathbf{A}_{q_{\parallel}}(z_{\text{QW}}) \cdot \mathbf{A}_{-q'_{\parallel}}(z_{\text{QW}}) a_{\lambda,l,k_{\parallel}+q_{\parallel}}^{\dagger} a_{\lambda,l,k_{\parallel}+q'_{\parallel}} \quad (\text{B.16})$$

$$H_C = \frac{1}{2} \sum_{\lambda,\lambda',l} \sum_{k_{\parallel},k'_{\parallel},q_{\parallel}} V_{q_{\parallel}}^{\lambda,\lambda'} a_{\lambda,l,k_{\parallel}+q_{\parallel}}^{\dagger} a_{\lambda',l,k'_{\parallel}-q_{\parallel}}^{\dagger} a_{\lambda',l,k'_{\parallel}} a_{\lambda,l,k_{\parallel}} \quad (\text{B.17})$$

with the current-matrix element $\mathbf{j}_{\lambda}(k_{\parallel}) = -|e|/\hbar(\partial\varepsilon_{k_{\parallel}}/\partial k_{\parallel})\mathbf{e}_x$. Again, we assumed strong confinement such that the vector potential is practically constant over the lateral extension of the QWI array. The Coulomb-matrix element is given by

$$V_{q_{\parallel}}^{\lambda,\lambda'} = \frac{e^2}{4\pi\varepsilon_0\varepsilon_{\text{BG}}} \frac{1}{\mathcal{L}} \int d\mathbf{r}_{\perp} d\mathbf{r}'_{\perp} dr_{\parallel} e^{-iq_{\parallel}r_{\parallel}} \frac{|\xi_0(\mathbf{r}_{\perp})|^2 |\xi_0(\mathbf{r}'_{\perp})|^2}{\sqrt{r_{\parallel}^2 + (\mathbf{r}_{\perp} - \mathbf{r}'_{\perp})^2}}. \quad (\text{B.18})$$

When Eq. (B.18) is evaluated for the confinement function, Eq. (B.13), one finds [118] a simple form

$$V_{q_{\parallel}}^{\lambda,\lambda'} \approx \frac{1}{\mathcal{L}} \sqrt{\frac{2\pi}{|q_{\parallel}|R}} e^{-|q_{\parallel}|R} \quad (\text{B.19})$$

Again, the explicit form of phonon contributions can be found in Ref. [6]. We notice that the QWI Hamiltonian, Eq. (B.14) has the same format as Eq. (2.34) when we combine bulk-index λ and wire index l into one general index via $(\lambda, l) \rightarrow \lambda$. Thus, all further derivations based on Eq. (2.34) are also valid for the QWI case.

B. Multiband Hamiltonian for Confined Systems

C. Singlet-Doublet Dynamics of Carriers

C.1. Off-resonant Interband Transitions

In this Appendix, we discuss the interband transitions induced by the off-resonant THz field in Eqs. (3.34)-(3.36)

$$i\hbar \frac{\partial}{\partial t} P_{\mathbf{k}_{\parallel}} \Big|_{\text{off-res}} = - \left[1 - f_{\mathbf{k}_{\parallel}}^e - f_{\mathbf{k}_{\parallel}}^h \right] \left[- \frac{|e|}{m_0} p_{c,v}(\mathbf{k}_{\parallel}) \langle A(t) \rangle_{\text{THz}} + \sum_{\mathbf{k}'_{\parallel}} V_{\mathbf{k}_{\parallel}-\mathbf{k}'_{\parallel}} P_{\mathbf{k}'_{\parallel}} \right] \quad (\text{C.1})$$

$$\hbar \frac{\partial}{\partial t} f_{\mathbf{k}_{\parallel}}^e \Big|_{\text{off-res}} = 2\text{Im} \left[P_{\mathbf{k}_{\parallel}} \left(- \frac{|e|}{m_0} p_{c,v}^*(\mathbf{k}_{\parallel}) \langle A(t) \rangle_{\text{THz}} + \sum_{\mathbf{k}'_{\parallel}} V_{\mathbf{k}_{\parallel}-\mathbf{k}'_{\parallel}} P_{\mathbf{k}'_{\parallel}}^* \right) \right], \quad (\text{C.2})$$

$$\hbar \frac{\partial}{\partial t} f_{\mathbf{k}_{\parallel}}^h \Big|_{\text{off-res}} = 2\text{Im} \left[P_{\mathbf{k}_{\parallel}} \left(- \frac{|e|}{m_0} p_{c,v}^*(\mathbf{k}_{\parallel}) \langle A(t) \rangle_{\text{THz}} + \sum_{\mathbf{k}'_{\parallel}} V_{\mathbf{k}_{\parallel}-\mathbf{k}'_{\parallel}} P_{\mathbf{k}'_{\parallel}}^* \right) \right]. \quad (\text{C.3})$$

As we show in the following, these non-resonant terms must be included to describe (i) the correct low frequency response in the THz regime (ii) the correct modulation of the optical field by the THz field. To simplify the analysis, we consider a fictitious Hamiltonian

$$H = \sum_{\lambda, \mathbf{k}_{\parallel}} \varepsilon_{\mathbf{k}_{\parallel}}^{\lambda} a_{\lambda, \mathbf{k}_{\parallel}}^{\dagger} a_{\lambda, \mathbf{k}_{\parallel}} + \sum_{\mathbf{k}_{\parallel}} \sum_{\lambda \neq \lambda'} \frac{|e|}{m_0} p_{\lambda, \lambda'}(\mathbf{k}_{\parallel}) \langle A \rangle_{\text{THz}} a_{\lambda, \mathbf{k}_{\parallel}}^{\dagger} a_{\lambda', \mathbf{k}_{\parallel}} \quad (\text{C.4})$$

where only the off-resonant interband contributions of the THz interaction are included; the Coulomb interaction, the optical contributions, and the remaining THz contributions are ignored. Moreover, we limit the investigation to two bands.

The dynamics of the single-particle quantities is then given by

$$i\hbar \frac{\partial}{\partial t} P_{\mathbf{k}_{\parallel}} = \left(\varepsilon_{\mathbf{k}_{\parallel}} - i\gamma \right) P_{\mathbf{k}_{\parallel}} + \left(1 - f_{\mathbf{k}_{\parallel}}^e - f_{\mathbf{k}_{\parallel}}^h \right) \frac{|e|}{m_0} p_{c,v}(\mathbf{k}_{\parallel}) \langle A \rangle_{\text{THz}} \quad (\text{C.5})$$

$$\hbar \frac{\partial}{\partial t} f_{\mathbf{k}_{\parallel}}^{e/h} = -2\text{Im} \left[P_{\mathbf{k}_{\parallel}} \left(\frac{|e|}{m_0} p_{c,v}(\mathbf{k}_{\parallel}) \langle A \rangle_{\text{THz}} \right)^{\star} \right] \quad (\text{C.6})$$

where we introduced a phenomenological dephasing constant γ . The off-resonant terms contribute to the THz response at *low* frequencies and to the optical response at *high* frequencies. Thus, it is convenient to separate polarization and densities into

$$P_{\mathbf{k}_{\parallel}} = P_{\mathbf{k}_{\parallel}}^{\text{slow}} + P_{\mathbf{k}_{\parallel}}^{\text{fast}}, \quad f_{\mathbf{k}_{\parallel}} = f_{\mathbf{k}_{\parallel}}^{\text{st.}} + f_{\mathbf{k}_{\parallel}}^{\text{fast}} \quad (\text{C.7})$$

C. Singlet-Doublet Dynamics of Carriers

where P^{fast} and f^{fast} oscillate rapidly roughly with the bandgap frequency while P^{slow} oscillates on the timescale of the THz field and $f^{\text{st.}}$ is stationary. The total density $n_{2D} = \sum_{\mathbf{k}_{\parallel}, \lambda=\{e,h\}} f_{\mathbf{k}_{\parallel}}^{\lambda, \text{st.}}$ follows from the stationary part. Inserting Eq. (C.7) into Eq. (C.5), we find for the slowly varying polarization

$$i\hbar \frac{\partial}{\partial t} P_{\mathbf{k}_{\parallel}}^{\text{slow}} = \left(\varepsilon_{\mathbf{k}_{\parallel}} - i\gamma \right) P_{\mathbf{k}_{\parallel}}^{\text{slow}} + \left(1 - f_{\mathbf{k}_{\parallel}}^{e, \text{st.}} - f_{\mathbf{k}_{\parallel}}^{h, \text{st.}} \right) \frac{|e|}{m_0} p_{c,v}(\mathbf{k}_{\parallel}) \langle A \rangle_{\text{THz}} \quad (\text{C.8})$$

when non-resonant terms are neglected. The solution of Eq. (C.8) is obtained via Fourier transformation

$$P_{\mathbf{k}_{\parallel}}^{\text{slow}}(\omega) = \frac{\left[1 - f_{\mathbf{k}_{\parallel}}^{e, \text{st.}} - f_{\mathbf{k}_{\parallel}}^{h, \text{st.}} \right] \frac{|e|}{m_0} p_{c,v}(\mathbf{k}_{\parallel}) \langle A(\omega) \rangle_{\text{THz}}}{\varepsilon_{\mathbf{k}_{\parallel}}^v - \varepsilon_{\mathbf{k}_{\parallel}}^c + \hbar\omega + i\gamma}. \quad (\text{C.9})$$

In the THz regime, $\hbar\omega$ is very small compared to the band gap energy and can be neglected in the denominator (the same holds for $i\gamma$). Inserting Eq. (C.9) into Eq. (3.9), we obtain for the Fourier-transformed macroscopic interband polarization

$$[\partial_t P](\omega) = \frac{1}{\mathcal{S}} \sum_{\mathbf{k}_{\parallel}} \left[(1 - f_{\mathbf{k}_{\parallel}}^{e, \text{st.}} - f_{\mathbf{k}_{\parallel}}^{h, \text{st.}}) \frac{2|e|^2 |p_{c,v}(\mathbf{k}_{\parallel})|^2}{m_0^2 \varepsilon_{\mathbf{k}_{\parallel}}^c - \varepsilon_{\mathbf{k}_{\parallel}}^v} \langle A(\omega) \rangle_{\text{THz}} \right]. \quad (\text{C.10})$$

where we assumed $\langle A(\omega) \rangle_{\text{THz}}^* = \langle A(\omega) \rangle_{\text{THz}}$ without loss of generality. The joint contribution of $[\partial_t P]$ and the $\langle A \rangle$ -dependent intraband current J_{A, m_0} , Eq. (3.8), is then

$$\begin{aligned} J_A(\omega) &\equiv [\partial_t P](\omega) + J_{A, m_0}(\omega) = -\frac{|e|^2}{\mathcal{S}} \sum_{\mathbf{k}_{\parallel}} \left[f_{\mathbf{k}_{\parallel}}^{e, \text{st.}} \left(\frac{1}{m_0} + \frac{2}{m_0^2} \frac{|p_{c,v}(\mathbf{k}_{\parallel})|^2}{\varepsilon_{\mathbf{k}_{\parallel}}^c - \varepsilon_{\mathbf{k}_{\parallel}}^v} \right) \right. \\ &\quad \left. - (1 - f_{\mathbf{k}_{\parallel}}^{h, \text{st.}}) \left(-\frac{1}{m_0} + \frac{2}{m_0^2} \frac{|p_{c,v}(\mathbf{k}_{\parallel})|^2}{\varepsilon_{\mathbf{k}_{\parallel}}^c - \varepsilon_{\mathbf{k}_{\parallel}}^v} \right) \right] \langle A(\omega) \rangle_{\text{THz}} \\ &= -\frac{|e|^2}{\mathcal{S}} \sum_{\mathbf{k}_{\parallel}} \left(\frac{f_{\mathbf{k}_{\parallel}}^{e, \text{st.}}}{m_e(\mathbf{k}_{\parallel})} + \frac{f_{\mathbf{k}_{\parallel}}^{h, \text{st.}}}{m_h(\mathbf{k}_{\parallel})} \right) \langle A(\omega) \rangle_{\text{THz}} \end{aligned} \quad (\text{C.11})$$

Here, we identified the effective electron and hole masses (see App. A). Furthermore, we neglected the contribution from the full valence band $(1 - f_{\mathbf{k}_{\parallel}}^{h, \text{st.}}) \rightarrow -f_{\mathbf{k}_{\parallel}}^{h, \text{st.}}$ since

$$\sum_{\mathbf{k}_{\parallel}} \frac{1}{m_h(\mathbf{k}_{\parallel})} = -\frac{1}{\hbar^2} \sum_{\mathbf{k}_{\parallel}} \frac{\partial^2 \varepsilon_{\mathbf{k}_{\parallel}}^v}{\partial k_x^2} \propto \int_{\Omega_{\text{BR}}} d^2 \mathbf{k}_{\parallel} \frac{\partial^2 \varepsilon_{\mathbf{k}_{\parallel}}^v}{\partial k_x^2} \propto \oint_{\partial \Omega_{\text{BR}}} \frac{\partial \varepsilon_{\mathbf{k}_{\parallel}}^v}{\partial k_x} = 0 \quad (\text{C.12})$$

as the slope of the bandstructure usually vanishes at the edge of the Brillouin zone Ω_{BR} . The off-resonant terms also lead to changes of the interband polarization which oscillates with optical frequencies. The equations of motion for the rapidly varying microscopic polarization and densities read

$$i\hbar \frac{\partial}{\partial t} P_{\mathbf{k}_{\parallel}}^{\text{fast}} = \left(\varepsilon_{\mathbf{k}_{\parallel}} - i\gamma \right) P_{\mathbf{k}_{\parallel}}^{\text{fast}} - 2f_{\mathbf{k}_{\parallel}}^{\text{fast}} \left[\frac{|e|}{m_0} p_{c,v}(\mathbf{k}_{\parallel}) \langle A \rangle_{\text{THz}} \right] \quad (\text{C.13})$$

$$\hbar \frac{\partial}{\partial t} f_{\mathbf{k}_{\parallel}}^{\text{fast}} = -2\text{Im} \left[P_{\mathbf{k}_{\parallel}}^{\text{fast}} \left(\frac{|e|}{m_0} p_{c,v}(\mathbf{k}_{\parallel}) \langle A \rangle_{\text{THz}} \right)^* \right] \quad (\text{C.14})$$

where we again neglect non-resonant contributions and write $f_{\mathbf{k}_{\parallel}} \equiv f_{\mathbf{k}_{\parallel}}^{e/\hbar}$. The formal solution of the carrier dynamics, Eq. (C.14), is given by

$$f_{\mathbf{k}_{\parallel}}^{\text{fast}} = \frac{i}{\hbar} \frac{|e|}{m_0} \left[\int_{-\infty}^t du P_{\mathbf{k}_{\parallel}}^{\text{fast}}(u) (p_{c,v}(\mathbf{k}_{\parallel}) \langle A(u) \rangle_{\text{THz}})^* - \underbrace{[P_{\mathbf{k}_{\parallel}}^{\text{fast}}(u)]^* p_{c,v}(\mathbf{k}_{\parallel}) \langle A(u) \rangle_{\text{THz}}}_{\text{non-resonant}} \right] \quad (\text{C.15})$$

The second term in (C.15) represents a non-resonant contribution. We now express the polarization as $P_{\mathbf{k}_{\parallel}}^{\text{fast}}(t) = \tilde{P}_{\mathbf{k}_{\parallel}}(t) \exp(-i(\varepsilon_{\mathbf{k}_{\parallel}}^c - \varepsilon_{\mathbf{k}_{\parallel}}^v)t/\hbar)$ such that $\tilde{P}_{\mathbf{k}_{\parallel}}$ is slowly varying. Partial integration then yields

$$\begin{aligned} f_{\mathbf{k}_{\parallel}}^{\text{fast}} &= \frac{i}{\hbar} \frac{|e|}{m_0} \int_{-\infty}^t du P_{\mathbf{k}_{\parallel}}^{\text{fast}}(u) p_{c,v}^*(\mathbf{k}_{\parallel}) \langle A(u) \rangle_{\text{THz}} \quad (\text{C.16}) \\ &= -\frac{P_{\mathbf{k}_{\parallel}}^{\text{fast}}(t) \frac{|e|}{m_0} p_{c,v}^*(\mathbf{k}_{\parallel}) \langle A(t) \rangle_{\text{THz}}}{\varepsilon_{\mathbf{k}_{\parallel}}^c - \varepsilon_{\mathbf{k}_{\parallel}}^v} + \underbrace{\int_{-\infty}^t du \left(\frac{\partial[\tilde{P}_{\mathbf{k}_{\parallel}} \langle A \rangle_{\text{THz}}]}{\partial u} \frac{|e|}{m_0} p_{c,v}^*(\mathbf{k}_{\parallel}) \right) \frac{e^{-\frac{i}{\hbar}(\varepsilon_{\mathbf{k}_{\parallel}}^c - \varepsilon_{\mathbf{k}_{\parallel}}^v)u}}{\varepsilon_{\mathbf{k}_{\parallel}}^c - \varepsilon_{\mathbf{k}_{\parallel}}^v}}_{\text{small}} \\ &\approx -\frac{|e| p_{c,v}^*(\mathbf{k}_{\parallel}) \langle A(t) \rangle_{\text{THz}}}{m_0 (\varepsilon_{\mathbf{k}_{\parallel}}^c - \varepsilon_{\mathbf{k}_{\parallel}}^v)} P_{\mathbf{k}_{\parallel}}^{\text{fast}}(t) \end{aligned}$$

where the second term in the second line is small since the THz photon energy is negligible compared to the bandgap energy. As the final step, we insert Eq. (C.16) into Eq. (C.13) and obtain

$$i\hbar \frac{\partial}{\partial t} P_{\mathbf{k}_{\parallel}}^{\text{fast}}(t) = (\varepsilon_{\mathbf{k}_{\parallel}} - i\gamma) P_{\mathbf{k}_{\parallel}}^{\text{fast}}(t) + \left(\frac{e^2}{2\mu(\mathbf{k}_{\parallel})} \langle A(t) \rangle_{\text{THz}}^2 \right) P_{\mathbf{k}_{\parallel}}^{\text{fast}}(t). \quad (\text{C.17})$$

Here, we identified the reduced effective electron-hole mass $\mu(\mathbf{k}_{\parallel})$, Eq. (A.15).

The A^2 -dependent renormalization of the kinetic energies is always positive and it can be directly related to the so-called ponderomotive energy which is the average kinetic energy of a charged classical particle in a harmonic electro-magnetic field as discussed in Chapter 6. The appearance of effective masses in the intraband current J_A , Eq. (C.11), guarantees a Drude-like THz response at low frequencies as discussed in Section 4.2.

The A^2 -dependent renormalization as well as the correct Drude response at low frequencies could also have been obtained without including the non-resonant interband contributions by simply replacing the bare electron mass in H_{A^2} , Eq. (2.39), with the effective mass in each band. This is often done in the literature. However, this procedure lacks a microscopic justification. Moreover, it is important to note that we neglected the Coulomb interaction in our derivation such that the A^2 contributions could be, in fact, different in a full microscopic analysis which includes the Coulomb parts in the semiconductor Bloch equations.

C.2. Explicit Dynamics of Two-Particle Correlations

In this Appendix, we present the full equations of motion for the incoherent doublets c_X , $c_{c,c;c,c}$ and $c_{v,v;v,v}$. For the exciton correlations, we obtain

$$\begin{aligned}
 i\hbar \frac{\partial}{\partial t} c_X^{\mathbf{q}_{\parallel}, \mathbf{k}'_{\parallel}, \mathbf{k}_{\parallel}} &= \left(\tilde{\varepsilon}_{\mathbf{k}'_{\parallel} + \mathbf{q}_{\parallel}}^e + \tilde{\varepsilon}_{\mathbf{k}'_{\parallel}}^h - \tilde{\varepsilon}_{\mathbf{k}_{\parallel} - \mathbf{q}_{\parallel}}^h - \tilde{\varepsilon}_{\mathbf{k}_{\parallel}}^e \right) c_X^{\mathbf{q}_{\parallel}, \mathbf{k}'_{\parallel}, \mathbf{k}_{\parallel}} + [G_{\text{phon}}]_X^{\mathbf{q}_{\parallel}, \mathbf{k}'_{\parallel}, \mathbf{k}_{\parallel}} \\
 &+ V_{\mathbf{k}_{\parallel} - \mathbf{k}'_{\parallel} - \mathbf{q}_{\parallel}} \left[(1 - f_{\mathbf{k}_{\parallel}}^e)(1 - f_{\mathbf{k}_{\parallel} - \mathbf{q}_{\parallel}}^h) f_{\mathbf{k}'_{\parallel} + \mathbf{q}_{\parallel}}^e f_{\mathbf{k}'_{\parallel}}^h - f_{\mathbf{k}_{\parallel}}^e f_{\mathbf{k}_{\parallel} - \mathbf{q}_{\parallel}}^h (1 - f_{\mathbf{k}'_{\parallel} + \mathbf{q}_{\parallel}}^e)(1 - f_{\mathbf{k}'_{\parallel}}^h) \right] \\
 &+ V_{\mathbf{k}_{\parallel} - \mathbf{k}'_{\parallel} - \mathbf{q}_{\parallel}} \left[(f_{\mathbf{k}_{\parallel} - \mathbf{q}_{\parallel}}^h - f_{\mathbf{k}'_{\parallel}}^h) \sum_{\mathbf{l}_{\parallel}} c_{e+X}^{\mathbf{q}_{\parallel} + \mathbf{k}'_{\parallel} - \mathbf{l}_{\parallel}, \mathbf{l}_{\parallel}, \mathbf{k}_{\parallel}} + (f_{\mathbf{k}_{\parallel}}^e - f_{\mathbf{k}'_{\parallel} + \mathbf{q}_{\parallel}}^e) \sum_{\mathbf{l}_{\parallel}} c_{h+X}^{\mathbf{q}_{\parallel} - \mathbf{k}_{\parallel} + \mathbf{l}_{\parallel}, \mathbf{k}'_{\parallel}, \mathbf{l}_{\parallel}} \right] \\
 &+ [1 - f_{\mathbf{k}_{\parallel}}^e - f_{\mathbf{k}_{\parallel} - \mathbf{q}_{\parallel}}^h] \sum_{\mathbf{l}_{\parallel}} V_{\mathbf{l}_{\parallel} - \mathbf{k}_{\parallel}} c_X^{\mathbf{q}_{\parallel}, \mathbf{k}'_{\parallel}, \mathbf{l}_{\parallel}} - [1 - f_{\mathbf{k}'_{\parallel} + \mathbf{q}_{\parallel}}^e - f_{\mathbf{k}_{\parallel}}^h] \sum_{\mathbf{l}_{\parallel}} V_{\mathbf{l}_{\parallel} - \mathbf{k}'_{\parallel}} c_X^{\mathbf{q}_{\parallel}, \mathbf{l}_{\parallel}, \mathbf{k}_{\parallel}} \\
 &+ [f_{\mathbf{k}_{\parallel} - \mathbf{q}_{\parallel}}^h - f_{\mathbf{k}'_{\parallel} + \mathbf{q}_{\parallel}}^e] \sum_{\mathbf{l}_{\parallel}} V_{\mathbf{l}_{\parallel} - \mathbf{q}_{\parallel}} c_X^{\mathbf{l}_{\parallel}, \mathbf{k}'_{\parallel}, \mathbf{k}_{\parallel}} - [f_{\mathbf{k}_{\parallel}}^e - f_{\mathbf{k}'_{\parallel}}^h] \sum_{\mathbf{l}_{\parallel}} V_{\mathbf{l}_{\parallel} - \mathbf{q}_{\parallel}} c_X^{\mathbf{l}_{\parallel}, \mathbf{q}_{\parallel} + \mathbf{k}'_{\parallel} - \mathbf{l}_{\parallel}, \mathbf{k}_{\parallel} - \mathbf{q}_{\parallel} + \mathbf{l}_{\parallel}} \\
 &+ [f_{\mathbf{k}'_{\parallel} + \mathbf{q}_{\parallel}}^e - f_{\mathbf{k}_{\parallel}}^e] \sum_{\mathbf{l}_{\parallel}} V_{\mathbf{l}_{\parallel} - \mathbf{q}_{\parallel}} c_X^{\mathbf{q}_{\parallel} - \mathbf{k}_{\parallel} + \mathbf{l}_{\parallel}, \mathbf{k}'_{\parallel}, \mathbf{l}_{\parallel}} + [f_{\mathbf{k}'_{\parallel}}^h - f_{\mathbf{k}_{\parallel} - \mathbf{q}_{\parallel}}^h] \sum_{\mathbf{l}_{\parallel}} V_{\mathbf{l}_{\parallel} - \mathbf{k}'_{\parallel}} c_X^{\mathbf{q}_{\parallel} + \mathbf{k}'_{\parallel} - \mathbf{l}_{\parallel}, \mathbf{l}_{\parallel}, \mathbf{k}_{\parallel}} \\
 &- j(\mathbf{k}'_{\parallel} + \mathbf{q}_{\parallel} - \mathbf{k}_{\parallel}) c_X^{\mathbf{q}_{\parallel}, \mathbf{k}'_{\parallel}, \mathbf{k}_{\parallel}} \langle A(t) \rangle_{\text{THz}} \tag{C.18}
 \end{aligned}$$

The dynamics of c_X is evidently coupled to electron-electron $c_{c,c;c,c}$ and hole-hole correlations $c_{v,v;v,v}$ whose dynamics is given by

$$\begin{aligned}
 i\hbar \frac{\partial}{\partial t} c_{c,c;c,c}^{\mathbf{q}_{\parallel}, \mathbf{k}'_{\parallel}, \mathbf{k}_{\parallel}} &= \left(\tilde{\varepsilon}_{\mathbf{k}_{\parallel} - \mathbf{q}_{\parallel}}^e + \tilde{\varepsilon}_{\mathbf{k}'_{\parallel} + \mathbf{q}_{\parallel}}^e - \tilde{\varepsilon}_{\mathbf{k}'_{\parallel}}^e - \tilde{\varepsilon}_{\mathbf{k}_{\parallel}}^e \right) c_{c,c;c,c}^{\mathbf{q}_{\parallel}, \mathbf{k}'_{\parallel}, \mathbf{k}_{\parallel}} + [G_{\text{phon}}]_{c,c;c,c}^{\mathbf{q}_{\parallel}, \mathbf{k}'_{\parallel}, \mathbf{k}_{\parallel}} \\
 &+ V_{\mathbf{k}_{\parallel} - \mathbf{k}'_{\parallel} - \mathbf{q}_{\parallel}} \left[f_{\mathbf{k}_{\parallel} - \mathbf{q}_{\parallel}}^e f_{\mathbf{k}'_{\parallel} + \mathbf{q}_{\parallel}}^e (1 - f_{\mathbf{k}_{\parallel}}^e)(1 - f_{\mathbf{k}'_{\parallel}}^e) - f_{\mathbf{k}_{\parallel}}^e f_{\mathbf{k}'_{\parallel}}^e (1 - f_{\mathbf{k}_{\parallel} - \mathbf{q}_{\parallel}}^e)(1 - f_{\mathbf{k}'_{\parallel} + \mathbf{q}_{\parallel}}^e) \right] \\
 &+ V_{\mathbf{q}_{\parallel}} \left[f_{\mathbf{k}_{\parallel} - \mathbf{q}_{\parallel}}^e f_{\mathbf{k}'_{\parallel} + \mathbf{q}_{\parallel}}^e (1 - f_{\mathbf{k}_{\parallel}}^e)(1 - f_{\mathbf{k}'_{\parallel}}^e) - f_{\mathbf{k}_{\parallel}}^e f_{\mathbf{k}'_{\parallel}}^e (1 - f_{\mathbf{k}_{\parallel} - \mathbf{q}_{\parallel}}^e)(1 - f_{\mathbf{k}'_{\parallel} + \mathbf{q}_{\parallel}}^e) \right] \\
 &+ V_{\mathbf{q}_{\parallel}} \left[(f_{\mathbf{k}'_{\parallel} + \mathbf{q}_{\parallel}}^e - f_{\mathbf{k}_{\parallel}}^e) \sum_{\mathbf{l}_{\parallel}} c_{e+X}^{\mathbf{k}_{\parallel} - \mathbf{q}_{\parallel} - \mathbf{l}_{\parallel}, \mathbf{l}_{\parallel}, \mathbf{k}_{\parallel}} - (f_{\mathbf{k}_{\parallel}}^e - f_{\mathbf{k}_{\parallel} - \mathbf{q}_{\parallel}}^e) \sum_{\mathbf{l}_{\parallel}} c_{e+X}^{\mathbf{q}_{\parallel} + \mathbf{k}'_{\parallel} - \mathbf{l}_{\parallel}, \mathbf{l}_{\parallel}, \mathbf{k}'_{\parallel}} \right] \\
 &- V_{\mathbf{k}_{\parallel} - \mathbf{k}'_{\parallel} - \mathbf{q}_{\parallel}} \left[(f_{\mathbf{k}'_{\parallel} + \mathbf{q}_{\parallel}}^e - f_{\mathbf{k}_{\parallel}}^e) \sum_{\mathbf{l}_{\parallel}} c_{e+X}^{\mathbf{k}_{\parallel} - \mathbf{q}_{\parallel} - \mathbf{l}_{\parallel}, \mathbf{l}_{\parallel}, \mathbf{k}'_{\parallel}} - (f_{\mathbf{k}'_{\parallel}}^e - f_{\mathbf{k}_{\parallel} - \mathbf{q}_{\parallel}}^e) \sum_{\mathbf{l}_{\parallel}} c_{e+X}^{\mathbf{q}_{\parallel} + \mathbf{k}'_{\parallel} - \mathbf{l}_{\parallel}, \mathbf{l}_{\parallel}, \mathbf{k}_{\parallel}} \right] \\
 &+ [1 - f_{\mathbf{k}_{\parallel} - \mathbf{q}_{\parallel}}^e - f_{\mathbf{k}'_{\parallel} + \mathbf{q}_{\parallel}}^e] \sum_{\mathbf{l}_{\parallel}} V_{\mathbf{l}_{\parallel} - \mathbf{q}_{\parallel}} c_{c,c;c,c}^{\mathbf{l}_{\parallel}, \mathbf{k}'_{\parallel}, \mathbf{k}_{\parallel}} - [1 - f_{\mathbf{k}_{\parallel}}^e - f_{\mathbf{k}'_{\parallel}}^e] \sum_{\mathbf{l}_{\parallel}} V_{\mathbf{l}_{\parallel} - \mathbf{q}_{\parallel}} c_{c,c;c,c}^{\mathbf{l}_{\parallel}, \mathbf{q}_{\parallel} + \mathbf{k}'_{\parallel} - \mathbf{l}_{\parallel}, \mathbf{k}_{\parallel} - \mathbf{q}_{\parallel} + \mathbf{l}_{\parallel}} \\
 &- [f_{\mathbf{k}_{\parallel}}^e - f_{\mathbf{k}_{\parallel} - \mathbf{q}_{\parallel}}^e] \sum_{\mathbf{l}_{\parallel}} V_{\mathbf{l}_{\parallel} - \mathbf{k}_{\parallel}} c_{c,c;c,c}^{\mathbf{q}_{\parallel}, \mathbf{k}'_{\parallel}, \mathbf{l}_{\parallel}} + [f_{\mathbf{k}'_{\parallel} + \mathbf{q}_{\parallel}}^e - f_{\mathbf{k}_{\parallel}}^e] \sum_{\mathbf{l}_{\parallel}} V_{\mathbf{l}_{\parallel} - \mathbf{k}_{\parallel}} c_{c,c;c,c}^{\mathbf{q}_{\parallel} - \mathbf{k}_{\parallel} + \mathbf{l}_{\parallel}, \mathbf{k}'_{\parallel}, \mathbf{l}_{\parallel}} \\
 &+ [f_{\mathbf{k}'_{\parallel} + \mathbf{q}_{\parallel}}^e - f_{\mathbf{k}'_{\parallel}}^e] \sum_{\mathbf{l}_{\parallel}} V_{\mathbf{l}_{\parallel} - \mathbf{k}'_{\parallel}} c_{c,c;c,c}^{\mathbf{q}_{\parallel}, \mathbf{l}_{\parallel}, \mathbf{k}_{\parallel}} - [f_{\mathbf{k}'_{\parallel}}^e - f_{\mathbf{k}_{\parallel} - \mathbf{q}_{\parallel}}^e] \sum_{\mathbf{l}_{\parallel}} V_{\mathbf{l}_{\parallel} - \mathbf{k}'_{\parallel}} c_{c,c;c,c}^{\mathbf{q}_{\parallel} + \mathbf{k}'_{\parallel} - \mathbf{l}_{\parallel}, \mathbf{l}_{\parallel}, \mathbf{k}_{\parallel}} \tag{C.19}
 \end{aligned}$$

and

$$\begin{aligned}
 i\hbar \frac{\partial}{\partial t} c_{v,v;v,v}^{\mathbf{q}_{\parallel}, \mathbf{k}'_{\parallel}, \mathbf{k}_{\parallel}} &= \left(-\tilde{\varepsilon}_{\mathbf{k}_{\parallel} - \mathbf{q}_{\parallel}}^h - \tilde{\varepsilon}_{\mathbf{k}'_{\parallel} + \mathbf{q}_{\parallel}}^h + \tilde{\varepsilon}_{\mathbf{k}'_{\parallel}}^h + \tilde{\varepsilon}_{\mathbf{k}_{\parallel}}^h \right) c_{v,v;v,v}^{\mathbf{q}_{\parallel}, \mathbf{k}'_{\parallel}, \mathbf{k}_{\parallel}} + [G_{\text{phon}}]_{v,v;v,v}^{\mathbf{q}_{\parallel}, \mathbf{k}'_{\parallel}, \mathbf{k}_{\parallel}} \\
 &- V_{\mathbf{k}_{\parallel} - \mathbf{k}'_{\parallel} - \mathbf{q}_{\parallel}} \left[f_{\mathbf{k}_{\parallel} - \mathbf{q}_{\parallel}}^h f_{\mathbf{k}'_{\parallel} + \mathbf{q}_{\parallel}}^h (1 - f_{\mathbf{k}_{\parallel}}^h)(1 - f_{\mathbf{k}'_{\parallel}}^h) - f_{\mathbf{k}_{\parallel}}^h f_{\mathbf{k}'_{\parallel}}^h (1 - f_{\mathbf{k}_{\parallel} - \mathbf{q}_{\parallel}}^h)(1 - f_{\mathbf{k}'_{\parallel} + \mathbf{q}_{\parallel}}^h) \right] \\
 &- V_{\mathbf{q}_{\parallel}} \left[f_{\mathbf{k}_{\parallel} - \mathbf{q}_{\parallel}}^h f_{\mathbf{k}'_{\parallel} + \mathbf{q}_{\parallel}}^h (1 - f_{\mathbf{k}_{\parallel}}^h)(1 - f_{\mathbf{k}'_{\parallel}}^h) - f_{\mathbf{k}_{\parallel}}^h f_{\mathbf{k}'_{\parallel}}^h (1 - f_{\mathbf{k}_{\parallel} - \mathbf{q}_{\parallel}}^h)(1 - f_{\mathbf{k}'_{\parallel} + \mathbf{q}_{\parallel}}^h) \right] \\
 &- V_{\mathbf{q}_{\parallel}} \left[(f_{\mathbf{k}'_{\parallel} + \mathbf{q}_{\parallel}}^h - f_{\mathbf{k}'_{\parallel}}^h) \sum_{\mathbf{l}_{\parallel}} c_{e+X}^{\mathbf{k}_{\parallel} - \mathbf{q}_{\parallel} - \mathbf{l}_{\parallel}, \mathbf{l}_{\parallel}, \mathbf{k}_{\parallel}} - (f_{\mathbf{k}_{\parallel}}^h - f_{\mathbf{k}_{\parallel} - \mathbf{q}_{\parallel}}^h) \sum_{\mathbf{l}_{\parallel}} c_{h+X}^{\mathbf{q}_{\parallel} + \mathbf{k}'_{\parallel} - \mathbf{l}_{\parallel}, \mathbf{l}_{\parallel}, \mathbf{k}'_{\parallel}} \right] \\
 &+ V_{\mathbf{k}_{\parallel} - \mathbf{k}'_{\parallel} - \mathbf{q}_{\parallel}} \left[(f_{\mathbf{k}'_{\parallel} + \mathbf{q}_{\parallel}}^h - f_{\mathbf{k}_{\parallel}}^h) \sum_{\mathbf{l}_{\parallel}} c_{h+X}^{\mathbf{k}_{\parallel} - \mathbf{q}_{\parallel} - \mathbf{l}_{\parallel}, \mathbf{l}_{\parallel}, \mathbf{k}'_{\parallel}} - (f_{\mathbf{k}'_{\parallel}}^h - f_{\mathbf{k}_{\parallel} - \mathbf{q}_{\parallel}}^h) \sum_{\mathbf{l}_{\parallel}} c_{h+X}^{\mathbf{q}_{\parallel} + \mathbf{k}'_{\parallel} - \mathbf{l}_{\parallel}, \mathbf{l}_{\parallel}, \mathbf{k}_{\parallel}} \right] \\
 &- [1 - f_{\mathbf{k}_{\parallel} - \mathbf{q}_{\parallel}}^h - f_{\mathbf{k}'_{\parallel} + \mathbf{q}_{\parallel}}^h] \sum_{\mathbf{l}_{\parallel}} V_{\mathbf{l}_{\parallel} - \mathbf{q}_{\parallel}} c_{v,v;v,v}^{\mathbf{l}_{\parallel}, \mathbf{k}'_{\parallel}, \mathbf{k}_{\parallel}} + [1 - f_{\mathbf{k}_{\parallel}}^h - f_{\mathbf{k}'_{\parallel}}^h] \sum_{\mathbf{l}_{\parallel}} V_{\mathbf{l}_{\parallel} - \mathbf{q}_{\parallel}} c_{v,v;v,v}^{\mathbf{l}_{\parallel}, \mathbf{q}_{\parallel} + \mathbf{k}'_{\parallel} - \mathbf{l}_{\parallel}, \mathbf{k}_{\parallel} - \mathbf{q}_{\parallel} + \mathbf{l}_{\parallel}} \\
 &+ [f_{\mathbf{k}_{\parallel}}^h - f_{\mathbf{k}_{\parallel} - \mathbf{q}_{\parallel}}^h] \sum_{\mathbf{l}_{\parallel}} V_{\mathbf{l}_{\parallel} - \mathbf{k}_{\parallel}} c_{v,v;v,v}^{\mathbf{q}_{\parallel}, \mathbf{k}'_{\parallel}, \mathbf{l}_{\parallel}} - [f_{\mathbf{k}'_{\parallel} + \mathbf{q}_{\parallel}}^h - f_{\mathbf{k}_{\parallel}}^h] \sum_{\mathbf{l}_{\parallel}} V_{\mathbf{l}_{\parallel} - \mathbf{k}_{\parallel}} c_{v,v;v,v}^{\mathbf{q}_{\parallel} - \mathbf{k}_{\parallel} + \mathbf{l}_{\parallel}, \mathbf{k}'_{\parallel}, \mathbf{l}_{\parallel}} \\
 &- [f_{\mathbf{k}'_{\parallel} + \mathbf{q}_{\parallel}}^h - f_{\mathbf{k}'_{\parallel}}^h] \sum_{\mathbf{l}_{\parallel}} V_{\mathbf{l}_{\parallel} - \mathbf{k}'_{\parallel}} c_{v,v;v,v}^{\mathbf{q}_{\parallel}, \mathbf{l}_{\parallel}, \mathbf{k}_{\parallel}} + [f_{\mathbf{k}'_{\parallel}}^h - f_{\mathbf{k}_{\parallel} - \mathbf{q}_{\parallel}}^h] \sum_{\mathbf{l}_{\parallel}} V_{\mathbf{l}_{\parallel} - \mathbf{k}'_{\parallel}} c_{v,v;v,v}^{\mathbf{q}_{\parallel} + \mathbf{k}'_{\parallel} - \mathbf{l}_{\parallel}, \mathbf{l}_{\parallel}, \mathbf{k}_{\parallel}} \quad (\text{C.20})
 \end{aligned}$$

We here introduced the abbreviations $c_{e(h)+X} = c_{e(h)} + c_X$ and the renormalized energies

$$\tilde{\varepsilon}_{\mathbf{k}_{\parallel}}^{e(h)} = \varepsilon_{\mathbf{k}_{\parallel}}^{e(h)} - \sum_{\mathbf{k}'_{\parallel}} V_{\mathbf{k}_{\parallel} - \mathbf{k}'_{\parallel}} f_{\mathbf{k}'_{\parallel}}^{e(h)}. \quad (\text{C.21})$$

The explicit form of the phonon contributions $[G_{\text{phon}}]_{\lambda,\nu,\lambda,\nu}$ can be found in Ref. [6].

C.3. Scattering Contributions

In this Appendix, we discuss scattering contributions in the singlet-doublet equations (3.48)-(3.57) in the incoherent regime.

In many investigations of semiconductor processes, e.g., exciton formation [22, 23, 25] or excitation-induced dephasing [51], it is essential to provide a microscopic description of Coulomb and phonon-induced scattering processes. In this Thesis, we investigate the THz-induced dynamics of exciton correlations on a picosecond timescale assuming that formation of the many-body state has already taken place. For such an investigation, the qualitative features can be understood even when the microscopic scattering is simplified.

The two-particle correlations $c_{c,c;c,c}$ and $c_{v,v;v,v}$ do not directly couple to the THz field. Since they provide electron and hole scattering, they effectively lead to a decay of the THz current, J_{THz} . Their contribution together with the phonon-scattering in Eq. (3.61) can be modeled via

$$\hbar \frac{\partial}{\partial t} J_{\text{THz}} \Big|_{\text{scatt}} = -\gamma_J J_{\text{THz}} \quad (\text{C.22})$$

C. Singlet-Doublet Dynamics of Carriers

where γ_J is a phenomenological dephasing constant.

To discuss the effect of $c_{c,c;c,c}$, $c_{v,v;v,v}$ and phonon scattering on the carrier densities, we distinguish the two different regimes where the many-body state is either dominated by (i) plasma contributions or (ii) exciton populations. For plasma-like conditions, the scattering leads to an equilibration of the carrier distributions and their influence in Eqs. (3.48),(3.49) can be modeled via

$$\hbar \frac{\partial}{\partial t} f_{\mathbf{k}_{\parallel}} \Big|_{\text{scatt}} = -\gamma_f (f_{\mathbf{k}_{\parallel}} - f_{\mathbf{k}_{\parallel}}^{\text{FD}}) \quad (\text{C.23})$$

where γ_f is a constant and $f_{\mathbf{k}}^{\text{FD}}$ a Fermi-Dirac distribution at lattice temperature. However, when a large population of excitons is present (as assumed, e.g., in Chapter 7), the carrier distributions are not given by Fermi-Dirac distributions but rather by Eq. (7.5) and the carrier dynamics is completely determined by the exciton correlations c_X . In this case, the scattering contribution, Eq. (C.23), does not appear.

The three-particle scattering terms in Eq. (3.54) can also be modeled phenomenologically. Again, we distinguish the two regimes mentioned above. For plasma-like conditions, it is often sufficient to assume a constant dephasing-mode for all electron-hole correlations such that

$$T_X^{\mathbf{q}_{\parallel}, \mathbf{k}'_{\parallel}, \mathbf{k}_{\parallel}} = -i\gamma_T c_X^{\mathbf{q}_{\parallel}, \mathbf{k}'_{\parallel}, \mathbf{k}_{\parallel}}. \quad (\text{C.24})$$

However, when the THz dynamics of exciton populations is studied, Eq. (C.24) is usually not realistic. Instead, we demand that (i) the correlations describing transitions between exciton states decay while (ii) exciton populations do not decay. This is justified because, in semiconductors, the phase coherence of transition correlations is typically destroyed within picoseconds due to many-body scattering while the populations relax on a much longer nanosecond timescale. With help of the exciton basis introduced in Appendix D, the triplet scattering can thus be written as

$$T_X^{\mathbf{q}_{\parallel}, \mathbf{k}'_{\parallel}, \mathbf{k}_{\parallel}} = -i\gamma_T \left(c_X^{\mathbf{q}_{\parallel}, \mathbf{k}'_{\parallel}, \mathbf{k}_{\parallel}} - \sum_{\lambda} \Delta N_{\lambda, \lambda}(\mathbf{q}_{\parallel}) \phi_{\lambda, \mathbf{q}}^{\text{R}}(\mathbf{k}_{\parallel} - \mathbf{q}_{\parallel}^e) \phi_{\lambda, \mathbf{q}}^{\text{R}}(\mathbf{k}'_{\parallel} + \mathbf{q}_{\parallel}^h) \right) \quad (\text{C.25})$$

where $\Delta N_{\lambda, \lambda}(\mathbf{q}_{\parallel})$ and the exciton wavefunctions are updated in time during the numerical computation.

D. Exciton Basis

For low density conditions, it is often convenient to discuss the THz-induced dynamics in the exciton basis. In this Appendix, we introduce the exciton basis and discuss the properties of the excitonic wavefunctions. We then formulate the relevant equations of motion in the exciton basis for both coherent and incoherent conditions. Note that, in our numerical computations, we usually solve the equations of motions in the Bloch basis, and use the exciton basis only for analytical insights and interpretation of results.

D.1. Wannier Equation

The eigenvalue problem of the homogeneous part of the equation of motion for the microscopic polarization, Eq. (3.34), leads to the generalized Wannier equation

$$\left(\tilde{\varepsilon}_{\mathbf{k}_{\parallel}}^e + \tilde{\varepsilon}_{\mathbf{k}_{\parallel}}^h\right) \phi_{\lambda}^{\text{R}}(\mathbf{k}_{\parallel}) - (1 - f_{\mathbf{k}_{\parallel}}^e - f_{\mathbf{k}_{\parallel}}^h) \sum_{\mathbf{l}_{\parallel}} V_{\mathbf{l}_{\parallel}-\mathbf{k}_{\parallel}} \phi_{\lambda}^{\text{R}}(\mathbf{l}_{\parallel}) = E_{\lambda} \phi_{\lambda}^{\text{R}}(\mathbf{k}_{\parallel}). \quad (\text{D.1})$$

Here, E_{λ} is the energy, and $\phi_{\lambda}^{\text{R}}(\mathbf{k}_{\parallel})$ is the wavefunction of the exciton state λ . Since the operator acting on ϕ is not hermitian, we obtain both right-handed $\phi_{\lambda}^{\text{R}}(\mathbf{k}_{\parallel})$ and left-handed $\phi_{\lambda}^{\text{L}}(\mathbf{k}_{\parallel})$ solutions of Eq. (D.1) which are related via $\phi_{\lambda}^{\text{L}}(\mathbf{k}_{\parallel}) = \phi_{\lambda}^{\text{R}}(\mathbf{k}_{\parallel}) / (1 - f_{\mathbf{k}_{\parallel}}^e - f_{\mathbf{k}_{\parallel}}^h)$. The excitonic wavefunctions fulfill a normalization conditions and a completeness relations given by

$$\sum_{\mathbf{k}_{\parallel}} \phi_{\lambda}^{\text{L}}(\mathbf{k}_{\parallel}) \phi_{\nu}^{\text{R}}(\mathbf{k}_{\parallel}) = \delta_{\lambda,\nu}, \quad \sum_{\lambda} \phi_{\lambda}^{\text{L}}(\mathbf{k}_{\parallel}) \phi_{\lambda}^{\text{R}}(\mathbf{k}'_{\parallel}) = \delta_{\mathbf{k}_{\parallel}, \mathbf{k}'_{\parallel}}. \quad (\text{D.2})$$

Since the Wannier equation (D.1) is invariant under the transformation $\mathbf{k}_{\parallel} \rightarrow -\mathbf{k}_{\parallel}$, the excitonic wavefunctions have a well-defined parity given by $\pi(\lambda) = 1$ for $\phi_{\lambda}(-|\mathbf{k}_{\parallel}|) = \phi_{\lambda}(|\mathbf{k}_{\parallel}|)$ and $\pi(\lambda) = -1$ for $\phi_{\lambda}(-|\mathbf{k}_{\parallel}|) = -\phi_{\lambda}(|\mathbf{k}_{\parallel}|)$. The exciton wavefunctions provide a transformation for the microscopic polarization via

$$p_{\lambda} = \sum_{\mathbf{k}_{\parallel}} \phi_{\lambda}^{\text{L}}(\mathbf{k}_{\parallel}) P_{\mathbf{k}_{\parallel}}, \quad P_{\mathbf{k}_{\parallel}} = \sum_{\lambda} \phi_{\lambda}^{\text{R}}(\mathbf{k}_{\parallel}) p_{\lambda}. \quad (\text{D.3})$$

While $P_{\mathbf{k}_{\parallel}}$ denotes the polarization for a certain Bloch wavevector, p_{λ} describes the polarization in the exciton state λ .

The homogeneous part of the exciton-correlation dynamics Eq. (3.54), leads to the following eigenvalue problem

$$\left(\tilde{\varepsilon}_{\mathbf{k}_{\parallel}+\mathbf{q}_{\parallel}}^e + \tilde{\varepsilon}_{\mathbf{k}_{\parallel}-\mathbf{q}_{\parallel}}^h\right) \phi_{\lambda;\mathbf{q}}^{\text{R}}(\mathbf{k}_{\parallel}) - (1 - f_{\mathbf{k}_{\parallel}+\mathbf{q}_{\parallel}}^e - f_{\mathbf{k}_{\parallel}-\mathbf{q}_{\parallel}}^h) \sum_{\mathbf{l}_{\parallel}} V_{\mathbf{l}_{\parallel}-\mathbf{k}_{\parallel}} \phi_{\lambda;\mathbf{q}}^{\text{R}}(\mathbf{l}_{\parallel}) = E_{\lambda;\mathbf{q}} \phi_{\lambda;\mathbf{q}}^{\text{R}}(\mathbf{k}_{\parallel}) \quad (\text{D.4})$$

D. Exciton Basis

where $\mathbf{q}_{\parallel}^{e(h)} \equiv \mathbf{q}_{\parallel} m_{e(h)}(\mathbf{0})/(m_e(\mathbf{0}) + m_h(\mathbf{0}))$ is defined via the effective masses at the Γ -point. Evidently, Eq. (D.4) is a modified version of Eq. (D.1) where the exciton wavefunctions and energies can depend on the center-of-mass momentum \mathbf{q}_{\parallel} . Again, the right-handed $\phi_{\lambda;\mathbf{q}}^R(\mathbf{k}_{\parallel})$ and left-handed $\phi_{\lambda;\mathbf{q}}^L(\mathbf{k}_{\parallel}) = \phi_{\lambda;\mathbf{q}}^R(\mathbf{k}_{\parallel})/(1 - f_{\mathbf{k}_{\parallel}+\mathbf{q}_{\parallel}}^e - f_{\mathbf{k}_{\parallel}-\mathbf{q}_{\parallel}}^h)$ solutions fulfill a normalization condition and a completeness relation via

$$\sum_{\mathbf{k}_{\parallel}} \phi_{\lambda;\mathbf{q}}^L(\mathbf{k}_{\parallel})\phi_{\nu;\mathbf{q}}^R(\mathbf{k}_{\parallel}) = \delta_{\lambda,\nu}, \quad \sum_{\lambda} \phi_{\lambda;\mathbf{q}}^L(\mathbf{k}_{\parallel})\phi_{\lambda;\mathbf{q}}^R(\mathbf{k}'_{\parallel}) = \delta_{\mathbf{k}_{\parallel},\mathbf{k}'_{\parallel}}. \quad (\text{D.5})$$

For investigations close to the bandgap, the bandstructure can usually be assumed parabolic $\varepsilon_{\mathbf{k}_{\parallel}}^{\lambda} = \varepsilon_{\mathbf{0}}^{\lambda} + \hbar^2\mathbf{k}_{\parallel}^2/(2m_{\lambda})$. In this case, we can identify

$$\varepsilon_{\mathbf{k}_{\parallel}+\mathbf{q}_{\parallel}}^e + \varepsilon_{\mathbf{k}_{\parallel}-\mathbf{q}_{\parallel}}^h = \frac{\hbar^2\mathbf{k}_{\parallel}^2}{2\mu} + \frac{\hbar^2\mathbf{q}_{\parallel}^2}{2M} \quad (\text{D.6})$$

where $\mu = m_e m_h / (m_e + m_h)$ is the reduced electron-hole mass and $M = m_e + m_h$ the total mass. When, furthermore, the \mathbf{q} -dependent contributions in the energy renormalizations and Pauli-blocking factor are small in Eq. (D.4), the exciton energies are given by

$$E_{\lambda;\mathbf{q}} = E_{\lambda;\mathbf{0}} + \frac{\hbar^2\mathbf{q}_{\parallel}^2}{2M} \quad (\text{D.7})$$

implying that the CM dependence is trivial. In Section D.4, we find that the THz dynamics depends only on *differences* of exciton energies, $E_{\lambda;\mathbf{q}} - E_{\nu;\mathbf{q}}$. When the exciton energies are given by Eq. (D.7), the CM energies cancel such that the THz field is not sensitive to the CM momentum. In this case, it is sufficient to solve the Wannier equation (D.4) for $\mathbf{q}_{\parallel} = 0$ only. However, when the bandstructure is strongly non-parabolic or when energy renormalizations or Pauli-blocking is important, the excitonic-transition energies can depend on the CM momentum (see, e.g., Section 7.4).

The exciton wavefunctions, $\phi_{\lambda;\mathbf{q}}(\mathbf{k}_{\parallel})$, provide the following transformations for the electron-hole correlations

$$c_X^{\mathbf{q}_{\parallel},\mathbf{k}'_{\parallel},\mathbf{k}_{\parallel}} = \sum_{\lambda,\nu} \phi_{\lambda;\mathbf{q}}^R(\mathbf{k}_{\parallel} - \mathbf{q}_{\parallel}^e)\phi_{\nu;\mathbf{q}}^R(\mathbf{k}'_{\parallel} + \mathbf{q}_{\parallel}^h)\Delta N_{\lambda,\nu}(\mathbf{q}_{\parallel}), \quad (\text{D.8})$$

$$\Delta N_{\lambda,\nu}(\mathbf{q}_{\parallel}) = \sum_{\mathbf{k}_{\parallel},\mathbf{k}'_{\parallel}} \phi_{\lambda;\mathbf{q}}^L(\mathbf{k}_{\parallel} - \mathbf{q}_{\parallel}^e)\phi_{\nu;\mathbf{q}}^L(\mathbf{k}'_{\parallel} + \mathbf{q}_{\parallel}^h)c_X^{\mathbf{q}_{\parallel},\mathbf{k}'_{\parallel},\mathbf{k}_{\parallel}}. \quad (\text{D.9})$$

We discuss the meaning of $\Delta N_{\lambda,\lambda}(\mathbf{q})$ in the next Section.

D.2. Pair-Correlation Function and Exciton Populations

The electron-hole pair-correlation function

$$g_{eh}(\mathbf{r}) = \langle \psi_e^{\dagger}(\mathbf{r}_{\parallel})\psi_h^{\dagger}(\mathbf{0})\psi_h(\mathbf{0})\psi_e(\mathbf{r}_{\parallel}) \rangle \quad (\text{D.10})$$

determines the conditional probability to find an electron at the position \mathbf{r} when a hole is located at $\mathbf{r} = \mathbf{0}$. Thus, $g_{eh}(\mathbf{r})$ allows us to identify correlations in the electron-hole relative coordinate. Expressing the field operators in the Bloch basis, we can separate the correlation function into a singlet part and a correlated part

$$g_{eh}(\mathbf{r}) = \frac{1}{\mathcal{S}^2} \sum_{\mathbf{k}_{\parallel}, \mathbf{k}'_{\parallel}, \mathbf{p}_{\parallel}, \mathbf{p}'_{\parallel}} e^{-i(\mathbf{k}_{\parallel} - \mathbf{k}'_{\parallel}) \cdot \mathbf{r}_{\parallel}} \langle a_{c, \mathbf{k}_{\parallel}}^{\dagger} a_{c, \mathbf{k}'_{\parallel}} a_{v, \mathbf{p}_{\parallel}} a_{v, \mathbf{p}'_{\parallel}}^{\dagger} \rangle = g_{eh}(\mathbf{r})_S + \Delta g_{eh}(\mathbf{r}). \quad (\text{D.11})$$

where

$$g_{eh}(\mathbf{r}_{\parallel})_S = n_e n_h + \left| \frac{1}{\mathcal{S}} \sum_{\mathbf{k}_{\parallel}} P_{\mathbf{k}_{\parallel}} e^{i\mathbf{k}_{\parallel} \cdot \mathbf{r}_{\parallel}} \right|^2, \quad (\text{D.12})$$

$$\Delta g_{eh}(\mathbf{r}_{\parallel}) = \frac{1}{\mathcal{S}^2} \sum_{\mathbf{k}_{\parallel}, \mathbf{k}'_{\parallel}, \mathbf{q}_{\parallel}} c_X^{\mathbf{q}_{\parallel}, \mathbf{k}'_{\parallel}, \mathbf{k}_{\parallel}} e^{i(\mathbf{k}'_{\parallel} + \mathbf{q}_{\parallel} - \mathbf{k}_{\parallel}) \cdot \mathbf{r}_{\parallel}}. \quad (\text{D.13})$$

The singlet part contains a background contribution $n_{2D}^2 = n_e n_h$ and the microscopic polarization. The correlated part is determined by the exciton correlations. Inserting Eqs. (D.3), (D.8) into Eqs. (D.12) and (D.13), we find

$$g_{eh}(\mathbf{r}_{\parallel})_S = n_e n_h + \sum_{\lambda, \nu} \left(\frac{1}{\mathcal{S}} p_{\lambda}^* p_{\nu} \right) [\phi_{\lambda}^R(\mathbf{r}_{\parallel})]^* \phi_{\nu}^R(\mathbf{r}_{\parallel}), \quad (\text{D.14})$$

$$\Delta g_{eh}(\mathbf{r}_{\parallel}) = \sum_{\lambda, \nu} \left(\frac{1}{\mathcal{S}} \sum_{\mathbf{q}_{\parallel}} \Delta N_{\lambda, \nu}(\mathbf{q}_{\parallel}) \right) [\phi_{\lambda; \mathbf{q}}^R(\mathbf{r}_{\parallel})]^* \phi_{\nu; \mathbf{q}}^R(\mathbf{r}_{\parallel}). \quad (\text{D.15})$$

For completely incoherent conditions, the genuine \mathbf{r}_{\parallel} -dependence follows entirely from the correlated part. When $\Delta g_{eh}(\mathbf{r}_{\parallel})$ displays an \mathbf{r}_{\parallel} -dependence proportional to $|\phi_{\lambda_0}^R(\mathbf{r}_{\parallel})|^2$, which corresponds to the presence of an exciton population in state λ_0 , the $\sum_{\lambda, \nu}$ sum is obviously dominated by the element $\lambda = \nu = \lambda_0$. We thus find that

$$\Delta n_{\lambda_0} \equiv \frac{\Delta N_{\lambda_0, \lambda_0}}{\mathcal{S}} \equiv \frac{1}{\mathcal{S}} \sum_{\mathbf{q}_{\parallel}} \Delta N_{\lambda_0, \lambda_0}(\mathbf{q}_{\parallel}) \quad (\text{D.16})$$

defines the density of incoherent excitons in state λ_0 .

D.3. Singlet Dynamics in Exciton Basis

Inserting Eq. (D.3) into Eq. (3.34), we find that the polarization dynamics in the exciton basis is given by

$$\begin{aligned} i\hbar \frac{\partial}{\partial t} p_{\lambda} &= \left(E_{\lambda} + \frac{|e|^2}{2\mu} \langle A \rangle_{\text{THz}}^2 \right) p_{\lambda} - \sum_{\nu} J_{\lambda, \nu} \langle A \rangle_{\text{THz}} p_{\nu} \\ &\quad - d_{c, v} \sqrt{\mathcal{S}} \phi_{\lambda}(\mathbf{r}_{\parallel} = \mathbf{0}) \langle E \rangle_{\text{opt}} - i\Gamma_{\lambda}. \end{aligned} \quad (\text{D.17})$$

D. Exciton Basis

Here, we assumed that μ and $d_{c,v}$ are independent of \mathbf{k}_{\parallel} and introduced the excitonic current-matrix element

$$J_{\lambda,\nu} = \sum_{\mathbf{k}_{\parallel}} \phi_{\lambda}^L(\mathbf{k}_{\parallel}) j(\mathbf{k}_{\parallel}) \phi_{\nu}^R(\mathbf{k}_{\parallel}). \quad (\text{D.18})$$

When $J_{\lambda,\nu}$ is nonvanishing, the THz field can induce transitions between excitonic states λ and ν . It can easily be shown that $J_{\lambda,\nu}$ is related to the excitonic dipole-matrix element $d_{\lambda,\nu}$ via

$$d_{\lambda,\nu} \equiv \int d^2\mathbf{r}_{\parallel} \phi_{\lambda}^L(\mathbf{r}_{\parallel}) (|e| \mathbf{e}_A \cdot \mathbf{r}_{\parallel}) \phi_{\nu}^R(\mathbf{r}_{\parallel}) = \frac{i\hbar}{E_{\nu} - E_{\lambda}} J_{\lambda,\nu}. \quad (\text{D.19})$$

Thus, $J_{\lambda,\nu}$ provides the typical dipole-selection rules equivalent to atomic selection rules. The term $-i\Gamma_{\lambda}$ in Eq. (D.17) represents doublet contributions which are difficult to express in the exciton basis.

The THz Current, Eq. (3.47), can also be expressed in the exciton basis [38]

$$\frac{\partial}{\partial t} J_{\text{THz}} = +\text{Im} \left[\frac{1}{\hbar\mathcal{S}} \sum_{\lambda,\nu} (E_{\nu} - E_{\lambda}) J_{\lambda,\nu} (p_{\lambda}^* p_{\nu}) \right] - \frac{\gamma_J}{\hbar} \quad (\text{D.20})$$

where $-\gamma_J/\hbar$ describes scattering contributions discussed in Appendix C.3. We find that only off-diagonal elements $p_{\lambda}^* p_{\nu \neq \lambda}$ contribute. Finally, the dynamics of $p_{\lambda} p_{\nu}$ is given by [38]

$$i\hbar \frac{\partial}{\partial t} (p_{\lambda}^* p_{\nu}) = (E_{\nu} - E_{\lambda}) (p_{\lambda}^* p_{\nu}) - \sum_{\beta} \left[J_{\nu,\beta} (p_{\lambda}^* p_{\beta}) - J_{\lambda,\beta} (p_{\beta}^* p_{\nu}) \right] \langle A \rangle_{\text{THz}} - i\Gamma_{\lambda,\nu}.$$

where $\Gamma_{\lambda,\nu} = \Gamma_{\lambda} + \Gamma_{\nu}$.

D.4. Singlet-Doublet Dynamics in Exciton Basis

Inserting Eqs. (D.8),(D.9) into Eq. (3.54), we can determine the dynamics of electron-hole correlations for incoherent conditions in the exciton basis. We find [38]

$$i\hbar \frac{\partial}{\partial t} \Delta N_{\lambda,\nu}(\mathbf{q}_{\parallel}) = (E_{\nu;\mathbf{q}} - E_{\lambda;\mathbf{q}}) \Delta N_{\lambda,\nu}(\mathbf{q}_{\parallel}) + (E_{\nu;\mathbf{q}} - E_{\lambda;\mathbf{q}}) N_{\lambda,\nu}^{\text{S}}(\mathbf{q}_{\parallel}) + D_{\lambda,\nu}^{\text{rest}}(\mathbf{q}_{\parallel}) - \sum_{\beta} \left[J_{\nu,\beta;\mathbf{q}} \Delta N_{\lambda,\beta}(\mathbf{q}_{\parallel}) - J_{\lambda,\beta;\mathbf{q}} \Delta N_{\beta,\nu}(\mathbf{q}_{\parallel}) \right] \langle A \rangle_{\text{THz}} + T_{\lambda,\nu}(\mathbf{q}_{\parallel}) + iG_{\lambda,\nu}^{\text{phon}}(\mathbf{q}_{\parallel}) \quad (\text{D.21})$$

Obviously, the THz field can induce transitions between exciton correlations when the excitonic current-matrix element

$$J_{\lambda,\nu;\mathbf{q}} = \sum_{\mathbf{k}_{\parallel}} \phi_{\lambda;\mathbf{q}}^L(\mathbf{k}_{\parallel}) [j_e(\mathbf{k}_{\parallel} + \mathbf{q}_{\parallel}^e) + j_h(\mathbf{k}_{\parallel} - \mathbf{q}_{\parallel}^h)] \phi_{\nu;\mathbf{q}}^R(\mathbf{k}_{\parallel}) \quad (\text{D.22})$$

D.5. Solutions of the Terahertz-Bloch Equations

is non-vanishing. When a diagonal correlation $\Delta N_{\lambda,\lambda}$ is present the THz field creates off-diagonal elements $\Delta N_{\lambda,\nu \neq \lambda}$ which can thus be identified as excitonic-transition correlations. The single-particle-scattering S_X in Eq. (3.54) produces

$$N_{\lambda,\nu}^S(\mathbf{q}_{\parallel}) = \sum_{\mathbf{k}_{\parallel}} \phi_{\lambda;\mathbf{q}}^L(\mathbf{k}_{\parallel}) f_{\mathbf{k}_{\parallel}+\mathbf{q}_{\parallel}}^e f_{\mathbf{k}_{\parallel}-\mathbf{q}_{\parallel}}^h \phi_{\nu;\mathbf{q}}^L(\mathbf{k}_{\parallel}). \quad (\text{D.23})$$

The remaining Coulomb-induced doublets, phonon-induced doublets and triplet-scattering contributions are abbreviated by $D_{\lambda,\nu}^{\text{rest}}$, $G_{\lambda,\nu}^{\text{phon}}$ and $T_{\lambda,\nu}$, respectively. Again, the formulation of the scattering contributions is cumbersome in the exciton basis.

Using Eqs. (D.8),(D.9) and properties of the Wannier equation (D.4), we find [38] that the THz current dynamics, Eq. (3.61), converts into

$$\frac{\partial}{\partial t} J_{\text{THz}} = +\text{Im} \left[\frac{1}{\hbar \mathcal{S}} \sum_{\mathbf{q}_{\parallel}, \lambda, \nu} (E_{\nu;\mathbf{q}} - E_{\lambda;\mathbf{q}}) J_{\lambda,\nu;\mathbf{q}} \Delta N_{\lambda,\nu}(\mathbf{q}_{\parallel}) \right] - \frac{\gamma_J}{\hbar}. \quad (\text{D.24})$$

where γ_J again denotes scattering contributions discussed in Appendix C.3. Obviously, only off-diagonal correlations, i.e., excitonic-transition correlations lead to a non-vanishing current.

The dynamics of the carrier distributions, Eq. (3.48), can also be expressed in the exciton basis,

$$\hbar \frac{\partial}{\partial t} f_{\mathbf{k}}^e = \text{Im} \left[\sum_{\lambda,\nu,\mathbf{q}_{\parallel}} \Delta N_{\lambda,\nu}(\mathbf{q}_{\parallel}) (E_{\nu;\mathbf{q}} - E_{\lambda;\mathbf{q}}) \phi_{\lambda;\mathbf{q}}^L(\mathbf{k}_{\parallel} - \mathbf{q}_{\parallel}^e) \phi_{\nu;\mathbf{q}}^R(\mathbf{k}_{\parallel} - \mathbf{q}_{\parallel}^e) \right] + \Gamma_{c,c;\mathbf{k}_{\parallel}} \quad (\text{D.25})$$

with a similar equation for $f_{\mathbf{k}}^h$. Again, only off-diagonal exciton correlations contribute. Scattering contributions are symbolized via $\Gamma_{c,c;\mathbf{k}_{\parallel}}$.

D.5. Solutions of the Terahertz-Bloch Equations

The terahertz-Bloch equations (TBE) (7.2) can be formulated for each center-of-mass momentum \mathbf{q} separately

$$\hbar \frac{\partial}{\partial t} \begin{pmatrix} S_x(\mathbf{q}_{\parallel}) \\ S_y(\mathbf{q}_{\parallel}) \\ S_z(\mathbf{q}_{\parallel}) \end{pmatrix} = \begin{pmatrix} 2J_{1s,2p;\mathbf{q}} A_{\text{THz}} \\ 0 \\ -\hbar\omega_{2p,1s;\mathbf{q}} \end{pmatrix} \times \begin{pmatrix} S_x(\mathbf{q}_{\parallel}) \\ S_y(\mathbf{q}_{\parallel}) \\ S_z(\mathbf{q}_{\parallel}) \end{pmatrix} - \begin{pmatrix} \gamma S_x(\mathbf{q}_{\parallel}) \\ \gamma S_y(\mathbf{q}_{\parallel}) \\ 0 \end{pmatrix} \quad (\text{D.26})$$

where $S_x(\mathbf{q}_{\parallel}) = \text{Re}[\Delta N_{1s2p}(\mathbf{q}_{\parallel})]$, $S_y(\mathbf{q}_{\parallel}) = \text{Im}[\Delta N_{1s2p}(\mathbf{q}_{\parallel})]$, and $S_z(\mathbf{q}_{\parallel}) = 1/2[\Delta N_{2p2p}(\mathbf{q}_{\parallel}) - \Delta N_{1s1s}(\mathbf{q}_{\parallel})]$. To solve the coupled equations, it is convenient to introduce the polarization, $S_-(\mathbf{q}_{\parallel}) \equiv S_x(\mathbf{q}_{\parallel}) + iS_y(\mathbf{q}_{\parallel})$, in a rotating frame $\tilde{S}_-(\mathbf{q}_{\parallel}) = S_-(\mathbf{q}_{\parallel}) \exp(i\omega_{\text{THz}}t)$ and define $\tilde{S}_x(\mathbf{q}_{\parallel}) = \text{Re}[\tilde{S}_-(\mathbf{q}_{\parallel})]$ and $\tilde{S}_y(\mathbf{q}_{\parallel}) = \text{Im}[\tilde{S}_-(\mathbf{q}_{\parallel})]$. As initial condition, we choose $(S_x(\mathbf{q}_{\parallel}), S_y(\mathbf{q}_{\parallel}), S_z(\mathbf{q}_{\parallel})) = (0, 0, -1/2)$

D. Exciton Basis

We solve Eq. (D.26) for continuous-wave THz excitation, $A_{\text{THz}} = A_0 \cos(2\pi\nu_{\text{THz}}t)$, and apply a RWA thus neglecting terms oscillating with $2\nu_{\text{THz}}$. For finite detuning $\Delta_{\mathbf{q}} = E_{2p,1s;\mathbf{q}} - \hbar\nu_{\text{THz}}$ and without dephasing, the solution is

$$\begin{aligned}\tilde{S}_x(\mathbf{q}_{\parallel}) &= \frac{(\Delta_{\mathbf{q}}/\hbar)\omega_{\text{R};\mathbf{q}}}{2\kappa_{1;\mathbf{q}}^2} [1 - \cos(\kappa_{1;\mathbf{q}}t)], \\ \tilde{S}_y(\mathbf{q}_{\parallel}) &= \frac{\omega_{\text{R};\mathbf{q}}}{2\kappa_{1;\mathbf{q}}} \sin(\kappa_{1;\mathbf{q}}t), \\ S_z(\mathbf{q}_{\parallel}) &= -\frac{1}{2\kappa_{1;\mathbf{q}}^2} [(\Delta_{\mathbf{q}}/\hbar)^2 + \omega_{\text{R};\mathbf{q}}^2 \cos(\kappa_{1;\mathbf{q}}t)]\end{aligned}\quad (\text{D.27})$$

with $\kappa_{1;\mathbf{q}} = \sqrt{\omega_{\text{R};\mathbf{q}}^2 + (\Delta_{\mathbf{q}}/\hbar)^2}$ and the Rabi frequency $\omega_{\text{R};\mathbf{q}} = J_{1s,2p;\mathbf{q}}A_0/\hbar$. For finite dephasing γ and resonant excitation, the solution is given by

$$\begin{aligned}\tilde{S}_x(\mathbf{q}_{\parallel}) &= 0, \\ \tilde{S}_y(\mathbf{q}_{\parallel}) &= \frac{1}{2} \frac{\omega_{\text{R}}}{\kappa_{2;\mathbf{q}}} \sin(\kappa_{2;\mathbf{q}}t) e^{-\gamma t/(2\hbar)}, \\ S_z(\mathbf{q}_{\parallel}) &= -\frac{1}{2} \left[\cos(\kappa_{2;\mathbf{q}}t) + \frac{\gamma/\hbar}{2\kappa_{2;\mathbf{q}}} \sin(\kappa_{2;\mathbf{q}}t) \right] e^{-\gamma t/(2\hbar)}\end{aligned}\quad (\text{D.28})$$

with $\kappa_{2;\mathbf{q}} = \sqrt{\omega_{\text{R};\mathbf{q}}^2 - (\gamma/(2\hbar))^2}$. For pulses $A_{\text{THz}} = A_{\text{env}}(t) \cos(2\pi\nu_{\text{THz}}t)$ with a slowly varying envelope A_{env} , the Rabi frequency $\omega_{\text{R};\mathbf{q}}(t) = J_{1s,2p;\mathbf{q}}A_{\text{env}}(t)/\hbar$ becomes time-dependent. The adiabatic solution is then obtained by replacing the arguments of the sine and cosine in Eqs. (D.27) and (D.28) with the time integral $\Omega_{\text{R};\mathbf{q}}(t) \equiv \int_{-\infty}^t \kappa_{\mathbf{q}}(u) du$. As long as the density is low and the exciton wavefunctions do not extend into the region of the Brillouin zone where the bandstructure is non-parabolic, the \mathbf{q}_{\parallel} -dependence in Eqs. (D.27),(D.28) is negligible.

Within the two-level approximation only the $1s$ - $2p$ excitonic-transition correlation $S_- = \sum_{\mathbf{q}_{\parallel}} \Delta N_{1s,2p}(\mathbf{q}_{\parallel})$ contributes to the THz current. Neglecting the scattering contributions γ_J and the \mathbf{q}_{\parallel} -dependence of excitonic transitions, Eq. (D.24) yields

$$\frac{\partial}{\partial t} J_{\text{THz}} = \frac{2}{\hbar \mathcal{S}} E_{2p,1s} J_{1s,2p} \text{Im} [S_-]. \quad (\text{D.29})$$

By writing $S_- = \tilde{S}_- e^{-i\omega_{\text{THz}}t}$, we can integrate $\text{Im} [\tilde{S}_- e^{-i\omega_{\text{THz}}t}]$ by parts and obtain

$$\begin{aligned}J_{\text{THz}} &= \frac{2}{\hbar \mathcal{S}} E_{2p,1s} J_{1s,2p} \text{Im} \left[\tilde{S}_- \frac{i}{\omega_{\text{THz}}} e^{-i\omega_{\text{THz}}t} - \int_{-\infty}^t du \frac{\partial \tilde{S}_-(u)}{\partial u} \frac{i}{\omega_{\text{THz}}} e^{-i\omega_{\text{THz}}u} \right] \\ &\approx \frac{2}{\mathcal{S}} \frac{\omega_{2p,1s}}{\omega_{\text{THz}}} \text{Re} [S_-]\end{aligned}\quad (\text{D.30})$$

where we assumed that \tilde{S}_- varies slowly in time, which is valid when the Rabi frequency is much smaller than the THz frequency. Thus, only the real part, $\text{Re} [S_-]$, contributes to J_{THz} .

Bibliography

- [1] K. Leo, M. Wegener, J. Shah, D. S. Chemla, E. O. Göbel, T. C. Damen, S. Schmitt-Rink, and W. Schäfer, “Effects of coherent polarization interactions on time-resolved degenerate four-wave mixing”, *Phys. Rev. Lett.* **65**, 1340 (1990).
- [2] Y. Z. Hu, R. Binder, S. W. Koch, S. T. Cundiff, H. Wang, and D. G. Steel, “Excitation and polarization effects in semiconductor four-wave-mixing spectroscopy”, *Phys. Rev. B* **49**, 14382 (1994).
- [3] L. Bányai, D. B. T. Thoai, E. Reitsamer, H. Haug, D. Steinbach, M. U. Wehner, M. Wegener, T. Marschner, and W. Stolz, “Exciton-phonon quantum kinetics: Evidence of memory effects in bulk gas”, *Phys. Rev. Lett.* **75**, 2188 (1995).
- [4] A. Mysyrowicz, D. Hulin, A. Antonetti, A. Migus, and W. T. Masselink, “‘dressed excitons’ in a multiple-quantum-well structure evidence for an optical stark effect with femtosecond response time”, *Phys. Rev. Lett.* **56**, 2748 (1986).
- [5] C. Sieh, T. Meier, F. Jahnke, A. Knorr, S. W. Koch, P. Brick, M. Hübner, C. Ell, J. Prineas, G. Khitrova, and H. M. Gibbs, “Coulomb memory signatures in the excitonic optical stark effect”, *Phys. Rev. Lett.* **82**, 3112 (1999).
- [6] M. Kira and S. W. Koch, “Many-body correlations and excitonic effects in semiconductor spectroscopy”, *Progress in Quantum Electronics* **30**, 155 (2006).
- [7] S. W. Koch, M. Kira, G. Khitrova, and H. M. Gibbs, “Semiconductor excitons in new light”, *Nature Mater.* **5**, 523 (2006).
- [8] H. Haug and S. W. Koch, *Quantum Theory of the Optical and Electronic Properties of Semiconductors* (World Scientific Publ., Singapore, 2004 (fourth edition)).
- [9] T. Y. Chang and T. J. Bridges, “Laser action at 452, 496, and 541 μm in optically pumped CH_3F ”, *Optics Communications* **1**, 423 (1970).
- [10] L. R. Elias, G. Ramian, J. Hu, and A. Amir, “Observation of single-mode operation in a free-electron laser”, *Phys. Rev. Lett.* **57**, 424 (1986).
- [11] E. Bründermann, D. R. Chamberlin, and E. E. Haller, “High duty cycle and continuous terahertz emission from germanium”, *Appl. Phys. Lett.* **76**, 2991 (2000).
- [12] M. Tonouchi, “Cutting-edge terahertz technology”, *Nature Photonics* **1**, 97 (2007).

- [13] C. Kübler, R. Huber, and A. Leitenstorfer, “Ultrabroadband terahertz pulses: generation and field-resolved detection”, *Semiconductor Science Technology* **20**, 128 (2005).
- [14] R. A. Kaindl, M. A. Carnahan, D. Hägele, R. Lövenich, and D. S. Chemla, “Ultrafast terahertz probes of transient conducting and insulating phases in an electron-hole gas”, *Nature (London)* **423**, 734 (2003).
- [15] I. Galbraith, R. Chari, S. Pellegrini, P. J. Phillips, C. J. Dent, A. F. van der Meer, D. G. Clarke, A. K. Kar, G. S. Buller, C. R. Pidgeon, B. N. Murdin, J. Allam, and G. Strasser, “Excitonic signatures in the photoluminescence and terahertz absorption of a $\text{GaAs}/\text{Al}_x\text{Ga}_{1-x}\text{As}$ multiple quantum well”, *Phys. Rev. B* **71**, 073302 (2005).
- [16] R. Huber, R. A. Kaindl, B. A. Schmid, and D. S. Chemla, “Broadband terahertz study of excitonic resonances in the high-density regime in $\text{GaAs}/\text{Al}_x\text{Ga}_{1-x}\text{As}$ quantum wells”, *Phys. Rev. B* **72**, 161314 (2005).
- [17] M. Kubouchi, K. Yoshioka, R. Shimano, A. Mysyrowicz, and M. Kuwata-Gonokami, “Study of orthoexciton-to-paraexciton conversion in Cu_2O by excitonic Lyman spectroscopy”, *Phys. Rev. Lett.* **94**, 016403 (2005).
- [18] R. Huber, B. A. Schmid, Y. R. Shen, D. S. Chemla, and R. A. Kaindl, “Stimulated terahertz emission from intraexcitonic transitions in Cu_2O ”, *Phys. Rev. Lett.* **96**, 017402 (2006).
- [19] M. Beard, G. Turner, and C. Schmuttenmaer, “Terahertz spectroscopy”, *Journal of Physical Chemistry B* **106**, 7146 (2002).
- [20] N. Nagai, R. Kumazawa, and R. Fukasawa, “Direct evidence of inter-molecular vibrations by THz spectroscopy”, *Chemical Physics Letters* **413**, 495 (2005).
- [21] B. Ferguson and X.-C. Zhang, “Materials for terahertz science and technology”, *Nature Materials* **1**, 26 (2002).
- [22] M. Kira, W. Hoyer, T. Stroucken, and S. W. Koch, “Exciton formation in semiconductors and the influence of a photonic environment”, *Phys. Rev. Lett.* **87**, 176401 (2001).
- [23] W. Hoyer, M. Kira, and S. W. Koch, “Influence of Coulomb and phonon interaction on the exciton formation dynamics in semiconductor heterostructures”, *Phys. Rev. B* **67**, 155113 (2003).
- [24] M. Kira, W. Hoyer, and S. W. Koch, “Terahertz signatures of the exciton formation dynamics in non-resonantly excited semiconductors”, *Solid State Communications* **129**, 733 (2004).

- [25] M. Kira and S. W. Koch, “Exciton-population inversion and terahertz gain in semiconductors excited to resonance”, *Phys. Rev. Lett.* **93**, 076402 (2004).
- [26] M. Kira and S. W. Koch, “Quantum-optical spectroscopy of semiconductors”, *Phys. Rev. A* **73**, 013813 (2006).
- [27] S. D. Ganichev and W. Prettl, *Intense terahertz excitation of semiconductors* (Oxford Univ. Press, 2006).
- [28] C. W. Luo, K. Reimann, M. Woerner, T. Elsaesser, R. Hey, and K. H. Ploog, “Phase-resolved nonlinear response of a two-dimensional electron gas under femtosecond intersubband excitation”, *Phys. Rev. Lett.* **92**, 047402 (2004).
- [29] J. Kono, M. Y. Su, T. Inoshita, T. Noda, M. S. Sherwin, S. J. Allen, Jr., and H. Sakaki, “Resonant terahertz optical sideband generation from confined magnetoexcitons”, *Phys. Rev. Lett.* **79**, 1758 (1997).
- [30] A. H. Chin, J. M. Bakker, and J. Kono, “Ultrafast electroabsorption at the transition between classical and quantum response”, *Phys. Rev. Lett.* **85**, 3293 (2000).
- [31] A. H. Chin, O. G. Calderón, and J. Kono, “Extreme midinfrared nonlinear optics in semiconductors”, *Phys. Rev. Lett.* **86**, 3292 (2001).
- [32] K. B. Nordstrom, K. Johnsen, S. J. Allen, A.-P. Jauho, B. Birnir, J. Kono, T. Noda, H. Akiyama, and H. Sakaki, “Excitonic dynamical Franz-Keldysh effect”, *Phys. Rev. Lett.* **81**, 457 (1998).
- [33] J. F. Dynes, M. D. Frogley, M. Beck, J. Faist, and C. C. Phillips, “ac Stark splitting and quantum interference with intersubband transitions in quantum wells”, *Phys. Rev. Lett.* **94**, 157403 (2005).
- [34] M. Kira, F. Jahnke, and S. W. Koch, “Microscopic theory of excitonic signatures in semiconductor photoluminescence”, *Phys. Rev. Lett.* **81**, 3263 (1998).
- [35] R. Huber, F. Tauser, A. Brodschelm, M. Bichler, G. Abstreiter, and A. Leitenstorfer, “How many-particle interactions develop after ultrafast excitation of an electron-hole plasma”, *Nature (London)* **414**, 286 (2001).
- [36] C. Cohen-Tannoudji, J. Dupont-Roc, and G. Grynberg, *Photons and Atoms - Introduction to Quantum Electrodynamics* (Wiley, 1989 (third edition)).
- [37] M. Kira, F. Jahnke, W. Hoyer, and S. W. Koch, “Quantum theory of spontaneous emission and coherent effects in semiconductor microstructures”, *Prog. Quantum Electron.* **23**, 189 (1999).
- [38] M. Kira, “Lecture notes on excitons in semiconductors, lecture in physics, philipps-university marburg”, (2004).

- [39] P. Y. Yu and M. Cardona, *Fundamentals of Semiconductors* (Springer, Berlin, Heidelberg, New York, 1996).
- [40] W. Hoyer, A. Knorr, J. V. Moloney, E. M. Wright, M. Kira, and S. W. Koch, “Photoluminescence and terahertz emission from femtosecond laser-induced plasma channels”, *Phys. Rev. Lett.* **94**, 115004 (2005).
- [41] W. Hoyer, J. V. Moloney, E. M. Wright, M. Kira, and S. W. Koch, “Thermal wakefield oscillations of laser-induced plasma channels and their spectral signatures in luminescence”, *Journal of Physics Conference Series* **11**, 153 (2005).
- [42] H. W. Wyld, Jr. and B. D. Fried, “Quantum mechanical kinetic equations”, *Annals of Physics* **23**, 374 (1963).
- [43] J. Fricke, “Transport equations including many-particle correlations for an arbitrary quantum system: A general formalism”, *Annals of Physics* **252**, 479 (1996).
- [44] W. Hoyer, M. Kira, and S. W. Koch, in *Nonequilibrium Physics at Short Time Scales*, K. Morawetz, ed. (Springer, Berlin, 2004), pp. 309–335.
- [45] M. Kira and S. W. Koch, “Microscopic theory of optical excitations, photoluminescence, and terahertz response in semiconductors”, *Eur. J. Phys. D* **36**, 143 (2005).
- [46] H. J. M. F. E. Harris and D. L. Freeman, *Algebraic and diagrammatic methods in many-fermion theory* (Oxford Press, New York, 1992 (first edition)).
- [47] M. Kira, W. Hoyer, and S. W. Koch, “Microscopic theory of the semiconductor terahertz response”, *phys. stat. sol. (b)* **238**, 443 (2003).
- [48] J. E. Sipe and E. Ghahramani, “Nonlinear optical response of semiconductors in the independent-particle approximation”, *Phys. Rev. B* **48**, 11705 (1993).
- [49] R. J. Elliott, “Intensity of optical absorption by excitons”, *Phys. Rev.* **108**, 1384 (1957).
- [50] T. Stroucken, A. Knorr, P. Thomas, and S. W. Koch, “Coherent dynamics of radiatively coupled quantum-well excitons”, *Phys. Rev. B* **53**, 2026 (1996).
- [51] F. Jahnke, M. Kira, S. W. Koch, G. Khitrova, E. K. Lindmark, T. R. Nelson, Jr., D. V. Wick, J. D. Berger, O. Lyngnes, H. M. Gibbs, and K. Tai, “Excitonic nonlinearities of semiconductor microcavities in the nonperturbative regime”, *Phys. Rev. Lett.* **77**, 5257 (1996).
- [52] X. Li, T. Zhang, C. N. Borca, and S. T. Cundiff, “Many-body interactions in semiconductors probed by optical two-dimensional fourier transform spectroscopy”, *Phys. Rev. Lett.* **96**, 057406 (2006).

- [53] I. Kuznetsova, P. Thomas, T. Meier, T. Zhang, X. Li, R. P. Mirin, and S. T. Cundiff, “Signatures of many-particle correlations in two-dimensional fourier-transform spectra of semiconductor nanostructures”, *Solid State Communications* **142**, 154 (2007).
- [54] H. Kamada, H. Gotoh, J. Temmyo, T. Takagahara, and H. Ando, “Exciton rabi oscillation in a single quantum dot”, *Phys. Rev. Lett.* **87**, 246401 (2001).
- [55] X. Li, Y. Wu, D. Steel, D. Gammon, T. H. Stievater, D. S. Katzer, D. Park, C. Piermarocchi, and L. J. Sham, “An all-optical quantum gate in a semiconductor quantum dot”, *Science* **301**, 809 (2003).
- [56] R. D. R. Bhat and J. E. Sipe, “Optically injected spin currents in semiconductors”, *Phys. Rev. Lett.* **85**, 5432 (2000).
- [57] J. Hübner, W. W. Rühle, M. Klude, D. Hommel, R. D. Bhat, J. E. Sipe, and H. M. van Driel, “Direct observation of optically injected spin-polarized currents in semiconductors”, *Phys. Rev. Lett.* **90**, 216601 (2003).
- [58] R. Elliott, in *Polarons and Excitons* (Oliver and Boyd, Edinburgh, 1963), pp. 269–293.
- [59] F. Jahnke, M. Ruopp, M. Kira, and S. W. Koch, “Ultrashort pulse propagation and excitonic nonlinearities in semiconductor microcavities”, *Advances in Solid State Physics* 37, *Advances in Solid State Physics, Volume 37* **37**, 191 (1998).
- [60] B. Cole, J. Williams, B. King, M. Sherwin, and C. Stanley, “Coherent manipulation of semiconductor quantum bits with terahertz radiation”, *Nature (London)* **410**, 60 (2001).
- [61] S. Schmitt-Rink, D. S. Chemla, and D. A. B. Miller, “Linear and nonlinear optical properties of semiconductor quantum wells”, *Advances in Physics* **38**, 89 (1989).
- [62] D. S. Chemla and J. Shah, “Many-body and correlation effects in semiconductors”, *Nature (London)* **411**, 549 (2001).
- [63] R. Kumar, A. S. Vengurlekar, S. S. Prabhu, J. Shah, and L. N. Pfeiffer, “Picosecond time evolution of free electron-hole pairs into excitons in gas quantum wells”, *Phys. Rev. B* **54**, 4891 (1996).
- [64] S. Nüsse, P. Haring Bolivar, H. Kurz, V. Klimov, and F. Levy, “Carrier cooling and exciton formation in gas”, *Phys. Rev. B* **56**, 4578 (1997).
- [65] W. Hoyer, C. Ell, M. Kira, S. W. Koch, S. Chatterjee, S. Mosor, G. Khitrova, H. M. Gibbs, and H. Stolz, “Many-body dynamics and exciton formation studied by time-resolved photoluminescence”, *Phys. Rev. B* **72**, 075324 (2005).

Bibliography

- [66] M. Umlauff, J. Hoffmann, H. Kalt, W. Langbein, J. M. Hvam, M. Scholl, J. Söllner, M. Heuken, B. Jobst, and D. Hommel, “Direct observation of free-exciton thermalization in quantum-well structures”, *Phys. Rev. B* **57**, 1390 (1998).
- [67] S. Siggelkow, W. Hoyer, M. Kira, and S. W. Koch, “Exciton formation and stability in semiconductor heterostructures”, *Phys. Rev. B* **69**, 073104 (2004).
- [68] F. Stern, “Polarizability of a two-dimensional electron gas”, *Phys. Rev. Lett.* **18**, 546 (1967).
- [69] Y. Yacoby, “High-frequency franz-keldysh effect”, *Physical Review* **169**, 610 (1968).
- [70] A. P. Jauho and K. Johnsen, “Dynamical franz-keldysh effect”, *Phys. Rev. Lett.* **76**, 4576 (1996).
- [71] K. Johnsen and A.-P. Jauho, “Linear optical absorption spectra of mesoscopic structures in intense thz fields: Free-particle properties”, *Phys. Rev. B* **57**, 8860 (1998).
- [72] A. Srivastava, R. Srivastava, J. Wang, and J. Kono, “Laser-induced above-band-gap transparency in gaas”, *Phys. Rev. Lett.* **93**, 157401 (2004).
- [73] K. Johnsen and A.-P. Jauho, “Quasienergy spectroscopy of excitons”, *Phys. Rev. Lett.* **83**, 1207 (1999).
- [74] S. Hughes and D. S. Citrin, “Creation of highly anisotropic wave packets in quantum wells: Dynamical franz-keldysh effect in the optical and terahertz regimes”, *Phys. Rev. B* **59**, 5288 (1999).
- [75] C. J. Dent, B. N. Murdin, and I. Galbraith, “Phase and intensity dependence of the dynamical franz-keldysh effect”, *Phys. Rev. B* **67**, 165312 (2003).
- [76] J. R. Danielson, Y.-S. Lee, J. P. Prineas, J. T. Steiner, M. Kira, and S. W. Koch, “Interaction of strong single-cycle terahertz pulses with semiconductor quantum wells”, *Phys. Rev. Lett.* **99**, 237401 (2007).
- [77] A. V. Maslov and D. S. Citrin, “Optical absorption and sideband generation in quantum wells driven by a terahertz electric field”, *Phys. Rev. B* **62**, 16686 (2000).
- [78] T. Müller, W. Parz, G. Strasser, and K. Unterrainer, “Pulse-induced quantum interference of intersubband transitions in coupled quantum wells”, *Appl. Phys. Lett.* **84**, 64 (2004).
- [79] S. G. Carter, V. Birkedal, C. S. Wang, L. A. Coldren, A. V. Maslov, D. S. Citrin, and M. S. Sherwin, “Quantum coherence in an optical modulator”, *Science* **310**, 651 (2005).

- [80] T. J. M. Boyd and J. J. Sanderson, *The Physics of Plasmas* (Physics of Plasmas, 2003).
- [81] C. Cohen-Tannoudji, J. Dupont-Roc, and G. Grynberg, *Atom-photon interactions* (Wiley, 1992 (third edition)).
- [82] M. Wegener, *Extreme Nonlinear Optics* (Springer, Berlin, Heidelberg, New York, 2005).
- [83] T. Tritzschler, O. D. Mücke, and M. Wegener, “Extreme nonlinear optics of two-level systems”, *Phys. Rev. A* **68**, 033404 (2003).
- [84] D. Golde, T. Meier, and S. W. Koch, “Microscopic analysis of extreme nonlinear optics in semiconductor nanostructures”, *J. Opt. Soc. Am. B* **23**, 2559 (2006).
- [85] J. S. Bakos, “Ac stark effect and multiphoton processes in atoms”, *Physics Reports* **31**, 209 (1977).
- [86] K. Bergmann, H. Theuer, and B. W. Shore, “Coherent population transfer among quantum states of atoms and molecules”, *Reviews of Modern Physics* **70**, 1003 (1998).
- [87] N. V. Vitanov and S. Stenholm, “Analytic properties and effective two-level problems in stimulated raman adiabatic passage”, *Phys. Rev. A* **55**, 648 (1997).
- [88] H. J. Metcalf, P. V. D. Straten, and D. S. Weiss, “Laser cooling and trapping”, *Physics Today* **54**, 020000 (2001).
- [89] L. Allen and J. Eberly, *Optical resonance and two-level atoms* (John Wiley and Sons, Inc., New York, 1975).
- [90] I. I. Rabi, “Space quantization in a gyrating magnetic field”, *Phys. Rev.* **51**, 652 (1937).
- [91] I. I. Rabi, S. Millman, P. Kusch, and J. R. Zacharias, “The molecular beam resonance method for measuring nuclear magnetic moments the magnetic moments of $li63$, $li73$ and $f199$ ”, *Phys. Rev.* **55**, 526 (1939).
- [92] S. T. Cundiff, A. Knorr, J. Feldmann, S. W. Koch, E. O. Göbel, and H. Nickel, “Rabi flopping in semiconductors”, *Phys. Rev. Lett.* **73**, 1178 (1994).
- [93] B. R. Mollow, “Power spectrum of light scattered by two-level systems”, *Physical Review* **188**, 1969 (1969).
- [94] J. T. Steiner, M. Kira, and S. W. Koch, “Optical nonlinearities and rabi flopping of an exciton population in a semiconductor interacting with strong terahertz fields”, *Phys. Rev. B* **77**, 165308 (2008).

- [95] J. W. Davenport, “Ultraviolet photoionization cross sections for n^2 and co ”, Phys. Rev. Lett. **36**, 945 (1976).
- [96] G. Mainfray and G. Manus, “Multiphoton ionization of atoms”, Reports on Progress in Physics **54**, 1333 (1991).
- [97] R. R. Freeman, P. H. Bucksbaum, H. Milchberg, S. Darack, and S. Schumacher, “Above-threshold ionization with subpicosecond laser pulses”, Phys. Rev. Lett. **59**, 1092 (1987).
- [98] P. B. Corkum, N. H. Burnett, and F. Brunel, “Above-threshold ionization in the long-wavelength limit”, Phys. Rev. Lett. **62**, 1259 (1989).
- [99] P. M. Paul, E. S. Toma, P. Breger, G. Mullot, F. Augé, P. Balcou, H. G. Muller, and P. Agostini, “Observation of a train of attosecond pulses from high harmonic generation”, Science **292**, 1689 (2001).
- [100] C. Winterfeldt, C. Spielmann, and G. Gerber, “Colloquium: Optimal control of high-harmonic generation”, Reviews of Modern Physics **80**, 117 (2008).
- [101] E. A. Gibson, A. Paul, N. Wagner, R. Tobey, S. Backus, I. P. Christov, M. M. Murnane, and H. C. Kapteyn, “High-order harmonic generation up to 250 eV from highly ionized argon”, Phys. Rev. Lett. **92**, 033001 (2004).
- [102] A. de Bohan, P. Antoine, D. B. Milošević, and B. Piraux, “Phase-dependent harmonic emission with ultrashort laser pulses”, Phys. Rev. Lett. **81**, 1837 (1998).
- [103] A. Baltuška, T. Udem, M. Uiberacker, M. Hentschel, E. Goulielmakis, C. Gohle, R. Holzwarth, V. S. Yakovlev, A. Scrinzi, T. W. Hänsch, and F. Krausz, “Attosecond control of electronic processes by intense light fields”, Nature **421**, 611 (2003).
- [104] J. Itatani, J. Levesque, D. Zeidler, H. Niikura, H. Pépin, J. C. Kieffer, P. B. Corkum, and D. M. Villeneuve, “Tomographic imaging of molecular orbitals”, Nature **432**, 867 (2004).
- [105] P. W. Baumeister, “Optical absorption of cuprous oxide”, Phys. Rev. **121**, 359 (1961).
- [106] G. M. Kavoulakis, Y.-C. Chang, and G. Baym, “Fine structure of excitons in cu_2o ”, Phys. Rev. B **55**, 7593 (1997).
- [107] R. J. Elliott, “Symmetry of excitons in cu_2o ”, Phys. Rev. **124**, 340 (1961).
- [108] D. W. Snoke, J. P. Wolfe, and A. Mysyrowicz, “Evidence for bose-einstein condensation of a two-component exciton gas”, Phys. Rev. Lett. **64**, 2543 (1990).
- [109] K. E. O’Hara and J. P. Wolfe, “Relaxation kinetics of excitons in cuprous oxide”, Phys. Rev. B **62**, 12909 (2000).

- [110] S. A. Moskalenko, D. W. Snoke, and K. Burnett, “Bose-einstein condensation of excitons and biexcitons and coherent nonlinear optics with excitons”, *Physics Today* **54**, 050000 (2001).
- [111] M. Jörger, T. Fleck, C. Klingshirn, and R. von Baltz, “Midinfrared properties of cuprous oxide: High-order lattice vibrations and intraexcitonic transitions of the 1s paraexciton”, *Phys. Rev. B* **71**, 235210 (2005).
- [112] M. French, R. Schwartz, R. Redmer, and H. Stolz, “Electronic band structure of Cu_2O by spin density functional theory”, *J. Phys.: Condens. Matter* **21**, 015502 (2009).
- [113] K. Johnsen and G. M. Kavoulakis, “Probing bose-einstein condensation of excitons with electromagnetic radiation”, *Phys. Rev. Lett.* **86**, 858 (2001).
- [114] T. Kampfrath, J. Nötzold, and M. Wolf, “Sampling of broadband terahertz pulses with thick electro-optic crystals”, *Appl. Phys. Lett.* **90**, 231113 (2007).
- [115] N. W. Ashcroft and S. Rodriguez, “Solid state physics”, *American Journal of Physics* **46**, 116 (1978).
- [116] S. D. Ganichev, E. V. Beregulin, and I. D. Yaroshetskii (1993), vol. 1985 of *Society of Photo-Optical Instrumentation Engineers (SPIE) Conference Series*, pp. 523–525.
- [117] Z. Dobrovolskis, K. Grigoras, and A. Krotkus, “Measurement of the hot-electron conductivity in semiconductors using ultrafast electric pulses”, *Applied Physics A: Materials Science & Processing* **48**, 245 (1989).
- [118] W. Hoyer, “Quantentheorie zu exzitonenbildung und photolumineszenz in halbleitern”, PhD Thesis, Philipps-University Marburg (2002).

Bibliography

Wissenschaftlicher Werdegang

Name	Johannes T. Steiner
Geburtsdatum	30. Januar 1980
Geburtsort	Attendorn
05/1999	Abitur am Albert-Schweitzer-Gymnasium in Plettenberg
10/2000	Beginn des Diplom-Studiengangs Physik an der Philipps-Universität in Marburg
10/2002	Vordiplom im Fach Physik
10/2002	Vordiplom im Fach Mathematik
09/2005	Diplom im Fach Physik
01/2006	Beginn der Promotion in der AG "Theoretische Halbleiterphysik" an der Philipps-Universität in Marburg